

# **Multi-scale Modelling of Oxygen Carriers in Chemical Looping Combustion Process**

by

Yue Yuan

A thesis  
presented to the University of Waterloo  
in fulfillment of the  
thesis requirement for the degree of  
Doctor of Philosophy  
in  
Chemical Engineering

Waterloo, Ontario, Canada, 2021

©Yue Yuan 2021

## Examining Committee Member

The following served on the Examining Committee for this thesis. The decision of the Examining Committee is by majority vote.

External Examiner	Hugo de Lasa Professor Chemical and Biomedical Engineering, University of Western Ontario
Supervisors	Luis Ricardez Sandoval Associate Professor Chemical Engineering, University of Waterloo
	Xiuqing Dong Professor Chemical Engineering, Tianjin University
Internal Member	Eric Croiset Professor Chemical Engineering, University of Waterloo
	Aiping Yu Associate Professor Chemical Engineering, University of Waterloo
	Haoxi Jiang Professor Chemical Engineering, Tianjin University
Internal-external Member	Marcel Nooijen Professor Chemistry, University of Waterloo

## **AUTHOR'S DECLARATION**

This thesis consists of material all of which I authored or co-authored: see Statement of Contributions included in the thesis. This is a true copy of the thesis, including any required final revisions, as accepted by my examiners.

I understand that my thesis may be made electronically available to the public.

## Statement of Contributions

Chapters 1 and 7 were written entirely by me. My supervisor, Luis Ricardez-Sandoval, provided suggestions and recommendations regarding their contents.

**Chapter 2** of this thesis consists of partial content of the following paper that was co-authored by myself, my colleague Huabei You and my supervisor, Prof. Luis Ricardez-Sandoval.

“Recent advances on first-principles modeling for the design of materials in CO<sub>2</sub> capture technologies.” *Chinese Journal of Chemical Engineering*, 2019, 27, 1554-1565. <https://doi.org/10.1016/j.cjche.2018.10.017>

That paper was written majorly by me, a section of this paper was written by Huabei You. My supervisor Prof. Luis Ricardez-Sandoval supervised this work.

**Chapter 3** of this thesis consists of the following paper that was co-authored by myself and my supervisors, Prof. Luis A. Ricardez-Sandoval and Prof. Xiuqin Dong.

“A density functional theory analysis on syngas adsorption on NiO (100) surface.” *Applied Surface Science*, 2019, 498, 143782. <https://doi.org/10.1016/j.apsusc.2019.143782>

That paper was written entirely by myself and edited by my supervisors.

**Chapter 4** of this thesis consists of the following paper that was co-authored by myself and my supervisors, Prof. Luis Ricardez-Sandoval and Prof. Xiuqin Dong.

“A multi-scale simulation of syngas combustion reactions by Ni-based oxygen carriers for chemical looping combustion.” *Applied Surface Science*, 2020, 531, 147277. <https://doi.org/10.1016/j.apsusc.2020.147277>

That paper was written entirely by myself and edited by my supervisors.

**Chapter 5** of this thesis consists of the following paper that was co-authored by myself and my supervisors, Prof. Luis Ricardez-Sandoval and Prof. Xiuqin Dong.

“Insights into syngas combustion on a defective NiO surface for chemical looping combustion: oxygen migration and vacancy effects.” *The Journal of Physical Chemistry C*, 2020. <https://doi.org/10.1021/acs.jpcc.0c07144>

That paper was written entirely by myself and edited by my supervisors.

Reprinted (adapted) with permission from (Yuan, Yue, Xiuqin Dong, and Luis Ricardez-Sandoval. "Insights into Syngas Combustion on a Defective NiO Surface for Chemical Looping Combustion: Oxygen Migration and Vacancy Effects." *The Journal of Physical Chemistry C* (2020)). Copyright (2020) American Chemical Society.

**Chapter 6** of this thesis is an unpublished manuscript that was co-authored by myself and my supervisors. I devised the idea and conducted simulations. Prof. Luis Ricardez-Sandoval supervised the work. Prof. Xiuqin Dong revised this work.

## ABSTRACT

Climate change is one of the major concerns affecting society. Given the severe effects of global warming, efficient CO<sub>2</sub> capture and storage (CCS) technologies have become an urgent necessity. One of the major challenges of CO<sub>2</sub> disposal is the intensive energy consumption associated with current CO<sub>2</sub> capture technologies. Chemical looping combustion (CLC) is an emerging technology that requires lower energy expenditure compared to other CO<sub>2</sub> capture methods. The key is to use an oxygen carrier (OC), which avoids direct contact between air and a fossil fuel. OC development is thus key to improve CLC performance.

Although numerous studies have been reported in the literature regarding OC development, the majority of these studies entail experimental investigations. Theoretical studies on this subject have been limited. As a result, the reaction mechanisms, the microscopic insights into the OC performance and the significant factors influencing OC performance are still not clear even for some of the most popular OCs such as NiO. In addition, multi-scale simulations combining density functional theory (DFT) analysis and microscopic modelling in this area are scarce.

This study provides a comprehensive investigation of syngas adsorption and combustion, using NiO as the OC through developing multi-scale models that take into account the effects of oxygen vacancies and nearest neighbours.

An analysis of the syngas adsorption principle on NiO while considering the neighbouring effects was considered first. In particular, this work described the adsorption principles of syngas (i.e. CO and H<sub>2</sub>) on a clean NiO (100) surface under single and multiple first nearest neighbouring effects using DFT analysis. The results showed that the adsorption stability of CO and H<sub>2</sub> is mostly weakened by the first neighbour compared to the second, third and fourth neighbours. With the same species as nearest neighbours (i.e. uniform adsorption), syngas adsorption stability was reduced when the number of neighbours increased. However, when compared to uniform adsorption, the adsorption stability of CO and H<sub>2</sub> was slightly stronger with neighbouring sites occupied with different species (hybrid adsorption). In addition, a lower degree of symmetry seemed to strengthen CO and H<sub>2</sub> adsorption. Results from this DFT study showed that the adsorption stability of CO and H<sub>2</sub> in the presence of neighbours is highly related to steric, hybrid and symmetry effects. This study is key for the development of a multi-scale model for this system.

Next, DFT calculations of syngas combustion with NiO were conducted to reveal the elementary reaction mechanisms: CO oxidation proceeds through a one-step mechanism while H<sub>2</sub> oxidation proceeds through a three-step mechanism. Among them, H<sub>2</sub> decomposition was proven to be the controlling step that dominated the overall syngas combustion process. These results were used to build a DFT-based mean-field (MF) multi-scale model, which verified the accuracy of the proposed reaction kinetics. The results from this multi-scale model showed that high temperatures and low pressures will lead to high CO<sub>2</sub>/H<sub>2</sub>O product ratios. The reaction kinetics obtained from this study were used to further analyze other factors that affect OC performance.

A theoretical analysis of the studied system was conducted to gain insights on the vacancy effects on syngas adsorption, syngas oxidation and oxygen migration. The adsorption analysis and the proposed reaction mechanisms showed that the presence of the defective sites benefit the syngas oxidation reactions. In particular, H<sub>2</sub> oxidation changed from a 3-step process on a perfect surface (i.e. without vacancies) to a 2-step process on a defective surface. The CO oxidation reaction was shown to dominate the overall syngas oxidation process. In addition, the outward diffusion direction of oxygen migration was observed from the bulk side to the surface. The resulting reaction kinetics and the vacancy effects were validated against experimental data using the DFT-based MF multi-scale model.

The neighbouring effects on syngas oxidation were studied next using DFT calculations. An analysis on the activation energy showed that CO oxidation is slightly weakened by the CO neighbours, but it is enhanced in the presence of H<sub>2</sub> neighbours. Meanwhile, H<sub>2</sub> decomposition, hydrogen migration and H<sub>2</sub>O formation were mostly enhanced by their neighbours, with the exception of the three H<sub>2</sub> neighbour configuration. In addition, the CO neighbours resulted in more significant changes in the reaction equilibrium. The resulting neighbouring effects on syngas adsorption and combustion were used to establish a DFT-based kinetic Monte Carlo (kMC) multi-scale model. The results from this model indicated that CO adsorption is the most sensitive step to neighbouring effects while CO oxidation is the least sensitive. OC conversion is enhanced by the neighbouring effects on CO adsorption and H<sub>2</sub>O formation. Moreover, the neighbouring effects on the H<sub>2</sub> chemisorption weakened the OC conversion. The significant changes observed in OC conversion with and without neighbouring effects implied that this studied phenomena are key to predict a realistic OC performance.

Overall, the multi-scale models developed in this research revealed the adsorption principle and reaction mechanisms of the studied system, while also considering the critical influencing factors of vacancies and nearest neighbours. Electronic analyses were additionally conducted on each step in this investigation to further support the conclusions. The vacancies generally enhance the OC performance. The neighbouring effects, meanwhile, benefit the syngas oxidations but weaken the syngas adsorption process. The significant changes caused by the effects of vacancies and the nearest neighbours implied that it is critical to consider these effects to capture the OC performance. The developed multi-scale models related the electronic-distribution-based DFT results to the experimental observations at the macroscopic scale. Therefore, the challenge of validating the results from DFT analyses by the experimental observations were overcome. Additionally, the developed multi-scale models also estimated the reaction kinetics and their influencing factors under practical operating conditions. The proposed DFT-based kMC model provided a method to consider the dynamic effects caused by the changing surface environment. This multi-scale study served to fill some of the current gaps in the literature in this area.

**Key words:** Chemical looping combustion; Oxygen carrier; Density functional theory; Kinetic Monte Carlo; Mean-field; Multi-scale simulation

## Acknowledgement

I would express my sincere gratitude to my supervisors, Prof. Luis Ricardez-Sandoval and Prof. Xiuqin Dong. Thank them for their continuous support, patience and suggestions during my PhD study.

I would also like to thank my examining committee: Prof. Hugo de Lasa, Prof. Marcel Nooijen, Prof. Eric Croiset, Prof. Aiping Yu, and Prof. Haoxi Jiang for their time and valuable comments.

Thanks to my master-period supervisor Prof. Minhua Zhang for his support and guidance all along. I also wish to acknowledge all the other professors in my group that supported me for my PhD study: Prof. Jiyan Zhang, Prof. Yifei Chen, Prof. Yingzhe Yu, Prof. Zhongfeng Geng and Prof. Jing Ma.

Thanks to all of my group members from both Tianjin University and University of Waterloo for their help and company. Particularly, I would like to thank Dr. Jingde Li, Dr. Grigoriy Kimaev, Dr. Mina Rafiei, Donovan Chaffart, Kavitha Menon, Mahshad Valipour, Huabei You, Han Wang, Ilse Mariana, Manuel Alejandro, Marco Antonio Lucio Hernandez, Yael Izamal Valdez Navarro, Oscar Palma Flores, Gabriel Patron, Yanshuo Peng, Rui Yao, Dr. Wenyi Wang, Dr. Dan Fan, Dr. Hao Gong, Dr. Lihang Chen.

In the end, I would like to express my appreciation to my beloved family, my parents, Shizhong Yuan, Tao Ma and my deceased husband Di Li. I cannot go through this long journey towards this milestone without their support, especially my dearest husband who should have been here with me for this special time. Hopefully, you can still feel my appreciation and love wherever you are now.



## Table of Contents

Examining Committee Member.....	ii
AUTHOR'S DECLARATION .....	iii
Statement of Contributions .....	iv
ABSTRACT.....	vi
Acknowledgement .....	viii
List of Figures .....	xii
List of Tables .....	xvi
List of Acronyms .....	xvii
List of Symbols.....	xviii
Chapter 1 Introduction and Motivation.....	1
1.1 Motivation .....	1
1.2 Research Objectives .....	4
1.3 Research Contributions .....	5
1.4 Outline.....	6
Chapter 2 Background and Literature Review.....	8
2.1 Chemical looping combustion.....	8
2.2 Oxygen carrier.....	11
2.3 Multi-scale modelling .....	14
2.4 Density Functional Theory .....	17
2.5 Microscopic modelling.....	24
2.5.1 Mean-field approximation .....	24
2.5.2 Kinetic Monte Carlo.....	25
2.6 Summary .....	28
Chapter 3 A Density Functional Theory Analysis on Syngas Adsorption on NiO (100) Surface .....	29
3.1 Introduction .....	29
3.2 Computational details.....	30
3.3 Results and discussion.....	32
3.3.1 Structure characterization.....	33

3.3.2 Structural property analysis.....	34
3.3.3 Adsorption energy analysis .....	38
3.3.4 Electron property analysis .....	43
3.4 Summary .....	50
Chapter 4 A Multi-scale Simulation of Syngas Combustion Reactions by Ni-based Oxygen Carriers for Chemical Looping Combustion.....	51
4.1 Introduction.....	51
4.2 Computational details.....	52
4.2.1 Reaction mechanism establishment.....	52
4.2.2 Electronic analysis.....	53
4.2.3 Reaction rate constant.....	53
4.3 Results and discussion.....	54
4.3.1 Reaction mechanisms and structure-related energetic results .....	54
4.3.2 Coupling electronic analysis.....	56
4.3.3 DFT-based Mean-field analysis .....	61
4.4 Summary .....	69
Chapter 5 Insights into Syngas Combustion on Defective NiO Surface for Chemical Looping Combustion: Oxygen Migration and Vacancy Effects .....	70
5.1 Introduction.....	70
5.2 Computational details.....	71
5.3 Results and discussion.....	71
5.3.1 Bulk oxygen diffusion .....	71
5.3.2 Defective adsorption.....	73
5.3.3 Projected density of states analysis of syngas adsorption .....	75
5.3.4 Reaction mechanism: CO oxidation.....	78
5.3.5 Reaction mechanism: H <sub>2</sub> oxidation .....	81
5.3.6 Model Verification .....	83
5.3.7 Crystal orbital Hamilton population analysis.....	87
5.4 Summary .....	92
Chapter 6 Multi-scale modelling of Syngas Combustion on NiO Surface under Neighbouring Effects .....	93

6.1 Introduction .....	93
6.2 Computational details.....	94
6.2.1 Density functional theory and the DFT-based reaction kinetics .....	94
6.2.2 kinetic Monte Carlo .....	95
6.3 Results and discussion.....	96
6.3.1 Neighbouring effects: CO oxidation .....	96
6.3.2 Neighbouring effects: H <sub>2</sub> decomposition .....	100
6.3.3 Neighbouring effects: H migration.....	103
6.3.4 Neighbouring effects: H <sub>2</sub> O formation .....	107
6.3.5 Neighbouring effects on reaction equilibrium.....	109
6.3.6 Coupling electronic analysis of neighbouring effects .....	112
6.3.7 DFT-based kMC multiscale model .....	115
6.4 Summary .....	130
Chapter 7 Conclusions and Future Work.....	132
7.1 Conclusions .....	132
7.2 Future work .....	136
Copyright Permissions .....	139
Bibliography .....	140
Appendix A.....	152
Appendix B.....	158

## List of Figures

Figure 1-1 Combustion of fossil fuels to the overall energy supply in 2018.....	2
Figure 2-1 An overview of CO <sub>2</sub> capture technologies.....	9
Figure 2-2 Reaction scheme of (a) type I CLC process and (b) type II CLC process .....	10
Figure 2-3 kMC scheme.....	26
Figure 3-1 Stable adsorption configuration on NiO with (a) CO adsorbate (b) H <sub>2</sub> adsorbate. Blue (Ni), red (O), black (C), white (H) .....	32
Figure 3-2 Studied nearest neighbour sites labeled as 1, 2, 3 and 4, adsorption site labeled as 0. Blue (Ni), red (O).....	33
Figure 3-3 Symmetry categories of the adsorption system, (a) symmetry 1, (b) symmetry 2 (c) symmetry 3. Blue (Ni), red (O), yellow (the occupied sites on the surface).....	34
Figure 3-4 Adsorption energy of uniform loading molecules .....	38
Figure 3-5 Uniform adsorption (black) and hybrid adsorption (blue) of (a) CO adsorption comparison; (b) H <sub>2</sub> adsorption comparison .....	40
Figure 3-6 Fully occupied nearest neighbouring site (a) CO adsorption and (b) H <sub>2</sub> adsorption .....	42
Figure 3-7 Comparison between non-adsorbed system and adsorbed system (a) 3d Ni orbitals and CO molecular orbitals: non-adsorbed system (b) 3d Ni orbitals and CO molecular orbitals: adsorbed system (c) 3d orbitals of attached Ni and non-attached Ni (d) molecular orbitals of non-attached CO and attached CO .....	43
Figure 3-8 Comparison between non-adsorbed system and adsorbed system (a) 3d Ni orbitals and H <sub>2</sub> molecular orbitals: non-adsorbed system (b) 3d Ni orbitals and H <sub>2</sub> molecular orbitals: adsorbed system (c) 3d orbitals of attached Ni and non-attached Ni (d) molecular orbitals of non-attached H <sub>2</sub> and attached H <sub>2</sub> .....	45
Figure 3-9 Neighbour effect on CO and H <sub>2</sub> adsorption shown in (a) 3d orbitals of Ni connected with CO (b) CO molecular orbitals (c) 3d orbitals of Ni connected with H <sub>2</sub> (d) H <sub>2</sub> molecular orbitals.....	46
Figure 3-10 Symmetry effect on CO and H <sub>2</sub> adsorption shown in (a) 3d orbitals of Ni connected with CO (b) CO molecular orbitals (c) 3d orbitals of Ni connected with H <sub>2</sub> (d) H <sub>2</sub> molecular orbitals.....	48

Figure 3-11 Hybrid effect on CO and H <sub>2</sub> adsorption shown in (a) 3d orbitals of Ni connected with CO (b) CO molecular orbitals (c) 3d orbitals of Ni connected with H <sub>2</sub> (d) H <sub>2</sub> molecular orbitals.....	49
Figure 4-1 Energy profile of CO oxidation. Blue (Ni), red (O), black (C).....	54
Figure 4-2 Energy profile of H <sub>2</sub> oxidation. Blue (Ni), red (O), white (H).....	55
Figure 4-3 Electronic analysis of the CO oxidation process: (a) coupling analysis from reactant to product (b) COHP analysis from reactant to TS <sub>CO</sub> . Blue (Ni), red (O), black (C)	57
Figure 4-4 Electronic analysis of H <sub>2</sub> dissociation (a) coupling analysis from reactant to TS <sub>H1</sub> (b) pCOHP analysis from TS <sub>H1</sub> to product. Blue (Ni), red (O), white (H).....	58
Figure 4-5 pCOHP analysis of H migration from product 1 to product 2 (a) H-Ni interaction (b) H-O interaction. Blue (Ni), red (O), white (H) .....	60
Figure 4-6 pCOHP analysis of H <sub>2</sub> O formation (a) H-O interaction from TS <sub>H3</sub> to product 3 (b) O-Ni interaction from product 2 to TS <sub>H3</sub> . Blue (Ni), red (O), white (H).....	61
Figure 4-7 Comparison between oxygen consumed from the MF model (solid line) and solid conversion from experimental observations <sup>190</sup> (dashed line) at compositions of CO/H <sub>2</sub> = 1(black) and CO/H <sub>2</sub> = 3 (red) in the gas phase .....	64
Figure 4-8 (a) Comparison between the solid conversion from the MF model (line) and the solid conversion from the experimental observations <sup>191</sup> (scatter) at temperatures of 923.15 K (blue), 873.15 K (red) and 823.15 K (black); (b) pressure analysis of the oxygen consumed from the MF model at 0.1 MPa (black) and 2 MPa (red) .....	66
Figure 4-9 Product ratio CO <sub>2</sub> /H <sub>2</sub> O, composition: CO/H <sub>2</sub> = 3/1 (cyan), CO/H <sub>2</sub> =1/1 (blue), CO/H <sub>2</sub> = 1/3 (red), temperature range: 823.15 K - 923.15 K, pressure range: 0.1 MPa - 2 MPa .....	68
Figure 5-1 Oxygen migration analysis: (a) stability analysis of defective configurations (b) energy profile of oxygen migration (2 <sup>nd</sup> layer to the surface through TS <sub>bulk1</sub> , 3 <sup>rd</sup> layer to the 2 <sup>nd</sup> layer through TS <sub>bulk2</sub> ) .....	72
Figure 5-2 Adsorption energy comparisons of (a) CO and (b) H <sub>2</sub> between the defective surface (left) and the perfect surface (right). OV: Oxygen vacancy.....	74
Figure 5-3 Electron distribution comparisons of (a) CO molecular orbitals and (b) Ni 3d orbitals between the CO adsorption configurations with (red: vacancy top, blue: vacancy-adjacent Ni top) and without vacancies (black).....	76

Figure 5-4 Electron distribution comparisons of (a) H<sub>2</sub> molecular orbitals and (b) Ni 3d orbitals between the H<sub>2</sub> adsorption configurations with (red) and without vacancies (black) 77

Figure 5-5 Comparison of the CO oxidation energy profile between the perfect surface (black: from Reactant<sub>1</sub> to Product<sub>CO1</sub> through TS<sub>CO1</sub>) and the defective surface (blue: from Reactant<sub>2</sub>, CO adsorbed at vacancy top to Product<sub>CO2</sub> through TS<sub>CO2</sub>; red: from Reactant<sub>3</sub>, CO adsorbed at vacancy-adjacent Ni top to Product<sub>CO3</sub> through TS<sub>CO3</sub>) . Blue atom (Ni), red atom (O), black atom (C) ..... 79

Figure 5-6 Comparison of H<sub>2</sub> oxidation energy profile between the perfect surface (black: step 1 from Reactant<sub>perfect</sub> to Product<sub>1perfect</sub> through TS<sub>1perfect</sub>; step 2 from Product<sub>1perfect</sub> to Product<sub>2perfect</sub> through TS<sub>2perfect</sub>; step 3 from Product<sub>2perfect</sub> to Product<sub>3perfect</sub> through TS<sub>3perfect</sub>) and the defective surface (red: step 1 from Reactant<sub>defective</sub> to Product<sub>1defective</sub> through TS<sub>1defective</sub>; step 2 from Product<sub>1defective</sub> to Product<sub>2defective</sub> through TS<sub>2defective</sub>). Blue atom (Ni), red atom (O), white atom (H)..... 82

Figure 5-7 Comparison between oxygen consumed from the MF model (solid line) and solid conversion from experimental observations (dashed line) at compositions of CO/H<sub>2</sub> = 1(black) and CO/H<sub>2</sub> = 3 (red) in the gas phase ..... 86

Figure 5-8 COHP analysis of (a) C-O interaction (enclosed in the blue circles) of TS<sub>CO</sub> (green), TS<sub>CO1</sub> (red) and TS<sub>CO2</sub> (blue) (b) C-Ni interaction (enclosed in the blue circles) of TS<sub>CO</sub> (green), TS<sub>CO1</sub> (red) and TS<sub>CO2</sub> (blue). Blue atom (Ni), red atom (O), black atom (C). 87

Figure 5-9 COHP analysis of (a) H-O interaction (enclosed in the blue circles) of TS<sub>2perfect</sub> (green) and TS<sub>1defective</sub> (blue) (b) Ni-H interaction (enclosed in the blue circles) of TS<sub>2perfect</sub> (green) and TS<sub>1defective</sub> (blue). Blue atom (Ni), red atom (O), white atom (H)..... 89

Figure 5-10 COHP analysis of (a) H-O interaction (enclosed in the blue circles) of TS<sub>3perfect</sub> (green) and TS<sub>2defective</sub> (blue) (b) Ni-H interaction (enclosed in the blue circles) of TS<sub>3perfect</sub> (green) and TS<sub>2defective</sub>(blue). Blue atom (Ni), red atom (O), white atom (H)..... 91

Figure 6-1 Activation energy of CO oxidation with (a) CO neighbours and (b) H<sub>2</sub> neighbours. Blue (Ni), red (O), black (C), white (H) ..... 97

Figure 6-2 Activation energy of **Step 1** of H<sub>2</sub> oxidation with (a) CO neighbours and (b) H<sub>2</sub> neighbours. Blue (Ni), red (O), black (C), white (H) ..... 101

Figure 6-3 Activation energy of **Step 2** of H<sub>2</sub> oxidation with (a) CO neighbours and (b) H<sub>2</sub> neighbours. Blue (Ni), red (O), black (C), white (H) ..... 105

Figure 6-4 Activation energy of <b>Step 3</b> of H <sub>2</sub> oxidation with (a) CO neighbours and (b) H <sub>2</sub> neighbours. Blue (Ni), red (O), black (C), white (H) .....	108
Figure 6-5 Reaction equilibrium shift of (a) CO oxidation, (b) step 1 of H <sub>2</sub> oxidation, (c) step 2 of H <sub>2</sub> oxidation and (d) step 3 of H <sub>2</sub> oxidation with CO and H <sub>2</sub> neighbours.....	110
Figure 6-6 Electronic analysis of neighbouring effects on CO oxidation (a) C-O interaction of TS <sub>CO</sub> (b) C-Ni interaction of TS <sub>CO</sub> .....	112
Figure 6-7 Electronic analysis of neighbouring effects on H <sub>2</sub> decomposition (a) H-H interaction of TS <sub>H1</sub> (b) H1s-Ni3dz2 interaction of TS <sub>H1</sub> .....	114
Figure 6-8 Reaction parameters for (a) CO reactions, (b) H <sub>2</sub> dissociation and (c) H <sub>2</sub> O formation in consideration of single species neighbours as CO (red circle) or H <sub>2</sub> (blue triangle) and hybrid neighbours (green cube).....	119
Figure 6-9 Comparisons of the surface coverages of (a) CO and (b) H on 20×20, 30×30, 50×50 and 70×70 lattice, respectively. ....	121
Figure 6-10 Comparison between (a) the oxygen consumed from the kMC model and (b) solid conversion from experimental observations <sup>190</sup> at compositions of CO/H <sub>2</sub> = 1 (blue) and CO/H <sub>2</sub> = 3 (red) in the gas phase; Comparison between (c) the solid conversion from the MF model and (d) the solid conversion from the experimental observations (scatter) <sup>191</sup> at temperatures of 823.15 K (blue), 873.15 K (red) and 923.15 K (green) (e) pressure analysis of the oxygen consumed from the MF model at 0.1 MPa (blue) and 2 MPa (red).....	123
Figure 6-11 Comparison between the full neighbour consideration scenario (red) and no neighbour consideration on CO adsorption scenario (blue) of (a) CO coverage (b) H coverage (c) produced CO <sub>2</sub> per site and (d) produced H <sub>2</sub> O per site; or no neighbour consideration on H <sub>2</sub> chemisorption scenario (blue) of (e) CO coverage (f) H coverage (g) produced CO <sub>2</sub> per site and (h) produced H <sub>2</sub> O per site.....	126
Figure 6-12 Comparison between the full neighbour consideration scenario (red) and no neighbour consideration on CO oxidation scenario (blue) of (a) CO coverage (b) H coverage (c) produced CO <sub>2</sub> per site and (d) produced H <sub>2</sub> O per site; or no neighbour consideration on H <sub>2</sub> O chemisorption scenario (blue) of (e) CO coverage (f) H coverage (g) produced CO <sub>2</sub> per site and (h) produced H <sub>2</sub> O per site.....	128

## List of Tables

Table 3-1 Structure properties of CO adsorption on NiO.....	34
Table 3-2 Structural properties of H <sub>2</sub> adsorption on NiO.....	37
Table 4-1 Reaction rate parameters .....	64
Table 4-2 Operating conditions .....	68
Table 5-1 Reaction barriers of bulk oxygen migration.....	73
Table 5-2 Energy barriers of the proposed elementary reactions .....	84
Table 5-3 Characteristic time comparison .....	86
Table 6-1 Clean surface elementary reactions and their activation energies.....	115
Table 6-2 CO adsorption energy analysis.....	117
Table 6-3 H <sub>2</sub> adsorption energy analysis .....	118
Table 6-4 Sensitivity analysis .....	125



## List of Acronyms

CLC	Chemical Looping Combustion
CI-NEB	Climbing-Image Nudged Elastic Band
CLOU	Chemical Looping Uncoupling
COHP	Crystal Orbital Hamilton Population
DFT	Density Functional Theory
DFT+U	DFT combined with the Hubbard Hamiltonian method
Fcc	face-centered cubic
GDC	Gadolinium-doped Ceria
GGA	Generalized Gradient Approximation
HF	Hartree Fock
ICSD	Inorganic Crystal Structure Database
iG-CLC	in-situ Gasification Chemical Looping Combustion
IS	Industrial Sustainability
kMC	kinetic Monte Carlo
LDA	Local-density Approximation
MD	Molecular Dynamic
MF	Mean-field
ML	Machine learning
NNGM	Nucleation and Nuclei Growth Model
OC	Oxygen Carrier
ODEs	Ordinary Differential Equations
OV	Oxygen Vacancy
PAW	Projector-augmented Wave
pCOHP	projected COHP
pDOS	Projected Density of States
SCM	Shrinking Core Model
TS	Transition State
TST	Transition-State Theory
VASP	Vienna Ab Initio Simulation Package
ZPE	Zero-point Energy

## List of Symbols

$A_{\text{site}}$	area of one single site
$C_{i,g}$	gas phase concentration of species $i$
$E_a$	activation energy
$E_{a,\text{backward}}$	backward activation energy
$E_{a,\text{forward}}$	forward activation energy
$E_{a,\text{product}}$	system energy of product
$E_{a,\text{reactant}}$	system energy of reactant
$E_{a,\text{TS}}$	system energy of transition state
$E_{\text{backward}}$	backward energy barrier
$E_{\text{desorption}}$	Planck's constant
$E_{\text{diff}}$	energy difference between the forward energy barrier and the backward energy barrier
$E_{\text{forward}}$	forward energy barrier
$E_{\text{freefuel}}$	free fuel energy
$E_{\text{surface}}$	surface energy
$E_{\text{system}}$	system energy
$E_{\text{ZP,backward}}$	backward reaction zero-point energy difference
$E_{\text{ZP,forward}}$	forward reaction zero-point energy difference
$h$	Planck's constant
$K$	reaction equilibrium constant
$\sum_i(k_i)_j$	the total rate of all possible events at the specific site $j$
$k_{a,\text{ad}}$	adsorption rate
$k_B$	Boltzmann constant
$k_{\text{co,ad}}$	CO adsorption rate constant
$k_{\text{co,rec}}$	CO reaction rate constant
$k_{\text{desorption}}$	desorption rate constant
$k_{\text{H}_2,\text{ad}}$	H <sub>2</sub> adsorption rate constant
$k_{\text{H}_2,\text{break}}$	H <sub>2</sub> decomposition rate constant

$k_{\text{H}_2\text{O,form}}$	H <sub>2</sub> O formation rate constant
$k_i$	i event rate parameter
$k_{i,\text{ad}}$	adsorption rate constant
$k_{i,\text{d}}$	desorption rate constant
$k_{i,\text{rec}}$	reaction rate constant
$m$	mass of species a
$m_{\text{O,con}}$	mass of oxygen transferred from the OC particle to gas phase
$m_{\text{O,OC}}$	mass of oxygen present when the OC particle is fully oxidized
$n$	number of vibrational frequencies
$\eta$	ratio between the number of oxygens on the surface and the number of total oxygens in OC particle when it is fully oxidized.
$N_{\text{electron}}$	the number of the electrons in the system
$N$	the total number of the reaction sites along one direction of the 2D lattice
$N_i$	the number of possible sites for event i
$N_{\text{O,con}}$	number of reacted oxygens per available site
$n_{\text{O,con}}$	number of reacted oxygen
$n_{\text{O,OC}}$	number of oxygens on the surface
$N_{\text{CO}}$	number of the CO neighbours
$N_{\text{H}_2}$	number of the H <sub>2</sub> neighbours
$n_{\text{O,surface}}$	number of oxygens of the fully oxidized OC surface
$Num_{\text{full}}$	kMC output from the scenario with full consideration of neighboring effects
$Num_{\text{full}}$	kMC output from the scenario with no neighboring effects on one specific event
$P_a$	partial pressure of species a
$Q_{\text{vib}}^{\text{prod}}$	vibrational partition function of product
$Q_{\text{vib}}^{\text{reac}}$	vibrational partition functions of reactant
$Q_{\text{vib}}^{\text{TS}}$	vibrational partition functions of transition state
$R$	total rate of the kMC system
$R_{\text{O,con}}$	reacted oxygen rate
$S_a$	sticking coefficient
$S_a$	sticking coefficient of species a
$T$	system temperature
$t_{\text{maxi}}$	the maximum simulation time
$t_{\text{system}}$	kMC system time

$\Delta t$	time interval of kMC
$W_{backward}$	backward reaction rate
$W_{forward}$	forward reaction rate
$X_{O,con}$	solid conversion ratio
$\Delta E_{adsorption}$	adsorption energy
$\theta_{CO}$	CO coverage
$\theta_{H_2}$	H <sub>2</sub> coverage
$\theta_{HNiHO}$	HNiHO coverage
$\theta_O$	empty oxygen coverage
$\theta_{empty}$	empty site coverage
$\lambda$	weight of reaction parameters
$\pi$	Archimedes' constant
$\tau$	characteristic time
$\rho_1$	random number for site election in kMC
$\rho_2$	random number for event election in kMC
$\rho_3$	random number for time evolution in kMC
$\omega_1^{prod}$	vibrational frequency of product
$\omega_1^{react}$	vibrational frequency of reactant
$\omega_1^{TS}$	vibrational frequency of transition state
$\Delta\sigma$	percent deviation

# Chapter 1 Introduction and Motivation

## 1.1 Motivation

With the continuous growth in human population, the demand for food, energy and fundamental living resources has significantly increased. According to Godfray *et al.*<sup>1</sup>, world hunger significantly affects more than 14% of the world population this century. It is also expected that by 2050, an increase of 70-100% in food supply will be required to meet the population's demands. To circumvent this issue, industrial activities have increased to comply with global demands. The necessary rise in industrial production has brought severe environmental problems and the inevitable drop in non-renewable resources. The sustainability of the environment and resources is becoming a major global concern. In terms of industrial development, the production of valuable materials and products need to satisfy the increasing population demands; however, this needs to be performed in a sustainable fashion such that there is a balance between available resources and manufacture of valuable products. New materials and technologies are in urgent need to advance industrial development by considering environment and resource sustainability. Among all the studied aspects of industrial sustainability (IS), the continuous growth in CO<sub>2</sub> emissions from fossil fuel combustion have attracted attention due to their environmental impact and global sustainability<sup>2-3</sup>.

According to the International Energy Agency (IEA) report in 2020<sup>4</sup>, fossil fuel accounted for almost 81% of the overall energy supply in 2016, as shown in Figure 1-1. Due to the current energy demands, fossil fuels are still not replaceable by renewables due to their relatively low costs and continuous development of efficient combustion<sup>5-7</sup>. Nonetheless, the impact on the environment from the combustion process of fossil fuels has become one of the most severe problems. One of the most serious consequences of fossil fuel combustion is greenhouse gas effects. Among all the greenhouse gas emissions, CO<sub>2</sub> represents almost 75% of greenhouse

gases. Furthermore, CO<sub>2</sub> has relatively long residence times, i.e. it remains in the atmosphere for long periods of time<sup>8</sup>. Thus, technologies aimed at reducing CO<sub>2</sub> emissions are key to achieve environmental and resource sustainability while satisfying the current energy requirements for industrial activities. One approach that can be considered to reduce CO<sub>2</sub> emissions to the atmosphere is through the deployment of technologies that can capture, store, manage and eventually utilize the CO<sub>2</sub> produced from large stationary sources such as fossil-fired power plants. The development of efficient CO<sub>2</sub> capture systems engaged with the continuous production of power from fossil fuels is appealing since it could drive the sustainable development of fossil-fired energy technologies with near-zero emissions.

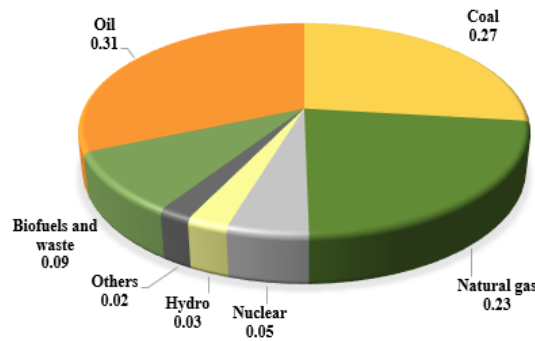


Figure 1-1 Combustion of fossil fuels to the overall energy supply in 2018

In general, CO<sub>2</sub> disposal technologies usually sacrifice part of the overall system energy utilization efficiency to achieve the purpose of CO<sub>2</sub> capture.<sup>9-11</sup> To reduce the energy penalty, Chemical Looping Combustion (CLC) has attracted attention in past decades due to the inherent CO<sub>2</sub> separation that occurs in this process thus avoiding the need of additional capital and operational expenditures. This leads to a relatively low CLC energy costs compared to other carbon capture and storage technologies<sup>12</sup>. An indirect combustion of fuels is achieved using an oxygen carrier (OC) in CLC process, which minimizes the irreversible entropy during the combustion process. OCs act as an oxygen medium, preventing the direct contact between air and fossil fuels thereby reducing the energy costs of the CO<sub>2</sub> disposal since energy intensive gas-gas separation process are avoided. Improving OC performance is, therefore, one of the key drivers for CLC development. More details of CLC technology are further discussed in section 2.1.

In the studies of OC development, certain properties of OCs are desired for specific applications of the CLC process such as high reactivity and long-term stability.<sup>13</sup> Though there are extensive experimental studies of OC development available in the literature, the computational reports are still comparably limited. Nowadays, computational studies are trending because they can accelerate materials' screening and provide fine-scale insights that cannot be obtained from experiments. Among all the computational methods, Density functional theory (DFT) is one of the most popular calculation approaches used to provide atomic structural analysis and reaction kinetics based on the electron distribution of the system under consideration. Although DFT is widely used in materials' development (e.g. catalyst design), the number of DFT analyses in OC development is relatively limited. The most studied OC using DFT analysis are Fe-based OCs<sup>14-16</sup> followed by Cu-based OCs<sup>17</sup>. Ni-based OCs are one of the most popular OCs in CLC; however, only a limited number of DFT studies for NiO has been reported<sup>18</sup>. As a result, the reaction mechanisms and the significant influencing factors of fossil fuel combustion using NiO as OC have not been investigated and reported in the open literature.

Typically, the adjacent structural properties have significant effects on the adsorption and reaction sites in heterogeneous system, which is reflected by the changes observed in the material properties (e.g. the reaction activity).<sup>19-22</sup> It is therefore necessary to consider aspects such as the surface oxygen vacancies and the nearest neighbours in the CLC process (e.g. neighbouring adsorbed species) since the adjacent properties are expected to considerably affect the OC performance. Currently, only a few theoretical reports of surface oxygen vacancies are available in the literature, most of which have been focused on the CH<sub>4</sub> oxidation process<sup>16 23</sup>. Those studies have indicated that the oxygen vacancies significantly enhance OC performance. Consequently, the vacancy effects have not been fully explored in the theoretical studies. Regarding the effects of the nearest neighbours, to the author's knowledge, there are no computational studies considering this factor currently available within the area of OC development.

Outcomes from DFT analysis are mostly energetic results and atomic structural characteristics, which can be difficult to validate using experimental observations. A multi-scale modelling approach can thus be used to relate the reaction kinetics obtained from the

DFT analysis to the larger temporal and spatial evolution of the system, which enables a direct comparison with the experimental observations. A mean-field (MF) model can be constructed based on the reaction kinetics obtained from the DFT analysis, in order to predict the dynamic properties of the system, i.e. coverages of the surface species, within a reasonable time range (e.g. 1 min), which can be used to verify the proposed reaction kinetics from DFT analysis.<sup>24</sup> The MF model, however, assumes homogeneous distribution for all the surface species, i.e. the effect of adjacent adsorbed species such as nearest neighbours are not taken into account.<sup>25</sup> To investigate the effects of the nearest neighbours, kinetic Monte Carlo (kMC) models can be built to account for the temporal evolution of the neighbouring effects by integrating these effects into the rates of the possible events (i.e. elementary reactions) based on the reaction mechanisms. DFT-based kMC multi-scale models have shown great potential of bridging the energy-based reaction kinetics with the measured statistical properties of the system.<sup>26-27</sup> However, the only DFT-based kMC scheme reported for OC development was proposed by Andersson *et al.*<sup>28</sup> and focused on the multi-scale integration of the CH<sub>4</sub> reforming process using Fe<sub>2</sub>O<sub>3</sub> as OC. However, no neighbouring effects are considered in this work. Therefore, DFT-based kMC multi-scale models that take into account the effects of the nearest neighbours are not available in the open literature. The lack of multi-scale theoretical reports in OC development makes it difficult to relate the microscopic phenomena to experimental observations, thus imposing a limitation towards the commercial development of this technology.

## 1.2 Research Objectives

In order to contribute to the aforementioned gaps in the literature for OC development, this Ph.D. study presents a systematic multi-scale modelling framework of syngas combustion with NiO as OC. This research will take into account neighbouring and vacancy effects in the system, thus advancing our understanding of these aspects in OC development. The reaction kinetics are revealed in the studied system while taking into consideration the aforementioned effects. Multi-scale models can be developed to validate the obtained reaction kinetics and



microscopic phenomena via comparison to the experimental observations at conditions that CLC processes are typically operated. The specific objectives of this thesis are as follows:

- Perform a DFT analysis to reveal the principle of syngas adsorption in consideration of the neighbouring effects on NiO and provide an electron distribution analysis that theoretically supports the specific insights gathered from DFT.
- Provide insights into the syngas combustion on NiO by developing a DFT-based MF model for the validation of the reaction mechanisms and property predictions of the system (e.g. product selectivity) under practical operating conditions (e.g. inlet composition, temperature and pressure).
- Investigate the vacancy effects on the adsorption and reaction mechanisms of syngas on a defective NiO surface, i.e. a surface that has an oxygen vacancy in the surface layer. Provide insights into the oxygen bulk migration process that contributes to the oxygen supply. Establish a DFT-based MF model using reaction kinetics developed on the defective surfaces to further validate the insights gained from this phenomena.
- Reveal the effects of nearest neighbours on the syngas oxidation using NiO. To accomplish this goal, a DFT-based kMC model is developed that accounts for the dynamic neighbouring effects caused by the changing surface environment. The proposed multi-scale model will be used to validate the insights gained from this process and to predict the properties of the studied system under practical operating conditions.

### **1.3 Research Contributions**

This PhD study contributed to the body of work in OC development as follows:

- The neighbouring effects from the specific neighbour configurations are provided for the OC development to fill in this gap in the literature. It is shown that taking the effects of first nearest neighbours into consideration on the syngas adsorption is critical to accurately predict OC performance. The DFT analysis shows that adsorption stability is affected by the hybrid, steric and symmetry effects caused by the nearest neighbours. The increasing number of neighbours presents to weaken the adsorption stability of both CO

and H<sub>2</sub>. Particularly, the first loaded neighbour suppresses syngas adsorption the most significantly. A highly symmetric neighbour configuration tends to increase the adsorption energy, whereas the hybrid nearest neighbours result in higher adsorption stability compared to the uniform nearest neighbours.

- The elementary reaction mechanism for syngas combustion on NiO is established. A DFT-based MF model is developed based on the obtained reaction kinetics to verify the accuracy of the DFT calculations and estimate the reaction kinetics under practical operating conditions. An electron distribution analysis is provided to further support the outcomes of this study. H<sub>2</sub> decomposition is proven to be the controlling step of syngas oxidation on a perfect NiO surface.
- The vacancy effects on syngas adsorption and oxidation with NiO are investigated for OC development. The reaction mechanism of the studied system on a defective NiO surface are revealed and validated through a DFT-based MF multi-scale model. An electronic distribution analysis is performed to further support the insights into the vacancy effects. Surface vacancies are proven to enhance the syngas oxidation process.
- The effects of first nearest neighbours of syngas combustion on the NiO surface are provided. A DFT-based kMC multi-scale model is developed to investigate the neighbouring effects on both syngas adsorption and combustion in a dynamic surface environment. The neighbouring effects are observed to significantly enhance the syngas oxidation by NiO, and are therefore critical to adequately capture OC performance. This model fills in the gap by providing a tool that predicts the OC performance as affected by the temporal evolution of the first nearest neighbours in a changing surface environment.

## 1.4 Outline

The remainder of this thesis is organized as follows:

Chapter 2 presents an overview of CLC and OC development, multi-scale modelling, DFT, and microscopic modelling (i.e. the MF and kMC methods). The literature gaps within

the theoretical studies of OC development are identified to motivate the development of this study.

Chapter 3 provides a comprehensive insight into the syngas adsorption on the NiO surface. Neighbouring effects are considered to investigate adsorption stability. The hybrid effects, symmetry effects and steric effects are emphasized to explain the syngas adsorption affected by the nearest neighbours. An electronic analysis is performed to further support the DFT calculations.

Chapter 4 presents a theoretical study that reveals the reaction mechanism of syngas combustion by NiO as OC. The resulting reaction kinetics are used to develop a MF model. The DFT-based MF model predicts the performance of the studied system under practical operating conditions. Validation of the DFT-based MF model was performed and also shows the predictability properties of the proposed reaction mechanism. An electronic analysis is performed in this part of the research to further validate the DFT results.

Chapter 5 investigates one of the critical factors affecting the OC performance: oxygen vacancies. A comprehensive analysis of both adsorption and reactions is provided. The relevant oxygen migration in the bulk is also studied to provide insights into the oxygen supply from NiO. A DFT-based MF model is employed, which considers the vacancy effects on the reaction kinetics. In addition, the DFT-based MF model is validated in this section to show the accuracy of the DFT results. An electronic analysis is conducted to support the DFT outcomes.

Chapter 6 provides a systematic analysis of the neighbouring effects on OC performance. An explicit investigation of reaction mechanisms in the presence of different neighbour configurations was performed. The resulting neighbouring effects on reactions and absorption, obtained from Chapter 1, are employed to establish a kMC model. The proposed multi-scale model was validated using experimental observations available in the literature and evaluated under the practical operating conditions. An electronic analysis is also provided to support the outcomes from this study.

Chapter 7 presents the conclusions of this study. Future research studies are also outlined at the end of this chapter.

## Chapter 2 Background and Literature Review

CLC has great potential as an energy supply, which achieves an environmentally friendly and sustainable use of fossil fuel. OC development has been one of the key aspects investigated during the last decades to improve CLC performance. However, most of the studies of OC development are experimental reports, i.e. only a limited number of theoretical studies in this area are available in the literature. Multi-scale modelling involving fine and coarse scale phenomena is expected to provide valuable guidance for OC development, since they can predict microscopic phenomena and be used for validation purposes (e.g. against experimental reports). In addition, these models can be used to perform computer aided materials design and guide expensive and costly experimental studies in this area. The information presented in section 2.1 and section 2.2 has been published.<sup>29</sup>

This chapter presents an overview on the current state-of-the art studies on OC, in particular those involving theoretical studies of OC development as a support for the main motivation for this study. This chapter will first provide a general introduction to the CLC process and OC development in sections 2.1 and 2.2, respectively. Section 2.3 outlines the multi-scale coupling methods and a detailed description of the multi-scale simulation scenario used in this study. The principles behind DFT, MF and kMC are discussed in sections 2.4 and 2.5. A literature review on the computational studies of OC development is also provided in these two sections. Section 2.6 summarized the gaps in the literature that motivate this study.

### 2.1 Chemical looping combustion

Fossil fuel combustion is currently irreplaceable as the major energy resource in the world. The inevitable issue of CO<sub>2</sub> emissions caused by fossil fuel combustion has become a focus of industrial sustainability. Therefore, technologies to reduce greenhouse emissions, especially CO<sub>2</sub>, are key to curbing global warming. As displayed in Figure 2-1, CO<sub>2</sub> disposal technologies are usually classified as pre-combustion, which reduces carbon capacity of fuels before combustion occurs; post-combustion, where the flue gases generated after combustion are cleaned; and oxy-fuel combustion, which makes use of pure O<sub>2</sub> as the oxidizer. Post-

combustion is a relatively mature commercial technology that favours low-pressure processes.<sup>8, 30</sup> However, the energy penalty of CO<sub>2</sub> separation while adopting post-combustion technologies (e.g. amine-based solvents) is from 25% to 40%<sup>31</sup>. The post-combustion process has the challenge of the ambient pressure and low CO<sub>2</sub> concentration in a large amount of gas stream, i.e. in the post-combustion process CO<sub>2</sub> partial pressure is usually less than 0.15 atm<sup>32</sup>. Pre-combustion technologies can significantly reduce the energy consumption associated with CO<sub>2</sub> capture, particularly in systems that operate at high pressures. However, low temperatures are usually required to maintain the high efficiency of this process. According to a previous study<sup>33</sup>, the energy penalty of the net plant efficiency in IGCC (Integrated Gasification Combined Cycle) plant with pre-combustion technology is from 7% to 9.5%. Compared to the pre and post combustion technologies, oxy-combustion usually adopts a recirculation process, which lowers the energy penalty through the separation of O<sub>2</sub> from the air before combustion. Despite its benefits, this technology is still intensive and requires significant energy demands, mostly in the separation of O<sub>2</sub> from the air. Despite the advances in these technologies, their mutual process of energy-intensive gas-gas separation generally lead to the decrease in the efficiency of the overall system energy utilization.<sup>31</sup> Chemical looping technology is therefore attracting attention due to its ability to separate CO<sub>2</sub> with minimum energy consumption.<sup>34</sup>

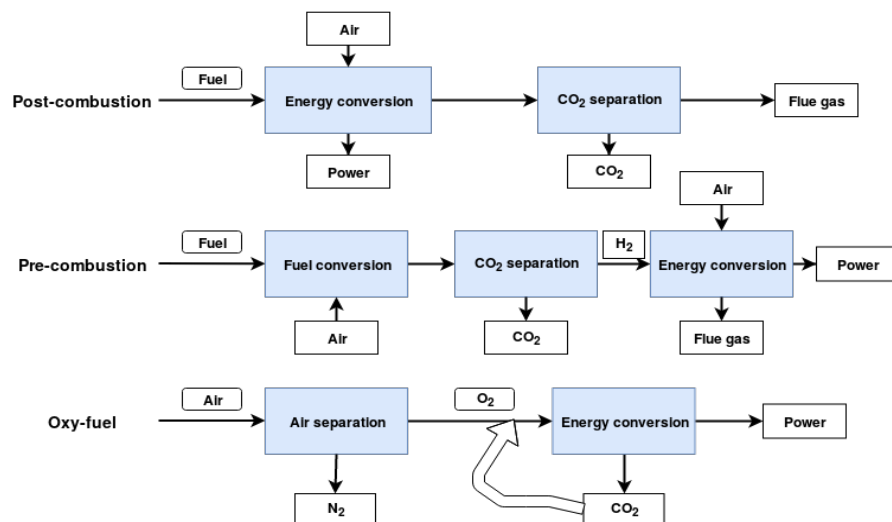


Figure 2-1 An overview of CO<sub>2</sub> capture technologies

The key concept in CLC is to process the fossil fuel combustion by introducing oxygen intermediates such that the CO<sub>2</sub> stream produced by the combustion is highly concentrated. The gas-gas separation process generally required for CO<sub>2</sub> disposal is avoided, and therefore the CLC process can achieve the energy supply from fossil fuel combustion with low energy cost.<sup>35-37</sup>

CLC has the *in-situ* CO<sub>2</sub> separation property, which makes the fuel combustion and CO<sub>2</sub> separation process to occur in a one-step scheme. The intermediate oxidation via metal-oxide (CuO) was proposed by Lewais and Gilliland in 1954 to convert CO to pure CO<sub>2</sub> while prohibiting the inert gas (mainly N<sub>2</sub>) within the air from mixing with the CO<sub>2</sub> flue gas.<sup>38</sup> Later, Richter and Knoche proposed a two-reactor scheme by allowing the intermediate contact of fuel with oxygen.<sup>39</sup> This resulted in a decrease in the irreversible entropy production during the fuel combustion process.<sup>39</sup> The formal term, CLC, was not introduced until 1987 by Ishida *et al.*<sup>40</sup>, who showed that CLC could be realized with high thermal efficiency. In a subsequent report, Ishida *et al.* (1994) combined the high energy efficiency CLC process with its inherent CO<sub>2</sub> separation property.<sup>41</sup> This relatively mature combustion system lead to the development of various chemical looping technologies. From then on, extensive research, mostly on reactor design and OC development, have been reported.<sup>7, 42-47</sup>

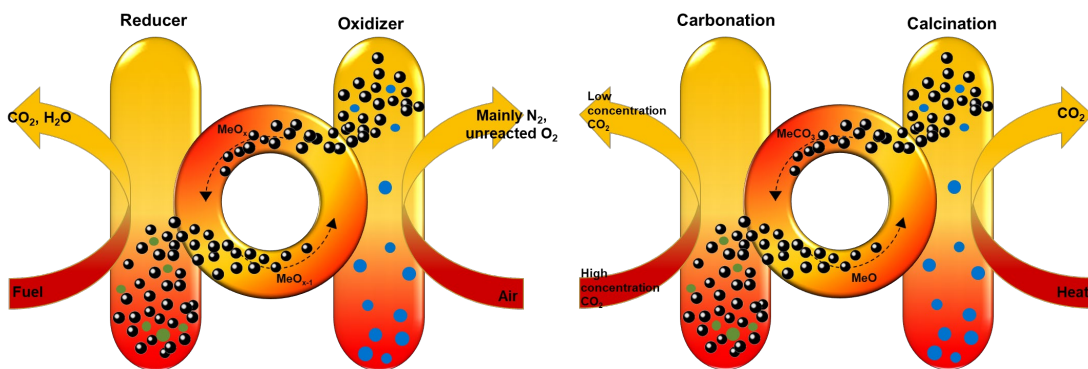


Figure 2-2 Reaction scheme of (a) type I CLC process and (b) type II CLC process

Based on the reaction properties, there are two types of chemical looping schemes that can proceed the fuel conversion process. As shown in Figure 2-2 (a), type I CLC processes the

indirect combustion of fuels by introducing an OC, which minimizes the irreversible entropy during the combustion process. In the first reactor (the reducer), metal oxides are reduced to process the full oxidation of either gas or solid fuels, e.g. syngas or coal. The reduced metal oxides are then transported into the second reactor (the combustor) to be re-oxidized by air, thus forming a loop. Through CLC, the combustion process is energy-effective since it simultaneously captures CO<sub>2</sub> and produces heat, thus promoting energy, environmental and ecosystem sustainability. As shown in Figure 2-2 (b), type II CLC also requires two reactors, i.e. a carbonator and a calciner, including CO<sub>2</sub> transport using CO<sub>2</sub> carriers. In the carbonator, CaO is carbonated by CO<sub>2</sub> into CaCO<sub>3</sub>, whereas in the calciner, the CaCO<sub>3</sub> undergoes a calcination reaction to release CO<sub>2</sub> at high temperatures. In general, the utilization of the intermediate (e.g. CaCO<sub>3</sub>) increases the efficiency of energy utilization for CO<sub>2</sub> disposal.<sup>48-49</sup> Guo *et al.*<sup>50</sup> combined experimental and DFT methods to study metal promoter effects in type II CLC process (e.g. Al, Mg, Zr and Na). Zr and Na benefit CO<sub>2</sub> adsorption while Al and Mg weaken the adsorption. Ca-based material, however, has only rarely been studied in computational studies.

The two key drivers for the development of CLC technology are reactor design and OC performance. The interactions between the OC and the fuels highly affect the conversion efficiency, which is determined by the shape and size of the reactors. Thus, reactors should be carefully designed to maintain adequate contact between fuels and OCs. Likewise, attrition, agglomeration and leakage should be controlled to minimize the loss of active OCs in the recirculation process. Another important aspect considered to improve the CLC process is OC development, which is the focus of this study.

## 2.2 Oxygen carrier

This section provides a general overview to OCs' desirable characteristics, the most studied OCs and typical methods to enhance OC performance. Numerous studies have shown that the properties of OC can significantly affect CLC performance.<sup>51-52</sup> Therefore, OC development has been the focus in the area of CLC investigation for decades. The active components of OCs are usually metal oxides, and specific characteristics are preferred for high

performance of CLC. High redox reactivity and desirable selectivity are usually the first consideration in the selection of OCs. Also, sufficient oxygen transport capacity is preferred for maintaining an acceptable rate of fossil fuel combustion.<sup>13</sup> To guarantee long-term stability, high mechanical strength for the resistance of OC to attrition, fragmentation and agglomeration is expected, especially under stringent operating conditions (e.g. 20 bar, around 1000°C).<sup>37, 53</sup> Another aspect to consider is the environmental impact of OC materials, i.e. Ni-based OCs are toxic and can be converted into stable nickel subsulphide (Ni<sub>3</sub>S<sub>2</sub>) especially in the in-situ Gasification Chemical Looping Combustion (iG-CLC) process.<sup>54</sup> The cost of OC is an aspect that cannot be ignored for large scale utilization.<sup>55</sup> Additionally, coke formation is of great significance for OC development since coke could be transported to the oxidizer, which may lead to CO<sub>2</sub> emissions. This issue can be controlled by adopting suitable operating temperatures for the CLC process and avoiding carbon-intensive fuels such as CH<sub>4</sub>.<sup>56</sup> An extensive research on OC development provides specific applications for different OCs, which are determined by their features. The most commonly studied OCs are Cu-based, Fe-based and Ni-based. Among them, Cu-based OCs stand out for their application in the Chemical Looping Uncoupling (CLOU) process because of their unique thermodynamic property, which enables these OCs to release O<sub>2</sub> in the fuel reactor for solid fuel combustion.<sup>57-58</sup> The CLOU process intensively employed the Cu-based OCs due to their advantages of high reactivity, large oxygen transport capacity and relatively low cost.<sup>59</sup> Meanwhile, Fe-based OCs are widely employed for syngas production in the iG-CLC process for solid fuel gasification, which rely on their low cost and environmental compatibility.<sup>60-61</sup> Ni-based OCs have also been widely investigated in experimental settings; particularly under harsh operating conditions.<sup>62-63</sup> Although Ni-based OCs have aforementioned detrimental environmental effects, the high reactivity of Ni-based OCs and their catalytic potential of breaking C-H bonds make them one of the most popular OCs.<sup>8, 13, 64 65</sup> In addition to the OC materials described above, other OC materials have also been studied in the literature. Ce-based OCs have the advantage of high oxygen mobility and storage capacity whereas Mn-based OCs are known for their good redox properties<sup>66</sup>. Similarly, Co-based OCs have been investigated for their high oxygen-transmission capacity<sup>67</sup>. Nowadays, perovskite-type materials are trending due to their property of high O<sup>2-</sup> anion mobility<sup>13</sup>. More and more materials are being developed and tested



for their desirable properties in specific utilization of the CLC process. A thorough review on OC materials is available elsewhere.<sup>55, 68</sup>

In order to improve OC performance, the addition of supports and metal promoters of OCs are usually considered based on previous reports.<sup>43, 69-72</sup> OC supports such as  $\text{TiO}_2$ ,  $\text{Al}_2\text{O}_3$  and  $\text{ZrO}_2$  are commonly used to strengthen the active components.<sup>62, 73-74</sup> Support effects have proven to enhance OC properties such as reactivity, stability and durability.<sup>75</sup>  $\text{TiO}_2$  has high chemical and thermal stress, but it shows low activity and impurity formation as a support of OC.<sup>8</sup> The favoured fluidization properties of  $\text{Al}_2\text{O}_3$  attracted particular attention to this support.  $\text{ZrO}_2$ , on the other hand, is proven to enhance the oxidation rates of OCs.<sup>66</sup>  $\text{CeO}_2$  has become an attractive support lately due to its ability to stimulate the formation of vacancies and increase oxygen transfer rates.<sup>76</sup> However, the impurity of OCs resulted from the addition of the supports has become a problem during the CLC process. The widely used  $\text{Al}_2\text{O}_3$  support leads to the formation of  $\text{NiAl}_2\text{O}_4$  under operating temperatures above  $1,000^\circ\text{C}$ , thus leading to a loss of reactivity. In addition, the metal promoters in mixed-metal-based OCs have shown their potentials for combining the advantages of several single metal-based OCs and overcome their limitations. For instance, Co-doped NiO OC with support showed excellent stability and reactivity in CLC due to its high metal oxide dispersion and strong sintering resistance.<sup>77 42</sup> Note that high metal oxide dispersion results in a larger active surface area for CLC reactions, while enhanced sintering resistance leads to lower activity decay.

It is observed that both supports and metal promoters contribute to the formation and migration of oxygen vacancies.<sup>78-80</sup> The oxygen vacancies generated by the reduction of OCs play an important role in improving the OC performance: multiple studies have shown that the defective sites of OCs benefit the reaction activities, and also provide active sites for both adsorption and reactions. Furthermore, since the fuels most prominently used in CLC are in the gas phase (e.g. syngas and  $\text{CH}_4$ ), the fuel oxidation by OCs is usually considered as an heterogeneous reaction, which is significantly affected by the temporal evolution of the surface configuration.<sup>21-22</sup> Despite the progress in this field, most of the studies in this area have focused on experimental research. In this work, the effects of vacancies and first nearest neighbours will be theoretically investigated given their relevance to OC development. The next section provides an overview on multiscale modelling whereas section 2.4 presents the

state-of-the art theoretical studies of OC development including the factors mentioned above, i.e. oxygen vacancy and first nearest neighbours.

## 2.3 Multi-scale modelling

Theoretical studies have gained attention with the advances in computer science and numerical methodologies. The development of the modelling methods allow researchers to investigate physical processes at varying length and time scales. Multi-scale modelling methods combine different modelling methodologies at various scales, which can range from electronic scale methods (e.g. DFT) to macroscopic scale modelling approaches (e.g. computational fluid dynamics). Therefore, multi-scale models can provide a comprehensive understanding of the systems that evolve at different temporal or spatial scales. For example, the thin film deposition process was investigated by Rasoulia *et al.*<sup>81</sup> using a closed-form multi-scale model, which was later employed within a nonlinear model predictive control (NMPC) algorithm for a robust control strategy for the application of this system under the uncertainties. Syngas and hydrogen generation on noble metals were studied using the multi-scale DFT-based microkinetic analysis for the insights into control and selectivity of this process.<sup>82</sup> Additionally, heat transfer was investigated using a multi-scale particle-resolved simulation that homogenizes the original multiphase system for the modeling its microwave heating process.<sup>83</sup> An example in the development of biology shows that multi-scale models can be applied for mammogram classification.<sup>84</sup> Regarding the improvement of the calculation efficiency, a non-closed-form multi-scale model using 2<sup>nd</sup> order Polynomial Chaos Expansions with Nonintrusive Spectral Projection (PCE NISP) for uncertainty analysis was proven to provide predictions at a comparable level of accuracy using half of the computational cost compared to the scenario using 2<sup>nd</sup> order Power Series Expansion (PSE) by Grigoriy *et al.*<sup>85</sup>. Additionally, a hybrid multi-scale model was developed to efficiently predict the film parameters by Chaffart *et al.*<sup>86</sup> in a thin film deposition process. This model was proven to accurately captured the film parameters within only a fraction of the computational cost of the previously reported kMC-based multi-scale model by combining the mechanistic multi-scale model with artificial neural networks. As for catalyst development, a DFT-based microkinetic

model was established by Ren *et al.*<sup>87</sup> to reveal the vacancy effects on a CO<sub>2</sub> reduction reaction at the three-phase boundary of Ni(111)/samarium-doped ceria surface, which suggested that the rate-controlling step on the defective surface is CO desorption regardless of the electrode overpotentials. Due to the multi-scale nature of the studied process of this research, CLC, OC performance can be captured under three domains: the electronic scale simulation, which evaluates the system properties based on electron distribution; the microscopic scale performance that considers the kinetic interactions at the atomic scale<sup>88</sup>; and the continuum scale phenomena that follow the classical physical laws such as Newton's laws of motion and the Maxwell equations<sup>89</sup>. DFT analysis is the most popular electronic scale modeling method, which can provide the energetic results, reaction kinetics, and atomic scale OC performance based on electron population analysis. On the other hand, the typical microscopic models, such as MF and kMC, are used to reveal the atomic scale system properties on the surface model. Regarding continuum methods, the time- and spatial-dependent mass, energy and momentum conservation laws are simulated by partial differential equations (PDEs). The macroscopic properties of the system can be obtained from solving those PDEs using numerical methods, such as finite difference analysis (FDA) and finite element analysis (FEA).<sup>89</sup> Multi-scale modeling studies can capture the OC performance at different scales by integrating two or more of the aforementioned simulation methods for a comprehensive understanding of the material properties.

In a multi-scale scenario, the DFT simulations provide the energetic results, reaction kinetics and the OC performance based on the electron distribution. Then the reaction kinetics and the reaction rate parameters interpreted from the DFT energetic results can be used as inputs to the microscopic models, e.g. MF and kMC for the prediction of the atomic scale system dynamic properties on the surface model, e.g. coverages of the surface species. Meanwhile, key surface information from the microscopic models such as species coverage, production rates and surface temperatures can be passed to the surface boundary conditions of the transport equations at the continuum scale.<sup>89</sup> Likewise, the key outputs from the continuum models, such as the partial pressures of the studied species and temperatures near the surface, can be fed back to the reaction rates in the microscopic models.

In this research, only the electronic scale and microscopic scale simulations are considered to achieve the research objectives outlined in Chapter 1. The continuum model is recommended for the future work to advance the understanding of the studied system. The simulation methods used in this study are DFT, MF and kMC, which will be explained in detail in sections 2.4 and 2.5. Specifically, the DFT outcomes including the reaction kinetics occurring at very fine scales can be connected to the system dynamic properties obtained from MF or kMC simulations. Consequently, the reaction kinetics proposed by DFT analysis can be verified by the experimental observations through the combination of DFT and the microscopic simulation, which is usually difficult due to the scale gap between measurable variables in the experiments and microscopic configurations.

The multi-scale scenarios used in this study, DFT-based MF and DFT-based kMC, have been previously proven to be powerful tools to study heterogeneous catalytic and reacting systems. For example, McEwen *et al.*<sup>24</sup> developed a DFT-based MF model to simulate temperature programmed desorption, which is shown to accurately reproduce the desorption behavior of benzene on Pt (111) and Pt<sub>3</sub>Sn (111). Mei *et al.*<sup>26</sup> studied the kinetics for the selective hydrogenation of acetylene over Pd(111) using DFT based kMC, which included both the energetic results and microscopic kinetic information such as the turnover frequency and the average surface coverage. Choi *et al.*<sup>90</sup> studied ethanol decomposition on Rh (111). Their DFT results proposed the elementary kinetics of ethanol decomposition on Rh (100), which were used in kMC and simplified the kMC events. Furthermore, kMC analysis confirms the most probable reaction paths established by DFT through the analysis of the surface coverage of the species. Li *et al.*<sup>91</sup> proposed a first-principle-based kMC research on carbon nanotube growth which provides kinetic results that agree well with the experimental outcomes.

In the area of OC development, multi-scale modelling studies are very limited. To the author's knowledge, there are only a few studies available currently. For instance, You *et al.*<sup>92</sup> proposed a multi-scale study combining the MF model and the gas diffusion model for the CO oxidation by NiO. That work focused on combining the surface reaction model with the continuum gas diffusion model. The explicit reaction kinetics were not reported in that work. In the aforementioned study, the sensitivity analysis on the pore size of OC and the rate constants showed reasonable tendencies, which implied that the established model generally

captured the OC performance in the studied system. In addition, Andersson *et al.*<sup>28</sup> conducted a multi-scale simulation using DFT, kMC, an intra-particle transport model and a fluid-particle multiphase flow model for the investigation of the reactivity of Fe<sub>2</sub>O<sub>3</sub> in a chemical looping reforming (CLR) reactor. Using the developed multi-scale modeling framework, the OC utilization in a specific process (Fe<sub>2</sub>O<sub>3</sub> reduction in a small-scale fluidized bed CLR reactor) was studied for a better descriptor of the OC performance. Despite these efforts, the lack of multi-scale studies in this area shows the urgent need of developing multi-scale models for a comprehensive description of OC performance.

## 2.4 Density Functional Theory

To improve the development of OCs, the reaction mechanisms and insights into the atomic scale behaviour of OCs can provide effective guidance to tune these materials. The experimental studies, however, cannot provide reaction kinetics and the atomic-scale structural information (e.g. favoured adsorption sites) due to the scale gap between measurable variables in the experiments and microscopic configurations. In addition, it is also challenging for experimental studies to discover the factors that affect the reaction kinetics at the atomic scale, e.g. the nearest neighbours adjacent to the reaction site. On the other hand, theoretical methods such as quantum chemistry are advantageous due to their ability to investigate the reaction mechanisms and extract the microscopic scale information at a high efficiency. The precedent quantum chemistry method, also referred to as Hartree Fock (HF), was first established in the 1920s, which was used to provide approximated solutions to the fundamental equation of quantum mechanics that describes a chemical system (i.e. Schrodinger's equation).<sup>93</sup> However, the HF method neglects electron interactions, and thus, its accuracy is limited. For the post-HF calculations, no more than 20 atoms can be simulated in the system owing to the intensity of the calculations required by this method.<sup>93</sup> In order to improve the accuracy and efficiency of quantum chemistry calculations, the DFT method was proposed.

Instead of the wavefunction, DFT calculations solve Schrodinger's equation for the unique functions of the electron density. This is the result of the first Hohenberg-Kohn theorem, which states that the ground-state energy from Schrodinger's equation is a unique

functional of the electron density. This unique electron density determines all the quantum mechanical properties of the system.<sup>94</sup> Therefore, a function of three spatial variables related to the electron density is expected rather than the wavefunction of  $3N_{electron}$  variables ( $N_{electron}$  being the number of the electrons in the system). Furthermore, the second Hohenberg-Kohn theorem states that the electron density that minimizes the overall energy functional is the true electron density related to the full solution of the Schrodinger's equation. This theorem provides the algorithm to solve the Schrodinger's equation by minimizing the system energy. Another important component of DFT is the utilization of the Kohn-Sham equation, which is established based on the assumption that the electron density for the fully interacting system can be expressed by a set of non-interacting particles.<sup>95</sup> The non-negligible many-body interactions are considered in the Kohn-Sham equation by including the exchange-correlation potential. Therefore, the problem of solving the many-body Schrodinger equation is avoided. Meanwhile, the optimum approximation for the many-body interactions has become key for accurate model predictions.

Local-density Approximation (LDA) is a critical approximation in DFT which states that the energy only depends on the electron density at the point where the functional is evaluated.<sup>96</sup> LDA can predict the functionals of exchange and correlation of a homogeneous electron gas system; but it is still not suitable for the prediction of solid state physics. The generalized gradient approximation (GGA) proposed by Perdew, Burke, and Ernzerhof represents an improvement to the LDA.<sup>97</sup> GGA takes into account the electron density as well as its gradient such that the inhomogeneous nature of molecular densities can be well described. On the basis of GGA, the hybrid functionals such as meta-GGAs and hyper-GGAs have also been developed to achieve higher accuracy and broader applicability.<sup>98-99</sup> A detailed review of the DFT method can be found elsewhere.<sup>95,100</sup>

In the field of CLC, DFT analysis has been mostly used to study the reactivity of OCs in the redox process. In terms of OC development for CLC applications using DFT analysis, Fe-based materials are the most widely studied materials<sup>14-16</sup> followed by Cu-based OCs<sup>17</sup>. Though NiO-based is one of the most popular OCs in CLC, only a limited number of DFT studies for NiO have been conducted<sup>18-101</sup>. Theoretical studies focused on other metals are

scarce in the literature.<sup>102-104</sup> The current state-of-the-art DFT studies for OC development is discussed next.

Dong *et al.*<sup>14</sup> conducted a DFT analysis on Fe<sub>2</sub>O<sub>3</sub> as an OC using CO as a gas fuel. That study showed that the Fe<sub>2</sub>O<sub>3</sub> (1102) surface has higher reaction activity with CO than the Fe<sub>2</sub>O<sub>3</sub> (0001) surface. In another study conducted by the same group, they reported that the high index surface Fe<sub>2</sub>O<sub>3</sub> (104) performs better than the low index (001) surface.<sup>105</sup> Carbon deposition<sup>106</sup> and mercury adsorption<sup>107</sup> were also investigated by the same group to assess the impurity effects on the Fe<sub>2</sub>O<sub>3</sub> surface. Methane decomposition mechanisms on Fe<sub>2</sub>O<sub>3</sub> have been studied using DFT by multiple groups. Different reaction pathways have been established on Fe<sub>2</sub>O<sub>3</sub> surfaces<sup>108-112</sup>. Due to the complexity of methane decomposition paths, this reaction mechanism is still under debate and will likely be the subject of future research in this area. In a different study, Fan *et al.*<sup>9</sup> considered the oxygen vacancy on the  $\alpha$ -Fe<sub>2</sub>O<sub>3</sub> (001) surface, which has been shown to enhance the partial oxidation of CH<sub>4</sub>. Later on, Guo *et al.*<sup>71</sup> tested the reduction reaction of more than 30 kinds of doped Fe<sub>2</sub>O<sub>3</sub> OC by analyzing the vacancy formation energy and proved that nine kinds of dopants including Li, Na and K enhance the deep reduction of Fe<sub>2</sub>O<sub>3</sub> into Fe<sub>3</sub>O<sub>4</sub> in chemical looping hydrogen production process. Other fuel molecules reacting on the Fe<sub>2</sub>O<sub>3</sub> surface, such as carbon atoms or CO, have been investigated.<sup>113-114</sup> Those DFT studies reported the reaction kinetics in a solid fuel CLC process. Miller *et al.*<sup>115</sup> reported calcium ferrite as an OC for chemical looping partial oxidation of methane. The results of DFT analysis suggest that the form Ca<sub>2</sub>Fe<sub>2</sub>O<sub>5</sub> contributes the most to the partial oxidation of methane for syngas as compared to other reduction forms of CaFe<sub>2</sub>O<sub>4</sub>. Supports such as Al<sub>2</sub>O<sub>3</sub>, ZrO<sub>2</sub> and MgO have also been studied as the inert support of Fe<sub>2</sub>O<sub>3</sub><sup>15, 116-117</sup>. Tan *et al.*<sup>15, 117</sup> investigated the ZrO<sub>2</sub> supported Fe<sub>2</sub>O<sub>3</sub> and MgO supported Fe<sub>2</sub>O<sub>3</sub>. Those studies showed that ZrO<sub>2</sub> could enhance the adsorption of CO while MgO lowered the reaction barriers of CO oxidation as compared to the pure Fe<sub>2</sub>O<sub>3</sub> OC.

Cu-based OCs are promising materials for the oxygen uncoupling (CLOU) process since O<sub>2</sub> is released in the reducer. Zhao *et al.*<sup>118</sup> studied the support effect on the sintering resistance of CuO. In their study of four different supports (TiO<sub>2</sub>, ZrO<sub>2</sub>, CuAl<sub>2</sub>O<sub>4</sub> and MgAl<sub>2</sub>O<sub>4</sub>), they found that all of these supports worked to reduce the energy barriers of the fuel combustion process. Among them, CuAl<sub>2</sub>O<sub>4</sub> showed the best performance in the CLOU process. Xu and

Zhao<sup>119</sup> studied a specially synthesized Cu-based OC with a core (Al<sub>2</sub>O<sub>3</sub>)-shell (TiO<sub>2</sub>) support. That study showed that this material could effectively prevent the impurity formation in the CLOU process. Studies involving graphene<sup>120</sup> and ZrO<sub>2</sub><sup>121</sup> supports have also been reported and have shown that graphene improves the reaction activity of the OC with CO, whereas ZrO<sub>2</sub> contributes to the CO oxidation. Liu *et al.*<sup>122</sup> demonstrated that Zr benefits the oxygen vacancy formation and migration on the CuO surface. This leads to a higher reactivity of CuO as the OC. In addition, Zhao *et al.*<sup>123</sup> investigated the CuO oxidation process, which provided the theoretical evidence of the complete oxidation process of Cu → Cu<sub>2</sub>O → CuO. In order to study the CuO reduction affected by the particle size, Zhu *et al.*<sup>124</sup> compared the structural transformations of bulk, surface and cluster CuO in the reduction process, which proved that small particles, i.e. cluster model, are more active to exchange oxygen with fuels.

Regarding Ni-based OCs, Guo *et al.*<sup>63</sup> reported that the impurity of H<sub>2</sub>S significantly suppressed the CO adsorption on both perfect and defective NiO surfaces. In addition, the Ni oxidation process in CLC was also investigated through DFT analysis. Fan *et al.*<sup>125</sup> showed that Ni as a later transition metal had a weaker interaction with O<sub>2</sub> compared to an earlier transition metal such as Co. Guo *et al.*<sup>101</sup> compared the performance of NiO/ZrO<sub>2</sub> and NiO/MgAl<sub>2</sub>O<sub>4</sub> as OCs to reform CH<sub>4</sub> into syngas. That study showed that the ZrO<sub>2</sub> support exhibited the highest reactivity. Cai *et al.*<sup>65</sup> proposed an analysis of O<sub>2</sub> decomposition on the defective NiO surface, which will be discussed in details in the following paragraph. Despite these efforts, the behaviour of Ni-based OC at an atomic scale remain unclear due to the low number of theoretical studies for this system, which motivates this comprehensive study of NiO.

As discussed in section 2.2, the mixed metal OCs are expected to improve performance with the addition of supports and metal promoters. In particular, specific structures of these mixed OCs were reported for their favorable characteristics in CLC process. Studies focusing on perovskites such as BaMnO<sub>3</sub> and SrMnO<sub>3</sub> have been reported. Results from those studies have shown that different compositions of these materials have resulted in different reaction activity performances.<sup>126-129</sup> Another bimetallic OCs, spinel-type oxides have also attracted much attention because of their possible higher oxygen capacity than that of perovskites.<sup>130-131</sup> Liu *et al.*<sup>132</sup> revealed that the Co atoms improved the reactivity of CoFe<sub>2</sub>O<sub>4</sub> to oxidize CO.



They also proved that the oxygen diffusion in a spinel  $\text{CoFe}_2\text{O}_4$  is easier than that in the  $\text{Fe}_2\text{O}_3$  OC. Want *et al.*<sup>133</sup> investigated the spinel  $\text{CuFe}_2\text{O}_4$  reaction with C and discovered that the  $\text{CuFe}_2\text{O}_4$  would be reduced into  $\text{Fe}_3\text{O}_4$  with the generation of  $\text{CO}_x$ . Fan *et al.*<sup>134</sup> reported a DFT analysis combined with experimental data that studied the nature ore ilmenite. In that work, the structure of ilmenite ( $\text{FeTiO}_3$ ) was chosen to represent the  $\text{TiO}_2$ -supported iron oxide. That study presented a comprehensive understanding of the  $\text{TiO}_2$  support effect on Fe-based OC and provides a representative demonstration of DFT study in this area. Since  $\text{FeTiO}_3$  is the active component of ilmenite in addition to  $\text{MgO}$  and  $\text{Al}_2\text{O}_3$ <sup>135</sup>, that study can be used as a basis to develop a new study of trace metal elements in ilmenite as mixed OCs.

A major aspect of the addition of supports and metal promoters is to stimulate vacancies, which are proven to improve the OC performance. Consequently, it is of great importance to study the effects of vacancies on the OC performance via theoretical studies. Su *et al.*<sup>136</sup> reported that oxygen vacancies can stabilize the  $\text{CH}_x$  radicals thus promoting  $\text{CH}_4$  dissociation. Fan *et al.*<sup>16</sup> showed that a high concentration of oxygen vacancies in iron oxide lowers the energy barriers of  $\text{CH}_4$  dehydrogenation and the cleavage energy of Fe-C bonds. Furthermore, that study showed that the vacancies would prefer to be substituted by the subsurface oxygen rather than the horizontal oxygen on the same layer. In terms of surface adsorption, Lee *et al.*<sup>23</sup> reported that the surface adsorption of  $\text{CH}_4$  would be promoted by the oxygen vacancies on the surface of gadolinium-doped ceria (GDC). Zhao *et al.*<sup>137</sup> focused on Cu-based OCs and showed that the defective sites significantly benefit the sulfur-sensitive CuO adsorption and reaction with gaseous COS, the main sulfur-containing species in the in-situ gasification chemical looping combustion process.<sup>138</sup> That study highlights the vital effect of the CuO OC oxygen vacancies on the degradation of CuO into copper sulfides. Cai *et al.*<sup>65</sup> showed that oxygen vacancies on NiO enhanced the CO adsorption and O dissociation. The vacancy effects are valued in the studies of mixed metal OCs particularly, because the addition of metal promoters and supports benefits the formation of the oxygen vacancies as mentioned before. Zachariah *et al.*<sup>139</sup> reported that the activation energy and the reaction rate of carbon doped with delta- $\text{Bi}_2\text{O}_3$  were improved due to a high oxygen vacancy concentration of the doped  $\text{Bi}_2\text{O}_3$ . Fan *et al.*<sup>80</sup> showed that Li doping-induced oxygen vacancies would benefit the adsorption of methyl radicals and suppress the C-H decomposition. Zhu *et al.*<sup>140</sup> showed that

oxygen vacancies introduced by Ce doping contributed to the reactivity of syngas generation from CH<sub>4</sub> via the hexaaluminate OC. Furthermore, the defective sites of perovskites were shown to serve as active sites for the breakage of H-O to generate H<sub>2</sub> in the steam methane reforming process.<sup>141-142</sup>

Moreover, oxygen ion generation is also facilitated by the oxygen vacancies in both the oxidation and the reduction processes of the OCs. Zhao *et al.*<sup>143</sup> showed that the defective sites would favour oxygen ion dissociation from water and therefore would benefit both the CO conversion and selectivity by the system's OC, Ca<sub>2</sub>Fe<sub>2</sub>O<sub>5</sub>. During the re-oxidation process, the surface vacancies were also proven to promote the decomposition of O<sub>2</sub> which would theoretically benefit the re-oxidation of OC. Furthermore, Li *et al.*<sup>144</sup> related the increase in the oxygen released with the low vacancy creation energy by comparing DFT results and experimental involving a CLOU process. In addition to improving the reactivity and the O<sub>2</sub> ion generation, a high concentration of the vacancies accelerates the oxygen migration from the bulk to the surface by vacancy diffusion and tunnel formation; hence, they are important processes that can increase the reaction rates as well as the OC capacity.<sup>76, 145-146</sup> Specific structures like metal promoters or perovskites have been used for this purpose. Xiang *et al.*<sup>78</sup> reported that doped CeO<sub>2</sub> would lead to abundant oxygen vacancies and promote oxygen mobility. Furthermore, they reported that the vacancies reduce the disadvantageous carbon deposition and sintering processes that need to be counteracted in order to maintain the reactivity and the stability of the doped OC, Fe<sub>2</sub>O<sub>3</sub>/CeO<sub>2</sub>. Hwang *et al.*<sup>147</sup> reported that the surface oxygen vacancy on the GDC improved the oxygen transfer rate of the studied OC during the OC reduction process, and that the lattice oxygen vacancies of the GDC were the preferred active sites of oxidation on the reduced OC. Chen *et al.*<sup>148</sup> found that the oxygen vacancies caused micro-structural evolution of the iron oxide and therefore led to the formation of a porous structure. Based on the established studies, vacancies play an essential role in improving OC performance. However, theoretical studies of oxygen vacancies are still limited and mostly focus on the CH<sub>4</sub> oxidation process. As a result, the vacancy effects at the microscopic scale are still not clear even for some commonly used systems, e.g. NiO OC combustion with syngas. In order to improve CLC performance, the studies providing a comprehensive analysis of the vacancy effects using NiO is still missing in the open literature.

Since the fuels most prominently used in chemical looping process are mostly in the gas phase (e.g. syngas and CH<sub>4</sub>), the fuel oxidation by OCs is usually a heterogeneous reaction, which is significantly affected by the temporal evolution of the surface configuration.<sup>21-22</sup> The adsorbed species as the nearest neighbours are expected to play a major role in OC performance. However, there are no neighbouring effects reported in the theoretical reports for OC development. On the other hand, it is proven that the effect of the neighbouring adsorbed molecules is relevant, particularly for adsorption studies on catalytic materials since they may change the structural configuration of the reacting surface. In the modification of semiconductor surfaces, Ren *et al.*<sup>149</sup> have shown that the neighbouring adsorbed H could induce the production of the ferromagnetic order of Si dangling bonds, which provides a way to promote magnetism on the Si (111) surface. It has been shown that neighbouring effects also play a key role in the decoration of polymers. The neighbouring linkers decorated on the adsorbents benefit the adsorption of specific molecules,<sup>150</sup> which could significantly increase the polymer saturated adsorption capacity. Hence, neighbouring effects impacts both the adsorbed molecules and the decorated surface. Furthermore, the surface decorated functional groups, which can be seen as the neighbouring occupied molecules, also affect the surface adsorption as well as the elementary reactions.<sup>151-152</sup> Note that the adsorption strength and the electronic structure of the OC surface are affected by the neighbours as well.<sup>92, 153-154</sup> Muhler *et al.*<sup>155</sup> reported that the pre-adsorbed CO<sub>2</sub> strengthens the adsorption stability of CO on the ZnO surface by tuning the Lewis acidity of the neighbouring Zn<sup>2+</sup> cation. In addition, the redox reaction activity on solid surfaces can be significantly affected by the neighbouring atoms in a wide range of heterogeneous systems. Futamata *et al.*<sup>156</sup> discovered that the Ru decorated on the Pt surface enhance the CO oxidation activity with Pt. Shahid Khan *et al.*<sup>157</sup> proved that the CO oxidation activity is also improved by the doped Cu on the MoS<sub>2</sub> nanosheet.

Overall, DFT analyses of the most widely used NiO are still limited so that the reaction mechanisms and microscopic insights of NiO with fossil fuels are not known with complete certainty. The effects of vacancies and the first nearest neighbours are expected to affect the OC performance significantly, which are rarely reported particularly for the NiO system.

## 2.5 Microscopic modelling

As mentioned in section 2.3, DFT analysis provides the energetic results and the atomic scale OC performance. Due to the gap of the scales between the DFT results and the experimental outcomes, it is difficult to validate the DFT results using experimental observations. Microscopic models such as MF and molecular simulations can be employed bridge the gap between DFT outcomes and experimentally observed properties.

### 2.5.1 Mean-field approximation

MF models assume that the adsorbed molecules on the surface are homogeneously distributed, and therefore they cannot consider the spatially heterogeneous surface behaviour.<sup>25</sup> For an OC development system, the variables to be solved by the MF model are the surface coverages of each of the adsorbing species. The surface coverage of the different species is calculated from the surface accumulation rate obtained from the adsorption, production, consumption and desorption events. The surface coverages of the species  $i$ ,  $\theta_i$  can be predicted as follows:

$$d\theta_i/dt = k_{i,ad}C_{i,g}\theta_{empty} - k_{i,rec}\theta_i - k_{i,d}\theta_i \quad (2-1)$$

where  $t$  is time;  $k_{i,ad}$ ,  $k_{i,rec}$  and  $k_{i,d}$  are the rate constants of adsorption, reaction and desorption;  $C_{i,g}$  is the concentration of species  $i$  in the gas phase;  $\theta_{empty}$  is the coverage of empty sites. Note that multi-step reactions would result into additional ordinary differential equations that can describe the evolution of the added surface species. DFT-based MF models have been shown to adequately capture the system behaviour.<sup>24, 158</sup> In the area of OC development, only one study was reported by You *et al.*<sup>92</sup> integrating the MF model into a multi-scale simulation (see section 2.3); hence the need to further investigate this phenomena from the theoretical point of view. Since the MF model cannot consider spatially heterogeneous surface behaviour, this model may not be adequate to incorporate key influencing factors such as the neighboring effects. Consequently, molecular simulations such

as kinetic Monte Carlo can be considered to accurately investigate the temporal evolution in heterogeneous systems such as OC behaviour.<sup>159</sup>

### **2.5.2 Kinetic Monte Carlo**

There are a number of different microscale modelling methods that can be implemented to simulate the evolution of heterogeneous systems. Molecular Dynamics (MD) methods are one of the most commonly employed modelling methods that can to obtain the dynamic properties of a system. MD methods aim to study the time evolution of a system by solving the classical equations of motion. Although MD can provide an accurate prediction of the system evolution subject to heterogeneous events, it is limited in regards to the time scale that can be realistically achieved, e.g. from nanoseconds to microseconds.<sup>160</sup> Experimental results involving time-dependent data cannot be compared to that of MD since the data is often collected at larger time scales (e.g. seconds). Alternatively, stochastic methods such as kMC can be implemented to study heterogeneous system behaviour over larger timescales. The idea of kMC is to extend the time limit of MD by analyzing the changes of the system's state instead of solving for the movement of the individual atoms. This basic principle was first established in the 1960s<sup>161</sup> and has been continually developed ever since. The currently-used kMC theory thus becomes the bridge between the microscopic insights and the measurable properties found in experimental studies.<sup>160</sup> kMC simulates the dynamic evolution of a system by treating the transition as a state-to-state process rather than following the trajectory of every entity in time. In heterogeneous catalysis, the kMC kinetic events are based on the reaction mechanisms on the atomic surface. These events are randomly selected and executed depending on the event probabilities interpreted from the event rates. After each event, the kMC system time is incremented based on the rates of all the events that are currently possible. Due to the state-to-state nature of this method, the kMC modelling approach is capable of simulating system events over the same timescales as would be recorded in experimental results. The timescales of kMC scenario are mostly determined using the reaction rate constants and the number of events happening on the surface. Additionally, kMC is a rejection free algorithm, which suggests that for each of the step there must be one event for the system to evolve. Furthermore, lattice-based kMC models are capable of achieving even longer simulation times by restricting

the movement of the studied molecules to a lattice mesh. This approach is particularly useful for surface-based systems such as OCs.<sup>91</sup> A general kMC simulation scheme is presented in Figure 2-3.

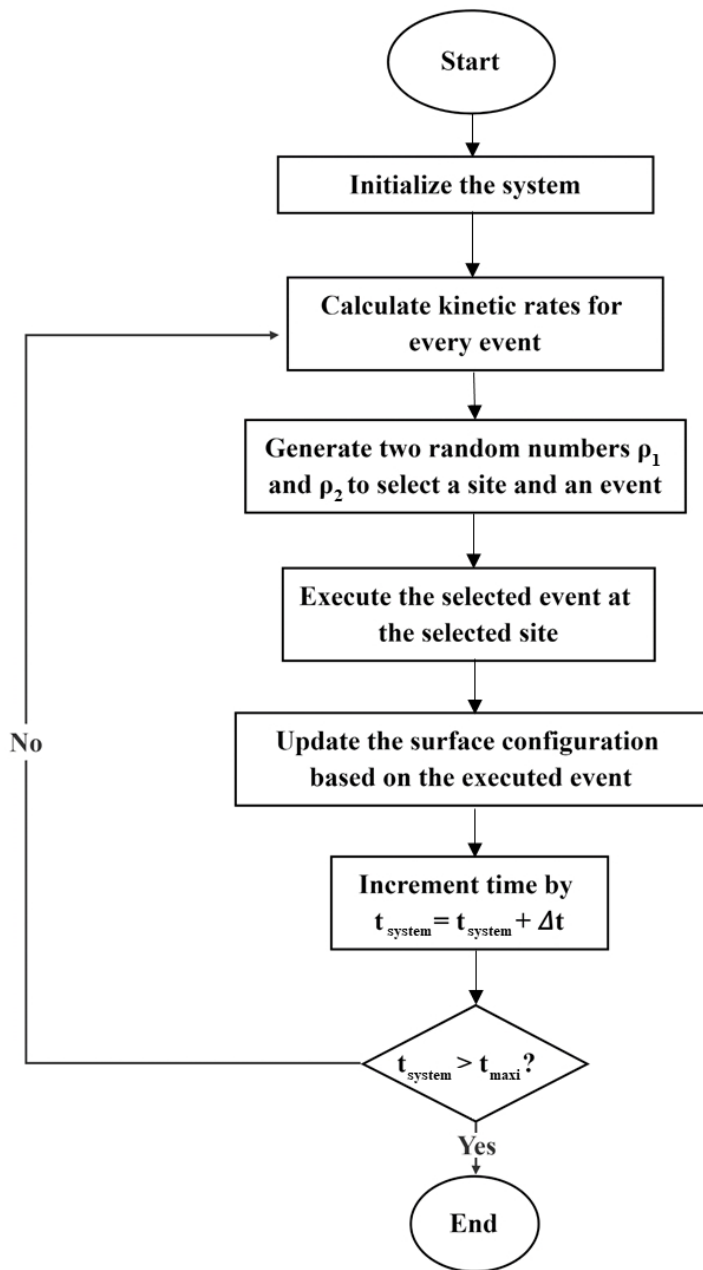


Figure 2-3 kMC scheme

As shown in Figure 2-3, kMC establishes the initial surface configuration of an  $N \times N$  lattice and the system time is defined as  $t_{\text{system}}=0$ . Note that  $N$  is the total number of the reaction sites along one direction of the 2D lattice. Following the surface establishment, all the possible surface events (i.e. the reaction mechanism events such as adsorption, reactions, etc.) and their corresponding rates are inputted into the system. If the surface is empty, then the absorption rate is the only non-zero rate for a given absorption site. For a DFT-based kMC model, the explicit reaction kinetics proposed by DFT are inputted in the system at this step. Subsequently, the total rate  $R$  of the system, i.e. the sum of all the possible events on the established surface, is calculated using Equation 2-2 as follows:

$$R = \sum_i N_i k_i \quad (2-2)$$

where  $N_i$  is the number of possible sites for the kMC event  $i$  and  $k_i$  is the rate parameter for event  $i$ , which is provided by the DFT calculations. Next, the kMC system generates two uniform random numbers  $\rho_1$  and  $\rho_2$  within the range of  $(0,1]$  and uses them to randomly select a specific surface event  $n$  at a specific surface site  $m$ , based on their kinetic rates as follows:

$$\sum_j^{m-1} (\sum_i k_i)_j < R \rho_1 < \sum_j^m (\sum_i k_i)_j \quad (2-3)$$

$$\sum_i^{n-1} k_i < (\sum_i k_i)_m \rho_2 < \sum_i^n k_i \quad (2-4)$$

where  $(\sum_i k_i)_j$  is the total rate of all possible events at the specific site  $j$ . The selected event is subsequently executed at the selected site. Then the surface configuration is updated based on the chosen event  $n$  at the selected site  $m$ . For instance, when the adsorption event is selected, the surface will add the adsorbate at the chosen site. For a heterogeneous system subject to neighbouring effects, the sites adjacent to the selected site are also updated to consider the effects of this new neighbor. To update the system time  $t_{\text{system}}$ , the time interval,  $\Delta t$ , is obtained by generating another uniform random number  $\rho_3$  in the scope of  $(0,1]$  as follows:

$$\Delta t = -\frac{1}{R} \ln \rho_3 \quad (2-5)$$

$$t_{\text{system}} = t_{\text{system}} + \Delta t \quad (2-6)$$

The evolution of the kMC system is expressed by the updates of the surface configurations and the kMC system time. Lastly, the system checks to see if the stopping criterion, i.e. the maximum simulation time ( $t_{\text{maxi}}$ ), has been reached. If the stopping criterion is fulfilled, then the kMC model stops. Otherwise, the kMC cycle will be repeated to further advance the system evolution. Despite the advantages of kMC modelling, there are very few studies within the literature that have applied this method to study OCs. The only report of OC development adopting kMC model was performed by Andersson *et al.*<sup>28</sup>, which is a multi-scale modelling study on CH<sub>4</sub> oxidation process (see section 2.3).

## 2.6 Summary

In summary, the theoretical studies of OC development are still limited within the literature. Consequently, the reaction mechanisms and microscopic insights remain unclear even for one of the most used OCs, NiO. The effects of vacancies and the nearest neighbors are expected to affect the OC performance significantly. Nevertheless, the microscopic insights into these effects are not fully explored. Studies involving multi-scale modelling can provide a comprehensive understanding of the OC performance at different temporal and spatial scales. However, only a few multi-scale modelling reports are available within the open literature. These gaps motivate the present multi-scale modelling study to advance the knowledge in this particular area.



# Chapter 3 A Density Functional Theory Analysis on Syngas Adsorption on NiO (100) Surface

## 3.1 Introduction

As discussed in the previous chapter, the lack of theoretical studies in this emerging area of CO<sub>2</sub> capture renders these insights unclear even for one of the most studied OCs, NiO.<sup>162-163</sup> NiO stands out, as an OC, due to its favourable kinetics, potential catalytic abilities and high performance under severe operating conditions despite its problems of high cost and toxicity.<sup>62</sup> Therefore, a DFT analysis of NiO can enhance our understanding on the microscopic behaviour of this OC and become key to improve its performance in the CLC process.

The first step in the redox reaction of NiO is the adsorption of fuel molecules to its surface. This phenomenon affects the electronic properties of both the surface of the OC materials and the adsorbed molecules. In addition, the first nearest neighbors are proven to significantly affect the adsorption behaviour in a heterogeneous system, as presented in Chapter 2. However, a theoretical study taking into account the neighbouring effects on the adsorption of fuel molecules on OC materials is not currently available in the open literature.

The aim of this chapter is to present a DFT analysis of syngas adsorption on NiO in consideration of the neighbouring effects to reveal the adsorption principles affected by the nearest neighbours. The studied fuel (syngas) is widely used in CLC as a promising, economical, abundant and environmentally friendly fuel and also represents the major product from methane reforming.<sup>164</sup> Additionally, syngas generated from biomass conversion is oxidized to produce power such as heat in CLC with inherent CO<sub>2</sub> disposal. The CO<sub>2</sub> originally needed to produce the biomass is obtained from the atmosphere. Therefore, negative CO<sub>2</sub> emissions can be achieved due to the removal of CO<sub>2</sub> from the atmosphere in this process.<sup>165</sup> In this work, all the possible configurations of the first nearest neighbours are considered to provide a systematic adsorption study for this process. The adsorption energy, as well as the electronic properties of the NiO surface, have been analyzed and reported in this work. The results of this study are expected to provide a solid foundation to investigate the reaction

mechanism and the neighbouring effects on a larger temporal and spatial scale for the studied OC system. Note that the results of this chapter have already been published.<sup>166</sup>

The rest of this chapter is presented as follows. Section 3.2 provides the computational details used in this study. The structural properties, adsorption energies and the corresponding electronic property analysis are shown in section 3.3. A summary of the DFT analysis of the neighbouring effects on syngas adsorption is provided in section 3.4.

### 3.2 Computational details

A spin-polarized DFT analysis was conducted with the Vienna Ab Initio Simulation Package (VASP). The Projector-augmented Wave (PAW)<sup>167-168</sup> method was employed as the description of the core electrons and the exchange-correlation functional the Generalized Gradient Approximation(GGA) of Perdew-Burke-Ernzerhof was chosen in this work.<sup>97</sup> The energy cut-off of 400 eV was considered; The Brillouin-Zone is properly separated by a  $2 \times 2 \times 1$  Monkhorst-Pack k grid, which can accurately predict the behaviour of the studied slab model with sufficient efficiency.<sup>101, 169</sup> For structure relaxation, the energy convergence criterion is set to  $1 \times 10^{-5}$  eV while the force convergence criterion is set to 0.05 eV/Å.

Moreover, the DFT combined with the Hubbard Hamiltonian method (DFT+U) was adopted to improve the prediction accuracy of the electronic properties by the traditional exchange-correlation functional, GGA. This is required since the studied system includes a transition metal (Ni). By applying the Hubbard-U correction, a more accurate prediction is obtained through the modification of the strong on-site Coulomb repulsion to simulate the electronic interactions related to the magnetic effects on the NiO solid<sup>170</sup>. The DFT + U method adopted the U and J modifiers to improve the conventional DFT analysis. U presents the strength of the on-site Coulomb repulsions while J represents the screened exchange energy. It has been shown that Hubbard-U corrections are essential to provide an accurate prediction of NiO electronic properties such as the density of the states. Note that the electronic properties of NiO are sensitive to the chosen modifiers (i.e. U and J)<sup>171</sup>. In this work, the electrons are accurately localized with the Coulomb repulsion U term applied on Ni as  $U = 6.3$  eV and  $J = 1.0$  eV.<sup>172</sup> It has also been shown that the chosen Hubbard-U correction parameters

can accurately predict the system properties through the consistency between the simulated lattice constants of NiO predicted by this study ( $a=b=c=4.161 \text{ \AA}$  and  $\alpha=\beta=\gamma=90^\circ$ ) and experimental observations ( $a=b=c=4.15 \text{ \AA}$  and  $\alpha=\beta=\gamma=90^\circ$ ).<sup>173</sup> The prediction of the bulk NiO property using the selected modification parameters U and J is proven to be accurate due to the validation of the experimental data. In addition to the simulated NiO lattice constants obtained in this report, the system description of NiO surface such as adsorption behaviours could be accurately predicted with the same Hubbard-U correction parameters employed in this study according to previous reports<sup>172, 174-175</sup>.

A 6-layer nickel oxide slab model has been constructed with the bottom three layers fixed to simulate syngas adsorption on the NiO surface. This slab model configuration has been shown to provide sufficiently accurate results.<sup>125</sup> The NiO bulk structure was obtained from the Inorganic Crystal Structure Database (ICSD) provided by FIZ Karlsruhe with the database code ICSD 182948 and proposed by Yang *et al.*<sup>30</sup>. NiO presents to be the same crystal structure to NaCl, i.e. a face-centered cubic (fcc). The nickel ion is connected with six oxygen ions and shows an octahedral symmetry.<sup>176</sup> Since the nonpolar plane, NiO (100) has been proven to be the most stable surface, a cleaved surface of NiO (100) with a 15 Å vacuum gap is used in this study to perform the adsorption calculations<sup>177-178</sup>. The surface mesh vector directions are set as U (001) and V (010). Carbon monoxide has only one carbon-oxygen bond which is about 1.144 Å long while the H<sub>2</sub> molecule also has only one hydrogen-hydrogen bond of 0.751 Å. The adsorption geometry of CO is at the top of the Ni atom with the C-O bond located vertically to the NiO surface. This configuration is the most stable geometry with the minimum energy.<sup>179</sup> The further reaction of CO with NiO is that the C atom in CO scavenges the O on NiO surface, which makes the vertical CO (with C close to the surface) a more reasonable geometry for further reactions. As for H<sub>2</sub> molecule, the selected geometry is also at the top of Ni due to the tendency of H<sub>2</sub> breaking at the top of Ni<sup>180</sup> and the linear molecule H<sub>2</sub> also keeps vertical with the surface from the aspect of stability and small steric effect. The optimized adsorption configurations are provided in Figure 3-1. Note that the studied adsorption system is physically adsorption, which results in moderate changes in the bond distances of CO and H<sub>2</sub>.

The DFT calculations in this study were performed on Shared Hierarchical Academic Research Computing Network (SHARCNET: [www.sharcnet.ca](http://www.sharcnet.ca)) supported by Compute/Calcul Canada.

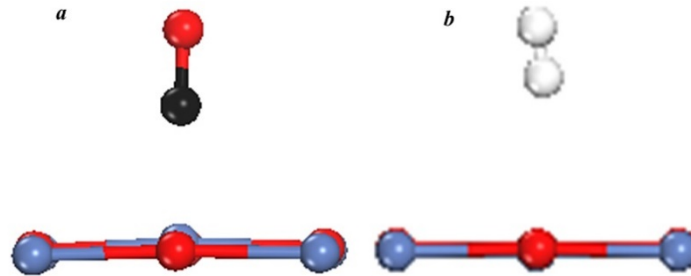


Figure 3-1 Stable adsorption configuration on NiO with (a) CO adsorbate (b) H<sub>2</sub> adsorbate. Blue (Ni), red (O), black (C), white (H)

The adsorption energy of syngas on NiO surface,  $\Delta E_{\text{adsorption}}$  is calculated as follows:

$$\Delta E_{\text{adsorption}} = E_{\text{system}} - E_{\text{freefuel}} - E_{\text{surface}} \quad (3-1)$$

where  $E_{\text{system}}$  is the overall energy of the system with the adsorbed CO or H<sub>2</sub> molecules,  $E_{\text{freefuel}}$  refers to the energy of the free fuel molecule (i.e. CO or H<sub>2</sub>) whereas  $E_{\text{surface}}$  represents the energy of the OC surface (NiO). Note that  $\Delta E_{\text{adsorption}}$  is not zero-point corrected since this system represents physically adsorption.

### 3.3 Results and discussion

This section presents the results obtained from this chapter. The sites considered on the NiO surface and the notation adopted for the adsorption geometries are presented first. The structural properties from the adsorption of syngas (i.e. CO and H<sub>2</sub>) on the NiO surface are presented next. The adsorption principles of CO and H<sub>2</sub> obtained according to the adsorption energy analysis with uniform neighbouring molecules, i.e. molecules of the same species, and the hybrid adsorption effects caused by the geometry containing different molecules at the

nearest neighbouring sites are presented thereafter. An analysis of the projected density of states, which supports the primary outcomes of this study at the electronic scale, are provided at the end of this section.

### 3.3.1 Structure characterization

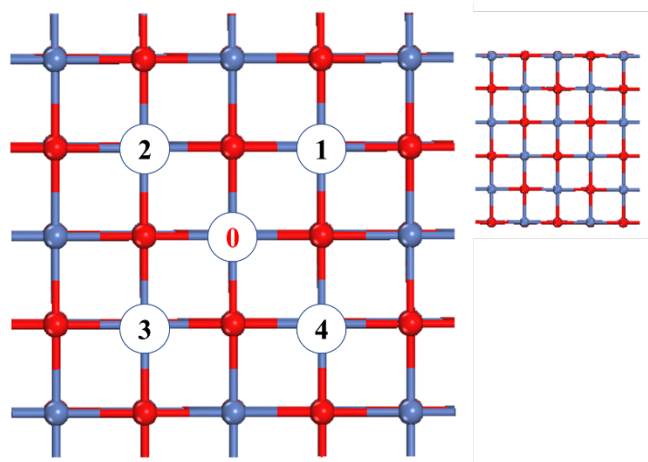


Figure 3-2 Studied nearest neighbour sites labeled as 1, 2, 3 and 4, adsorption site labeled as 0. Blue (Ni), red (O)

Figure 3-2 presents the NiO structure model used in the present study. As shown in this figure, four closest neighbouring sites are considered in this study to reveal the tendencies of the neighbouring effects on which the oxidation of CO and breaking of H<sub>2</sub> to form H<sub>2</sub>O are expected to occur. The four sites selected have the closest distances with the adsorption site labeled as 0 in the figure, which is expected to have the strongest interactions with the adsorbed CO or H<sub>2</sub> neighbours located in positions 1, 2, 3 and 4 in the figure. To distinguish between the different adsorption geometries, the following notation is established from heretofore: C and H stand for CO and H<sub>2</sub> occupied sites on the NiO surface, respectively; \* stands for an empty site. When naming a particular geometry, the order follows the site numbering indicated in Figure 3-2; the 5<sup>th</sup> position in the name suggests the 0<sup>th</sup> site. For example, the geometry HHHHH indicates the study of H<sub>2</sub> adsorption at the 0<sup>th</sup> site with 4 H<sub>2</sub> nearest neighbouring sites. If site 1 and 3 are empty and site 2 and 4 are occupied by CO and H<sub>2</sub>, respectively, then

that geometry will be referred to as \*C\*HC or \*C\*HH depending on whether CO or H<sub>2</sub> adsorption is considered at the 0<sup>th</sup> site.

### 3.3.2 Structural property analysis

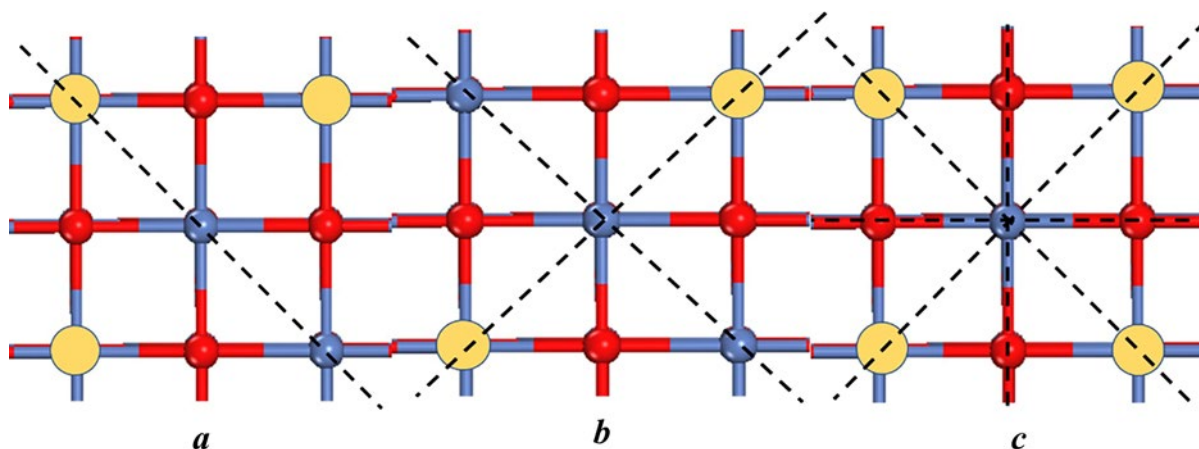


Figure 3-3 Symmetry categories of the adsorption system, (a) symmetry 1, (b) symmetry 2 (c) symmetry 3. Blue (Ni), red (O), yellow (the occupied sites on the surface)

Table 3-1 Structure properties of CO adsorption on NiO

Symmetry	Uniform Adsorption		Hybrid Adsorption	
	Geometry name	Distance <sup>a</sup> /Å	Geometry name	Distance <sup>a</sup> /Å
none	****C	2.058		
none	C***C	2.076	H***C	2.059
symmetry 1	CC**C	2.071	HH**C	2.056
symmetry 2	C*C*C	2.043	H*H*C	2.068
symmetry 1	CCC*C	2.091	HHH*C	2.076
symmetry 3	CCCC	2.050	HHHHC	2.067

a Distance between the C in CO and the closest Ni to the mentioned C on the surface

Three types of symmetries have been considered in the present system. As shown in Figure 3-3(a), symmetry 1 represents a line symmetry with only one axis of symmetry. As for symmetry 2, (Figure 3-3(b)), there are two axes of symmetry, which is also a point symmetry structure. Moreover, symmetry 3 has the highest degree of symmetry, which has four axes of symmetry (Figure 3-3(c)).

Table 3-1 and Table 3-2 present the distances between the CO and H<sub>2</sub> molecules and the adsorbed Ni site on the NiO surface, respectively. As mentioned above, uniform adsorption is used here to refer to the adsorption of CO (H<sub>2</sub>) with the same molecules of CO (H<sub>2</sub>) already adsorbed at the neighbouring sites while hybrid adsorption indicates CO or H<sub>2</sub> adsorption with the different molecules of H<sub>2</sub> or CO captured at the closest neighbouring sites.

As shown in Table 3-1, the distance between the adsorbed species and the adsorbed site increases from  $****C$  to  $C***C$ , which suggests that the adsorbed CO molecule would be repelled by the neighbouring attached CO molecule. However, when the neighbouring site is occupied by H<sub>2</sub> (i.e.  $H***C$ ), the repulsion effect is much smaller than that obtained from the neighbouring effect of CO. This change in behaviour is due to the steric effects, which are more significant for CO than for H<sub>2</sub>. Note that the distance between the carbon atom of adsorbed CO and its connected Ni on NiO (100) is reported to be 2.070 Å according to the experimental study<sup>181</sup>. The calculated distance between the carbon of CO and its connected Ni in this chapter is 2.076 Å at low coverage. Both carbon and oxygen atoms in the CO molecule have relatively larger van der Waal radius (1.885 Å and 1.514 Å) compared to that of H atom (1.394 Å) in H<sub>2</sub>; hence, higher steric repulsions are expected by the former species.

<sup>182</sup> The results shown in Table 3-1 for  $CC**C$  and  $CCC*C$  indicate that, when the structures belong to the same symmetry (symmetry 1), the repelling effects are more notable as the number of nearest neighbours increases. This behaviour was also observed for the hybrid adsorption of CO (i.e. between  $HH**C$  and  $HHH*C$ ). As for symmetry 2, the distance from  $C*C*C$  (2.043 Å) increases when the empty sites are replaced with two H<sub>2</sub> neighbours ( $CHCHC$ , 2.058 Å). As shown in Table 3-1, the distance in the highest degree of symmetry (i.e.  $CCCCC$ ) is smaller than that observed for  $****C$ . This observation may be expected since the linear CO molecule tends to tilt to weaken the steric effect between the neighbours and the

adsorbed molecule while the tilting in a highly symmetric geometry is very unlikely to happen. Also, a comparison between the distances obtained for CC\*\*C (symmetry 1), C\*C\*C (symmetry 2) and CCCCC (symmetry 3) tend to suggest that a high degree of symmetry of a uniform CO adsorption may lead to shorter distances even when the number of nearest neighbours is higher. On the other hand, the hybrid adsorption geometries of CO with H<sub>2</sub> occupied sites did not present the same behaviour, i.e. the distance predicted for HH\*\*C (symmetry 1) is smaller than that obtained for H\*H\*C (symmetry 2); similarly, the distance of HHHHC (symmetry 3) is larger than that of \*\*\*\*C (i.e. no neighbouring sites), as shown in Table 3-1. Consequently, the neighbouring effects of hybrid CO adsorption with H<sub>2</sub> as neighbouring sites would not be affected by the degree of symmetry as much as that observed from the uniform CO occupied sites. Nevertheless, H<sub>2</sub> nearest neighbours present shorter distances compared to CO nearest neighbours with the same number of neighbouring molecules; except for the case of four (full) nearest neighbours HHHHC and H\*H\*C at symmetry 2, which present larger distances than that of CCCCC and C\*C\*C. As mentioned above, this is caused by the stronger symmetry effects of the neighbouring CO molecule. These results suggest that a high coverage NiO surface will not enhance CO adsorption due to low availability of active NiO sites and the high degree of symmetry. The neighbouring attached CO molecules lead to the more substantial repelling effect rather than the neighbouring



attached H<sub>2</sub>. These observations have been corroborated by an adsorption energy analysis that is presented in the next section.

Table 3-2 presents the structural properties of H<sub>2</sub> adsorption as a function of both the number and type of nearest neighbours. As shown in Table 3-2, a similar trend to that observed for CO adsorption is also observed for H<sub>2</sub> adsorption. An increase in the number of H<sub>2</sub> nearest neighbours results in stronger repelling effects with the same degree of symmetry (symmetry 1) whereas a high degree of symmetry for H<sub>2</sub> adsorption with H<sub>2</sub> neighbouring sites makes the tilting of the linear H<sub>2</sub> molecule very unlikely thus producing a structure with shorter distances between the adsorbed H<sub>2</sub> molecule and the surface. Regarding symmetry 2 configurations for H<sub>2</sub>, the distance in CHCHH (2.498 Å) is larger than that in C\*C\*H (2.492 Å) due to the increasing number of the neighbours. As shown in Table 3-2, the same number of CO occupied neighbouring sites often results in more significant repelling effects than those observed for H<sub>2</sub> occupied neighbouring sites, except for the case of CCCCH. The distance of CCCCH is smaller than that of HHHHH, which is mostly due to the stronger symmetry effect observed for CO neighbouring molecules than that of H<sub>2</sub>. A higher-coverage NiO surface tends to repel the H<sub>2</sub> from the surface due to the steric effects and the higher degree of symmetry. The attached CO neighbours will lead to a more significant repelling effect rather than having H<sub>2</sub> as nearest neighbours.

Table 3-2 Structural properties of H<sub>2</sub> adsorption on NiO

Symmetry	Uniform Adsorption		Hybrid Adsorption	
	Geometry name	Distance <sup>a</sup> /Å	Geometry name	Distance <sup>a</sup> /Å
none	****H	2.543		
none	H***H	2.759	C***H	2.959
symmetry 1	HH**H	2.519	CC**H	3.132
symmetry 2	H*H*H	2.491	C*C*H	2.492
symmetry 1	HHH*H	2.542	CCC*H	3.018
symmetry 3	HHHHH	2.501	CCCCH	2.499

a distance between the H closer to the surface in H<sub>2</sub> and the closest Ni to the mentioned H on the surface.

### 3.3.3 Adsorption energy analysis

To assess the energetic adsorption effects of syngas (CO and H<sub>2</sub>) on the NiO (100) surface, the adsorption of CO and H<sub>2</sub> with the same (uniform) neighbouring molecules was analyzed first. The adsorption energy can be regarded as the isothermal enthalpy change of adsorption in the system; this energy is often found to be negative, which indicates a spontaneously exothermic adsorption process. A large absolute value of the negative adsorption energy is an indication of large amounts of heat generated from the adsorption process. Thus, a release of heat (energy) is often observed during the adsorption process. Figure 3-4 shows the adsorption energy of CO with and without CO nearest neighbours (uniform adsorption). According to DFT analysis of CO adsorption on NiO, CO adsorbed on a clean NiO surface releases about 1.56 eV of heat. This suggests that on a periodic surface one of the 16 surface atoms was occupied. With one nearest neighbouring molecule of CO (3.194 Å), the adsorption energy of CO is reduced to only 18% of the total heat generated on the clean surface without

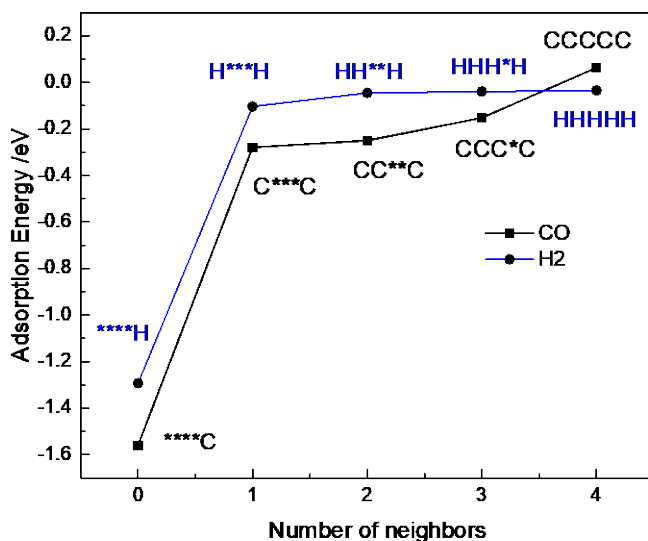


Figure 3-4 Adsorption energy of uniform loading molecules

CO neighbouring molecules. This implies that adsorption stability of CO is significantly weakened by its first loaded CO neighbour. It is noteworthy this computed adsorption energy (0.28 eV) agrees with the experimental result as 0.30 eV in the low-coverage regime<sup>183</sup>. With two or three neighbouring molecules of CO, the changes in the adsorption energy are less than 10% respecting that with no neighbours. These results indicate that the first adsorbate molecule on the NiO surface significantly weakens the adsorption of the same molecule on a nearby site. As for the geometry with four nearest neighbours, the adsorption energy changes to +0.06 eV. Hence, the CO adsorption with four nearest neighbours can hardly happen due to the endothermic process as indicated from the positive enthalpy change. To further support this analysis, the CO adsorption with five neighbouring occupied molecules was conducted and resulted in adsorption energy of + 0.03 eV. The 5<sup>th</sup> neighbouring site is the 2<sup>nd</sup> closest Ni to the adsorption site which has a distance of 4.167 Å from the adsorption site. The similar behaviour was observed for the H<sub>2</sub> adsorption on NiO with H<sub>2</sub> neighbouring molecules (uniform adsorption), as shown in Figure 3-4. The difference in adsorption energies decreases and flattens out with the 3<sup>rd</sup> and 4<sup>th</sup> loading molecules, respectively. Particularly for the H<sub>2</sub> loading with four nearest neighbours, the adsorption energy is the lowest due to its fully occupied neighbouring sites, which is still negative and indicates greater stability of the H<sub>2</sub> adsorption compared to that of the CO adsorption with four CO neighbours. The adsorption energy analysis of uniform adsorption suggests that the NiO surface with high coverage of uniform neighbours tends to be unreactive to adsorb CO and H<sub>2</sub>.

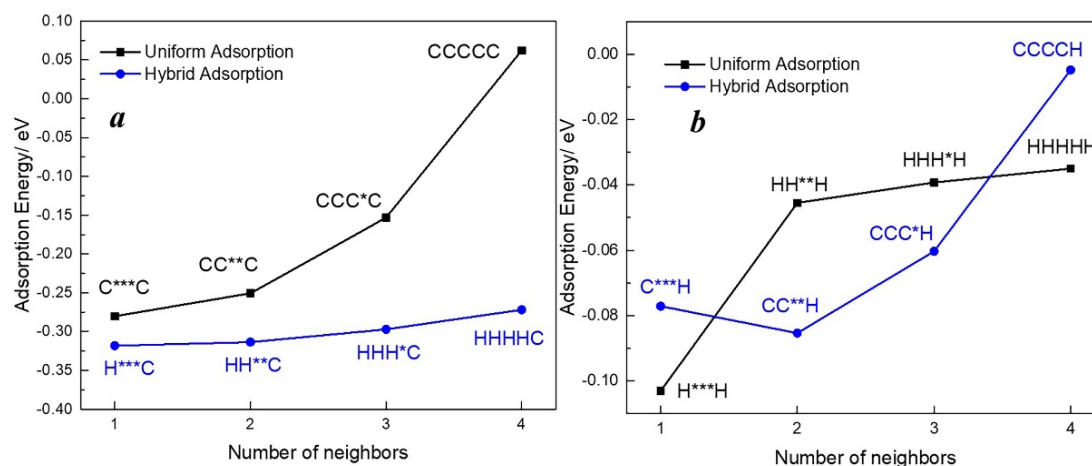


Figure 3-5 Uniform adsorption (black) and hybrid adsorption (blue) of (a) CO adsorption comparison; (b) H<sub>2</sub> adsorption comparison

Figure 3-5(a) presents a comparison between CO uniform adsorption and CO hybrid adsorption as a function of the number of nearest neighbours. Uniform adsorption energy with the same number of neighbours are also presented in this figure for comparison purposes. The neighbouring occupied geometry sharing the same x value means that they have the same number of occupied neighbouring molecules as well as the same degree of symmetry. Hybrid adsorption distinguishes from the uniform adsorption by the different neighbouring occupied molecules with the studied adsorption molecule. For example, the CO hybrid adsorption considers the neighbouring sites occupied by H<sub>2</sub> while the H<sub>2</sub> hybrid adsorption estimates the neighbouring sites employed by CO. As shown in Figure 3-5(a), the difference in adsorption energies between the uniform adsorption and hybrid adsorption increases as the number of nearest neighbours increases. The degree of symmetry increases from none symmetry (C\*\*\*C and H\*\*\*C) to symmetry 3(CCCCC and HHHHC) with the increasing number of neighbours. As discussed in the previous section, a higher degree of symmetry will lead to weaker adsorption stability for both CO and H<sub>2</sub> adsorption which is shown in Figure 3-5 and will be discussed in detail in the following paragraph. The results from Figure 3-5(a) shows that this effect is more significant on CO occupied neighbouring geometry since it contributes to more

considerable differences in adsorption energy between CO adsorption with CO neighbours than on CO adsorption with H<sub>2</sub> neighbours. As a result, it is expected that the stability of CO adsorption with H<sub>2</sub> neighbouring molecules is relatively higher when compared to uniform CO adsorption. Figure 3-5(a) also shows that the difference in energy between CCCCC and HHHHC (symmetry 3) is much more significant than that between C\*\*\*C and H\*\*\*C (no symmetry). The less reduced stability observed with hybrid nearest neighbours species compared to that with uniform adsorption may be due to the different electronic structures of the adsorbed molecule (CO) and the Ni on the surface (see section 3.3.4).

Figure 3-5(b) compares the energetic results for hybrid and uniform H<sub>2</sub> adsorption. As shown in this figure, H<sub>2</sub> adsorption is more stable with one H<sub>2</sub> nearest neighbour rather than with one CO nearest neighbour. This may be due to the much smaller effect of one H<sub>2</sub> molecule on the surface compared to that of CO as a neighbour (see section 3.3.4). When the number of the neighbouring occupied sites increases (HH\*\*H and HHH\*H), the H<sub>2</sub> uniform adsorption is weaker than the hybrid adsorption due to the magnified neighbouring H<sub>2</sub> effects, as shown in Figure 3-5(b). As mentioned in section 3.3.2, CO as neighbour leads to a more significant steric effect than H<sub>2</sub> does. Thus, the stability of H<sub>2</sub> adsorption is more negatively affected by the steric repulsions with hybrid CO neighbours rather than that with uniform H<sub>2</sub> neighbours. As mentioned above, a high degree of symmetry has a more profound effect on the CO occupied geometry. As shown in Figure 3-5(b), the stronger steric and symmetry effects caused by the presence of four CO neighbours in H<sub>2</sub> adsorption lead to a significant decrease in adsorption energy. From Figure 3-5, the hybrid effect weakens the negative impact of the neighbours on both CO and H<sub>2</sub> adsorption. Particularly, the adsorption energy of H<sub>2</sub> on a perfect NiO (100) surface obtained from experimental data tends to be low (smaller than 0.22 eV)<sup>184</sup>. The computed adsorption energy of H<sub>2</sub> in this work with low coverage is about 0.1 eV, which agrees with the experimental results.

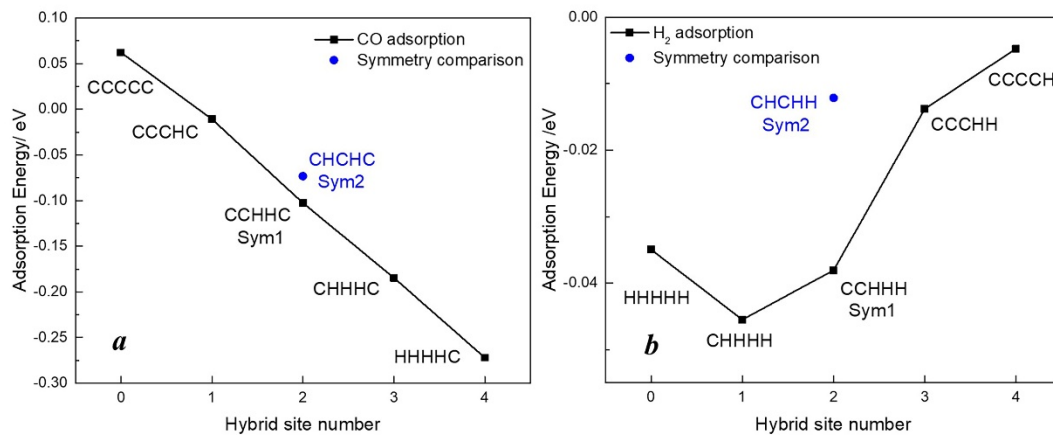


Figure 3-6 Fully occupied nearest neighbouring site (a) CO adsorption and (b) H<sub>2</sub> adsorption

Figure 3-6 shows the CO and H<sub>2</sub> adsorption with four nearest neighbours using molecules of different species, whereas their location is given by the notation described in section 3.3.1. CO adsorption is an exothermic process, thus generating a negative value of adsorption energy. A higher absolute value of adsorption energy indicates higher adsorption stability. According to Figure 3-6(a), an increase in the number of H<sub>2</sub> nearest neighbours leads to stronger CO adsorption (higher absolute value of adsorption energy). As shown in Figure 3-6(a), a higher degree of symmetry (symmetry 2 higher than symmetry 1) weakens the CO adsorption. As for H<sub>2</sub> adsorption (Figure 3-6(b)), this is affected by both hybrid and steric effects. Therefore, the heat generated from H<sub>2</sub> adsorption first increases caused by the attached CO included in the nearest neighbours (shown as CHHHH), which highlights the hybrid effect on H<sub>2</sub> capture, and then it tends to decrease since the CO steric effect dominates the process. Furthermore, Figure 3-6(b) also shows that adsorption stability is negatively affected by cases of higher degrees of symmetry. Through the comparison of the adsorption energy between CHCHH (symmetry 2) and CCHHH (symmetry 1), it is deduced that a higher degree of symmetry will reduce the heat generated from H<sub>2</sub> adsorption which indicates weaker adsorption stability.

### 3.3.4 Electron property analysis

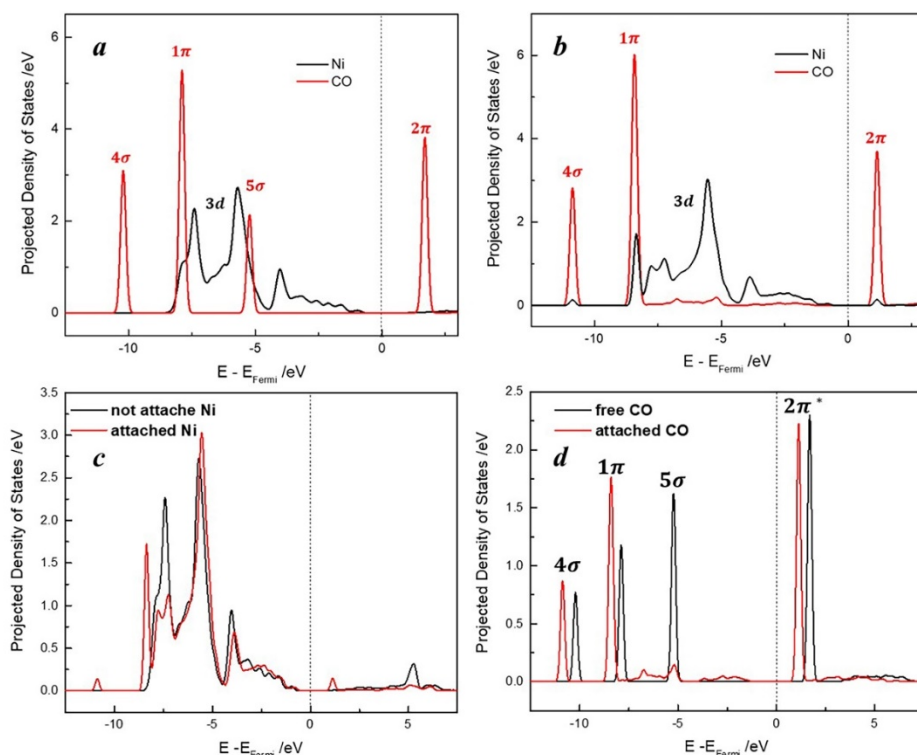


Figure 3-7 Comparison between non-adsorbed system and adsorbed system (a) 3d Ni orbitals and CO molecular orbitals: non-adsorbed system (b) 3d Ni orbitals and CO molecular orbitals: adsorbed system (c) 3d orbitals of attached Ni and non-attached Ni (d) molecular orbitals of non-attached CO and attached CO

The electronic properties of CO and H<sub>2</sub> uniform and hybrid adsorption have been analyzed to provide further insight into the neighbouring effects of these species on the NiO surface. Figure 3-7 presents the molecular orbitals of CO and Ni 3d orbitals, which provides a comparison between the free gas with NiO surface system and the adsorbed system. According to Figure 3-7(a),  $2\pi^*$  and  $5\sigma$  orbitals of CO and 3d orbitals of Ni have similar energy level. Note that  $1\pi$  orbital of CO mainly contributes to the bonding between C and O in CO

molecule<sup>185</sup>. Therefore, CO as an adsorbate primarily interacts with Ni by hybridization between  $5\sigma$  and  $2\pi^*$  orbitals of CO and 3d orbitals of Ni on the surface. This conclusion agrees with previous reports of CO adsorption<sup>186-187</sup>. Figure 3-7(b) shows that CO adsorption leads to the spreading of the d orbitals of Ni. A small peak of Ni 3d orbital appears at the same energy level as the  $2\pi^*$  orbital of CO. The electron occupation at  $5\sigma$  orbital of CO dramatically decreases and shifts to a lower energy level due to the  $5\sigma$ -d forward donation effect<sup>188</sup>. According to the comparison between the non-adsorbed system and the adsorbed system, as shown in Figure 3-7(c) and Figure 3-7(d), the 3d orbitals of Ni shift to a lower energy level and the molecular orbitals of CO shift in the same direction, which indicate a more stable system upon adsorption. The changes of  $5\sigma$  and  $2\pi^*$  orbitals shown in Figure 3-7(d) result from the  $5\sigma$ -d forward donation and d- $2\pi^*$  back-donation<sup>188, 185, 189</sup>.

Figure 3-8 provides a comparison between the free H<sub>2</sub> on NiO surface system and the adsorbed system to study the interactions between the H<sub>2</sub> molecular orbitals and the 3d orbitals of the transition metal Ni. Figure 3-8(a) shows that 3d orbitals of Ni have energy level overlapped with bonding  $\sigma$  orbital and antibonding  $\sigma^*$  orbital of H<sub>2</sub>. The interaction between the H<sub>2</sub> and surface Ni mainly results from the interactions between 3d orbitals and  $\sigma$  molecular orbital. H<sub>2</sub> adsorption leads to the spreading of  $\sigma^*$  orbital. According to Figure 3-8(c), no apparent change appears for 3d Ni orbitals except for the slightly spreading at the energy level of  $\sigma^*$  orbital. The H<sub>2</sub> adsorption barely affects the surface electronic structure. Compared to CO adsorption, H<sub>2</sub> has a weaker effect on the surface as an adsorbate. Therefore, stronger adsorption of CO compared to that of H<sub>2</sub> is expected. This also explains why the absolute value of the CO adsorption energy is much larger than that of H<sub>2</sub> adsorption, as shown in Figure 3-4. As for the molecular orbitals of H<sub>2</sub>, the peak of  $\sigma$  orbital shifts to a lower energy level due to the interaction between the surface Ni and H<sub>2</sub>, thus increasing the stability of the system.



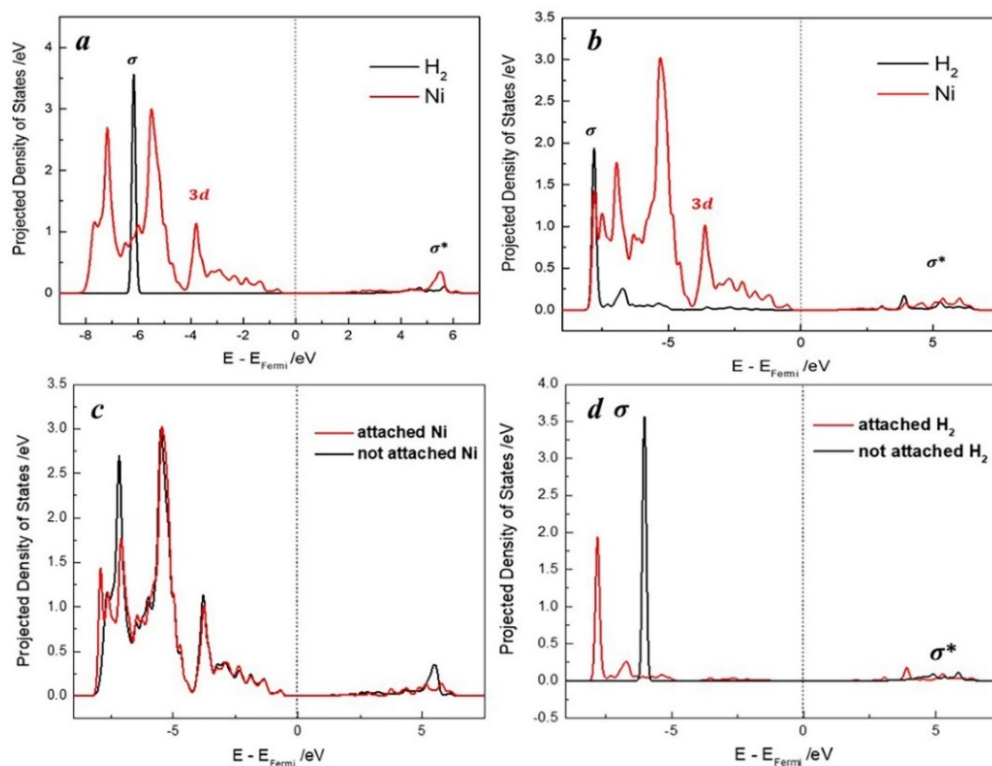


Figure 3-8 Comparison between non-adsorbed system and adsorbed system (a) 3d Ni orbitals and H<sub>2</sub> molecular orbitals: non-adsorbed system (b) 3d Ni orbitals and H<sub>2</sub> molecular orbitals: adsorbed system (c) 3d orbitals of attached Ni and non-attached Ni (d) molecular orbitals of non-attached H<sub>2</sub> and attached H<sub>2</sub>

By comparing Figure 3-7(c) and Figure 3-8(c), the frontier 3d orbitals of Ni are apparently affected to a larger extent by CO adsorbate compared to H<sub>2</sub>. A weaker interaction between H<sub>2</sub> and surface Ni suggests that it may be more favourable for H<sub>2</sub> to migrate from Ni site to its neighbour for further reactions. The weaker interaction is also corroborated by the lower adsorption energy of H<sub>2</sub> compared to that of CO, as discussed in section 3.3.3.

Figure 3-7 and Figure 3-8 provide the interactions between the adsorbates and studied surface. Based on previous analysis, the neighbouring effect of CO and H<sub>2</sub> on the studied surface and adsorbates are shown in Figure 3-9. To emphasize the neighbouring effect, the

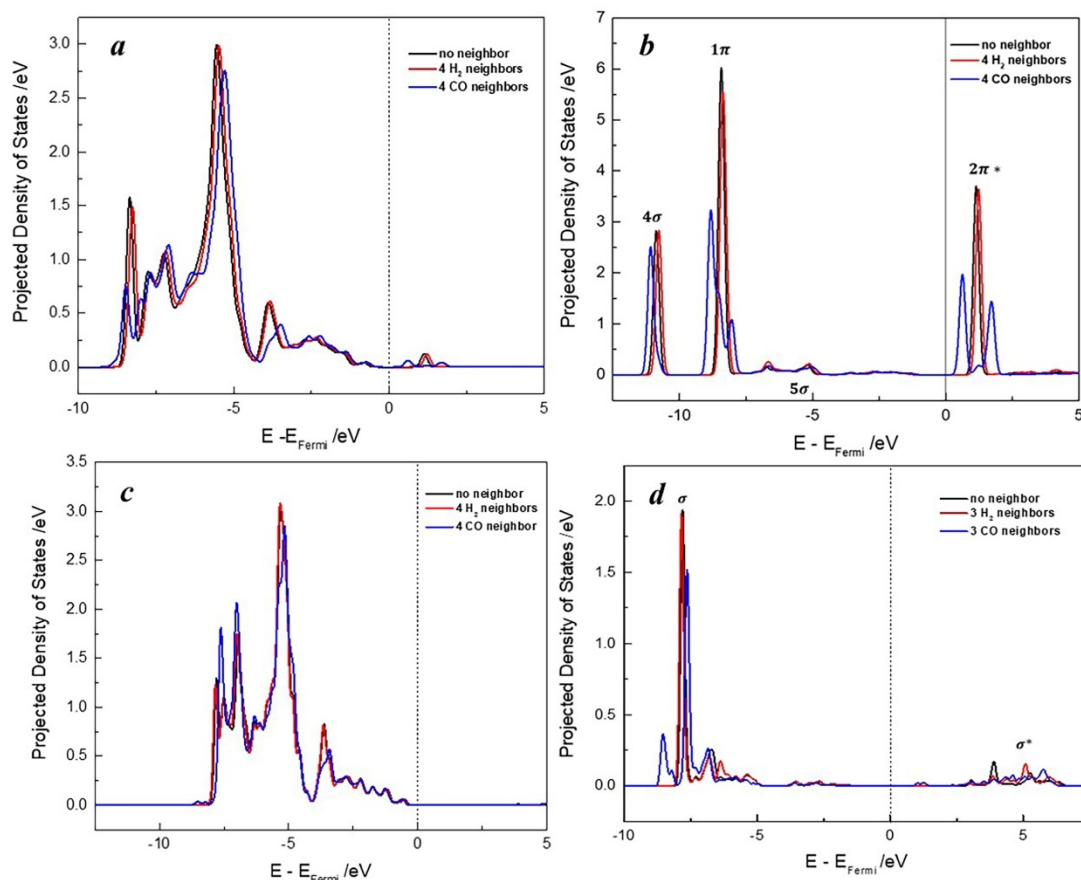


Figure 3-9 Neighbour effect on CO and H<sub>2</sub> adsorption shown in (a) 3d orbitals of Ni connected with CO (b) CO molecular orbitals (c) 3d orbitals of Ni connected with H<sub>2</sub> (d) H<sub>2</sub> molecular orbitals

extreme conditions are considered for both CO and H<sub>2</sub> adsorption as where the four nearest neighbour sites are fully occupied. With four nearest CO neighbours, the d orbitals of Ni at HOMO orbital broadens and its left edge shifts to a lower energy level in Figure 3-9(a) while no significant change appears for the d orbitals of Ni with 4 H<sub>2</sub> neighbours. Accordingly, the closest active site of Ni is more significantly affected by the neighbouring CO than by the neighbouring H<sub>2</sub>. Molecular orbital change shown in Figure 3-9(b) gives the same trend as abovementioned. The CO neighbours significantly influence the molecular orbitals of the adsorbed CO while H<sub>2</sub> neighbours only lead to a slight shift to a higher energy level. This

explains the more significant repelling effect on the adsorbed species coming from the CO neighbours to H<sub>2</sub> neighbours. This result agrees with the conclusions obtained from the adsorption energy in section 3.3.2. Hence, a clean NiO surface is more likely to attract CO molecules rather than a surface with high coverage. The peak at 2π\* antibonding orbital splits into two new peaks. The bonding between C and O in CO molecule appears to change by the significant effect of CO neighbours. As shown in Figure 3-9(c), the electron density occupancy of 3d orbitals of Ni with four CO neighbours spreads to a lower energy level while it almost remains constant with four H<sub>2</sub> neighbours. The fully occupied CO neighbouring configuration leads to an apparent broadening of the σ orbital of adsorbed H<sub>2</sub> compared to that resulted from a fully occupied H<sub>2</sub> neighbour configuration. The mentioned change also comes from the more substantial repelling effect caused by the CO neighbours. The aforementioned results corroborate the conclusions obtained from Figure 3-5 (b). Comparing Figure 3-9(a) and Figure 3-9(c), the change in the electronic structure of H<sub>2</sub> adsorbed surface stemming from neighbouring effect is not as apparent as that of CO adsorbed surface. This is due to the smaller difference in H<sub>2</sub> adsorption energy compared to that in CO, which is also reflected by the results presented in Figure 3-4.

Figure 3-10 compares the CO adsorption in CCHH and CHCH (symmetry2 compared to symmetry1) neighbouring configurations to emphasize the symmetry effect shown from the electron distribution. For CO adsorption in Figure 3-10(a), the 3d orbitals of Ni at low energy levels are slightly more packed and tend to spread in CCHHC system compared to that in CCHHC system. As shown in Figure 3-10(b), bonding orbitals of CO in CHCHC (symmetry 2) system broaden and experience a small shift compared to that in CCHHC system (symmetry 1). Therefore, a higher energy level of CHCHC system is expected as well as lower system stability. In particular, the antibonding orbital 2π\* in CHCHC (symmetry 2) system is more packed, thus weakening the bond of C and O in CO molecules. According to Figure 3-10(c) and Figure 3-10(d), H<sub>2</sub> adsorption in a system with a higher symmetry degree (CHCHH, symmetry2 ) leads to similar spreading on 3d orbital of Ni, σ and σ\* orbitals of H<sub>2</sub>. More packed

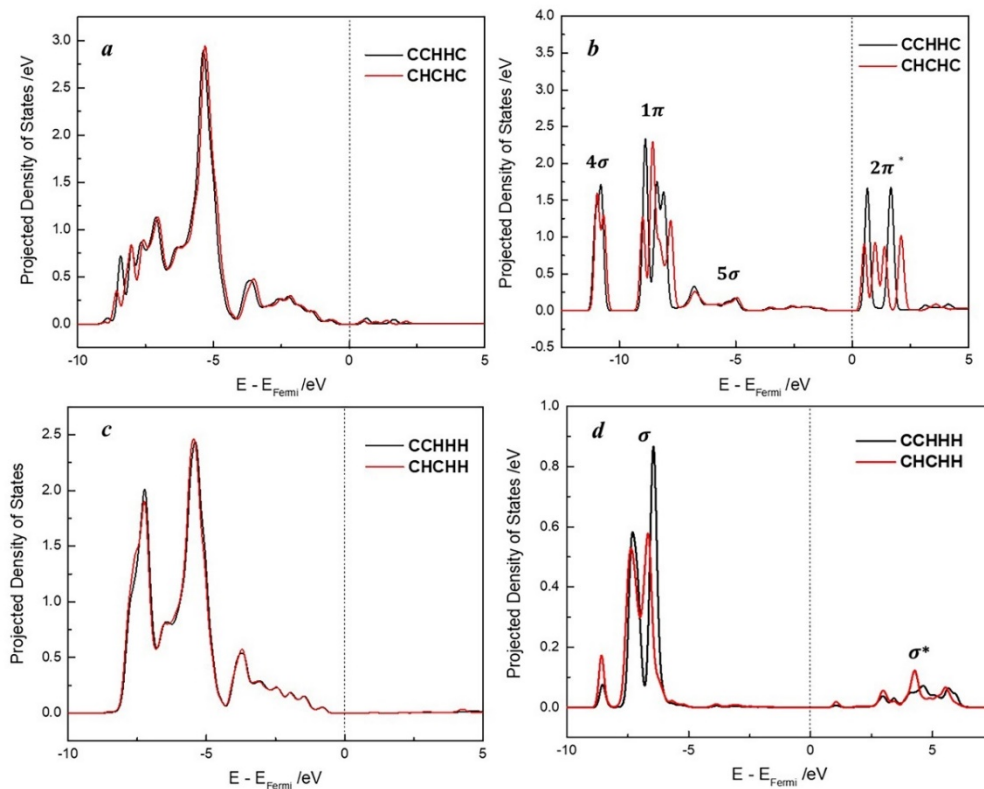


Figure 3-10 Symmetry effect on CO and H<sub>2</sub> adsorption shown in (a) 3d orbitals of Ni connected with CO (b) CO molecular orbitals (c) 3d orbitals of Ni connected with H<sub>2</sub> (d) H<sub>2</sub> molecular orbitals

antibonding  $\sigma^*$  orbital of H<sub>2</sub> demonstrates the weakened inner bond of H<sub>2</sub>. The geometry with a higher degree of symmetry (i.e. CHCHC and CHCHH) lowers the stability of the adsorption while structures that present a lower degree of symmetry (i.e. CCHHC and CCHHH) for both CO and H<sub>2</sub> adsorbed molecules do not show that effect. This result agrees with the findings presented in Figure 3-6, i.e. a higher degree of symmetry (symmetry two compared to symmetry 1) generates less adsorption heat.

Figure 3-11 presents the electronic property analysis for the hybrid adsorption effects. Figure 3-11(a) and Figure 3-11(b) show a larger spreading in both Ni 3d orbital and CO

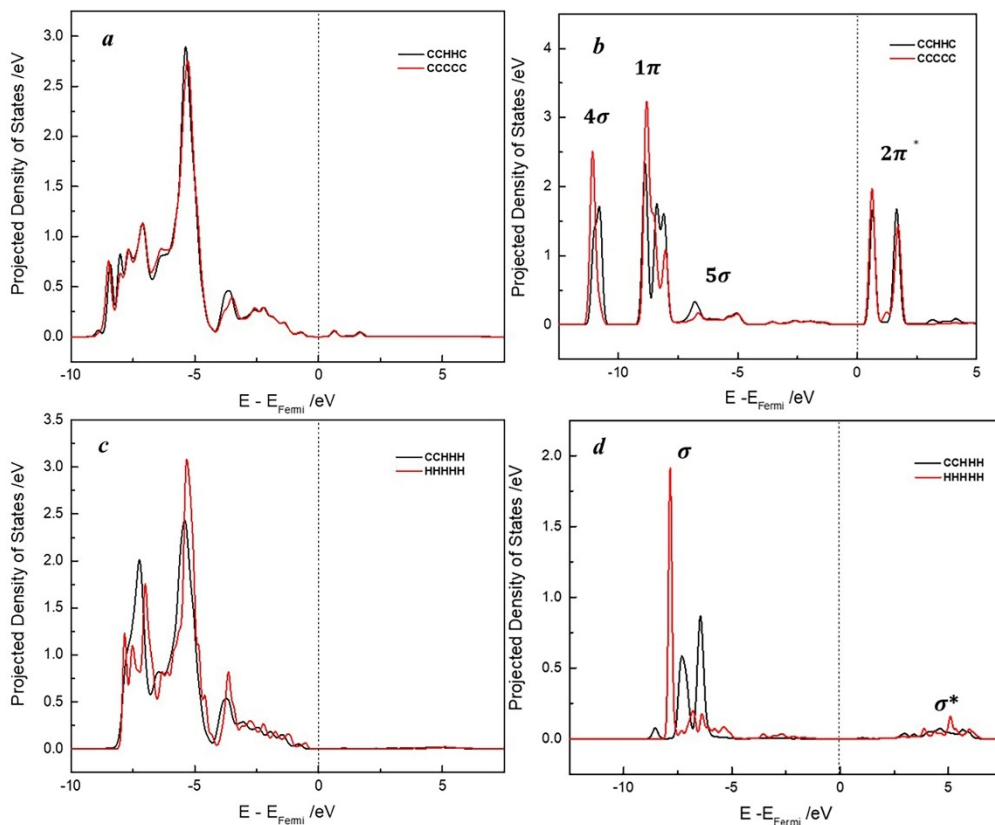


Figure 3-11 Hybrid effect on CO and H<sub>2</sub> adsorption shown in (a) 3d orbitals of Ni connected with CO (b) CO molecular orbitals (c) 3d orbitals of Ni connected with H<sub>2</sub> (d) H<sub>2</sub> molecular orbitals

molecular orbitals in CCHHC (with hybrid neighbours) system compared to that in CCCCC (without hybrid neighbours) system. Stronger interaction between CO and the surface is predicted. Figure 3-11(c) and Figure 3-11(d) reveal the a slightly smaller difference in the trend of Ni 3d orbital and H<sub>2</sub> molecular orbitals via the comparison between CCHHH (with hybrid neighbours) system and HHHHH system (without hybrid neighbours). This result indicates that hybrid effects will weaken the negative effect on both CO adsorption and H<sub>2</sub> adsorption caused by neighbours, which is supported by the adsorption energy analysis presented in Figure 3-5 and Figure 3-6.

### 3.4 Summary

This part of the research provided new insights into the adsorption of syngas (i.e. CO and H<sub>2</sub>) on the NiO surface (16 atoms on the surface of the 6-layer periodic slab model) while accounting for the neighbouring effects. A DFT analysis was performed to study the structural properties and adsorption energies in consideration of different occupied geometries of the nearest neighbors. An electron property analysis was conducted to further validate the DFT outcomes. The results show that an increasing number of neighbours weakens the adsorption stability. In particular, the first neighbour affects the adsorption stability the most significantly. A highly symmetric neighbour configuration leads to weak adsorption stability, while the hybrid neighbour configuration leads to a lower reduction in the adsorption stability compared to the uniform neighbour configuration. These results indicate that the adsorption stability of CO or H<sub>2</sub> can be predicted by analyzing the steric, hybrid and symmetry effects of the surface's nearest neighbours. The next nearest neighbours are expected to present similar effects as the nearest neighbours do, which should be evaluated in future studies. The neighbouring effects on the syngas adsorption presented in this chapter can be taken into account when building a microscopic model such as kMC, to further investigate this phenomena at larger temporal and spatial scales. To accomplish this goal, Chapter 3 builds a solid foundation that can be used to develop the elementary reaction mechanisms for the studied system.

# Chapter 4 A Multi-scale Simulation of Syngas Combustion Reactions by Ni-based Oxygen Carriers for Chemical Looping Combustion

## 4.1 Introduction

Theoretical studies of Ni-based OCs within the CLC process are limited, especially when compared to Fe-based OCs. These studies are furthermore predominantly focused on the oxidation of NiO and the effects of influencing factors such as the impurity, as discussed in Chapter 2. Consequently, the behaviour of Ni-based OCs at a microscopic scale is still rarely reported, even for the critical fuel oxidation process on NiO. In order to overcome these issues, DFT studies can be performed to gain insights on the elementary reaction mechanisms and the microscopic behaviour in the process of syngas combustion on NiO. In order to validate the proposed insights, a multi-scale model is required to relate the DFT outcomes to experimental observations.

Chapter 4 aims to present the elementary reaction mechanism of syngas combustion on an NiO OC. A DFT analysis was conducted to reveal the reaction kinetics and the microscopic performance of NiO in the syngas oxidation process. Moreover, this work performed different electronic analyses (see section 4.3.2), which were coupled together to further support the results from the DFT analysis. In order to validate the proposed reaction kinetics and estimate the reaction kinetics under practical operating conditions, a DFT-based MF multiscale model was established to study the impact of inlet compositions, temperatures and pressures on the CLC performance. The developed multi-scale model was validated using experimental observations available in the literature<sup>190-192</sup> and used to predict the product selectivity of the system subject to the coordinate effects of the studied operating conditions. This study was conducted using the basis of the stable adsorption configurations reported in Chapter 3. The developed multi-scale model and the outcomes presented this chapter have already been published.<sup>193</sup>

The rest of this chapter is organized as follows. Section 4.2 presents the computational details employed in this part of the study. Section 4.3 provides the structure-related energetic

results, the electronic analysis and the DFT-based MF predictions. A summary of this chapter is provided in section 4.4.

## 4.2 Computational details

The calculation details of DFT analysis and the surface NiO model are the same as explained in last chapter, section 3.2. The DFT-based MF model was implemented in Python 3.7.0.

### 4.2.1 Reaction mechanism establishment

The reaction activation energy can be obtained from the Transition State (TS) estimation using Climbing-Image Nudged Elastic Band (CI-NEB) method, which was conducted using VASP Transition State Tools (VTST) with the force convergence criterion as 0.05 eV/Å energy and energy convergence criterion as  $1 \times 10^{-4}$  eV. The expression for the zero-point energy (ZPE) corrected activation energies of the forward and backward reactions,  $E_{a,forward}$ ,  $E_{a,backward}$  are as follows:

$$E_{a,forward} = E_{a,TS} - E_{a,reactant} + E_{ZP,forward} \quad (4-1)$$

$$E_{a,backward} = E_{a,TS} - E_{a,product} + E_{ZP,backward} \quad (4-2)$$

$$E_{ZP,forward} = \sum_i \left(\frac{1}{2}\right) h \omega_i^{TS} - \sum_i \left(\frac{1}{2}\right) h \omega_i^{react} \quad (4-3)$$

$$E_{ZP,backward} = \sum_i \left(\frac{1}{2}\right) h \omega_i^{TS} - \sum_i \left(\frac{1}{2}\right) h \omega_i^{prod} \quad (4-4)$$

where  $h$  is Planck's constant,  $E_{a,reactant}$ ,  $E_{a,TS}$  and  $E_{a,product}$  are the system energies of the reactant, the TS and the product, respectively;  $\omega_i^{TS}$ ,  $\omega_i^{react}$  and  $\omega_i^{prod}$  are the frequency of the vibration of a atom  $i$  of the transition state, the reactant and the product respectively whereas  $E_{ZP,backward}$  and  $E_{ZP,forward}$  are the zero-point energy difference for the backward and forward reaction, respectively.



## 4.2.2 Electronic analysis

Further insights into the reported mechanisms and related neighbouring effects are provided through a combined electronic analysis. The crystal orbital Hamilton population (COHP) analysis is conducted using the Local Orbital Basis Suite Towards Electronic-Structure Reconstruction program (LOBSTER).<sup>194</sup> COHP interprets the bonding, nonbonding and antibonding contributions to reveal the interaction strength of the studied atom pairs.<sup>195</sup> The energy-resolved COHP plots are calculated by multiplying the density of states matrix to the Hamilton matrix elements representing the interaction between the orbitals. Furthermore, projected COHP (pCOHP) is also used in this work to describe the bonding property based on atomic orbitals separately as a tool analog motivated by projection technique.<sup>196</sup>

## 4.2.3 Reaction rate constant

For physical adsorption of CO and H<sub>2</sub>, the rate constant of adsorption,  $k_{i,ad}$  is calculated based on the temperature, pressure and the characteristics of the surface<sup>197</sup>, i.e.

$$k_{i,ad} = \frac{S_a P_a A_{site}}{\sqrt{2\pi m k_B T}} \quad (4-5)$$

where  $A_{site}$  denotes the area of one single site;  $S_a$  is sticking coefficient of species  $a$ ,  $P_a$  is the partial pressure of species  $a$ ,  $k_B$  is Boltzmann constant,  $m$  is the mass of species  $a$  molecule and  $T$  is the system's temperature. The reaction rate constants of the chemical reactions can be obtained following the Transition-State Theory (TST). The expression for the rate constant,  $k_{i,rec}$  is as follows:

$$k_{i,rec} = \frac{k_B T}{h} \frac{Q_{vib}^{TS}}{Q_{vib}^{react}} \exp\left(-\frac{E_a}{k_B T}\right) \quad (4-6)$$

$$Q_{vib}^{react} = \prod_n \frac{1}{1 - e^{-h\omega_1^{react}/k_B T}} \quad (4-7)$$

$$Q_{vib}^{TS} = \prod_{n-1} \frac{1}{1 - e^{-h\omega_1^{TS}/k_B T}} \quad (4-8)$$

where  $E_a$  is the Zero-point Energy (ZPE)-corrected activation barrier ( $E_{a,forward}$  or  $E_{a,backward}$ ).  $Q_{vib}^{TS}$  and  $Q_{vib}^{react}$  represent the vibrational partition functions of the transition state and the reactant, respectively. Because the most degrees of freedom of the molecules in the reactions are vibrations. The difference between  $Q_{vib}^{TS}$  and  $Q_{vib}^{react}$  is that  $Q_{vib}^{TS}$  ignores the imaginary vibrational frequency of the transition state, as shown by the index  $n$  in Equations 4-7 and 4-8.

## 4.3 Results and discussion

### 4.3.1 Reaction mechanisms and structure-related energetic results

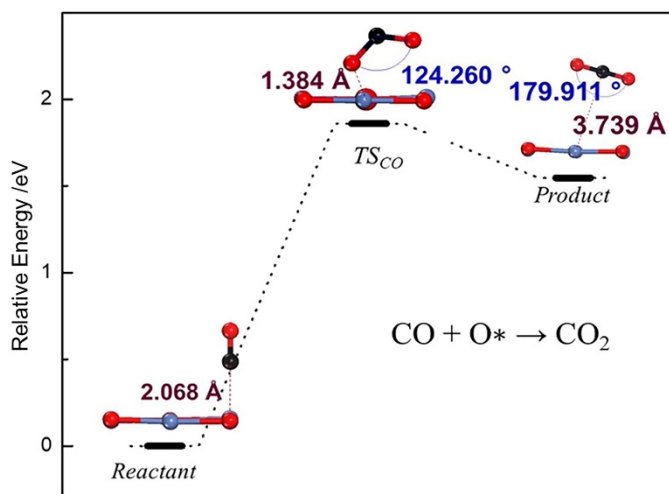


Figure 4-1 Energy profile of CO oxidation. Blue (Ni), red (O), black (C)

Stable adsorption configurations of both CO and H<sub>2</sub> have been reported in Chapter 3.<sup>166</sup> Based on the stable configurations of adsorbed CO and H<sub>2</sub> on the NiO surface, the oxidation mechanisms of syngas combustion are established by locating the saddle point of the elementary reactions. The established reaction mechanisms are discussed next for CO and H<sub>2</sub> combustion.

A one-step oxidation process is built for the CO reaction as shown in Figure 4-1. The CO atop the Ni scavenges the adjacent surface O and pulls the O about 1.384 Å away from its original position. The system experienced a relatively large energy barrier due to the energy consumption for breaking the Ni-O bonds at the surface. The linear molecule of CO<sub>2</sub> moves further away from the surface to form a stable configuration by enlarging the angle of O-C-O from 124.26° in the transition state of CO oxidation (TS<sub>CO</sub>) to almost 180°, as depicted in Figure 4-1. Along with the energy profile (reaction coordination), Figure 4-1 also provides the elementary reaction equation; note that the symbol \* indicates the species attached on the surface. The initial configuration of the CO attached system is more stable than the product configuration, which includes a slightly repelled CO<sub>2</sub>. This indicates that the CO<sub>2</sub> tends to leave the surface thus enhancing the forward oxidation process.

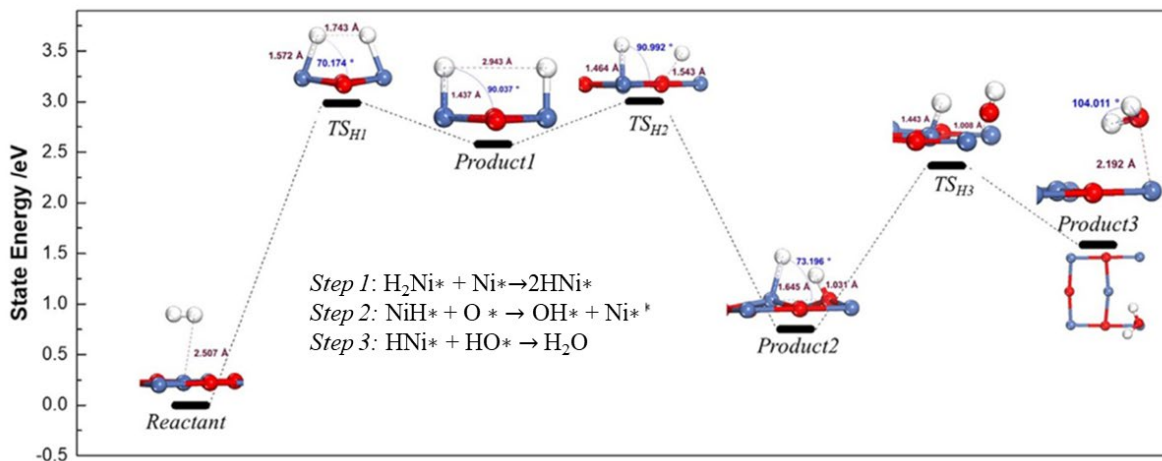
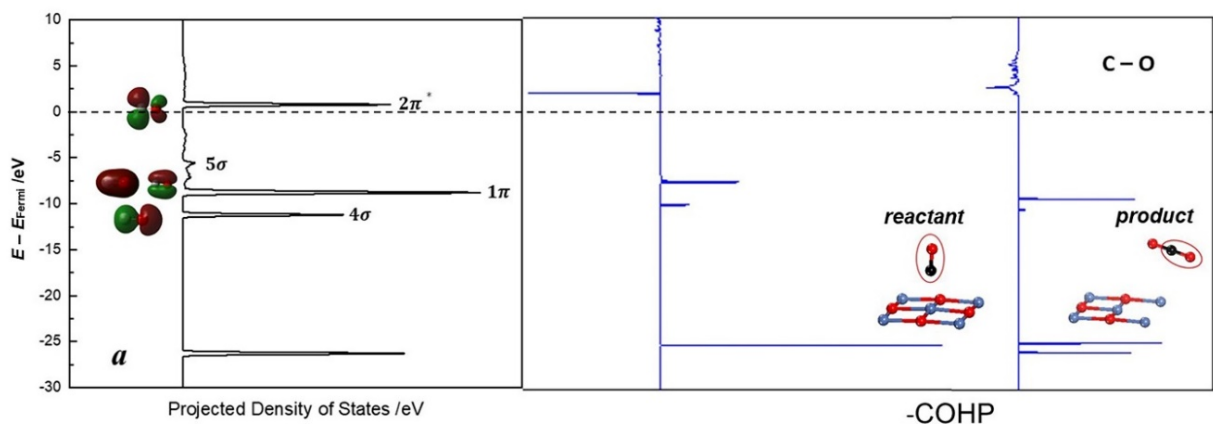


Figure 4-2 Energy profile of H<sub>2</sub> oxidation. Blue (Ni), red (O), white (H)

The H<sub>2</sub> oxidation process goes through a 3-step mechanism, as depicted in Figure 4-2. The surface H<sub>2</sub> is decomposed at the Ni top; then, the two single hydrogen atoms are attached to the two contiguous Ni on the surface and the bond between the two hydrogens is broken. as the first reaction step. The second reaction step involves H migration from Ni top to the O top. As shown in Figure 4-2, the remaining bond Ni-H tilts towards the O top H, which lengthens the Ni-H bond from 1.437 Å in product 1 to 1.645 Å in product 2. This second reaction step

was shown to be fast and necessary to facilitate the forward reaction. At the third reaction step, the surface O connected with H is pulled away from the surface and then connected with the H at the adjacent Ni top to form the H<sub>2</sub>O molecule at the Ni top. An angle of O-H-O about 114.199° in product 3 indicates the formation of water with an experimentally reported bond angle of about 105.<sup>o198-199</sup> As depicted in Figure 4-2, TS<sub>H1</sub>, TS<sub>H2</sub> and TS<sub>H3</sub> represent the configurations of the transition states for the first, second and third reaction steps of H<sub>2</sub> oxidation, respectively. The third reaction step needs to overcome the energy consumption for both Ni-H and Ni-O-Ni bond cleavage on the surface. However, the largest energy barrier found in this mechanism is still the first reaction step of H<sub>2</sub> breaking followed by the third and second step reactions, respectively. Therefore, the H<sub>2</sub> breaking at the Ni top turns out to be extremely difficult according to the aforementioned largest energy barrier and is considered the controlling step of the overall H<sub>2</sub> oxidation process.

### 4.3.2 Coupling electronic analysis



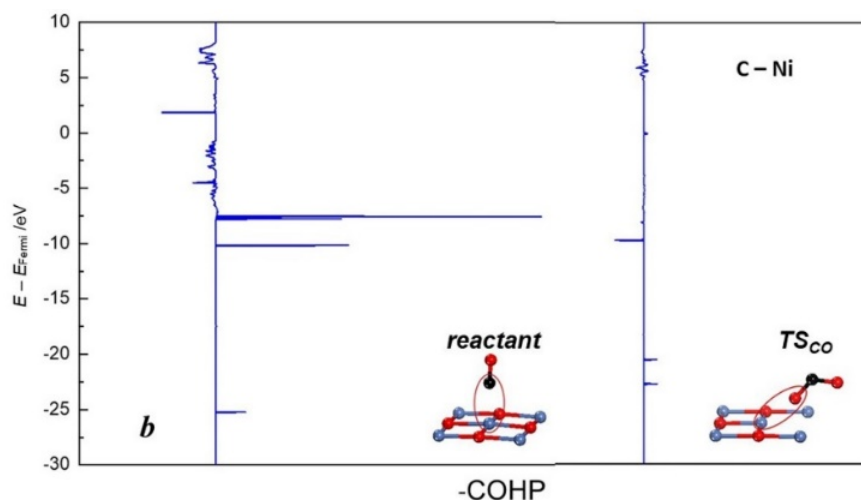


Figure 4-3 Electronic analysis of the CO oxidation process: (a) coupling analysis from reactant to product (b) COHP analysis from reactant to  $TS_{CO}$ . Blue (Ni), red (O), black (C)

This section presents a coupling electronic analysis aimed at providing a deeper understanding of the proposed reaction mechanisms on the clean surface by analyzing the electron distribution of the different configurations. COHP (crystal orbital Hamilton population, explained in section 4.2.2) and pCOHP (projected COHP) describe the interaction strength in the selected atom pair by partitioning the band structure energy into bonding, nonbonding and antibonding contributions. The corresponding projected density of states (pDOS) and molecular orbitals are coupled together to provide the details of the studied orbitals.

Figure 4-3 shows the pDOS of the adsorbed CO on the clean surface together with the calculated COHP of C-O and C-Ni. Due to the  $5\sigma$ -d forward donation of the attached CO on the NiO surface, the HOMO orbital  $5\sigma$  of CO is significantly weakened<sup>166</sup>, as shown in Figure 4-3(a). This figure also shows that the major contributor to the bonding of CO is  $1\pi$  orbital while the main interactions between CO and surface Ni come from the hybridization between  $2\pi^*$  and  $5\sigma$  orbitals of CO and Ni 3d orbital. Based on the COHP analysis of the C-O pair, the  $4\sigma$  orbital almost disappears with the formation of a more occupied  $\pi$  orbital at a relatively lower energy from reactant to product, which is a strong indication of the transition from CO to  $CO_2$  due to the tendency to establish the  $CO_2$  molecular orbital structure. In the reactant

configuration shown in Figure 4-3(b), the strong interaction between C and the surface Ni is mostly due to the occupied bonding orbitals. However, the bonding orbital, which is lower than the Fermi level in the product, shrinks until it becomes nearly negligible in the  $TS_{CO}$ , as depicted in Figure 4-3(b). The disconnection of C from the surface Ni also suggests the activation of the surface CO. Based on the analysis of Figure 4-3, CO oxidation is initiated by the disconnection of C in the surface-adsorbed CO from the surface Ni and then the activated CO scavenges the surface O to form  $CO_2$  as proposed in the CO oxidation mechanism presented in section 4.3.1.

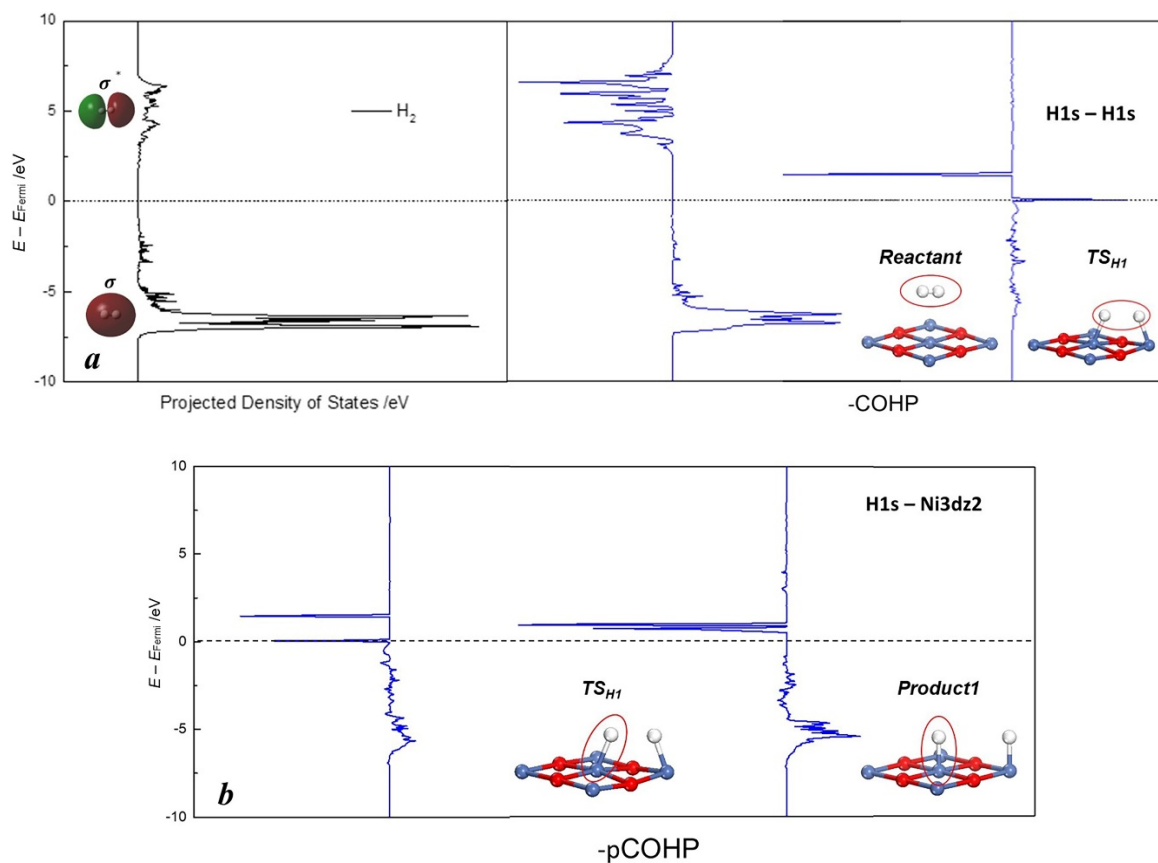
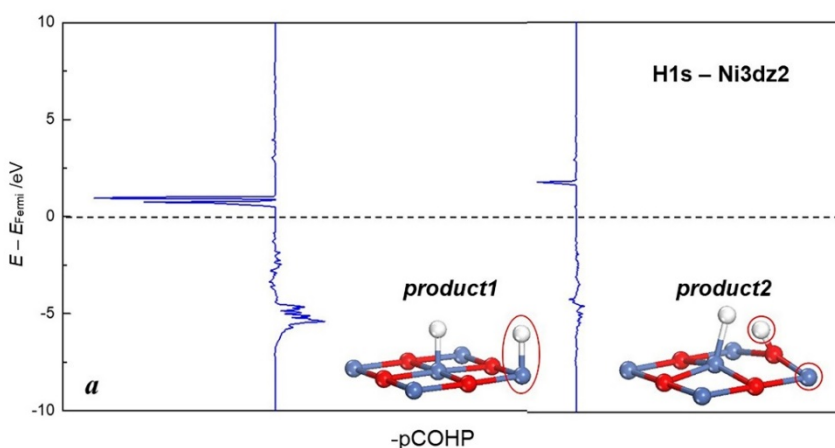


Figure 4-4 Electronic analysis of H<sub>2</sub> dissociation (a) coupling analysis from reactant to  $TS_{H1}$  (b) pCOHP analysis from  $TS_{H1}$  to product. Blue (Ni), red (O), white (H)

Figure 4-4 provides a coupling electronic analysis of the H<sub>2</sub> decomposition. The strong inner bond of the adsorbed H<sub>2</sub> can be predicted by the highly occupied bonding orbital  $\sigma$  at a low energy level according to the pDOS analysis of the surface H<sub>2</sub>. The shapes of the molecular orbitals of H<sub>2</sub> are also presented in Figure 4-4(a). The COHP analysis shown in Figure 4-4(a) elucidates the breaking of the H-H through the displacement of the bonding orbital from a relatively low energy level in the reactant to above Fermi level in TS<sub>H1</sub>. On the other hand, the antibonding interaction displayed in Figure 4-4(b) moves above the Fermi level from TS<sub>H1</sub> to product1, thus stabilizing the configuration by depleting the occupied antibonding orbital. A more spreading and significant bonding orbital contribution is also depicted in product1, which explains the strong interaction between Ni and H. The analysis of Figure 4-4 supports the established 1<sup>st</sup> step elementary reaction of H<sub>2</sub> oxidation involving the H<sub>2</sub> decomposition followed by the formation of the Ni-H bond.

At the H migration step, the interaction between the Ni and H is almost insignificant in product2, as shown in Figure 4-5(a). This implies the breaking of the Ni-H bond. On the contrary, the formation of the O-H bond is indicated in product2 with the existence of a more notably populated bonding orbital, as shown in Figure 4-5(b). Therefore, the breaking of the Ni-H bond and the formation of the O-H bond are illustrated according to the electron population change, which further explains the H migration process as the 2<sup>nd</sup> step elementary reaction of H<sub>2</sub> oxidation.



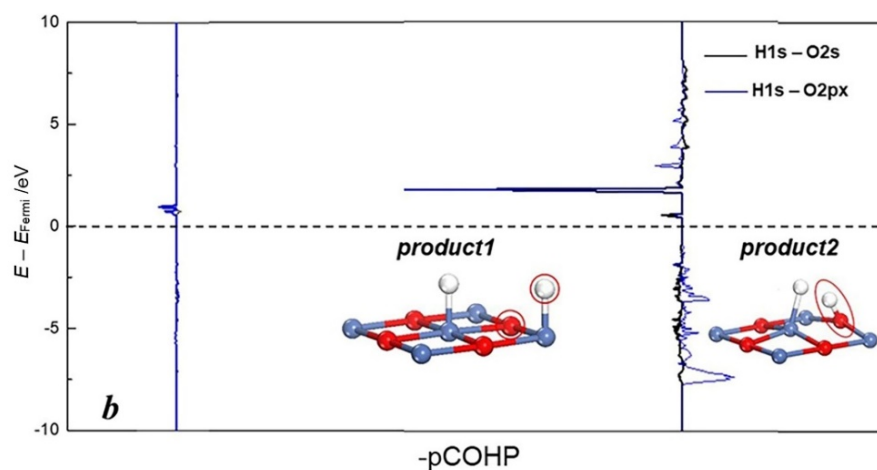
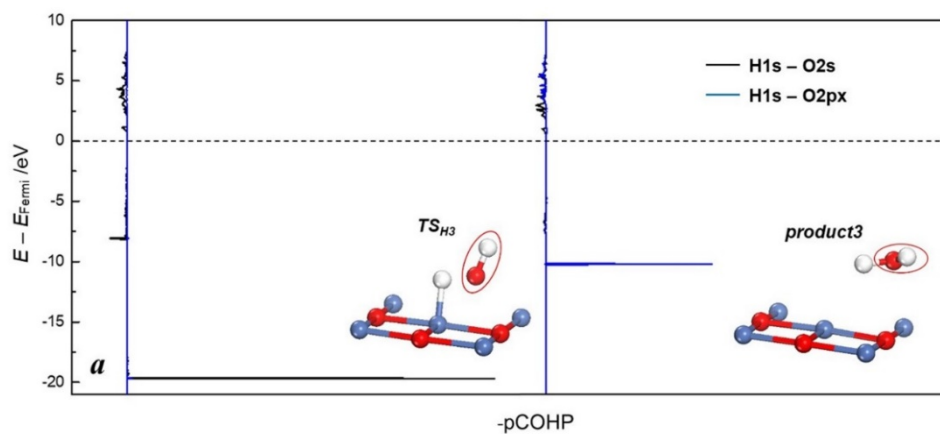


Figure 4-5 pCOHP analysis of H migration from product 1 to product 2 (a) H-Ni interaction (b) H-O interaction. Blue (Ni), red (O), white (H)

Moreover, Figure 4-6(a) shows that the interaction between the studied O and H mainly comes from the hybridization of the H 1s and O 2p orbitals in product 3, which is the same as the orbital hybridization between the O and H in H<sub>2</sub>O formation. This suggest the formation of H<sub>2</sub>O in product3. From product2 to TS<sub>H3</sub>, the antibonding orbital between O and Ni shifts downward to a lower energy level and presents more populated, which demonstrates the activation of product2 by weakening the connection between O and its adjacent Ni on the surface. Although the bonding orbital is also more occupied in product2 compared to that in





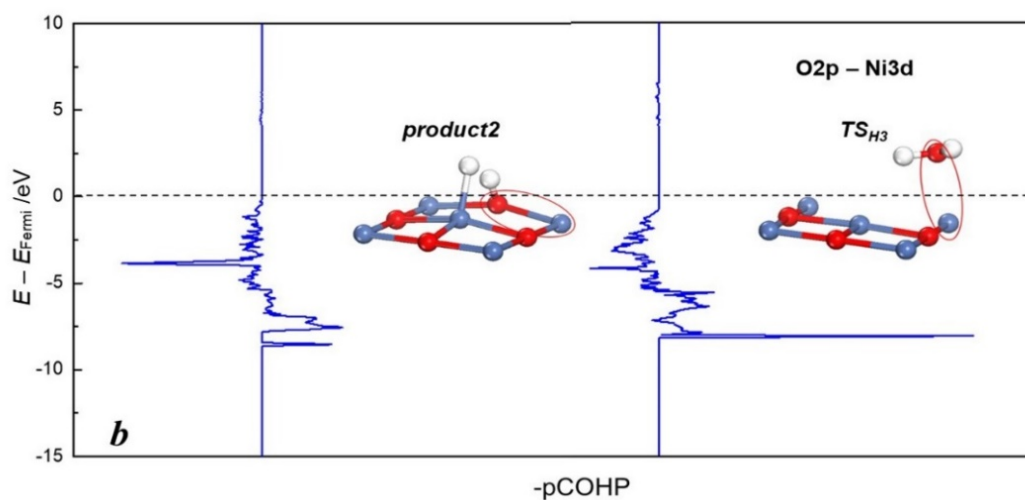


Figure 4-6 pCOHP analysis of H<sub>2</sub>O formation (a) H-O interaction from TS<sub>H3</sub> to product 3 (b) O-Ni interaction from product 2 to TS<sub>H3</sub>. Blue (Ni), red (O), white (H)

TS<sub>H3</sub>, the more considerable increase in the population of the antibonding orbital still suggests the bond cleavage of O-Ni. The analysis of Figure 4-6 supports the proposed elementary reaction of H<sub>2</sub>O formation in section 4.3.1.

### 4.3.3 DFT-based Mean-field analysis

#### 4.3.3.1. Mean-field Model

Based on the proposed elementary reaction mechanisms, the behaviour of these events at larger scales can be estimated using a MF model. This model assumes that the adsorbed species homogeneously distribute among the solid surface<sup>25</sup>. The dynamic coverage of each species on the surface can be calculated based on the proposed reaction mechanism and reaction rates estimated from DFT calculations, i.e. MF uses the energetic results from DFT to predict the expected distribution of the participating species in the surface (i.e. surface coverage). Hence, MF can also be used as a tool to validate the elementary reaction mechanisms and reaction kinetics parameters obtained from the previous DFT analysis. Based on the proposed reaction mechanism presented in section 4.3.1, the MF model developed in this study involves the following reactions:



where R2 and R5 represent the chem-desorption process with the products leaving instantaneously to the gas phase after formation. The activation energy of H migration from Ni top to the O top (step 2 in Figure 4-2) is almost one order of magnitude smaller than the activation barrier of the former step reaction of H<sub>2</sub> decomposition (step 1 in Figure 4-2). This mechanism suggests that H migration proceeds immediately after H<sub>2</sub> decomposition, as shown in Figure 4-2. Hence, these two elementary reactions (step 1 and step 2 in Figure 4-2) have been merged into a single reaction (R4, H<sub>2</sub> dissociation), as shown above. Note that the backward reaction is not considered for R4 since the backward activation energy is much smaller than that of the forward reaction, which suggests that the backward reaction rarely happens compared to the forward reaction. The current MF model assumes that there is sufficient oxygen supply from OC in the system, i.e. the bulk oxygen immediately replaces the surface oxygen vacancy once the oxygen is consumed by the reaction. This assumption is reasonable during the earlier stages of the reduction process where sufficient oxygen in the channels of the OC particles is present. Additionally, this model aims to investigate NiO as the only OC species, i.e. the effect of a support has not been considered and will be part of future studies. The time evolution of the surface species is expressed by the coverages of the surface adsorbed species CO, H<sub>2</sub>, the adjacent structure NiHOH (i.e. the surface structure of product 2 shown in Figure 4-2) and the surface O, i.e.  $\theta_{\text{CO}}$ ,  $\theta_{\text{H}_2}$ ,  $\theta_{\text{HNiHO}}$  and  $\theta_{\text{O}}$ . Note that the number of the surface oxygen is the same as Ni, which suggests the surface oxygen coverage of an empty surface is 0.5. The following Ordinary Differential Equations (ODEs) describe the reaction kinetics:

$$\theta_{\text{O}} = 0.5 - \theta_{\text{HNiHO}} \quad (4-9)$$

$$d\theta_{CO}/dt = k_{CO,ad}(0.5 - \theta_{CO} - \theta_{H_2} - \theta_{HNiHO}) - k_{CO,rec}\theta_{CO}\theta_O \quad (4-10)$$

$$d\theta_{H_2}/dt = k_{H_2,ad}(0.5 - \theta_{CO} - \theta_{H_2} - \theta_{HNiHO}) - k_{H_2,break}\theta_{H_2}\theta_O \quad (4-11)$$

$$d\theta_{HNiHO}/dt = k_{H_2,break}\theta_{H_2}\theta_O - k_{H_2O,form}\theta_{HNiHO} \quad (4-12)$$

where  $k_{CO,ad}$  and  $k_{H_2,ad}$  are the adsorption rate constants of R1 and R3, respectively, which are calculated based on the gas phase partial pressures of CO and H<sub>2</sub> as explained in Equation 4-5;  $k_{CO,rec}$ ,  $k_{H_2,break}$  and  $k_{H_2O,form}$  are reaction constants of R2, R4 and R5, respectively. Note that the rate constants depend on the pressure and temperatures. The consumed oxygen (i.e. number of reacted oxygens per available site),  $N_{O,con}$  can be calculated as follows:

$$dN_{O,con}/dt = R_{O,con} = k_{CO,rec}\theta_{CO}\theta_O + k_{H_2O,form}\theta_{HNiHO} \quad (4-13)$$

where  $R_{O,con}$  represents the reacted oxygen rate on the surface. Since the number of available sites for the reactions is the same as the number of oxygen sites on the surface,  $N_{O,con}$  is proportional to the solid conversion ratio,  $X_{O,con}$ , i.e.  $n_{O,surface}$

$$X_{O,con} = m_{O,con}/m_{O,OC} = n_{O,con}/(n_{O,surface} \eta) = N_{O,con} / \eta \quad (4-14)$$

$$\eta = n_{O,OC}/n_{O,surface} \quad (4-15)$$

where  $m_{O,con}$  represents the mass of oxygen transferred from the OC particle to gas phase and  $m_{O,OC}$  denotes the mass of oxygen present when the OC particle is fully oxidized.  $n_{O,con}$  represents the number of reacted oxygen whereas  $n_{O,surface}$  is the number of oxygens of the fully oxidized OC surface. In addition,  $\eta$  is the ratio between the number of oxygens on the surface ( $n_{O,OC}$ ) and the number of total oxygens in OC particle when it is fully oxidized. The reaction rate parameters are calculated based on the energetic results from the DFT analysis presented in the previous section. The computational details of these calculations are described in section 4.2.3.

### 4.3.3.2. MF Model Validation

Table 4-1 Reaction rate parameters

Reaction	Reaction parameters	Mol second <sup>-1</sup> site <sup>-1</sup>
R1	$k_{CO,ad}$	$1.88 \times 10^7$
R2	$k_{CO,rec}$	$4.47 \times 10^4$
R3	$k_{H_2,ad}$	$7.03 \times 10^7$
R4	$k_{H_2,break}$	$2.46 \times 10^{10}$
R5	$k_{H_2O,form}$	$1.91 \times 10^6$

$$T = 1,223 \text{ K}, P_{CO} = 1.515 \times 10^4 \text{ Pa}, P_{H_2} = 1.515 \times 10^4 \text{ Pa}, S_{CO} = 1, S_{H_2} = 1$$

;  $P_{CO}$  is the a partial pressure of CO and  $P_{H_2}$  is the partial pressure of H<sub>2</sub>

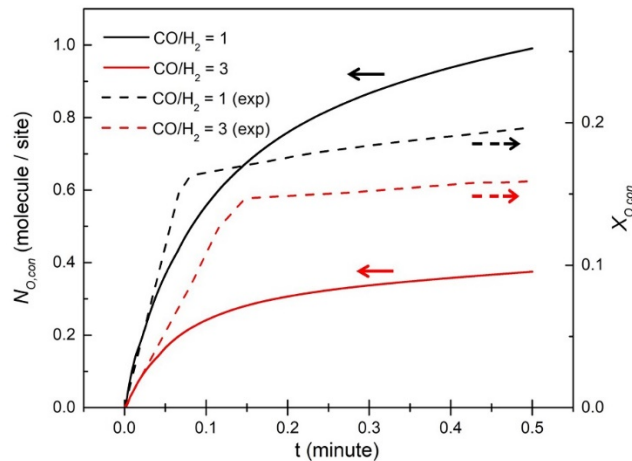


Figure 4-7 Comparison between oxygen consumed from the MF model (solid line) and solid conversion from experimental observations<sup>190</sup> (dashed line) at compositions of CO/H<sub>2</sub> = 1 (black) and CO/H<sub>2</sub> = 3 (red) in the gas phase

The MF model presented in the previous section was validated using experimental observations reported in the literature for this system<sup>190</sup>. Figure 4-7 provides the oxygen consumed in the system within the first 30 s at two different compositions of syngas. As shown in Equation 4-14, the consumed oxygen ( $N_{O,con}$ ) is proportional to the solid conversion ratio

( $X_{O,con}$ ). Hence, Figure 4-7 is used to illustrate the prediction capabilities of the proposed MF model through a comparison between oxygen consumed from the MF model (solid line) and solid conversion from experimental observations (dashed line). The operating conditions and corresponding reaction rate parameters adopted in the established MF model are listed in Table 4-1. As depicted in Figure 4-7, the oxygen consumed ( $N_{O,con}$ ) is larger with a CO/H<sub>2</sub> ratio of 1 than that with a CO/H<sub>2</sub> ratio of 3. Therefore, a high ratio of H<sub>2</sub> in the gas phase benefits the oxygen transformation according to the outcomes predicted by the MF model. The proposed MF model combines H<sub>2</sub> decomposition and H migration on a single reaction step; hence, the overall effect of the MF model shows that the H<sub>2</sub> oxidation process proceeds faster thus promoting H<sub>2</sub>O formation, as explained in section 4.3.3.1. The latter leads to the aforementioned increase in the oxygen transformation caused by the high ratio of H<sub>2</sub> in the gas phase. The MF model predictions are consistent with the experimental observations of solid conversion during the initial stages of the reactions, as displayed in Figure 4-7. Furthermore, there is a sharp increase in solid conversion within the first 0.1 minutes that tends to flat afterwards (dashed lines in Figure 4-7), which suggests that the system reached steady state after 0.1 minutes. This also means that a significant decrease in the solid conversion rate is expected at the beginning of the reaction (i.e. within the first 0.1 minutes). The same tendency is qualitatively predicted by the proposed MF model. A significant decrease in the consumed oxygen rate is predicted at approximately 0.1 minutes, which can be interpreted by the change in the slope of the oxygen consumed in the channel (solid lines in Figure 4-7). However, the predicted system reached steady state faster than the experimental results because the present model does not consider the inside channel and out of particle diffusion effects. Based on the above, outcomes from the MF model proposed in this work qualitatively agree with experimental observations reported in the literature. Accordingly, the MF model proposed in this work can also be used to predict the behaviour of OCs taking place in the channel of the OC particle under different operating conditions.

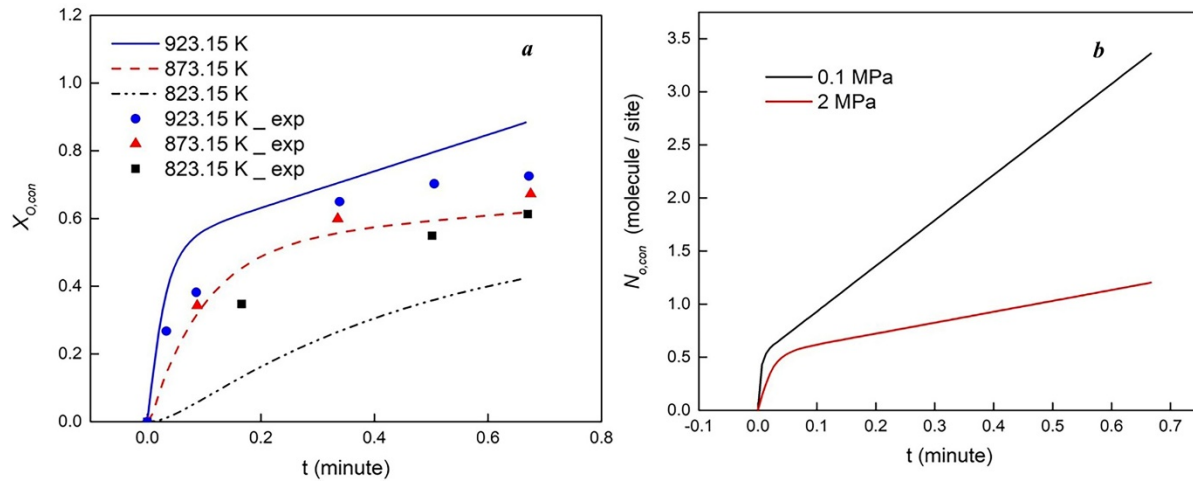


Figure 4-8 (a) Comparison between the solid conversion from the MF model (line) and the solid conversion from the experimental observations<sup>191</sup> (scatter) at temperatures of 923.15 K (blue), 873.15 K (red) and 823.15 K (black); (b) pressure analysis of the oxygen consumed from the MF model at 0.1 MPa (black) and 2 MPa (red)

Furthermore, sensitivity analyses featuring changes in temperature and pressure were performed on the MF model with the aim to gain insights into the performance of the proposed reaction kinetics on this process. The MF model predicts the number of reacted oxygens per oxygen site on the surface of the OC channel,  $N_{O,con}$ , under the assumption that there is an abundance of surface oxygens on the surface, i.e. the surface oxygen vacancy from reactions would be filled by the bulk oxygen instantaneously, as explained in section 4.3.3.1. Moreover, the MF model assumes a homogeneous distribution of the surface species thus neglecting neighbouring effects, as discussed in section 4.3.3.1. To account for these effects, the reaction parameters ( $k_{CO,rec}$ ,  $k_{H_2,break}$ ,  $k_{H_2O,form}$ ) have been adjusted by a weight  $\lambda$  such that the MF model can provide acceptable predictions. In addition, the sticking coefficients of CO and H<sub>2</sub> were adjusted to capture the actual adsorption process; a previous study has shown that not all atoms impinging upon the surface can be adsorbed<sup>200</sup>. The weight  $\lambda$  and the revised sticking coefficients were obtained from least squares fitting using experimental data reported in the literature<sup>191</sup> ( $\lambda = 0.87$ ,  $S_{CO} = 0.32$ ,  $S_{H_2} = 0.07$ ). Figure 4-8(a) compares the OC conversion ratio predicted by the MF model and that obtained from the experimental observations at different temperatures. As shown in this figure, an increase in temperature leads to a higher solid

conversion, which agrees with the experimental report <sup>191</sup>. Moreover, Figure 4-8(a) shows that the MF model predictions quantitatively agree with these experimental observations, e.g. the solid conversion at 873.15 K is around 62% at 40 seconds, which agrees with the reported experimental solid conversion (67%) <sup>191</sup>. Note that this model provides better predictions under high operating temperatures. Figure 4-8(b) shows that the oxygen consumed by the reactions decreases as the pressure within the OC channel increases. Previous experimental studies have reported the same observation, i.e. reduction in the reaction rates with an increase in pressure <sup>192</sup>. Moreover, the consumed oxygen experienced a fast increase at the beginning of the reaction followed by a regime of slower growth. The decrease in the rate of the consumed oxygen is due to the changes in the coverages of the surface species. The oxygen is consumed by the reaction of CO oxidation (R2) and NiHOH oxidation (R5). Hence the rate of oxygen consumed is directly related to the coverages of the adsorbed CO,  $\theta_{CO}$ , and the surface adjacent structure NiHOH,  $\theta_{NiHO}$ . As shown in Table 4-1,  $k_{CO,ad}$  is larger than  $k_{CO,rec}$ , i.e. the surface CO is oxidized at a lower rate than CO adsorption. Hence,  $\theta_{CO}$  keeps increasing which leads to the constant increase in the rate of the consumed oxygen by reaction R2. Nevertheless,  $\theta_{NiHO}$  initially increases; this increase comes from the faster reaction of H<sub>2</sub> dissociation (R4) compared to the NiHOH oxidation (R5), i.e.  $k_{H_2,break}$  is larger than  $k_{H_2O,form}$ . In addition, the H<sub>2</sub> adsorption (R3) is slower than the H<sub>2</sub> dissociation (R4), i.e.  $k_{H_2,ad}$  is smaller than  $k_{H_2,break}$ , which leads to the low surface coverage of H<sub>2</sub> after the initial reactions. The low coverage of surface H<sub>2</sub> significantly lowers the rate of the H<sub>2</sub> dissociation (R4), which eventually leads to a decrease in  $\theta_{NiHO}$ . These changes in  $\theta_{NiHO}$  results in the rate of the consumed oxygen by reaction R5 to increase at the beginning of the process followed by a decrease. The decrease in the consumed oxygen by reaction R5 lowers the overall rate of the consumed oxygen after the initial reactions. Overall, the MF predictions agree with the experimental observations as explained above.

#### 4.3.3.3. Model performance over different operating conditions

Table 4-2 Operating conditions

Temperature	Pressure	Inlet composition
K	Mpa	CO/H <sub>2</sub>
823.15	0.1	1/3
to	to	1/1
923.15	2.0	3/1

The previous section showed that the proposed MF model agree with experimental data reported in the literature. The aim of this section is to explore the MF model predictions under different operating conditions. Table 4-2 presents the range of values in the inlet compositions, temperatures and pressures at which the present study was performed. These set of operating conditions correspond to typical operating conditions for the studied CLC system<sup>190 191 192</sup>. The MF model predictions at different CO<sub>2</sub>/H<sub>2</sub>O product ratios under these operating conditions are depicted in Figure 4-9.

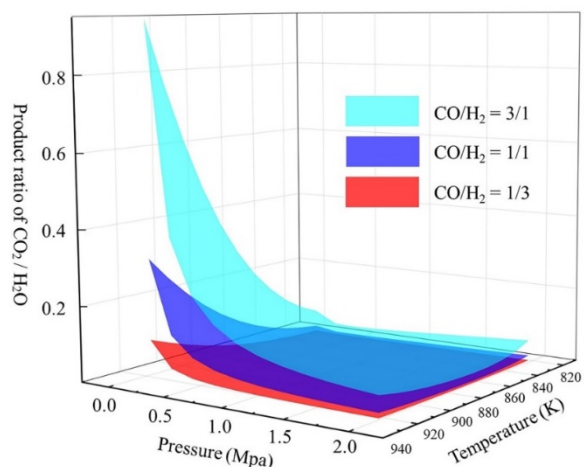


Figure 4-9 Product ratio CO<sub>2</sub>/H<sub>2</sub>O, composition: CO/H<sub>2</sub> = 3/1 (cyan), CO/H<sub>2</sub> = 1/1 (blue), CO/H<sub>2</sub> = 1/3 (red), temperature range: 823.15 K - 923.15 K, pressure range: 0.1 MPa - 2 MPa



As shown in Figure 4-9, the MF model predicts a higher CO<sub>2</sub>/H<sub>2</sub>O product ratio at high temperatures and low pressures. Note that the highest CO<sub>2</sub>/H<sub>2</sub>O product ratio is almost 0.94 at 923.15 K, 0.1 MPa and a CO/H<sub>2</sub> gas-phase ratio of 3. The MF model shows that the product ratio is more sensitive at high temperatures or low pressures compared to the rest of the operating conditions considered in this study (the pressure and the input composition or the temperature and the input composition). With a higher content of CO in the inlet stream, the change in the temperatures and pressures leads to a more significant change in the CO<sub>2</sub>/H<sub>2</sub>O product ratio. This suggests that CO oxidation is more sensitive to temperature and pressure changes. These results are key to achieve full combustion of syngas, and therefore improve fuel utilization efficiency and environmental sustainability for this process.

The proposed DFT-based MF model is proved to be valid for the prediction of the studied OC system based on its comparison with the experimental reports. The changes in performance predicted by the MF model can be used as a basis to identify suitable operating conditions when this process is operated at larger (macroscopic) scales. Furthermore, the validation MF model further confirms the DFT-based reaction kinetics and mechanisms proposed in this study.

#### **4.4 Summary**

Chapter 4 revealed the elementary reaction mechanisms of syngas combustion using NiO as the OC. Results from this study showed that the controlling step of the overall syngas oxidation reaction is the decomposition of H<sub>2</sub> on the NiO surface. A coupling electronic analysis was performed in this study to further support the insights gained from the DFT analysis. Moreover, a DFT-based MF model was developed to connect the atomic-scale outcomes from the DFT analysis to experimentally reported observations. The developed multi-scale model was subsequently validated using experimental data reported in the literature. The system predictions from this model showed that a high OC conversion and product selectivity of CO<sub>2</sub>/H<sub>2</sub>O can be expected when the system operates at high temperatures and low pressures. The reported reaction kinetics can be furthermore employed in Chapter 5 and Chapter 6 for the assessment of the key factors affecting the performance of this system.

# Chapter 5 Insights into Syngas Combustion on Defective NiO Surface for Chemical Looping Combustion: Oxygen Migration and Vacancy Effects

## 5.1 Introduction

The previous chapter presented the reaction kinetics of syngas combustion on NiO. To advance the understanding of this system, oxygen vacancies on the NiO surface can also be considered on the basis of the reported reaction kinetics to gain insights on this phenomenon. Among all the favoured properties of OCs, the redox activities, oxygen compacity and mobility of OCs are essential considerations.<sup>75 3, 201-202</sup> It has been shown that oxygen vacancies can benefit CLC performance from each of the aforementioned aspects, as discussed in Chapter 2.

Nevertheless, theoretical studies of oxygen vacancies for OC development primarily focus on the CH<sub>4</sub> oxidation process. Consequently, the study of the non-negligible role of vacancies in syngas combustion is quite limited in the open literature; this is especially the case for theoretical studies on the vacancy effects. Accordingly, the vacancy effects on the atomic-scale OC performance have not been widely investigated; particularly for the syngas combustion process on NiO. In order to provide insights on the vacancy effects within the studied system, this chapter provides a comprehensive analysis of vacancy formation, syngas adsorption and syngas oxidation using the OC, NiO. The energetic results, coupled with the electron distribution analysis, provide insights into the significant role of the defective sites based on the comparison between the calculations on the defective surface and those on the perfect surface (i.e. a surface without vacancies). Furthermore, the experimental observations reported in the same system within the literature are used to validate the proposed reaction mechanisms via a DFT-based MF model, which is developed using the reaction kinetics on a defective NiO surface. The insights presented this chapter have already been published.<sup>203</sup>

The rest of this chapter is organized as follows. Section 5.2 presents the computational details used in this chapter. Section 5.3 provides the structure-related energetic results, the electronic analysis and the DFT-based MF investigation. A summary of this chapter is provided in section 5.4.

## 5.2 Computational details

The DFT calculation details and NiO surface model are the same as discussed section 3.2. The DFT-based MF model was implemented in Python 3.7.0.

The adsorption energy of CO or H<sub>2</sub>,  $\Delta E_{\text{adsorption}}$  on NiO surface is calculated using Equation 3-1. The CI-NEB method is implied to locate the TS. The forward and backward reaction barriers,  $E_{\text{forward}}$ ,  $E_{\text{backward}}$  are calculated as follows:

$$E_{\text{forward}} = E_{\text{a,TS}} - E_{\text{a,reactant}} \quad (5-1)$$

$$E_{\text{backward}} = E_{\text{a,TS}} - E_{\text{a,product}} \quad (5-2)$$

where  $E_{\text{a,reactant}}$ ,  $E_{\text{a,TS}}$  and  $E_{\text{a,product}}$  represent the energies of the reactant, the TS and the product, respectively.

Further insights into the proposed mechanisms and the vacancy effects are provided through the electronic analysis. The COHP analysis describes the bonding properties to interpret the interactions between the studied atom pairs.<sup>195-196</sup> The related calculation details are explained in section 4.2.2.

## 5.3 Results and discussion

### 5.3.1 Bulk oxygen diffusion

Due to the surface reactions, the oxygen on the surface is continuously consumed to form the surface oxygen vacancy, then the vacancy is substituted by the sublayer oxygen. The vacancy distribution and oxygen migration play a vital role in OC performance.

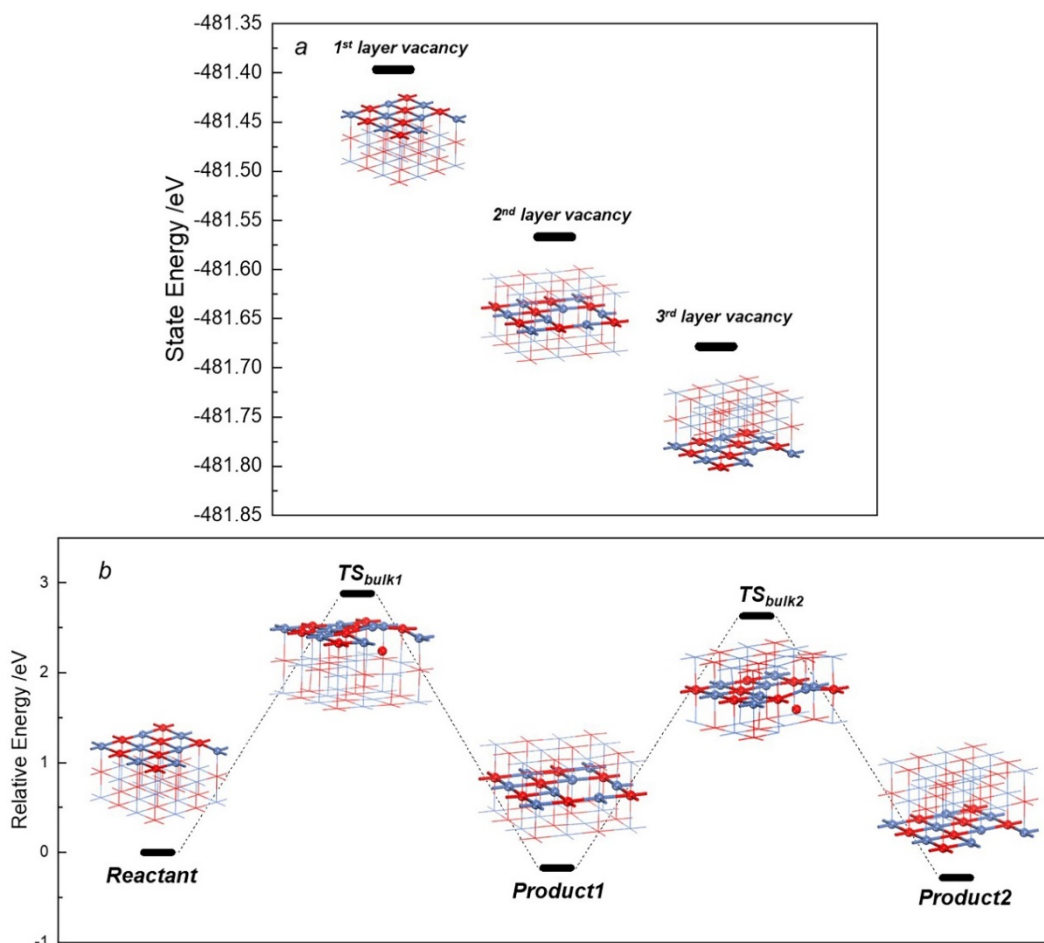


Figure 5-1 Oxygen migration analysis: (a) stability analysis of defective configurations (b) energy profile of oxygen migration (2<sup>nd</sup> layer to the surface through TS<sub>bulk1</sub>, 3<sup>rd</sup> layer to the 2<sup>nd</sup> layer through TS<sub>bulk2</sub>)

Figure 5-1 describes the direction of bulk oxygen diffusion and also reveals the mechanism of oxygen migration. As shown in Figure 5-1(a), the analysis of adsorption energies (with defective sites at the 1<sup>st</sup> layer, 2<sup>nd</sup> layer and 3<sup>rd</sup> layer) indicates that the most stable vacancy exists at the 3<sup>rd</sup> layer, followed by the 2<sup>nd</sup> layer and the eventually the 1<sup>st</sup> layer vacancy, respectively. This behaviour is mostly due to the slightly higher state energy of the 3<sup>rd</sup> layer vacancy configuration, i.e. 0.17 eV higher than the 2<sup>nd</sup> layer vacancy configuration and 0.28 eV higher than the 1<sup>st</sup> layer vacancy configuration. Therefore, the bulk oxygen is

expected to diffuse from the 3<sup>rd</sup> layer to the 2<sup>nd</sup> layer. Figure 5-1(b) elucidates the mechanism of bulk oxygen migration. The surface layer O reacts with the adsorbed CO or H<sub>2</sub> followed by the formation of the 1<sup>st</sup> layer vacancy indicated as the reactant in Figure 5-1(b). The 2<sup>nd</sup> layer O migrates to the 1<sup>st</sup> layer through TS<sub>bulk1</sub> to form the 2<sup>nd</sup> layer vacancy configuration as product1. The forward energy barrier of O diffusion from the 2<sup>nd</sup> layer (2.88 eV) to the 1<sup>st</sup> layer is smaller than the backward energy barrier (3.05 eV), which further illustrates the O migration direction from the bulk to the surface. The energetic results of O diffusion from the 3<sup>rd</sup> layer to the 2<sup>nd</sup> layer indicate the same outward direction of O migration (from the 3<sup>rd</sup> layer to the 2<sup>nd</sup> layer). The direction predicted on oxygen migration agrees with a previous study<sup>16</sup>, i.e. the oxygen diffuses from the subsurface to substitute the surface vacancy. Moreover, the O diffusion from the 3<sup>rd</sup> layer to the 2<sup>nd</sup> layer is expected to be more active than the O transport from the 2<sup>nd</sup> layer to the 1<sup>st</sup> layer due to the smaller energy barrier of the former reaction (2.80 eV) compared to the latter reaction (2.88 eV). The bulk oxygen migration guarantees a sufficient oxygen supply on the surface for the further oxidation of CO and H<sub>2</sub>.

Table 5-1 Reaction barriers of bulk oxygen migration

	Forward reaction barrier /eV	Backward reaction barrier /eV
Oxygen migration from 2 to 1	2.88	3.05
Oxygen migration from 3 to 2	2.80	2.91

### 5.3.2 Defective adsorption

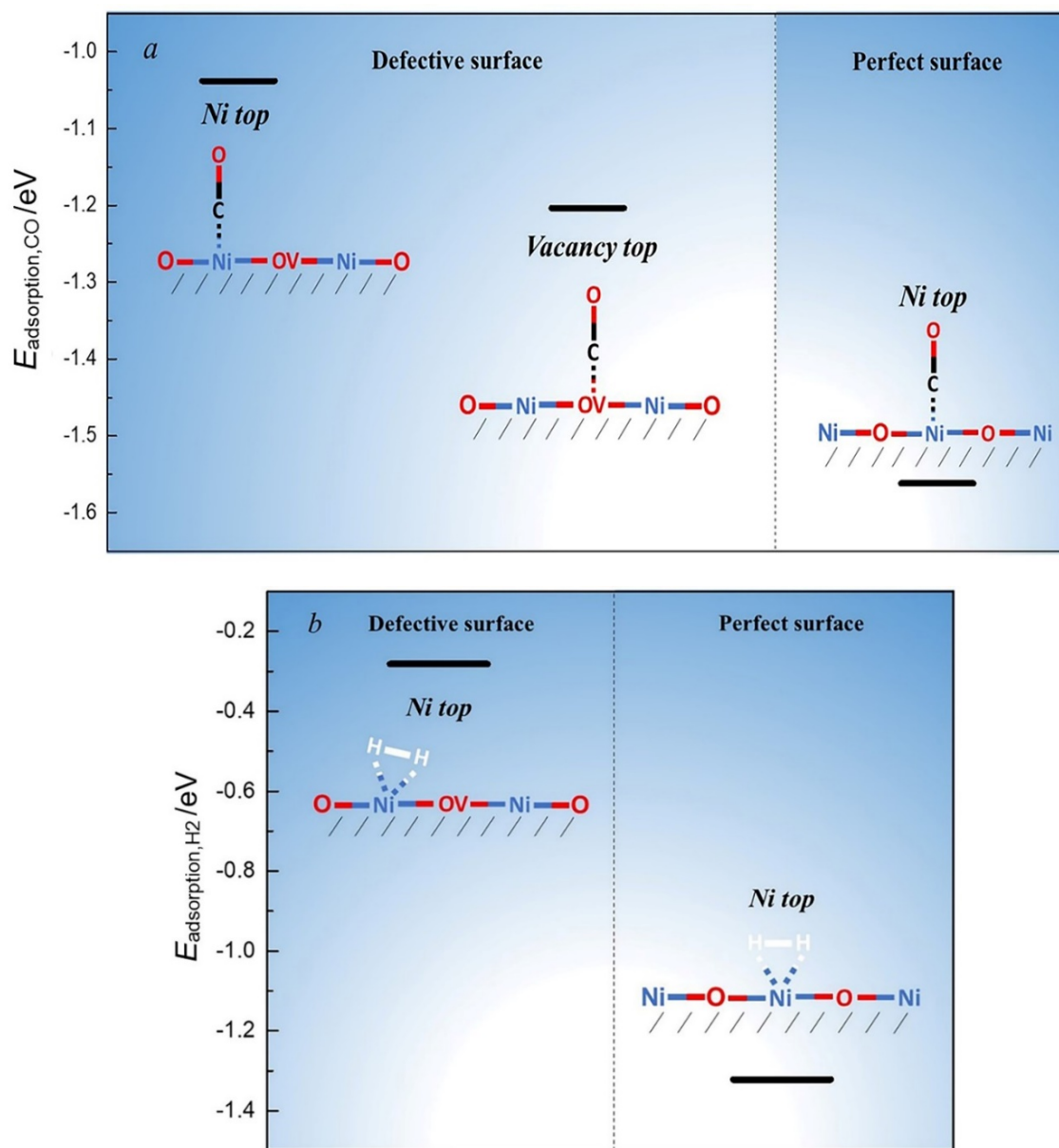


Figure 5-2 Adsorption energy comparisons of (a) CO and (b) H<sub>2</sub> between the defective surface (left) and the perfect surface (right). OV: Oxygen vacancy

Figure 5-2 compares the adsorption energies of CO and H<sub>2</sub> between a defective surface and a perfect surface. In comparison to the vacancy top configuration, the Ni top configurations

are considered for both CO and H<sub>2</sub> adsorption since Ni top was observed to be the stable adsorption and active reaction sites.<sup>166</sup> Results show that the more stable adsorption is observed on the perfect surface for both CO and H<sub>2</sub>. Accordingly, the relatively high state energies of both CO and H<sub>2</sub> adsorption configurations on the defective surface are expected, which tends to produce low energy barriers of the subsequent oxidation reactions, i.e. small energy differences between the reactants and the TSs. Therefore, in the presence of vacancies, the more active subsequent reactions are expected after the adsorption of both CO and H<sub>2</sub>. Vacancies tend to stimulate the oxidation reactions of syngas. In terms of CO adsorption presented in Figure 5-2(a), the CO at the Ni top with an adjacent vacancy is less stable than that observed at the vacancy top, which means the oxygen vacancies are active sites for CO adsorption while the adsorption configuration of Ni top with an adjacent vacancy will lead to more active CO oxidation. Accordingly, the corresponding energy barrier of CO oxidation at the Ni top should be lower than that at the vacancy top in the defective surface system; this will be explained in section 5.3.4. Regarding H<sub>2</sub> adsorption, the adsorption configuration at the vacancy top is not stable. Then the H<sub>2</sub> molecule migrates from the vacancy top to the adjacent Ni top, as shown in Figure 5-2(b). Low stability of adsorption with the neighbouring vacancy suggests an active reactant configuration of the subsequent H<sub>2</sub> oxidation.

### **5.3.3 Projected density of states analysis of syngas adsorption**

Followed by the analysis of adsorption energies, the pDOS analysis provides further evidence of the syngas adsorption based on the electron population.

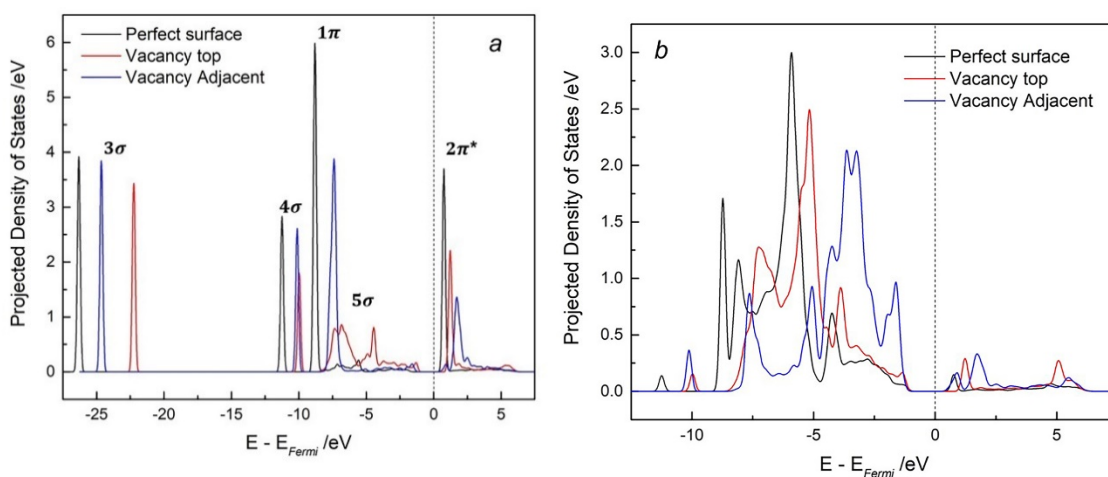


Figure 5-3 Electron distribution comparisons of (a) CO molecular orbitals and (b) Ni 3d orbitals between the CO adsorption configurations with (red: vacancy top, blue: vacancy-adjacent Ni top) and without vacancies (black)

The interactions between CO as an adsorbate with the nearest Ni come from the hybridization between the HOMO orbital ( $5\sigma$ ) and LUMO orbital ( $2\pi^*$ ) of CO and the 3d orbital of the nearest Ni. After adsorption, the molecular orbitals of CO are shifting to the lower energy level, which indicates a stable adsorption configuration on the surface. The  $5\sigma$ -d forward donation effect leads to a significant decrease in the electron occupancy of the  $5\sigma$  orbital of CO, while the d- $2\pi^*$  back-donation effect results in the increase in the electron population of the  $2\pi^*$  orbital.<sup>185, 188-189</sup> In addition, the mentioned  $5\sigma$  and  $2\pi^*$  orbitals tend to spread due to the interactions between the adsorbate and the surface. As shown in Figure 5-3 (a), the molecular orbitals of the adsorbed CO on the perfect surface stay at the lowest energy levels compared to the molecular orbitals of the attached CO in the other configurations. Likewise, the 3d orbital of Ni in the perfect surface configuration tends to stay at the lowest energy level, as shown in Figure 5-3(b). Therefore, the most stable CO adsorption configuration is observed on the perfect surface, as described in section 5.3.2. Comparing the electron populations in the two configurations with vacancies, the occupied orbitals (to the left



of the Fermi level) of CO on the vacancy top are localized at higher energy levels than that on the Ni top with an adjacent vacancy. However, the unoccupied orbitals (to the right of the Fermi level) of CO on the vacancy top stay at lower energy levels than that on the adjacent Ni top surface. Note that the 3d orbital of Ni in the vacancy top configuration apparently occupies a lower energy level than that in the Ni top configuration with an adjacent vacancy. These results suggest that the adsorption configuration at the vacancy top is more stable than that with an adjacent vacancy. Accordingly, a lower adsorption energy is observed on the vacancy top, as discussed in section 5.3.2. The strongest  $5\sigma$ -d forward donation effect leads to the most significant spreading of the  $5\sigma$  orbital on the vacancy top configuration, which is followed by that on the Ni top configuration with a defective site and the perfect surface configuration. Hence, the HOMO orbital of the CO on the vacancy stays closest to the Fermi level. Regarding the d- $2\pi^*$  back-donation, the  $2\pi^*$  orbitals of the CO on the vacancy-adjacent Ni top tend to be the most affected based on the most obvious spreading of the  $2\pi^*$  orbital. Note that the interactions between the adsorbate and the surface produce smaller gaps between the HOMO and LUMO orbitals of CO in the presence of vacancies, which indicates that the adsorption configurations are more active reactants of the subsequent reactions. This change in the electron occupation also suggests the oxygen vacancies benefit the further CO oxidation.

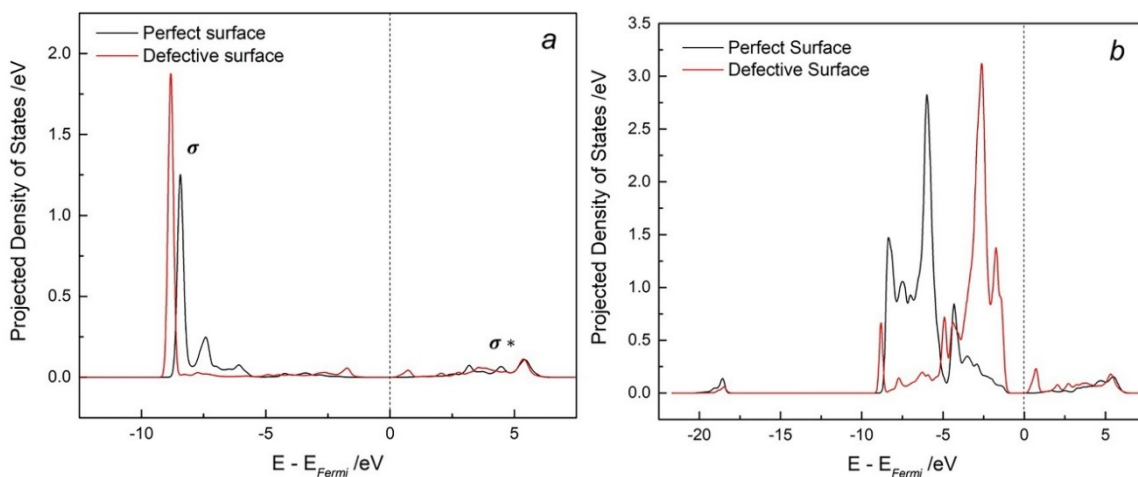


Figure 5-4 Electron distribution comparisons of (a) H<sub>2</sub> molecular orbitals and (b) Ni 3d orbitals between the H<sub>2</sub> adsorption configurations with (red) and without vacancies (black)

Figure 5-4 provides the pDOS analysis of the H<sub>2</sub> adsorption on both the perfect surface and the defective surface. As depicted in Figure 5-4(a), the more spreading molecular orbitals of H<sub>2</sub> on the perfect surface is observed. Likewise, the 3d orbital of the studied surface Ni on the perfect surface occupies the lower energy level. Therefore, the more stable H<sub>2</sub> adsorption is expected on the perfect surface, as indicated in section 5.3.2. In addition, the gap of the Ni 3d orbitals between the left and right side of the Fermi level shown in Figure 5-4(b) tends to be smaller in the presence of the neighbouring vacancy. A more active H<sub>2</sub> oxidation is thus expected on the defective surface (see section 5.3.5).

### **5.3.4 Reaction mechanism: CO oxidation**

Vacancies are expected to benefit the redox reactions based on the results presented above and a previous report.<sup>204</sup> Figure 5-5 shows the positive effects of the oxygen vacancies on the CO oxidation reaction. The mechanism of CO oxidation reaction on a perfect surface has been reported Chapter 4, i.e. the surface O is scavenged by the attached CO atop the adjacent Ni and reacted into CO<sub>2</sub> as a product.

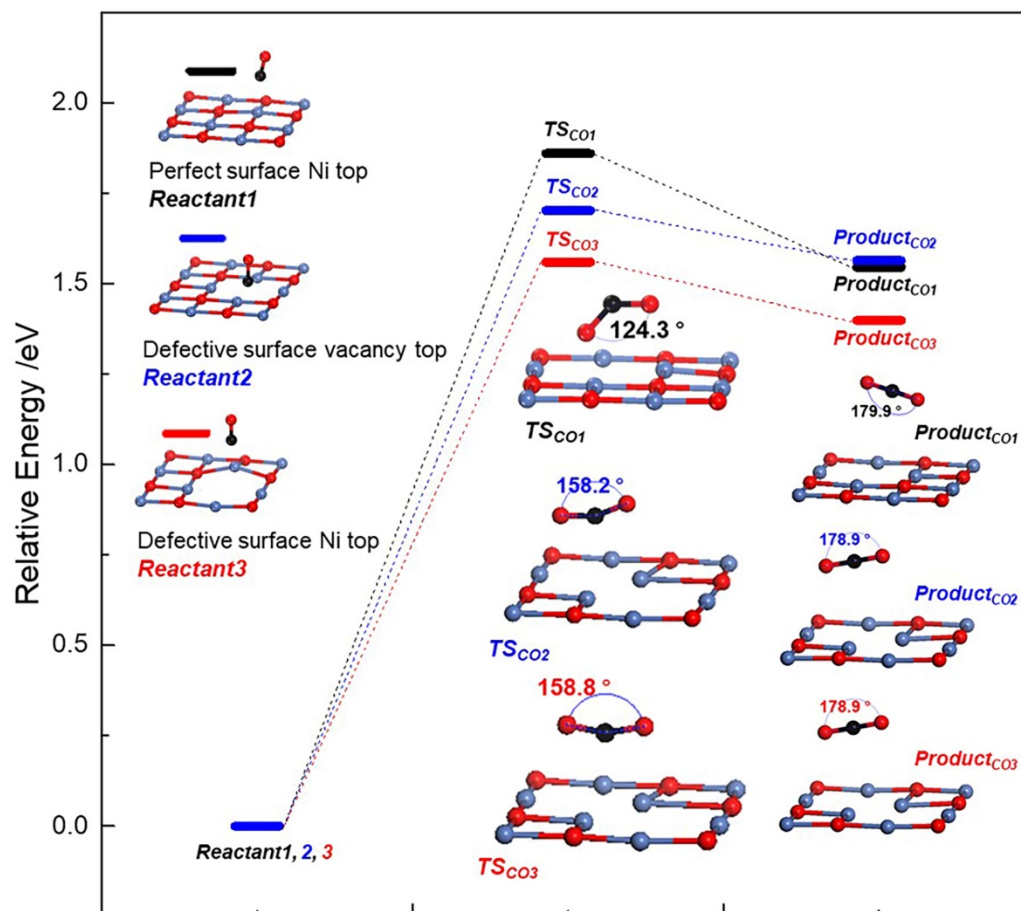


Figure 5-5 Comparison of the CO oxidation energy profile between the perfect surface (black: from Reactant1 to Product<sub>CO1</sub> through TS<sub>CO1</sub>) and the defective surface (blue: from Reactant2, CO adsorbed at vacancy top to Product<sub>CO2</sub> through TS<sub>CO2</sub>; red: from Reactant3, CO adsorbed at vacancy-adjacent Ni top to Product<sub>CO3</sub> through TS<sub>CO3</sub>). Blue atom (Ni), red atom (O), black atom (C)

Figure 5-5 presents two reaction mechanisms on the defective surface based on the vacancy top reactant (reactant2) and vacancy-adjacent Ni top reactant (reactant3). The energy barriers of the CO oxidation on the perfect surface is shown from reactant1 to product<sub>CO1</sub> through TS<sub>CO1</sub> (transition state of CO oxidation reaction on the perfect surface). The estimated forward energy barrier from Reactant1 to TS<sub>CO1</sub> is larger than the other two studied reaction

mechanisms on the defective surface. Thus, the oxygen vacancy on the surface benefits the CO oxidation based on the energetic results. Furthermore, the neighbouring vacancy of the adsorbed CO on the Ni top has a more significant effect on enhancing CO oxidation than the vacancy site that adsorbs the CO. The bond angle of O-C-O in  $\text{TS}_{\text{CO}_3}$  from the reactant of CO at adjacent vacancy Ni top is about  $158.8^\circ$ , which is the closest to that of a stable linear  $\text{CO}_2$  among the three studied TS. The lowest state energy of  $\text{TS}_{\text{CO}_3}$  is expected among the studied three TSs. Consequently, the neighbouring vacancy tends to activate the CO oxidation more significantly due to the low energy barrier from reactant3 to  $\text{TS}_{\text{CO}_3}$ . The backward activation energies are lower than the forward activation energies, which implies the  $\text{CO}_2$  reduction might happen on the reduced surface. The extremely small adsorption energies of  $\text{CO}_2$  in the product configurations (0.08 eV on perfect surface and 0.06 eV on defective surface) indicate that the produced  $\text{CO}_2$  hardly stays adsorbed on the surface and diffuses into the gas phase immediately after its production, which promotes CO conversion into  $\text{CO}_2$ . Note that these conclusions are obtained on the specific surface configurations presented in Figure 5-5, which do not consider other factors that may impact OC performance such as the nearest adsorbed species, i.e. CO or  $\text{H}_2$ , surface impurities or supporting effects.

Additionally, since the vacancy is likely to be occupied by CO based on the adsorption energy analysis presented in section 5.3.2, the CO oxidation mechanism was studied with an adjacent vacancy occupied by a CO neighbor. The results show that the forward and backward reaction barriers of the aforementioned configuration are much larger than those observed in all the other studied configurations. Moreover, the difference between the forward and backward reaction barriers in this system is smaller than those observed in each of the other studied systems. The observed deviations come from the coordinate effects of the nearest neighbor CO and the vacancy. Note that this manuscript focuses on the vacancy effects, which cannot be distinguished from the aforementioned coordinate effects on a defective surface with a vacancy-top CO neighbor. Therefore, the energetic results and their comparison to the other studied configurations are provided in Figure B2 within the supporting information.

### 5.3.5 Reaction mechanism: H<sub>2</sub> oxidation

The CO oxidation reaction is a 1-step process on both the perfect surface and defective surface. However, the H<sub>2</sub> oxidation on the defective surface changes into a 2-step reaction instead of a 3-step reaction on the perfect surface.

Figure 5-6 provides a comparison between the H<sub>2</sub> oxidation mechanisms with and without vacancies. As mentioned above, the H<sub>2</sub> attached at the Ni top is decomposed into two H and stays at the two contiguous Ni tops on the perfect surface. The migration of H from one of the Ni tops to the O top produces the adjacent structures of Ni-O and O-H shown in Figure 5-6. These two steps have been proven to be inevitable on a perfect NiO surface based on the DFT results, i.e. no valid TS was found in a one-step scenario as presented in Chapter 4. However, the H<sub>2</sub> decomposition into the adjacent structures of Ni-O and O-H only takes one step on the defective surface. Furthermore, the disconnection of the H-H bond without a neighbouring vacancy is highly unlikely to happen according to the calculated energy barrier. Accordingly, H<sub>2</sub> decomposition governs the overall H<sub>2</sub> oxidation process on the perfect surface. At the same time, the forward

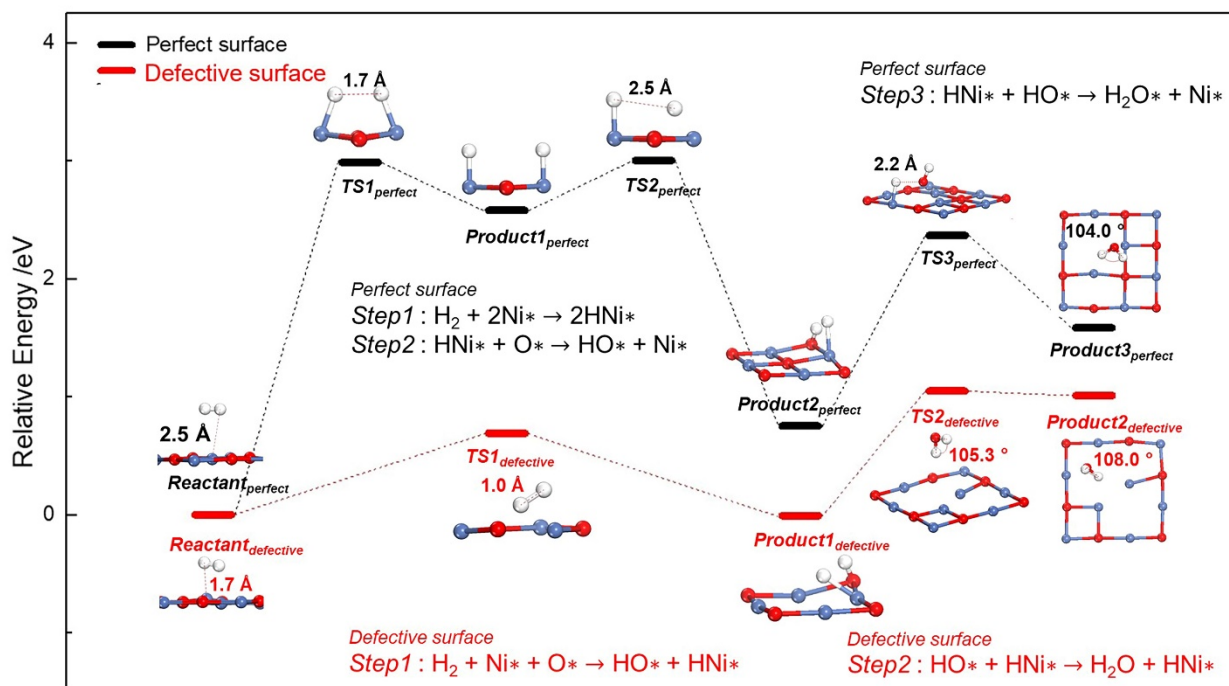


Figure 5-6 Comparison of H<sub>2</sub> oxidation energy profile between the perfect surface (black: step 1 from Reactant<sub>perfect</sub> to Product1<sub>perfect</sub> through TS1<sub>perfect</sub>; step 2 from Product1<sub>perfect</sub> to Product2<sub>perfect</sub> through TS2<sub>perfect</sub>; step 3 from Product2<sub>perfect</sub> to Product3<sub>perfect</sub> through TS3<sub>perfect</sub>) and the defective surface (red: step 1 from Reactant<sub>defective</sub> to Product1<sub>defective</sub> through TS1<sub>defective</sub>; step 2 from Product1<sub>defective</sub> to Product2<sub>defective</sub> through TS2<sub>defective</sub>). Blue atom (Ni), red atom (O), white atom (H)

energy barrier of H<sub>2</sub> decomposition is dramatically reduced by the neighbouring vacancy on NiO. The two H keep a distance of 1 Å with each other in TS1<sub>defective</sub> (TS of H<sub>2</sub> decomposition on the defective surface), which presents a more similar structure to the structure of H<sub>2</sub> compared to those observed for the two H in TS1<sub>perfect</sub> (1.7 Å) and TS2<sub>perfect</sub> (2.5 Å), respectively. The similarity between the two H in the TS1<sub>defective</sub> and an H<sub>2</sub> molecule is an indication of a stable configuration. Then compared to the state energies of both TS1<sub>perfect</sub> and TS2<sub>perfect</sub>, the state energy of TS1<sub>defective</sub> is lower. Moreover, the defective site leads to a smaller distance between the adsorbed H<sub>2</sub> and the surface Ni. This adsorption configuration in the presence of the vacancy is associated with an active reactant that leads to a lower energy barrier

of the H<sub>2</sub> decomposition reaction, as discussed in section 5.3.2. The 2<sup>nd</sup> step of H<sub>2</sub> oxidation on the defective surface is the same as the 3<sup>rd</sup> step of H<sub>2</sub> oxidation on the perfect surface: the adjacent O-H and Ni-H react to form a water molecule through TS2<sub>defective</sub>. The forward energy barrier of step 2 on the defective surface is lower than that of the same chemical transformation (step 3) on the perfect surface. In TS2<sub>defective</sub>, the bond angle of H-O-H is about 105.3°, which is close to the bond angle of H<sub>2</sub>O (105°),<sup>198-199</sup> hence, this suggests a stable configuration of TS2<sub>defective</sub>. The bond distance of H-O in TS3<sub>perfect</sub> (2.2 Å) is much longer than that observed for the produced H<sub>2</sub>O molecule(0.96 Å).<sup>199</sup> Hence, a high state energy of the relatively unstable TS3<sub>perfect</sub> is expected. Accordingly, the lower energy barrier of H<sub>2</sub>O formation is observed on a defective surface. As shown in Figure 5-6, the adjacent structures of Ni-H and O-H are pointing towards each other on the perfect surface in Product2<sub>perfect</sub>, whereas the vacancy attracts the two H and makes both Ni-H and O-H tilt slightly to the defective site in Product1<sub>defective</sub>. The produced bond angle of O-H-O in Product2<sub>defective</sub> is 108° which is slightly larger than the experimentally reported bond angle of 105° and the bond angle in Product3<sub>perfect</sub> of 104°. The backward energy barrier of the H<sub>2</sub>O formation reaction on the defective surface is much smaller than that on the perfect surface. The decomposition of the adsorbed H<sub>2</sub>O is more likely to happen with the existence of the defective site. Note that on the defective surface, the largest energy barrier is at the 2<sup>nd</sup> step to form H<sub>2</sub>O instead of H<sub>2</sub> decomposition on the perfect surface. As a result, H<sub>2</sub>O formation represents the controlling step of the H<sub>2</sub> oxidation reaction when there is a high coverage of vacancies on the surface. Accordingly, the reaction activity of OC in the H<sub>2</sub>O formation process needs to be considered to improve the OC performance in H<sub>2</sub> oxidation.

### 5.3.6 Model Verification

The energies barriers of the proposed elementary reactions are listed in ascending order in Table 5-1. As shown in this table, the H<sub>2</sub> oxidation process, including both H<sub>2</sub> decomposition and H<sub>2</sub>O formation, is easier to process compared to the CO oxidation. This observation comes from the relatively low energy barriers obtained for the H<sub>2</sub> oxidation reactions compared to those predicted for the CO oxidation reaction mechanisms. The CO oxidation process represents the controlling step of the overall syngas oxidation process. Therefore, a high ratio

Table 5-2 Energy barriers of the proposed elementary reactions

Reaction	$E_a$ /eV
H <sub>2</sub> decomposition	0.70
H <sub>2</sub> O formation	1.06
CO oxidation <sup>a</sup>	1.56
CO oxidation <sup>b</sup>	1.70

a Ni top reaction; b Vacancy top reaction

of H<sub>2</sub> to CO in the syngas will benefit OC reduction. This is in agreement with experimental observations reported by Labiano *et al.*<sup>190</sup>, which showed that the studied OC (active component as NiO) presents higher reactivities with the increasing ratio of H<sub>2</sub> to CO in the syngas. The same phenomena on OC conversion using syngas was also reported by Lasa *et al.*<sup>191</sup> The reactivities of the studied species with the highly performing oxygen carrier (active component as NiO) are as follows: H<sub>2</sub> > CO > CH<sub>4</sub>. Note that the trace amounts of CH<sub>4</sub> reported in the previous study are due to the syngas generation from biomass gasification.<sup>205</sup>

Table 5-3 presents the reaction rate constants of all the reactions and adsorptions calculated based on Equations 4-6 and 4-5. As shown in this table, the oxygen migration rate constants are much smaller than that of the adsorption and reactions. The units of the reaction rate constants are s<sup>-1</sup>. Therefore, these events can be treated as the first order reaction to obtain the characteristic time ( $\tau$ ), i.e.

$$\tau = \frac{1}{k_i} \quad (5-3)$$

where  $k_i$  is the rate constant with the unit s<sup>-1</sup>. As shown in Table 5-3, H<sub>2</sub> decomposition exhibits the largest rate constant followed by H<sub>2</sub>O formation and H<sub>2</sub> adsorption. The oxygen migration rate constants are much smaller than the other events, which is mostly due to the larger diffusion energies compared to the activation energies of CO oxidation and all three steps of H<sub>2</sub> oxidation. Consequently, the characteristic time for oxygen migration is much larger than that observed for the oxidation reactions and adsorptions. The oxygen migration



from the third layer to the second layer is faster than that from the second layer to the first layer, which agrees with the outcomes described in section 5.3.1. Moreover, the largest characteristic time of the oxygen migration process implies that the surface oxidation reactions and adsorptions are much faster when there is only a small amount of vacancies on the surface at the initial stage. However, when more oxygens of the surface are consumed, the rates of the surface oxidations and adsorptions are expected to decrease and be comparable with the oxygen migration rates to guarantee the oxygen supply in the OC particle. Note that there are no experimental studies currently available in the open literature that can be used to validate the characteristic time for this system.

To further validate the proposed reaction mechanism, the reaction kinetics obtained in the present study were used to inform a mean-field (MF) model. The considered events are the same as listed in section 4.3.3.1 from R1 to R5. But the reaction rate parameters are calculated based on the activation energies of the reactions on a defective NiO. Figure 5-7 compares the consumed oxygen obtained from the DFT-based MF model to the solid conversion ratio from the experimental observations.<sup>190</sup> With a high ratio of H<sub>2</sub> to CO (i.e. CO/H<sub>2</sub> = 1), the oxygen consumed is larger. This agrees with the tendency shown in the reported solid conversion ratio from the experimental work, e.g. a higher solid conversion ratio is achieved with a high ratio of H<sub>2</sub> to CO. Since the oxygen consumed is proportional to the solid conversion ratio, Figure 5-7 qualitatively validates the proposed reaction mechanisms using the DFT-based MF outputs. Note that the gradient change of the experimental observations is also shown in the predicted number of the consumed oxygen: the rate of increase in the solid conversion ratio is reduced at around 0.1 minutes in the experimental reports in Figure 5-7 (dashed lines), whereas the change in the rate of oxygen consumption appears within a much shorter time (within 0.01 minutes) according to the output of the proposed DFT-based MF model in Figure 5-7 (solid lines). This comes from the elimination of the syngas diffusion inside the particle channel and outside of the particle in the established model.

Table 5-3 Characteristic time comparison

	Activation energy /eV	Reaction rate constants /s <sup>-1</sup>	characteristic time /s
		1.88E+07	5.32E-08
CO react	1.59	3.20E+06	3.13E-07
H <sub>2</sub> adsorption		7.03E+07	1.42E-08
H <sub>2</sub> decomposition	0.63	1.10E+10	9.09E-11
H <sub>2</sub> O formation	1.17	3.71E+08	2.70E-09
Oxygen migration: 2 to 1 layer	2.87	1.50E+01	6.67E-02
Oxygen migration: 3 to 2 layer	2.79	2.87E+01	3.49E-02

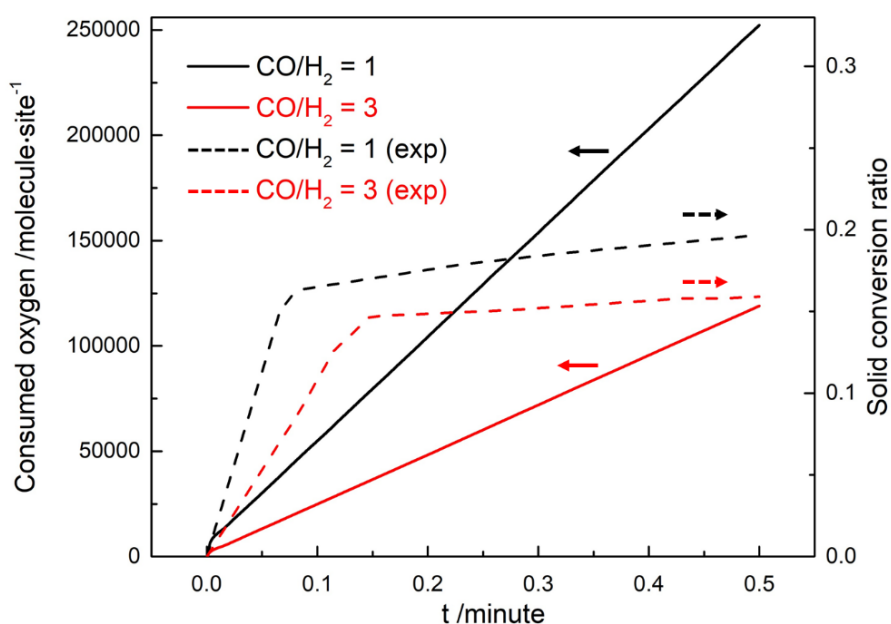


Figure 5-7 Comparison between oxygen consumed from the MF model (solid line) and solid conversion from experimental observations (dashed line) at compositions of CO/H<sub>2</sub> = 1 (black) and CO/H<sub>2</sub> = 3 (red) in the gas phase

Based on the above, the proposed reaction mechanisms of syngas combustion on defective surface has been shown to remain valid based on the predicted order of the reactivities of the

studied species. The results from the DFT-based MF model show the same tendency with the experimental observations, which further demonstrates the accuracy of the proposed reaction kinetics. Note that the O migration reactions and the neighbouring effects are not considered in this DFT-based MF model, which may explain the differences observed between the predicted results and the experimental observations. In addition, the active NiO OC component was supported by Al<sub>2</sub>O<sub>3</sub> in the aforementioned experimental reports; experimental studies involving only NiO as OC that can be used to validate this study are not currently available in the literature.

### 5.3.7 Crystal orbital Hamilton population analysis

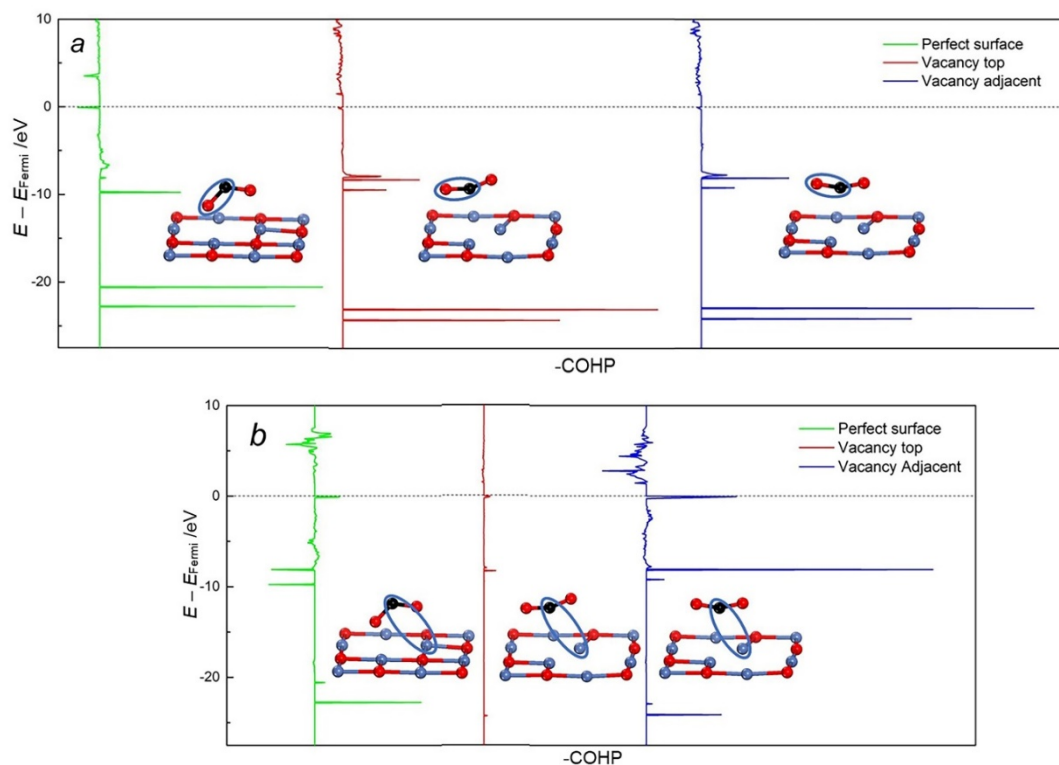


Figure 5-8 COHP analysis of (a) C-O interaction (enclosed in the blue circles) of TSCO (green), TSCO1 (red) and TSCO2 (blue) (b) C-Ni interaction (enclosed in the blue circles) of TSCO (green), TSCO1 (red) and TSCO2 (blue). Blue atom (Ni), red atom (O), black atom (C)

The established reaction mechanisms have shown that the neighbouring vacancy can effectively boost the syngas oxidation, which can be further explained based on the electron population distribution. A COHP analysis estimates the interactions between the reacted atoms and can further support the proposed vacancy effects on the oxidation process.

Figure 5-8 compares the interactions of the reacted C-O and C-Ni (enclosed in circles in the figure) of the TSs in the perfect surface configuration ( $TS_{CO1}$ ), the vacancy top configuration ( $TS_{CO2}$ ) and the vacancy-adjacent Ni top configuration ( $TS_{CO3}$ ). From the reactant to the product, the CO scavenged the nearby O on the surface and formed another C-O bonding to generate  $CO_2$ . As shown in Figure 5-8(a), the interaction of the reacted surface O and the C appears to be the weakest on the perfect surface. This conclusion comes from that the bonding orbitals in the defective configurations (vacancy top and vacancy-adjacent) are more occupied and shifting to the lower energy levels. Therefore, the electron population analysis shown in Figure 5-8(a) suggests that the O-C-O structures on the defective surface are more similar to the linear  $CO_2$ , which is likewise implied by the structural properties discussed in section 5.3.4. Once the CO seizes the surface O, the O-C-O structure distances from the surface to form a linear  $CO_2$  molecule and then it is re-adsorbed on the surface. The most populated bonding orbitals are observed on the Ni top with a neighbouring vacancy, as shown in Figure 5-8(b). The strongest adsorption is thus indicated in the vacancy-adjacent configuration. However, a moderate interaction of Ni-C is displayed on the vacancy top, whereas the antibonding orbitals are shifting to the energy levels lower than the Fermi level on the perfect surface (i.e. without vacancy). The occupied antibonding orbitals on the perfect surface suggests a weak adsorption. The most stable O-C-O structure adsorbed on the surface is observed in  $TS_{CO3}$ , which is also the closest structure to the product among the three studied configurations. Then the lowest state energy of TS is expected to be  $TS_{CO3}$ ; hence, this leads to the lowest energy barrier of CO oxidation. The COHP analysis shown in Figure 5-8 supports

the observations presented in sections 5.3.2 and 5.3.4, i.e. the neighbouring vacancy benefits the CO oxidation the most.

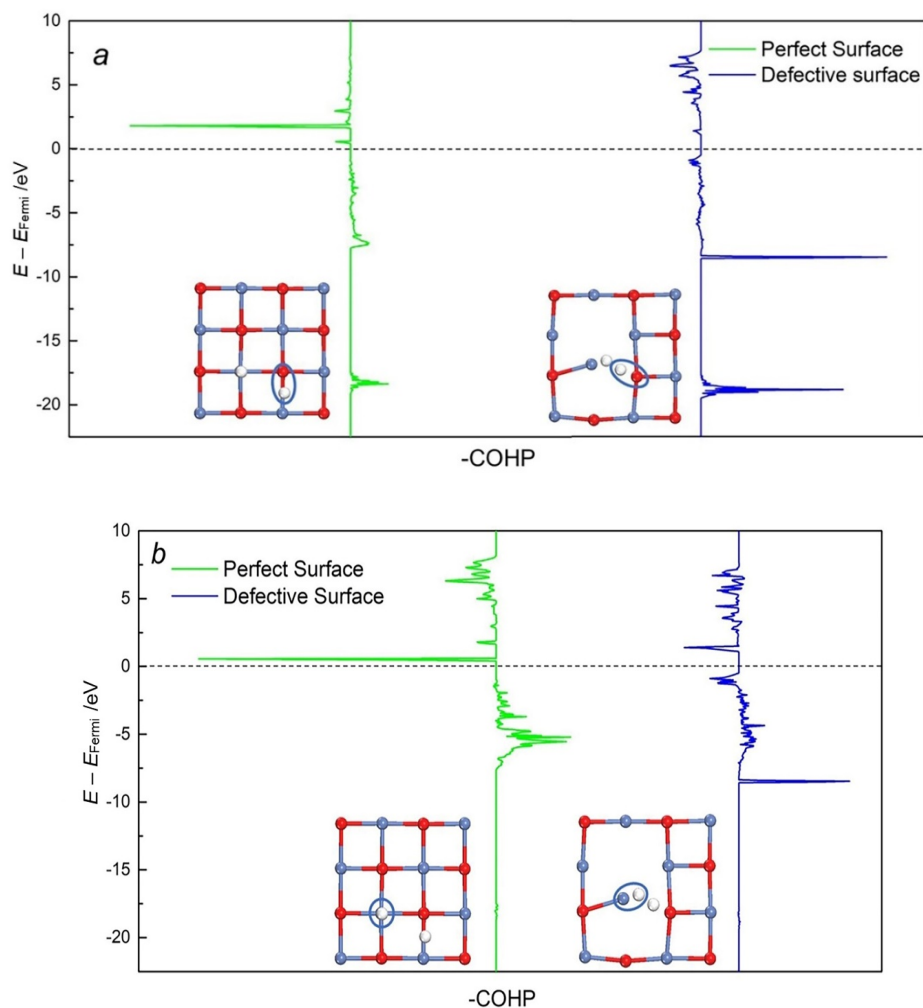
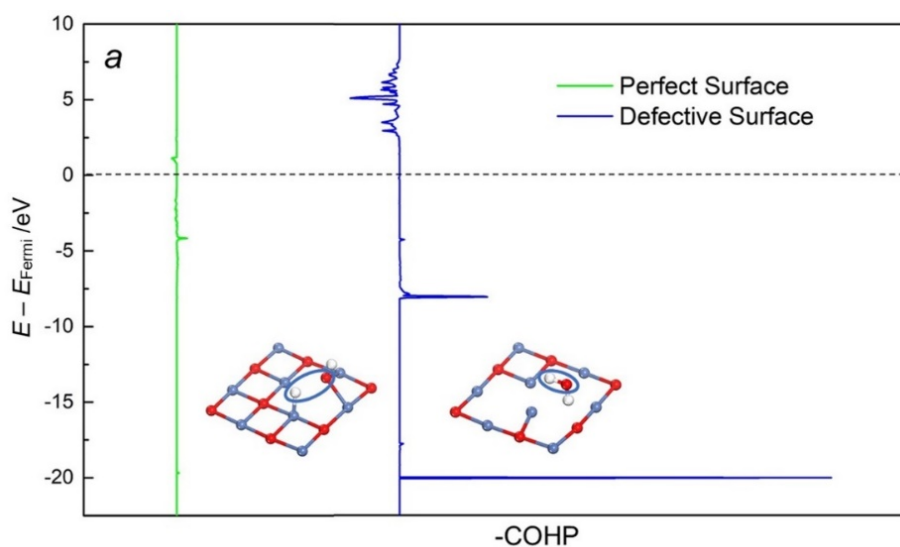


Figure 5-9 COHP analysis of (a) H-O interaction (enclosed in the blue circles) of TS2<sub>perfect</sub> (green) and TS1<sub>defective</sub> (blue) (b) Ni-H interaction (enclosed in the blue circles) of TS2<sub>perfect</sub> (green) and TS1<sub>defective</sub> (blue). Blue atom (Ni), red atom (O), white atom (H)

Figure 5-9 presents the COHP results for H<sub>2</sub> oxidation. This figure compares the interactions of the reacted O-H and Ni-H of the transition states (enclosed in circles in the figure) in the perfect surface configuration (TS2<sub>perfect</sub>) and defective surface configuration

(TS1<sub>defective</sub>) during the H<sub>2</sub> decomposition process. Note that this is not a direct comparison since these processes are not coming from the same step of reactions. However, at this step, the adjacent O-H and Ni-H structures are formed on both the perfect and defective surfaces. Based on Figure 5-9(a), a stronger bond between the reacted O and H is observed through the distinctly more occupied bonding orbitals on the defective surface compared to that on the perfect surface. However, the Ni-H interaction is shown to be more significant without the vacancy, as depicted in Figure 5-9(b). This suggests that the bonding orbital on the perfect surface is more populated while the antibonding orbital is moving to the energy level lower than the Fermi level under vacancy. The COHP analysis indicates the strong interaction of O-H and weak interaction of Ni-H in the presence of the vacancy. The H<sub>2</sub> decomposition on the defective surface proceeds through the surface two H approaching the O and distancing from the originally attached Ni. The transition state of H<sub>2</sub> decomposition on the defective surface (TS1<sub>defective</sub>) displays an adjacent two H structure close to the H<sub>2</sub> molecule as indicated above (see section 5.3.5). On the other hand, the H<sub>2</sub> decomposition without vacancy is accomplished by moving one H closer to O while the other H likely remains on the same position. The strong bonding between the Ni and H on the perfect surface can further support this observation.



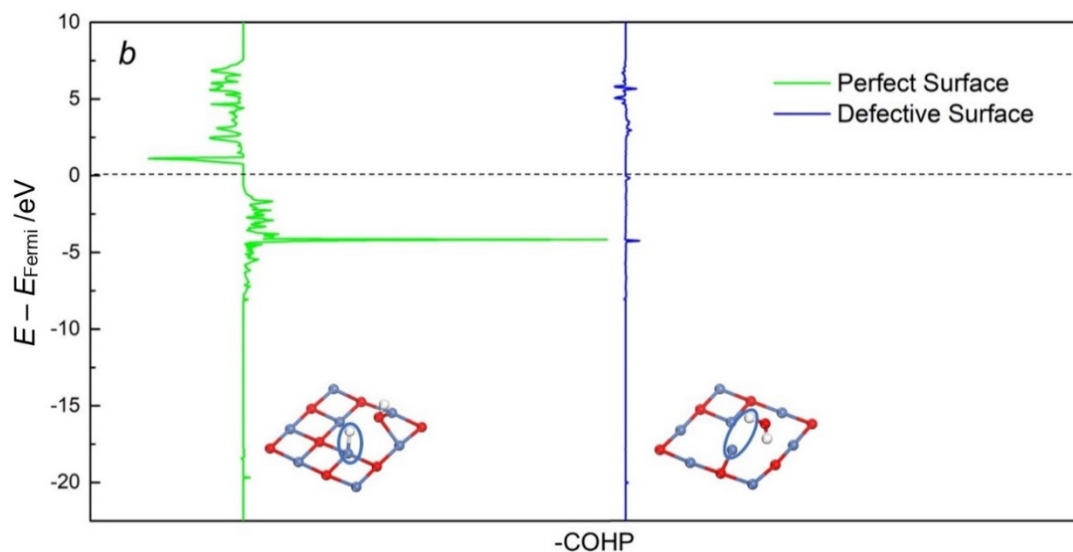


Figure 5-10 COHP analysis of (a) H-O interaction (enclosed in the blue circles) of  $\text{TS3}_{\text{perfect}}$  (green) and  $\text{TS2}_{\text{defective}}$  (blue) (b) Ni-H interaction (enclosed in the blue circles) of  $\text{TS3}_{\text{perfect}}$  (green) and  $\text{TS2}_{\text{defective}}$  (blue). Blue atom (Ni), red atom (O), white atom (H)

Following the  $\text{H}_2$  decomposition, the adjacent Ni-H and O-H react with each other to form an  $\text{H}_2\text{O}$  molecule through  $\text{TS3}_{\text{perfect}}$  and  $\text{TS2}_{\text{defective}}$  on a perfect surface and a defective surface, respectively. In this process, the H moves away from the Ni-H bonding and reacts with the O-H structure to form an  $\text{H}_2\text{O}$  molecule. With the existence of the neighbouring vacancy, the bonding orbitals between the studied O and H (enclosed in circles in the figure) are significantly more populated as presented in Figure 5-10(a). At the same time, there are no noticeable occupied bonding orbitals between the Ni and H (enclosed in circles in the figure) shown on the defective surface as depicted in Figure 5-10(b). These observations suggest that the transition state structure of  $\text{H}_2\text{O}$  formation with the neighbouring vacancy ( $\text{TS2}_{\text{defective}}$ ) is akin to the product configuration as discussed in section 5.3.5 in which the O-H structure is connected with the adjacent H and the Ni-H bonding breaks. Consequently, a lower energy barrier of  $\text{H}_2\text{O}$  formation is observed in the presence of the vacancy due to the high stability suggested by the aforementioned structural characteristics.

## 5.4 Summary

The outcomes presented in this Chapter revealed the intrinsic effects of vacancies on syngas adsorption and combustion on the OC NiO. The reaction mechanisms of the syngas combustion on a defective surface were disclosed. A throughout DFT analysis coupled with an electronic analysis showed that the vacancies act as the active sites for syngas adsorption and also tend to produce reactant configurations that are more active for both CO and H<sub>2</sub> oxidation. The vacancies significantly enhanced the syngas combustion, particularly for the H<sub>2</sub> decomposition reaction. Accordingly, the CO oxidation reaction was shown to be the controlling step of the syngas combustion process in the presence of relatively high vacancy coverages. The proposed kinetics were qualitatively verified through the validation of the DFT-based MF model via the experimental outcomes presented within the literature. Note that this verification is not a direct comparison due to scarce availability of experimental reports in this field and the assumptions considered for the proposed model. The experimentally reported order of the oxidation reactivities of the studied species (CO and H<sub>2</sub>) further proved the accuracy of the computational observations. In addition, the outward direction of the oxidation migration was assessed using the multi-scale model.

In addition to the vacancy effects, the neighbouring effects are another key aspect that impact the OC performance, as shown in Chapter 3. A multi-scale simulation will be discussed in Chapter 6 for a systematic understanding of the neighbouring effects on the studied system.



## **Chapter 6 Multi-scale modelling of Syngas Combustion on NiO Surface under Neighbouring Effects**

### **6.1 Introduction**

The results from Chapter 3 reported the considerable effects of neighbouring adsorbates on syngas adsorption in a CLC process on a NiO surface. In addition, the neighbouring atoms were proven to affect the redox activities in a wide range of heterogeneous systems, as discussed in Chapter 2. Consequently, the neighbouring effects are expected to be significant on syngas oxidation; however, this still remains as an open challenge in the literature.

In order to fill in the gap within this area of study, a DFT analysis of syngas combustion on NiO in consideration of the explicit neighbouring effects is proposed in this chapter. The reaction kinetics under neighboring effects were estimated using DFT and subsequently coupled with the adsorption principles obtained in Chapter 3 to develop a DFT-based kMC multi-scale model. This model takes the explicit neighbouring effects into consideration while analyzing the system behaviour. A key novelty in this research is that neighbouring effects caused by all the possible configurations at the nearest neighbouring sites were considered in a dynamic surface environment. That is, the change of the neighbour configuration caused by the syngas adsorption and combustion is explicitly considered for the execution of every event in the development of the DFT-based kMC model. To the author's knowledge, this is the first study that explicitly consider such phenomena for OC within the CLC process.

The rest of Chapter 6 is organized as follows. Section 6.2 presents the calculation details used in this part of study. Results from the multi-scale model developed in this work are shown in section 6.3. Section 6.4 provides a summary of this chapter.

## 6.2 Computational details

### 6.2.1 Density functional theory and the DFT-based reaction kinetics

The DFT calculation details and used NiO (100) slab model for the system are the same as explained in section 3.2.

The forward and backward activation energy  $E_{a,forward}$  and  $E_{a,backward}$  are calculated using the equations in section 4.2. To study the neighbouring effects on the reaction equilibrium, the reaction equilibrium constant  $K$  can be calculated based on the forward and backward reaction rates as follows:

$$E_{diff} = E_{forward} - E_{backward} \quad (6-1)$$

$$K = \frac{W_{forward}}{W_{backward}} = \frac{Q_{vib}^{prod}}{Q_{vib}^{react}} e^{E_{diff}/k_B T} \quad (6-2)$$

$$Q_{vib}^{prod} = \prod_n \frac{1}{1 - e^{-h\omega_i^{prod}/k_B T}} \quad (6-3)$$

where  $E_{forward}$  denotes the forward energy barrier whereas  $E_{backward}$  denotes the backward energy barrier;  $W_{forward}$  and  $W_{backward}$  are the forward and backward reaction rates, respectively;  $Q_{vib}^{prod}$  is the product vibrational partition function and  $Q_{vib}^{react}$  is the reactant vibrational partition function explained in Equations 6-3 and 4-7. Since the energy difference ( $E_{diff}$ ) between the forward energy barrier and the backward energy barrier results in a significant exponential change of the reaction equilibrium constant, this energy is compared with the increasing number of neighbours to investigate the neighbouring effects on reaction equilibrium.

To consider the neighbouring effects on the adsorption kinetics, the desorption rate parameters,  $k_{desorption}$ , are calculated as follows<sup>197</sup>:

$$k_{desorption} = \frac{k_B T}{h} \frac{Q_{vib}^{TS}}{Q_{vib}^{react}} \exp\left(-\frac{E_{desorption}}{k_B T}\right) \quad (6-4)$$

$$E_{desorption} = -\Delta E_{adsorption} \quad (6-5)$$

where  $E_{desorption}$  is the desorption energy; the vibrational partition functions  $Q_{vib}^{TS}$  of the transition state and the reactant is calculated using Equation 4-8. In equation 6-5,  $\Delta E_{adsorption}$  is the adsorption energy obtained by Equation 3-1.

Further insights into the neighbouring effects are provided through the electronic analysis. The COHP analysis was conducted and the related calculation details are explained in section 4.2.2.

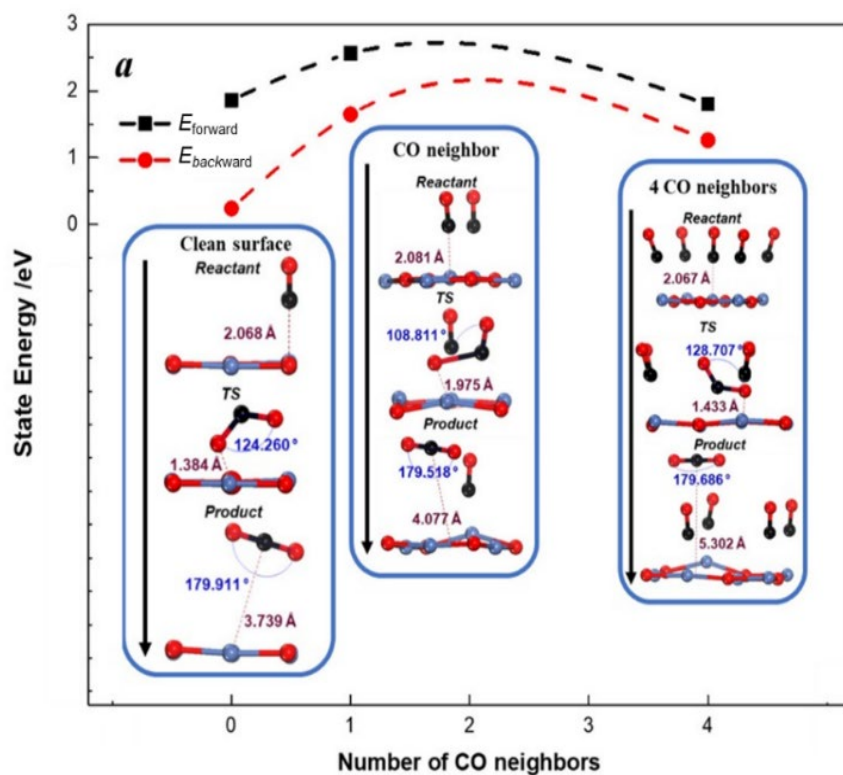
## 6.2.2 kinetic Monte Carlo

Based on the reaction kinetics established from the DFT analysis, the involved events in the system and their corresponding reaction kinetics are obtained. As explained in section 2.5.2, the kMC model proceeds the system evolution by performing the possible events based on the dynamic surface environment. Therefore, the neighbouring effects can be considered by employing different reaction parameters for the specific neighbour configurations in kMC, which cannot be involved in the proposed MF model explained in Chapter 4. The explicit neighbouring effects on the parameters will be described in section 6.3.7.1 and 6.3.7.2. Overall, the DFT-based kMC can fill in the information gap between the microscopic reaction kinetics from DFT analysis and the measurable experimental observations in consideration of the neighbouring effects. Furthermore, operating conditions (e.g. temperature and pressure) can be considered into the study of the neighbouring effects on the reaction kinetics by kMC model. The validation of the DFT-based kMC model by its comparison to the experimental results also demonstrates the accuracy of the DFT outcomes. The algorithm of the proposed kMC model is the same as the one explained in Chapter 2, section 2.5.2. The DFT-based kMC model was implemented in Python 3.7.0.

## 6.3 Results and discussion

### 6.3.1 Neighbouring effects: CO oxidation

Once the reaction mechanisms in the clean surface configuration were identified, the neighbouring effects on the syngas oxidation process were considered by displaying the structure-related energetic deviation caused by the neighbours. To simplify the analysis, one neighbour configuration and the fully occupied first neighbour configuration are considered here for each of the elementary reactions. In the case of CO oxidation, the four nearest neighbours are studied as the fully occupied nearest neighbour configuration while in the case of H<sub>2</sub> oxidation, the three nearest neighbours are considered to guarantee the empty sites of two adjacent Ni top for the H<sub>2</sub> decomposition. Our previous study of the neighbouring effects on adsorption has shown that the most significant change of the adsorption energy is introduced by the first loaded neighbour.<sup>166</sup> Therefore, it is expected that the most notable change on the surface will also occur with the first loaded neighbour. Nevertheless, the extreme nearest



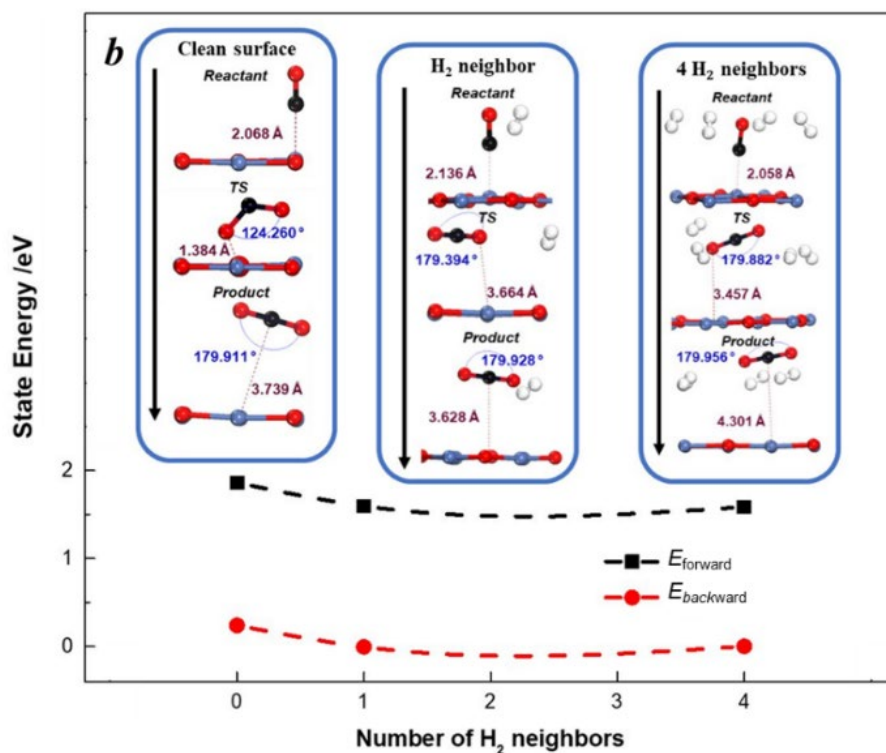


Figure 6-1 Activation energy of CO oxidation with (a) CO neighbours and (b) H<sub>2</sub> neighbours. Blue (Ni), red (O), black (C), white (H)

neighbour conditions are also studied here to provide a systematic analysis of increasing nearest neighbours.

Figure 6-1 presents a comparison of the activation energy in the CO oxidation process between configurations with one and four nearest neighbours as well as a clean surface. The corresponding structural properties of each configuration are also illustrated in that figure. As shown in Figure 6-1(a), the forward activation energy increases with the 1<sup>st</sup> loaded CO neighbour and decreases with fully occupied nearest neighbours to an energy level that is similar to that of the clean surface configuration. A similar behaviour is observed in the backward activation energy for this reaction. Only in the case of four CO neighbours, the backward activation energy is still much larger than that on the clean surface. Thus, the CO

neighbours generally weaken both the forward and backward reactions of CO oxidation. The forward activation energy is calculated based on the difference between the reactant and the TS for this reaction,  $TS_{CO}$ . During the transition process from the reactant to  $TS_{CO}$ , the physically-adsorbed CO molecule first scavenges the surface O and pulls the O molecule further from the surface. The smallest bond angle of O-C-O within the  $TS_{CO}$  exists with one CO neighbour as  $108.811^\circ$  in comparison with  $124.260^\circ$  with no neighbour and  $128.707^\circ$  with four CO neighbours. Thus, the highest activation energy observed in the configuration with one CO neighbour is more likely due to the largest difference between its  $TS_{CO}$  and the stable product, i.e. a linear  $CO_2$  molecule. Moreover, the increase in the activation energy with the load of a single CO neighbour also comes from the large energy consumed by pulling the surface O the farthest and the disconnect between the reacted O and the adjacent Ni atoms. On the other hand, the four CO neighbours lead to a larger angle of O-C-O and a larger pulling distance of the O in the TS compared to that on the clean surface. Based on the analysis of the forward activation in consideration of the CO neighbours, the neighbouring effects caused by the difference between the angle of O-C-O in  $TS_{CO}$  and the bond angle of  $CO_2$  is more prominent compared to that of the pulling distance. From the saddle point to the product, the reacted O is disconnected with the adjacent two Ni atoms on the surface. Then, the linear  $CO_2$  is produced and stays within a certain distance from the surface. In the product  $CO_2$ , the slight decrease of the O-C-O angle results from its interaction with the 1<sup>st</sup> loaded CO neighbour. The distance between  $CO_2$  and the surface also increases due to the single CO neighbour. With the fully occupied four CO neighbours,  $CO_2$  is repelled further away and the bond angle of  $CO_2$  rebounds slightly due to the larger distance between the  $CO_2$  product and the CO neighbours. The yielded  $CO_2$  with four CO neighbours keeps the longest distance with the surface due to the intense steric effect of the four CO neighbours. The change in the bond angle (O-C-O) from the  $TS_{CO}$  to the  $CO_2$  product for one CO neighbour was the largest observed followed by that obtained for the clean surface and with four CO neighbours. Due to the presence of a CO neighbour, the bond angles are affected thus causing a higher degree of transition from  $TS_{CO}$  to the product. Therefore, the backward activation energy increases with a larger degree of change in the bond angle. However, the changes in the distance between the product and the surface also affect the CO reaction on the clean and loaded NiO surface. The largest distance

between the produced CO<sub>2</sub> and the surface is observed in the four CO neighbour configuration, which indicates that, compared to that in the clean surface configuration, a larger backward activation energy is needed to push the produced CO<sub>2</sub> farther away from the surface. The CO neighbour configuration is dominated by the change in the bond angle while the four CO neighbour configuration is dominated by the change in the bond length.

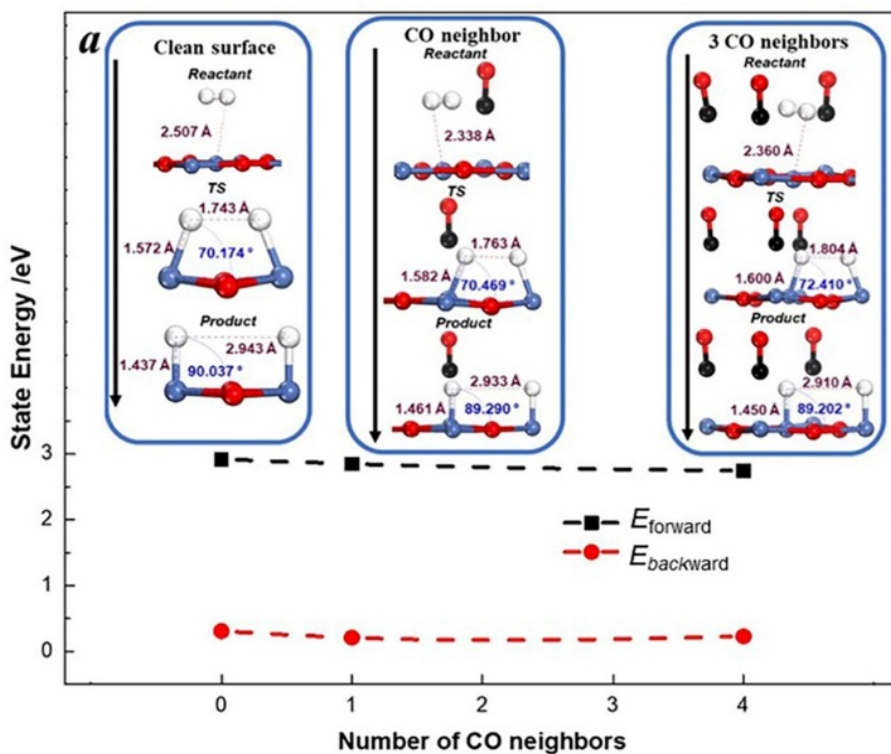
As depicted in Figure 6-1(b), both the forward and backward activation energies undergo a pronounced decrease with the 1<sup>st</sup> loaded H<sub>2</sub> and tend to remain almost unchanged as more H<sub>2</sub> is loaded on the surface. The decrease in the forward activation energy is mostly associated with the larger angle of O-C-O in the TS with H<sub>2</sub> neighbours. The smaller difference between the O-C-O structure and the linear CO<sub>2</sub> molecule indicates a more stable TS<sub>CO</sub> with a lower system energy. The larger distance between the surface reacted O and the surface should have led to an increase due to the loaded H<sub>2</sub> neighbours; however, this effect is neutralized by the aforementioned energetic change due to the changes in the angle. As described above, the difference between the angle of O-C-O in TS<sub>CO</sub> with the bond angle of CO<sub>2</sub> contributes more to the energetic change compared to the distance the surface reacted O is pulled away from the surface in TS<sub>CO</sub>. During the transition from TS<sub>CO</sub> to the product, the bond angle of O-C-O changes significantly on the clean surface (from approximately 124° to almost 180°) whereas this value remains almost unchanged in the presence of both a single H<sub>2</sub> neighbour and four H<sub>2</sub> neighbours, as shown in Figure 6-1. Furthermore, the degree of change in the distance between the reacted surface molecule and the surface from TS<sub>CO</sub> to the product decreases dramatically from almost double the distance on the clean surface to almost unchanged (with one single H<sub>2</sub> neighbour) as depicted in Table A3 in Appendix A. Hence, there is a significant decrease in the backward activation energy with the emergence of H<sub>2</sub> neighbours.

In summary, the distance that the reacted O is pulled away from the surface is expected to be larger in the presence of neighbours than that on the clean surface. Particularly, the first neighbour of both CO and H<sub>2</sub> leads to a larger distance between the reacted surface O and the NiO surface compared to the four neighbours. However, the produced CO<sub>2</sub> is repelled further away from the surface when there exist four nearest neighbours. H<sub>2</sub> neighbour also produces an increase in the bond angle of the TS<sub>CO</sub>. The H<sub>2</sub> neighbours result in a more significant structural change in TS<sub>CO</sub> (i.e. in terms of angles and distances) compared to that of the CO

neighbours. However, the activation energy is generally more affected by CO neighbours as shown in Appendix A (Table A12). The two studied species as the neighbours cause the same trend in the changes in the activation energy for both forward and backward reactions during CO oxidation, as depicted in Figure 6-1.

### 6.3.2 Neighbouring effects: H<sub>2</sub> decomposition

As shown in Figure 6-2, the H<sub>2</sub> oxidation process proceeds through three elementary steps. At the 1<sup>st</sup> step, H<sub>2</sub> decomposes into two H and locates at Ni tops. The neighbouring effects on the H<sub>2</sub> decomposition process are presented in Figure 6-2 for both CO and H<sub>2</sub> neighbours. As shown in Figure 6-2(a), the forward activation energy of H<sub>2</sub> decomposition drops with the existing of CO neighbours while the backward activation shows a similar tendency only with a slight rebound in the configuration with three CO neighbours. In the reactant, the CO neighbour decreases the distance between H<sub>2</sub> and the surface Ni while 3 CO





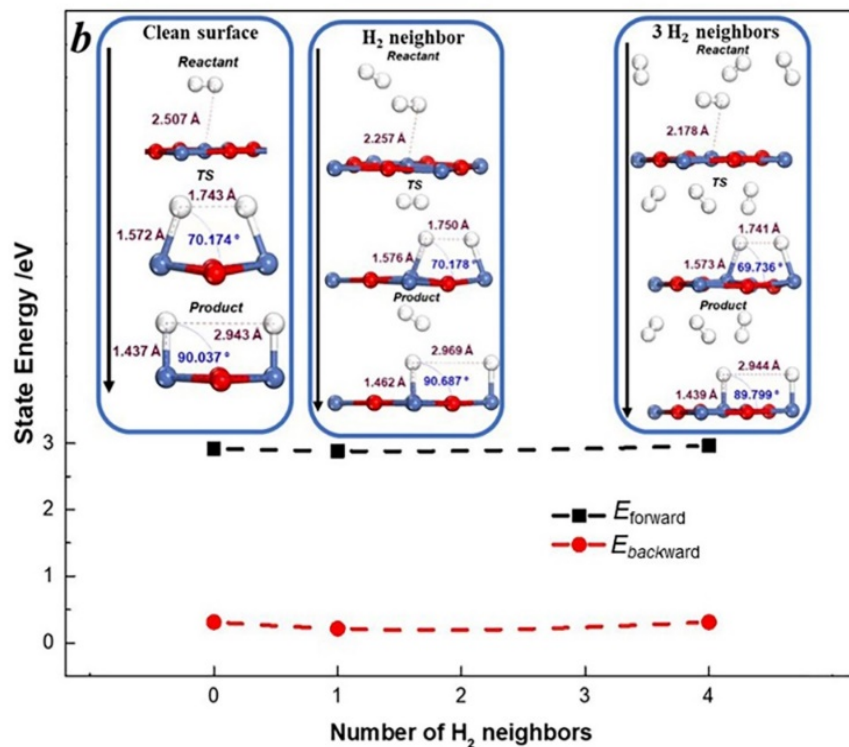


Figure 6-2 Activation energy of **Step 1** of H<sub>2</sub> oxidation with (a) CO neighbours and (b) H<sub>2</sub> neighbours. Blue (Ni), red (O), black (C), white (H)

neighbours push the centroid of H<sub>2</sub> away from the Ni top and slightly enlarges the distance. By inspecting the different TS<sub>H1</sub> displayed in Figure 6-2(a) for each configuration, the distance between the two dissociated H atoms increases with the loaded CO neighbours. This behaviour is also observed for the H-Ni-Ni angle. Regarding the structural changes caused by the CO neighbours, the structures of the TS are more similar to the products' configurations. This indicates more stable saddle point configurations; thus, there is a drop in the forward activation energy caused by the CO neighbours. The backward activation energy is determined by the transition process from the TS<sub>H1</sub> to the product. During this process, each of the single H atoms approaches the surface while distancing themselves from each other. As shown in Appendix A Table A4 and A5, the change in the angle of H-Ni-Ni and the distance of the H-H significantly decreases in the presence of CO neighbours. Consequently, the backward activation energy is reduced by the first CO neighbours as shown in Figure 6-2(a). Compared

to the configuration with a single CO neighbour, a slight rebound in the backward activation energy is observed in the configuration with three CO neighbours. This energy increase results from the most significant change in the Ni-H bond distance in the presence of 3 CO neighbours, as shown in Table A6 in Appendix A. Figure 6-2(a) shows that the H-H distance and the H-Ni bond length of the product are the longest with one CO neighbour. Accordingly, the H-Ni bond length in the product tends to negatively influence the backward activation energy.

Figure 6-2(b) exhibits the structure-related energetic change caused by the H<sub>2</sub> neighbours for the H<sub>2</sub> decomposition step. The forward activation energy experiences a decrease first followed by an increase to a higher energy level than that observed in the clean surface configuration. Moreover, the backward activation energy shows a similar tendency as the forward activation energy, except for the case of three H<sub>2</sub> neighbours where a similar energy level was observed to that of the clean surface. Similar to the case of CO neighbours, H<sub>2</sub> neighbours lead to a shorter distance between the H<sub>2</sub> and the surface Ni in the reactants shown in Figure 6-2(b). Akin to the single CO neighbour, the 1<sup>st</sup> loaded H<sub>2</sub> neighbour results in the increase in both the distance between the dissociated H atoms and the H-Ni-Ni angle in TS<sub>H1</sub> structure while the three H<sub>2</sub> neighbours lead to a decrease in both the angle and the distance in the TS<sub>H1</sub> structure. The aforementioned structure changes result in the reduction in the forward activation energy in the case of a single H<sub>2</sub> neighbour and the increase in the forward activation energy with the emergence of three H<sub>2</sub> neighbours, as displayed in Figure 6-2(b). Contrary to the products' configuration with CO neighbours, the 1<sup>st</sup> H<sub>2</sub> neighbour results in a longer distance between the two H compared to that on the clean surface. Nevertheless, the three H<sub>2</sub> neighbours result in a similar surface structure to that on the clean surface, which suggests a decrease in both the H-H distance and the angle of H-Ni-Ni from those observed with one H<sub>2</sub> neighbour. However, the same trend of stretching the Ni-H bond of the product due to the CO neighbours is also observed with the H<sub>2</sub> neighbours. In the single H<sub>2</sub> neighbour configuration, more significant changes in both H-H distance and H-Ni-Ni angle on the backward activation energy are balanced by the slight change in the Ni-H bond distance as shown in Appendix A (Table A4 to Table A6). Therefore, the 1<sup>st</sup> loaded H<sub>2</sub> neighbour results in lower backward activation energy compared to that of the clean surface. On the other hand, an almost negligible change in the backward activation energy within the 3 H<sub>2</sub> neighbour configuration from that

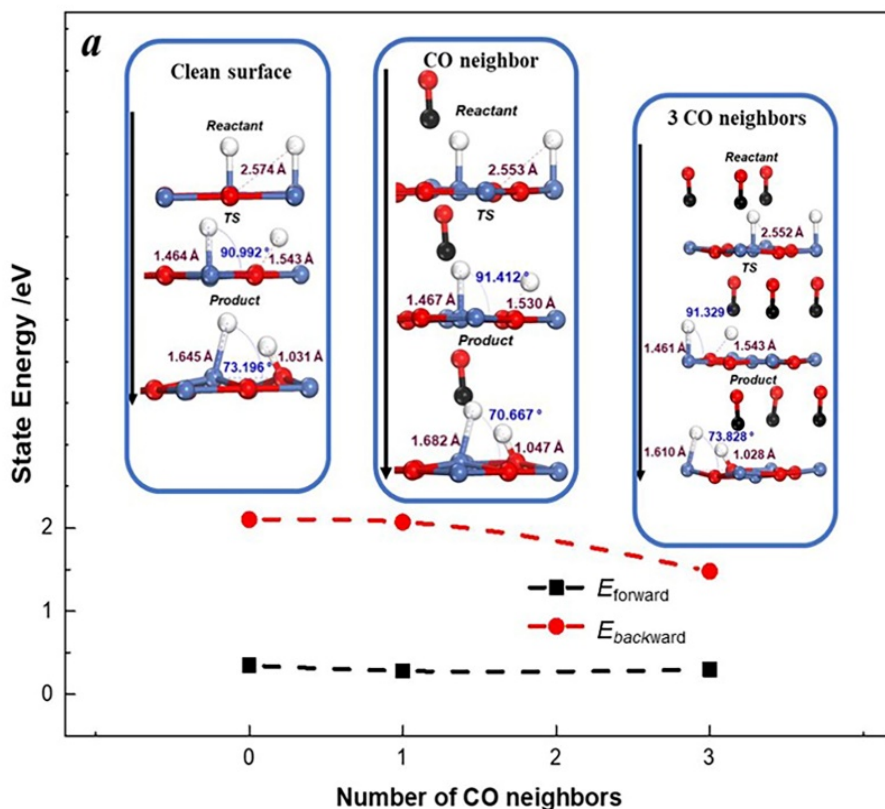
on the clean surface is dominated by a similar degree of change in the Ni-H bond distance, as shown in Appendix A (Table A6). Thus, the backward activation energy is mostly affected by the narrowing of the Ni-H bond distance.

Compared to the CO reaction, the energy change due to the neighbouring effects for the 1<sup>st</sup> H<sub>2</sub> oxidation reaction step is much less significant. Moreover, the changes in forward and backward activation energies generally follow the same behaviour, except for an inverse change in the forward activation energy from that in the backward activation energy in the three CO neighbour configuration, as depicted in Figure 6-2(a). In particular, the change in the backward activation energy is generally more considerable than that in the forward activation energy at this step except for the case of three H<sub>2</sub> neighbours. In terms of structural changes, the 1<sup>st</sup> loaded CO neighbour as well as the single H<sub>2</sub> neighbour generates a similar TS<sub>H1</sub> structure to the product. Accordingly, the lower forward activation energy is observed within the single neighbour configuration. However, the backward activation energy is dominated by the degree of change in the Ni-H bond distance from TS<sub>H1</sub> to the product. In addition, the Ni-H bond distances in both the TS<sub>H1</sub> and the product are enlarged by the CO and H<sub>2</sub> neighbouring effects. Furthermore, the products containing CO neighbours tend to present shorter distances between the dissociative H atoms whereas larger distances were observed for the case of H<sub>2</sub> neighbours.

### 6.3.3 Neighbouring effects: H migration

Figure 6-3 shows an analysis of the neighbouring effects on H migration. At this step, the migration of H from Ni top to O top results in a change in distance between H and O. In addition, the Ni-H and O-H interaction lead to the tilting of the Ni-H and O-H bonds towards each other. As depicted in Figure 6-3 (a), the 1<sup>st</sup> loaded CO neighbour results in a drop in both the forward and backward activation energies while three CO neighbours induce a rebound in

the forward activation energy but a further decrease in the backward activation energy. The change in the forward activation energy caused by the CO neighbours is related to a reduction in the bond distance of O-H from the reactant to  $TS_{H_2}$ , as shown in Figure 6-3(a). As indicated in Appendix A (Table A7), the single CO neighbour leads to an almost negligible increase in the degree of change in the aforementioned O-H bond distance. The three CO neighbours, on the other hand, generate a slight decrease in the distance. Since a larger change in the distance is expected to consume more energy, an increase (decrease) in the forward activation energy should be expected in the single-CO-configuration (three CO neighbour configuration). However, the lowest forward activation energy is observed in the presence of a single CO neighbour. This indicates that the length of the O-H bond in  $TS_{H_2}$  should also be considered in



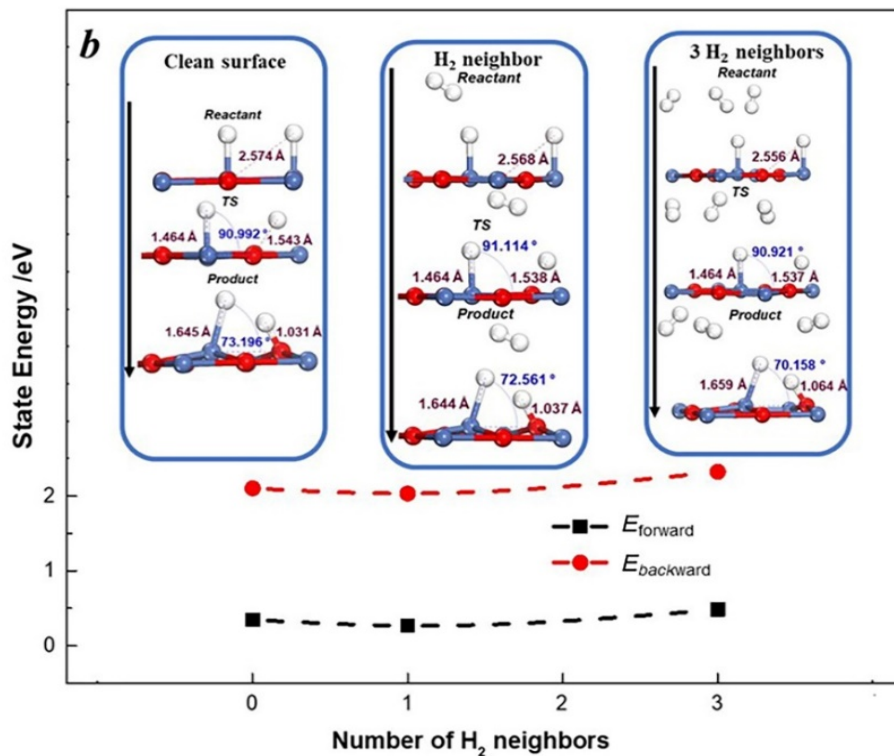


Figure 6-3 Activation energy of *Step 2* of H<sub>2</sub> oxidation with (a) CO neighbours and (b) H<sub>2</sub> neighbours. Blue (Ni), red (O), black (C), white (H)

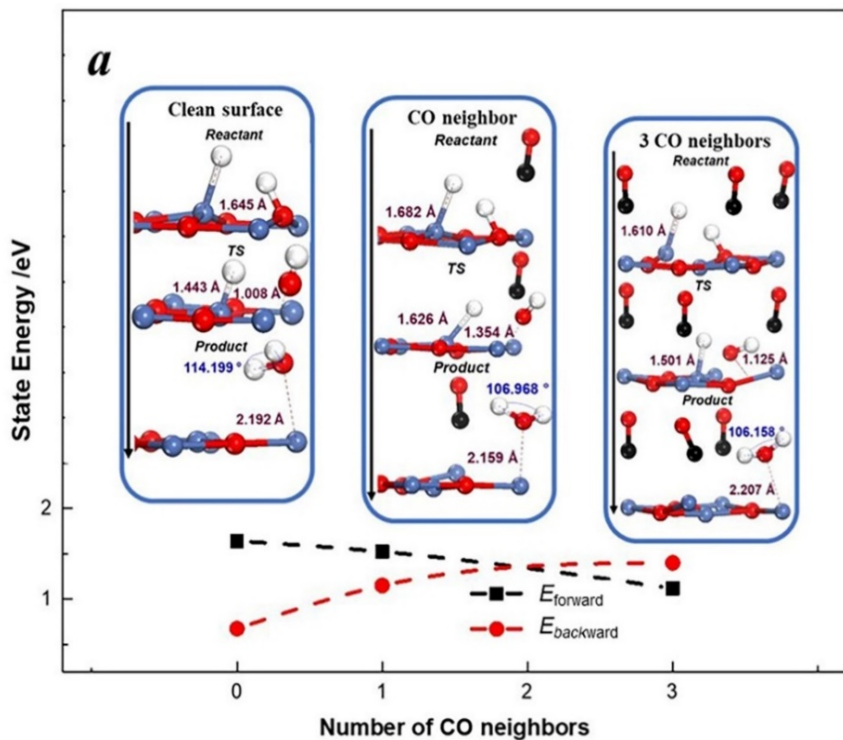
this case. The shortest O-H bond is an indication of similar structures between TS<sub>H<sub>2</sub></sub> and a stable product at a low energy level. Therefore, the lowest forward activation energy in the single CO neighbour configuration comes from the most stable TS<sub>H<sub>2</sub></sub> shown in Figure 6-3(a). To interpret the CO neighbouring effects on the backward activation energy, the decrease in the bond distance of O-H from TS<sub>H<sub>2</sub></sub> to the product are compared using the three configurations considered in this study. The least significant change is observed in the presence of a single CO neighbour; on the other hand, the changes observed in the case of three CO neighbours are similar to that of a clean surface, as presented in Appendix A (Table A7). Accordingly, the backward activation energy is reduced by the 1<sup>st</sup> loaded CO. However, a further drop is observed in the backward activation energy in the three CO neighbour configuration instead of a similar energy level to that on the clean surface, which is supported by the change in the

bond length. This may be due to the interactions between the Ni-H and O-H in the transition states and the products. As a result of those interactions, the least visible decrease in both Ni-H bond and H-Ni-Ni angle from  $TS_{H_2}$  to the product appears in the configuration with three CO neighbours, which presents a reduction in the backward activation energy. The  $H_2$  neighbour effects produce similar tendencies of change in the forward and backward activation energies, as displayed in Figure 6-3(b). The 1<sup>st</sup> loaded  $H_2$  neighbour shortens the distance between O and H in  $TS_{H_2}$ , which leads to a more stable structure compared to that on the clean surface, and reduces the forward activation energy. On the other hand, the H-Ni-O angle in  $TS_{H_2}$  of the three  $H_2$  neighbour configuration is the smallest among the three  $TS_{H_2}$  shown in Figure 6-3(b). This change in the structural property of this configuration should be considered a contributor to the increase in the forward activation energy. The backward activation energy is reduced in the case of a single  $H_2$  neighbour. This is because a less significant change in the O-H bond distance was observed in one  $H_2$  neighbour configuration compared to that on the clean surface from  $TS_{H_2}$  to the product. In case of the three  $H_2$  neighbour configuration, the interaction effects of Ni-H and O-H should be considered. The most significant changes in both the Ni-H bond and H-Ni-O angle are observed with the three  $H_2$  neighbour configuration, which explains the highest backward activation energy.

The forward and backward activation energy show similar tendencies for the configuration with either CO or  $H_2$  neighbours at the H migration step, except for the backward activation energy drop promoted by the three CO neighbours. The activation energy is generally reduced by the neighbouring effects. Except for the three  $H_2$  neighbour configuration, the activation energy increases in the presence of neighbours compared to that on the clean surface.

### 6.3.4 Neighbouring effects: H<sub>2</sub>O formation

At the final step of H<sub>2</sub> oxidation, the surface O disconnects with the adjacent Ni. As shown in Figure 6-4, the Ni-H bond is shortened to be in close proximity to the OH structure such that H<sub>2</sub>O is formed within a distance from the surface. Figure 6-4(a) presents the decrease of the forward activation energy and the increase of the backward activation energy with the increasing number of the loaded CO neighbours. In Figure 6-4(a), the distance that the reacted O in the TS<sub>H3</sub> is pulled from the surface increases by the single CO neighbour from 1.008 Å to 1.354 Å. Then this distance drops from 1.354 Å in the single CO neighbour configuration to 1.125 Å in the three CO neighbour configuration. The large displacement observed for the reacted O in the single CO neighbour configuration generates a higher forward activation energy than that predicted for the three CO neighbour configuration. On the other hand, the clean surface configuration produces the highest forward activation energy; this is mostly due to the



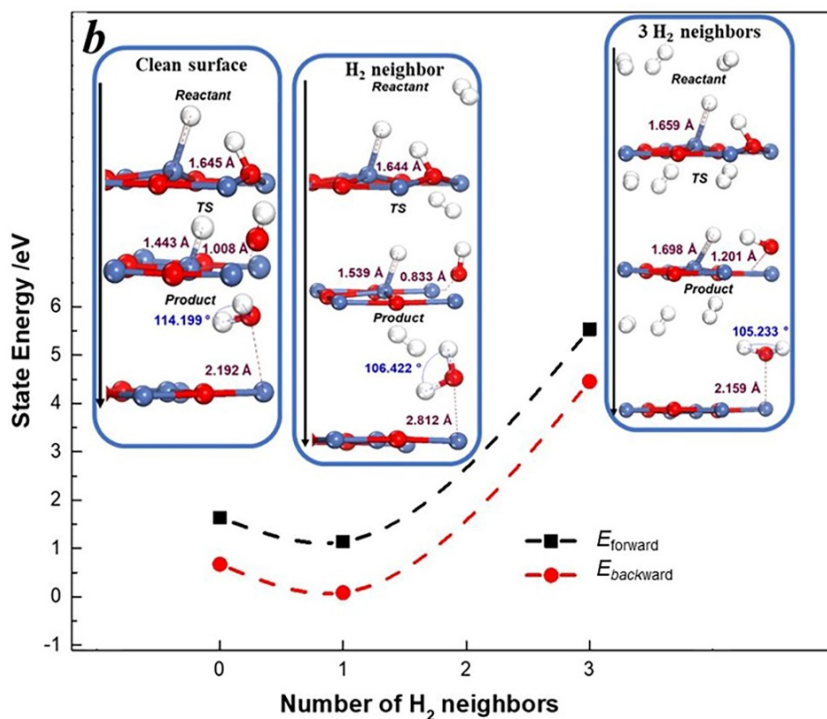


Figure 6-4 Activation energy of **Step 3** of H<sub>2</sub> oxidation with (a) CO neighbours and (b) H<sub>2</sub> neighbours. Blue (Ni), red (O), black (C), white (H)

most significant reduction on the distance of the Ni-H bond from the reactant to TS<sub>H3</sub>, as indicated listed in Appendix A (Table A11). Furthermore, the backward activation energy is dominated by the configurations of the product. With the increasing number of CO neighbours, the H-O-H angle in the product narrows down from 114.199° on the clean surface to 106.158° in the three CO neighbour configuration and gradually approaches the stable H<sub>2</sub>O molecule structure, which has a simulated bond angle of 104.405°. Therefore, the product shown in Figure 6-4(a) tends to be more stable with more CO neighbours, which results in a higher backward activation energy. Figure 6-4(b) displays the same tendency of a slight decrease in the forward and backward activation energies followed by a considerable increase in both energies. In the presence of a single H<sub>2</sub> neighbour, the O is pulled away from the surface to the shortest distance while three H<sub>2</sub> neighbours lead to the largest O-surface distance. Accordingly,



the forward activation energy shown in Figure 6-4(b) drops first and then experiences a considerable increase. As for the backward activation energy, the lowering of the O-H-O bond angle with the increasing number of H<sub>2</sub> neighbours should have brought a continuous drop in the backward activation energy. Nonetheless, the lowest backward activation energy is shown with 1<sup>st</sup> H<sub>2</sub> neighbour, which may be due to the longest distance between the produced H<sub>2</sub>O and the surface.

The neighbouring effects help to stabilize the H<sub>2</sub>O product; contrary to the other elementary reactions, the change in the forward activation energy shows an inverse tendency to that of the backward activation energy in the presence of CO neighbours. In terms of the configurations with H<sub>2</sub> neighbours, the forward and backward activation energy keep the same tendency of change again. It should be noted that the activation energy in the configuration containing 3 H<sub>2</sub> neighbours is up to 5 eV, which means that the reaction is almost improbable to happen under this configuration. In addition, the energy change caused by the neighbouring effects at the 3<sup>rd</sup> step of H<sub>2</sub> oxidation is more significant in comparison to the first and second steps of H<sub>2</sub> oxidation. Furthermore, the backward activation energy is more sensitive to the neighbouring effects at the H<sub>2</sub>O formation step.

### 6.3.5 Neighbouring effects on reaction equilibrium

The previous section has shown that the neighbouring effects have notable energetic and structural effects on the NiO system and that they significantly deviate from the behaviour observed for a clean surface. As explained in section 6.2, the energy difference ( $E_{\text{diff}}$ ) between the forward activation energy and the backward activation energy is further studied in this section to investigate the reaction equilibrium shift resulting from the presence of CO and H<sub>2</sub> neighbours.

Figure 6-5(a) illustrates the declining trend of  $E_{\text{diff}}$  of CO oxidation with loaded CO and H<sub>2</sub> neighbours. These results indicate that there is a shift in the forward reaction equilibrium due to the neighbouring effects. In fact, the CO neighbour promotes the mentioned forward shift more notably than the H<sub>2</sub> neighbour. For completeness, two intermediate values in energy difference involving two and three nearest neighbours were estimated using a customized

exponential fitting function for both the CO and H<sub>2</sub> neighbours. As shown in Figure 6-5(a), the predicted values follow the expected behaviour.

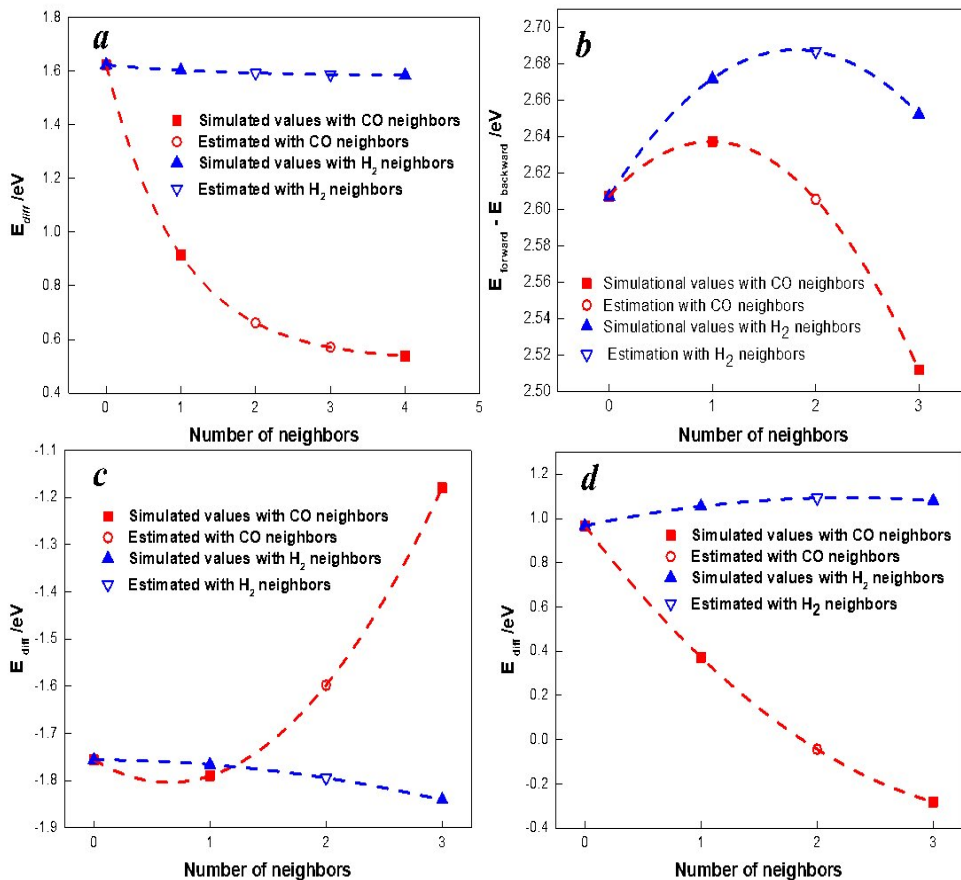


Figure 6-5 Reaction equilibrium shift of (a) CO oxidation, (b) step 1 of H<sub>2</sub> oxidation, (c) step 2 of H<sub>2</sub> oxidation and (d) step 3 of H<sub>2</sub> oxidation with CO and H<sub>2</sub> neighbours

From Figure 6-5(b), the reaction equilibrium shift of the H<sub>2</sub> decomposition reaction is insignificant compared to the CO oxidation reaction: the  $E_{diff}$  of CO oxidation in the presence of four CO neighbours is lower than half of that on the clean surface while the most significant change in  $E_{diff}$  of H<sub>2</sub> decomposition goes from 2.61 eV on the clean surface to 2.51 eV in the three CO neighbour configuration, as depicted in the Appendix A (Table A12). The predicted

$E_{\text{diff}}$  for this reaction increases with the loaded 1<sup>st</sup> neighbour and falls due to the addition of two CO or H<sub>2</sub> neighbours. This reveals the backward shift in the reaction equilibrium generated by the single neighbour. However, a forward shift is observed in the presence of the three CO neighbours while a backward shift is observed in the three H<sub>2</sub> neighbour configuration. As mentioned above, the 1<sup>st</sup> H<sub>2</sub> neighbour results in a more significant change than that caused by the 1<sup>st</sup> CO neighbour. The CO neighbours otherwise produce a more considerable fluctuation of the  $E_{\text{diff}}$ . As shown in Figure 6-5(b), a second order polynomial fitting function provides an adequate energetic prediction for the expected two nearest neighbour configurations.

Figure 6-5(c) describes the reaction equilibrium shifts of the H migration step in the presence of CO and H<sub>2</sub> neighbours. The 1<sup>st</sup> CO neighbour leads to a moderate shift in the forward direction of the reaction and then a dramatic backward shift is observed by three CO neighbours owing to the apparent decrease of the backward activation. As for H<sub>2</sub> neighbours, a minor decrease is predicted, which indicates a slight forward shift due to the loading of the H<sub>2</sub> neighbours. The intermediate values are provided in Figure 6-5(c) involving two neighbours.

As shown in Figure 6-5(d), CO neighbours promote a forward shift of the H<sub>2</sub>O formation. This is because the forward activation energy of this step is reduced by the CO neighbours while the backward activation energy is increased to almost double the value observed for the clean surface. On the other hand, the H<sub>2</sub> neighbours only cause a modest increase in  $E_{\text{diff}}$ . Based on the analysis of  $E_{\text{diff}}$  at this step, the reaction shifts backward by the loading of H<sub>2</sub> neighbours and shifts forward considerably due to the CO neighbours. As shown in the Appendix A (Table A12), CO neighbours resulted in a change in  $E_{\text{diff}}$  from 0.97 eV to -0.28 eV, which is considered the strongest neighbouring effect observed during the H<sub>2</sub> oxidation. Intermediate values are provided in Figure 6-5(d) involving two neighbours.

Based on the analysis of  $E_{\text{diff}}$  for each of the different reactions the neighbouring effects can decrease the  $E_{\text{diff}}$  of CO oxidation by up to 67%, whereas the  $E_{\text{diff}}$  of H<sub>2</sub> decomposition will only increase by 2%. This demonstrates that in general, the presence of neighbours will enhance the overall syngas oxidation kinetics.

### 6.3.6 Coupling electronic analysis of neighbouring effects

Followed by the insights on the reaction mechanism of the syngas combustion on the clean surface, the neighbouring effects on the reactions are explained here in terms of the atomic interactions caused by the electron population. The 1<sup>st</sup> neighbour leads to the most distinguished change of the activation energy of CO oxidation. Therefore, the single CO and H<sub>2</sub> neighbour configurations are investigated for the CO oxidation in this section. Moreover, the three CO and three H<sub>2</sub> neighbour configurations are considered for the H<sub>2</sub> oxidation process due to the maximum deviation of the activation energy from the clean surface. The H<sub>2</sub> decomposition is analyzed as the controlling step of H<sub>2</sub> oxidization.

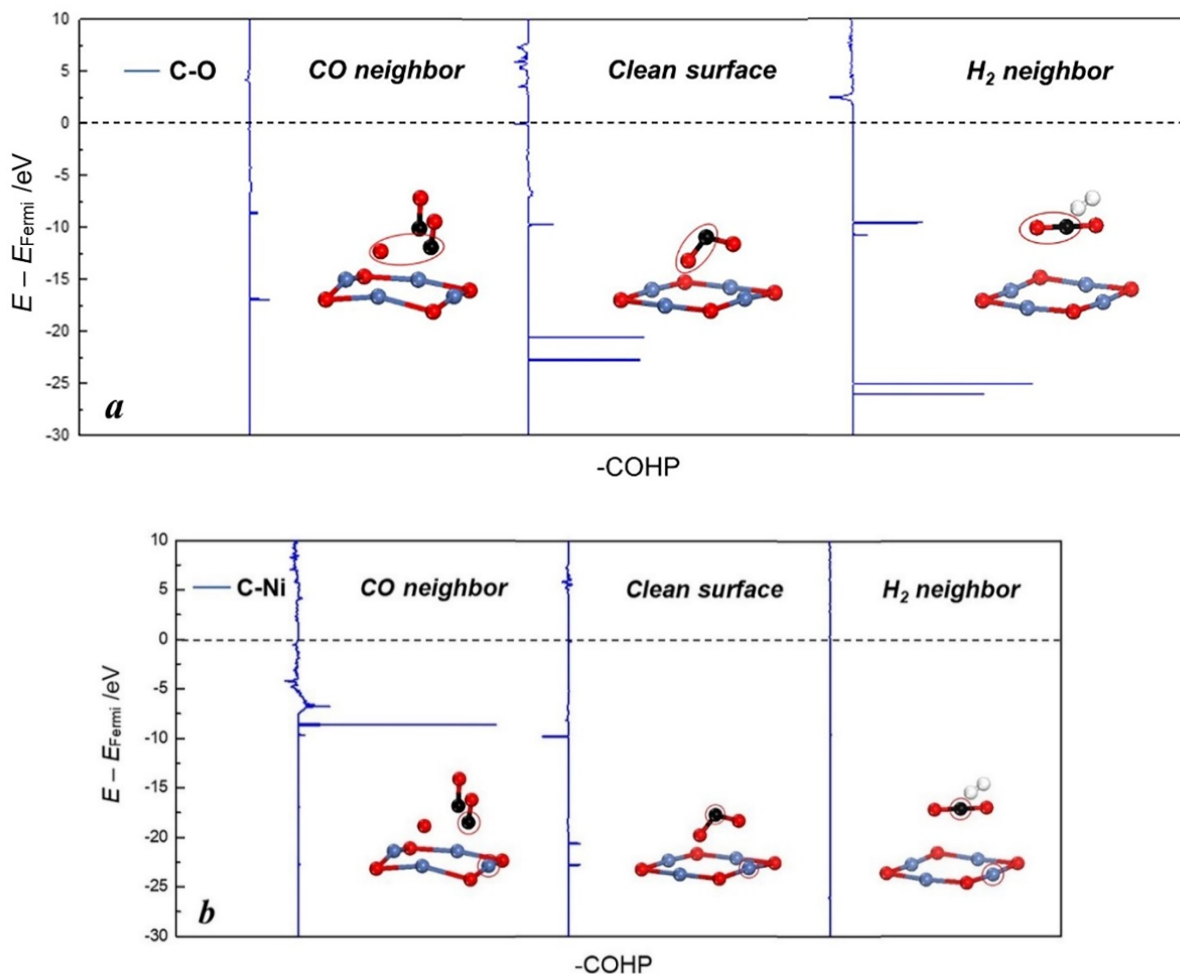
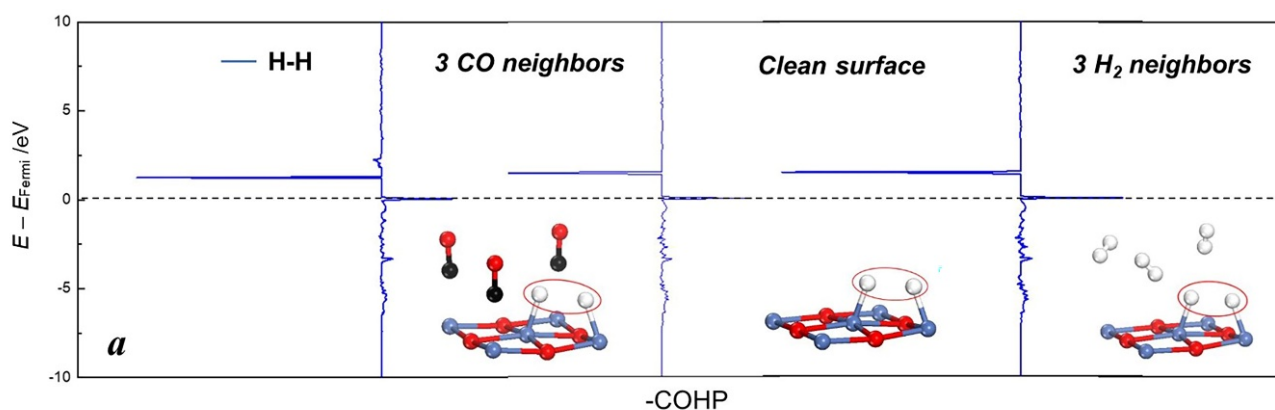


Figure 6-6 Electronic analysis of neighbouring effects on CO oxidation (a) C-O interaction of TS<sub>CO</sub> (b) C-Ni interaction of TS<sub>CO</sub>

Figure 6-6 compares the interactions of the selected C-O pair and C-Ni pair in  $\text{TS}_{\text{CO}}$  between the clean surface and the neighbour configurations (single neighbour configurations). The C in CO seized the surface O to form  $\text{CO}_2$ , which leads to the bonding between C and the surface O. The bonding orbitals are more occupied and undergo a slight shift to the lower energy level with the effect of  $\text{H}_2$  neighbour, as shown in Figure 6-6(a). However, the CO neighbour results in the negligible occupied orbitals. The displacement of the electron population stated above indicates that the interaction between the studied C and O in  $\text{TS}_{\text{CO}}$  is weakened by the CO neighbour but strengthened by the  $\text{H}_2$  neighbour. Therefore, contrary to the single CO neighbour, a more significant hybridization of the orbitals in the selected C-O pair is observed in the presence of the single  $\text{H}_2$  neighbour. This suggests that a more stable  $\text{TS}_{\text{CO}}$  can be predicted with the  $\text{H}_2$  neighbour effect and the single CO neighbour may produce a  $\text{TS}_{\text{CO}}$  configuration with a higher energy. This observation supports our DFT calculation results since both the forward activation energy and backward activation energy are reduced by the single  $\text{H}_2$  neighbour and increased by the single CO neighbour, respectively, as shown in Figure 6-1. The C in the reacted CO first leaves the surface Ni to catch the adjacent O. As depicted in Figure 6-6(b), the interaction between the C and surface Ni in  $\text{TS}_{\text{CO}}$  is facilitated by the CO neighbour and weakened in the  $\text{H}_2$  neighbour configuration. This indicates that, for a single CO neighbour, a higher degree of transition is needed from  $\text{TS}_{\text{CO}}$  to the product, which is in agreement with our DFT calculations. That is, the more significant change in the bond angle of O-C-O in the single CO neighbour configuration reveals a higher degree of transition



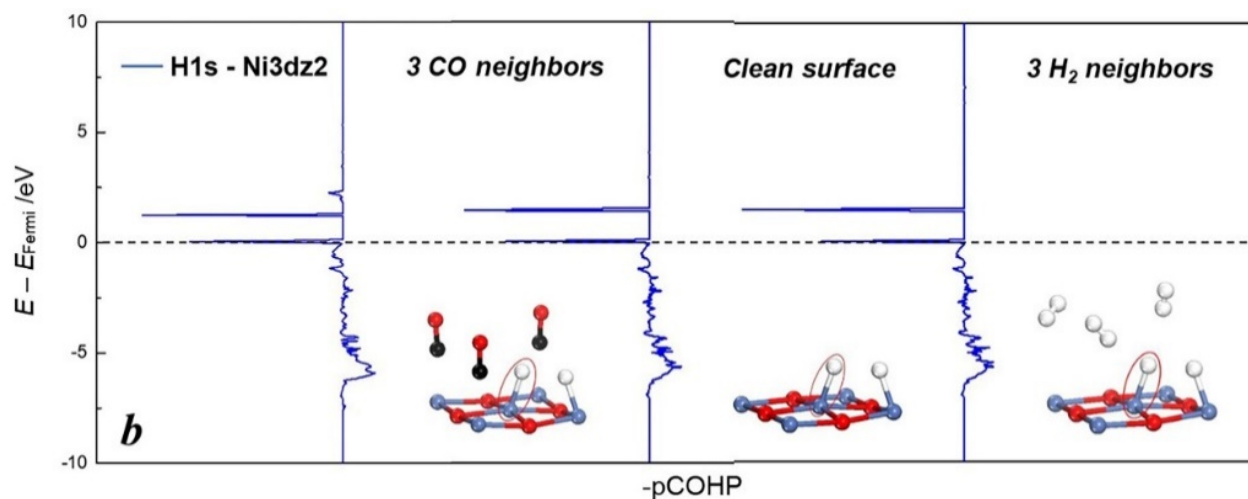


Figure 6-7 Electronic analysis of neighbouring effects on H<sub>2</sub> decomposition (a) H-H interaction of TS<sub>H1</sub> (b) H1s-Ni3dz2 interaction of TS<sub>H1</sub>

from TS<sub>CO</sub> to the product, thus increasing the backward activation energy. The opposite effect is observed for the case of a single H<sub>2</sub> neighbour.

To improve the H<sub>2</sub> oxidation process, the rate-controlling step (i.e. H<sub>2</sub> decomposition) should be taken into account. Figure 6-7 gives an insight into the break of the H-H bond and the formation of the Ni-H bond affected by the neighbouring effects (three CO and H<sub>2</sub> neighbour configurations). The H-H interaction is expected to be weakened by the three CO neighbours due to the reduced peak at the populated bonding orbital displayed in Figure 6-7(a). The three H<sub>2</sub> neighbours on the other hand strengthen the H-H interaction with a more occupied bonding orbital. The changes in the electron population analysis indicate that a more similar TS<sub>H1</sub> to the product in the presence of three CO neighbours is expected compared to that on the clean surface; nevertheless, the opposite effect is observed for the case of three H<sub>2</sub> neighbours, as shown in Figure 6-2. These observations are in agreement with the DFT results presented in section 6.3.2, i.e. a more similar structure between TS<sub>H1</sub> and the product in the presence of three CO neighbours than that observed for the case of a clean surface was detected; hence, the former configuration presents a lower system energy compared to that of a clean surface. On the other hand, the three H<sub>2</sub> neighbours produced an opposite effect. Figure 6-7(b) shows the interaction between the dissociative H and the surface Ni. As shown in this

figure, a slightly more occupied bonding orbital is presented with three CO neighbours while an almost negligible change in the occupancy of the orbitals is observed in three H<sub>2</sub> neighbour configuration. The stronger bonding interaction caused by the CO neighbours also indicates the higher degree of transition in the process from reactant to product<sup>1</sup>. Then, a more stable TS<sub>CO</sub> caused by CO neighbours can also be expected due to this phenomenon, which explains the lower activation energy with three CO neighbours and the moderate increase of the activation energy with 3 H<sub>2</sub> neighbours, as shown in Figure 6-2. Note that the changes shown in Figure 6-7 are less significant than those shown in Figure 6-6. This suggests that more significant changes are expected in the activation energy of the CO oxidation reaction than that of H<sub>2</sub> decomposition. The same conclusion is reached based on the structure-related energetic analysis presented in the previous sections.

### 6.3.7 DFT-based kMC multiscale model

The kMC model presented in this section has been developed using the results from the DFT analysis presented in the previous section while taking into consideration neighbouring effects. The kMC events are considered based on the proposed elementary reactions presented in section 4.3. The elementary reactions considered, and the corresponding activation energies are listed in Table 6-1.

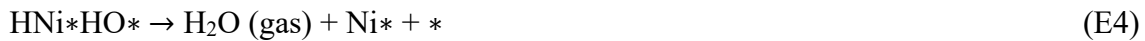
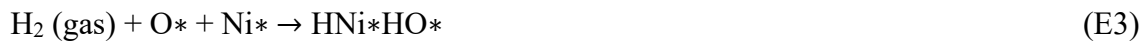
Table 6-1 Clean surface elementary reactions and their activation energies

	Reaction	$E_a$ / eV
$\text{CO}^* + \text{O}^* \rightarrow \text{CO}_2(\text{gas}) + 2^*$	CO oxidation	1.86
$\text{H}_2\text{Ni}^* + \text{Ni}^* \rightarrow 2\text{HNi}^*$	H <sub>2</sub> decomposition	2.92
$\text{HNi}^* + \text{O}^* \rightarrow \text{Ni}^* + \text{HO}^*$	H migration	0.35
$\text{HNi}^*\text{HO}^* \rightarrow \text{H}_2\text{O}(\text{gas}) + \text{Ni}^* + ^*$	H <sub>2</sub> O formation	1.64

As shown in the table, the activation energy of H migration from the Ni top to the adjacent O top is 88% smaller than the activation energy from the previous step of H<sub>2</sub> decomposition, which means the H migration process is much faster than the H<sub>2</sub> decomposition. This energetic

difference suggests that the H migration proceeds immediately after the H<sub>2</sub> decomposition. Therefore, the H<sub>2</sub> decomposition and H migration are combined as a single reaction, H<sub>2</sub> dissociation (R4 in Table 4-1). The integration of the H<sub>2</sub> decomposition and H migration is considered sufficiently accurate. due to validation of the model presented in Chapter 4 that also adopted this assumption. Moreover, the current kMC model assumes that the bulk oxygen immediately replaces the surface oxygen vacancy once the oxygen is consumed by the reaction. Therefore, there is sufficient oxygen supply from OC in the system. This oxygen migration process is supported by the analysis of bulk oxygen transfer presented in Chapter 5.

As shown in Table 4-1, the H<sub>2</sub> dissociation is much faster than its previous event of the H<sub>2</sub> adsorption and is also the fastest among all the considered events: the reaction parameter of H<sub>2</sub> dissociation (R4) is the largest and three orders of magnitude larger than that of the H<sub>2</sub> adsorption (R3). Therefore, this model also assumes that the H<sub>2</sub> dissociation happens directly after the H<sub>2</sub> adsorption. This implies the H<sub>2</sub> adsorption and H<sub>2</sub> dissociation can be combined into one H<sub>2</sub> chemisorption step, E4 as shown below. The H<sub>2</sub> chemisorption model has been proven to be valid for the system prediction involving the H<sub>2</sub> dissociation on the surface by previous reports.<sup>206-207</sup> Overall, the events considered for this kMC model are listed as follows:



These reactions are expected to occur in the NiO surface under different neighbor configurations. Hence, this work will explicitly estimate the reaction kinetics for each of these events under the more likely adjacent configurations that are expected to occur on the NiO surface. The developed kMC model is simulated using the scheme described in section 2.5.2 and illustrated in Figure 2-3.

### 6.3.7.1. Neighbouring model for adsorption



Table 6-2 CO adsorption energy analysis

CO neighbour number	Adsorption energy /eV	Adsorption rate ratio	H <sub>2</sub> neighbour number	Adsorption energy /eV	Adsorption rate ratio
0	-1.56	100.00%	0	-1.56	100.00%
1	-0.28	27.81%	1	-0.32	28.88%
2	-0.25	27.00%	2	-0.31	28.75%
3	-0.15	24.49%	3	-0.30	28.28%
4	0.06	19.75%	4	-0.27	27.58%

In order to relate the adsorption rates with the adsorption energies affected by the neighbouring molecules species, this work relates the adsorption rate with the inverse of the diffusion rate constants,  $k_{\text{desorption}}$ , in Equation 6-4, because the adsorption can be seen as the inverse process of the desorption.<sup>197</sup> Therefore, the adsorption rates affected by the neighboring effects can be predicted by the inverse of the diffusion rate interpreted from the adsorption energy. The adsorption rate ratio is obtained by comparing the inverse of  $k_{\text{desorption}}$  in the system containing the neighbour occupied surface and the clean surface, as listed in Table 6-2 and Table 6-3 for CO and H<sub>2</sub> adsorption, respectively. The adsorption energies of syngas on NiO surface used in this study were presented in Chapter 3. Compared to the decrease in the adsorption rate ratio caused by the first loaded neighbour from 100% to 27.81% (decrease by 72.19%), more neighbours only result in a moderate change in the adsorption rate ratio (decrease by less than 8%). In order to consider the neighbouring effects on the CO adsorption rate, modifiers of the adsorption rate that refine the neighbouring effects are obtained from the average of the adsorption rate ratio in the presence of first nearest neighbours. This indicates that the same species of neighbours lead to similar changes in the adsorption rate despite the number of the nearest neighbours. With CO neighbour, the CO adsorption rate modifier is 0.264, whereas for the H<sub>2</sub> neighbour the CO adsorption rate modifier changes into 0.284. However, the CO adsorption becomes an exothermic process with four CO neighbours; this is a strong indication that this process is highly unlikely to occur.

Hence, the rate modifier of CO adsorption with four CO neighbours was set to zero to imply the aforementioned phenomena.

Table 6-3 H<sub>2</sub> adsorption energy analysis

CO neighbour number	Adsorption energy / eV	Adsorption rate ratio	H <sub>2</sub> neighbour number	Adsorption energy / eV	Adsorption rate ratio
0	-1.29	100.00%	0	-1.29	100.00%
1	-0.08	29.65%	1	-0.10	30.42%
2	-0.09	29.89%	2	-0.05	28.72%
3	-0.06	29.15%	3	-0.04	28.54%
4	-4.70×10 <sup>-3</sup>	27.58%	4	-0.03	28.42%

Table 6-3 provides the H<sub>2</sub> adsorption energy and the H<sub>2</sub> adsorption rate ratio, considering the four nearest neighbours as CO or H<sub>2</sub>. The H<sub>2</sub> adsorption stability is significantly weakened by the 1<sup>st</sup> loaded neighbour and keeps the same trend as CO adsorption. The H<sub>2</sub> adsorption rate modifier with both CO and H<sub>2</sub> neighbours was set to 0.29 since similar changes in the H<sub>2</sub> adsorption rate ratio were observed by the CO and H<sub>2</sub> neighbours.

### 6.3.7.2. Neighbour model for oxidation

The explicit neighbouring effects on syngas oxidation are obtained from DFT analysis and has been presented in sections 6.3.1-6.3.4. All the DFT obtained reaction parameters were calculated using Equation 4-6. All the reaction parameters considered for the kMC model are labeled in Figure 6-8 including three categories of neighbour configurations for each of the reaction: in presence of only CO neighbours (red circles), in presence of only H<sub>2</sub> neighbours (blue triangles) and in presence of hybrid neighbours (green squares) containing both CO and H<sub>2</sub> neighbours at the same time. Among them, the reaction parameters calculated from DFT are: CO reaction with one and four nearest neighbours as CO or H<sub>2</sub>, and H<sub>2</sub> oxidation (three steps as shown in Figure 4-2) with one and three nearest neighbours as CO or H<sub>2</sub>. All the

specific configurations analyzed by DFT calculations were explained in detail in sections 6.3.1 to section 6.3.4. To simplify the analysis, neighbour configurations not analyzed by DFT calculations were predicted by the regression of the aforementioned DFT obtained reaction parameters. The regression of the single neighbor configurations was conducted using 1<sup>st</sup> order polynomial fitting, whereas the regression of the hybrid neighbor configurations was obtained using a weighted fitting wherein weighted modifiers were assigned to different species. Overall, 14 neighbour configurations are considered for each of the elementary reactions, R2,

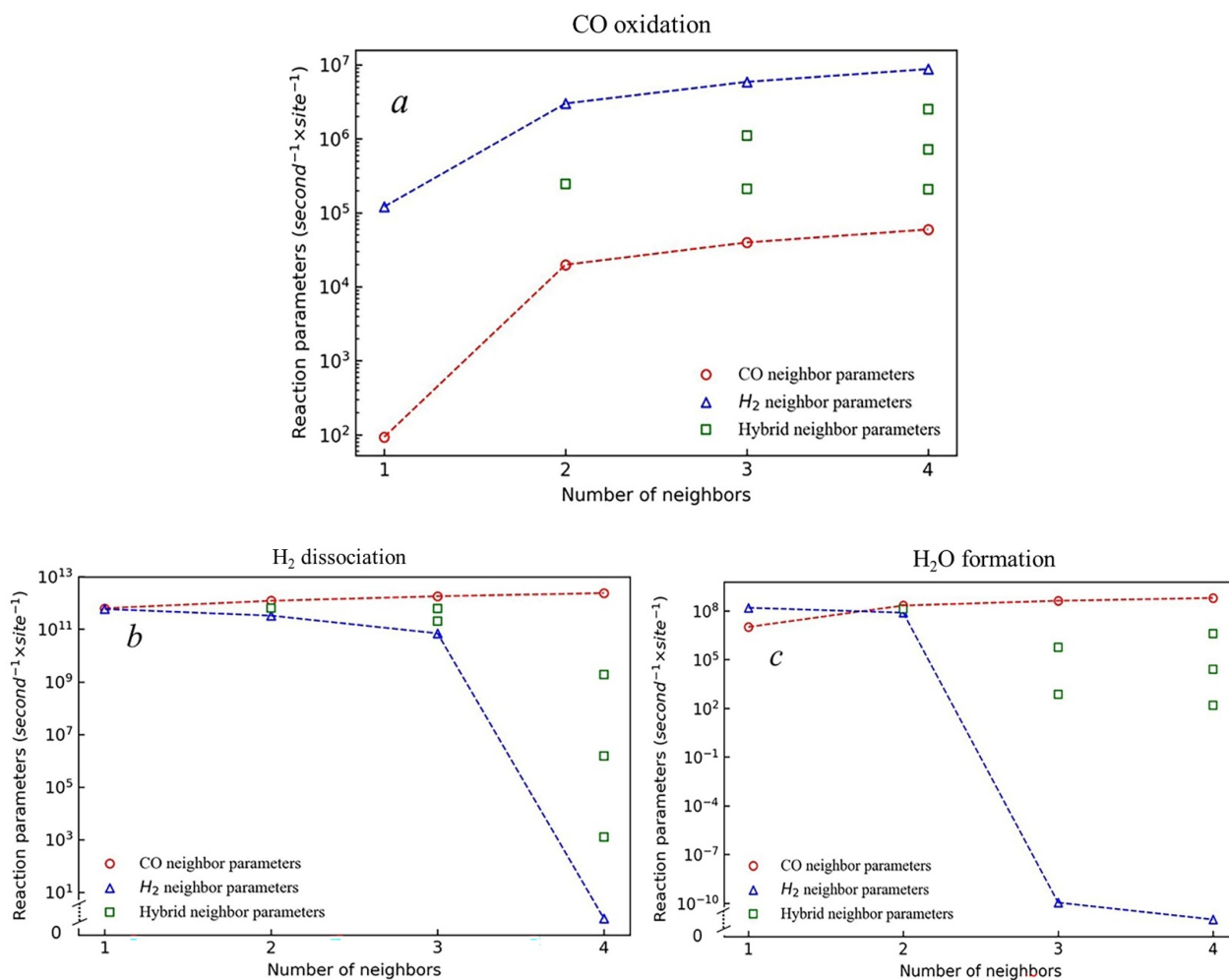


Figure 6-8 Reaction parameters for (a) CO reactions, (b) H<sub>2</sub> dissociation and (c) H<sub>2</sub>O formation in consideration of single species neighbours as CO (red circle) or H<sub>2</sub> (blue triangle) and hybrid neighbours (green cube)

R4 and R5 presented in Table 4-1. The complete set of reaction kinetic parameters used in this study is listed in Appendix A (from Table A13 to Table A15).

As shown in Figure 6-8(a), the loaded neighbours generally enhance the CO oxidation process, as implied by the increase in the reaction parameters caused by the neighbours. Only one CO neighbour configuration leads to a slight decrease in the reaction parameter compared to the CO oxidation on the clean surface ( $4.47 \times 10^4 \text{ s}^{-1}$ ). Note that the kMC model assumes that the H<sub>2</sub> decomposition (described in sections 6.3.2) and H migration (described in section 6.3.3) are merged into H<sub>2</sub> dissociation, R4 in Figure 6-8(b) as explained at the beginning of the section 6.3.7. Therefore, the neighbouring effects of both of these two reactions are considered in Figure 6-8(b), which is shown to benefit the H<sub>2</sub> dissociation process. Note that three H<sub>2</sub> neighbours significantly suppress the H<sub>2</sub> dissociation; this is caused by the boost in the forward activation energies of both H<sub>2</sub> decomposition and H migration reactions described in sections 6.3.2 and 6.3.3. Therefore, the predicted reaction parameter of the H<sub>2</sub> dissociation reaction in the presence of four nearest H<sub>2</sub> is  $0 \text{ s}^{-1}$ , which implies that four nearest H<sub>2</sub> neighbours avoid the H<sub>2</sub> dissociation to happen. Regarding H<sub>2</sub>O formation, the neighbours tend to benefit the reactions; however, three H<sub>2</sub> neighbours result in a considerable drop in the reaction parameters, as shown in Figure 6-8(c); this suggests that the predicted H<sub>2</sub>O formation with four H<sub>2</sub> neighbours is not likely to happen. This prediction comes from the significant increase in the activation energy of H<sub>2</sub>O formation reaction shown in Figure 6-4.

Overall, first nearest neighbours tend to benefit the syngas oxidation process. However, the fully occupied H<sub>2</sub> neighbour configuration tends to reduce the H<sub>2</sub> oxidation process. The explicit predictions for all the neighbouring effects follow the changes in the activation energies. The reaction parameters estimated in the presence of the different nearest neighbour configurations were used to establish a kMC model for this system. The validation of the kMC model predictions by experimental observations can, therefore, verify the accuracy of the DFT predictions.

### 6.3.7.3. Lattice size effects

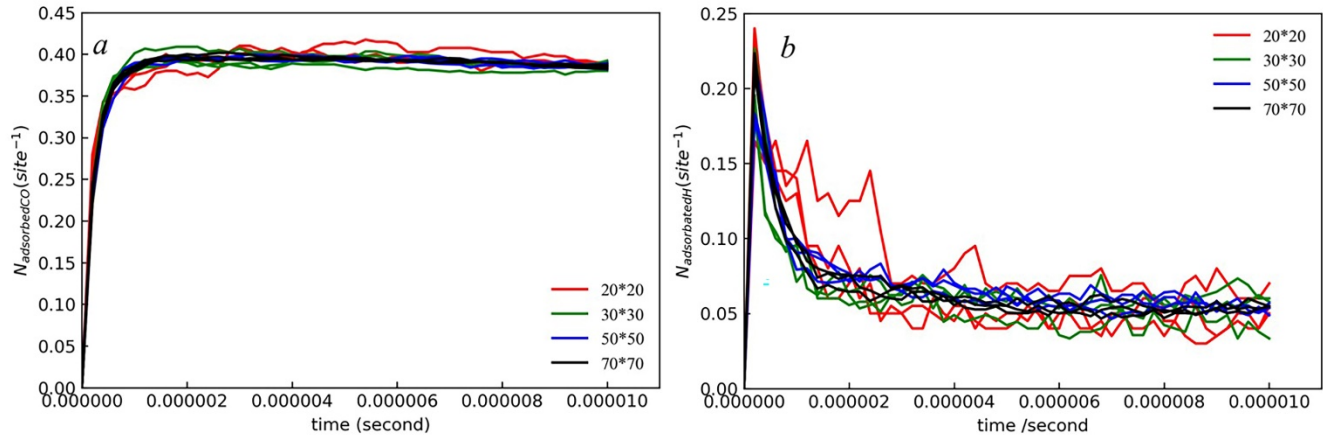


Figure 6-9 Comparisons of the surface coverages of (a) CO and (b) H on 20×20, 30×30, 50×50 and 70×70 lattice, respectively.

After establishing the kMC model with an explicit consideration of the neighbouring effects, the lattice size for the developed kMC model is investigated for efficient and accurate predictions of the system. Small lattice sizes result in short computational times but inaccurate results whereas large lattices return accurate results at the expense of high computational costs. Figure 6-9 compares the coverages of CO and H predicted by the developed kMC model using four lattice sizes, i.e. 20×20, 30×30, 50×50 and 70×70 (lattice spacing = 2.087 Å). Since the proposed kMC model assumes that the H<sub>2</sub> physical adsorption and H<sub>2</sub> decomposition can be merged into a single H<sub>2</sub> chemisorption process, the gas H<sub>2</sub> will be directly chemisorbed on the surface as H explained at the beginning of the section 6.3.7. Therefore, the output of the kMC model discussed in Figure 6-9(b) is the coverage of H. The reaction parameters listed in Table 4-1 show that the parameter of CO adsorption is larger than that of the CO oxidation, which explains increase in the CO coverage within a short time followed by smooth convergence to a steady-state, as displayed in Figure 6-9(a). However, the reaction parameter of H<sub>2</sub> chemisorption is similar to the H<sub>2</sub>O formation, and the parameter of the H<sub>2</sub>O formation reaction gradually becomes larger due to the neighbouring effects, as described in section 6.3.7.2.

Therefore, the coverage of H decreases to reach the steady-state as displayed in Figure 6-9(b). Figure 6-9 shows that all the tested lattice sizes produce similar averaged coverages for both CO and H. However, the three responses from 20×20 lattice are noisier compared to the predictions from other lattice sizes. The predictions using the 30×30 lattice contain less variability compared to the 20×20 lattice. The larger lattice sizes provide more steady predictions at the cost of longer computational times. For the same reaction time in the kMC model, the computational time using 30×30 lattice is 29 s while the computational time using 50×50 lattice is 132 s and the computational time using 70×70 lattice is 401 s. Moving from a 30x30 surface to a 50×50 shows no significant improvement in reducing the noise as displayed in Figure 6-9. Likewise, the computational time from a 50×50 lattice increases the CPU costs more than four times to those observed for a 30×30 lattice. Therefore, for the prediction of the system properties, an average of the predictions from three independent kMC simulations on a 30×30 lattice is adopted in the following section to capture the behaviour of the surface evolution. Furthermore, the steady-state coverages of the species on the surface are reached within a short time because the current kMC model does not consider the channel diffusion process and also assumes sufficient oxygen on the surface, as discussed at the beginning of the section 6.3.7, which is supported by the oxygen migration analysis presented in Chapter 5.

#### **6.3.7.4. Multiscale model verification**

As shown in Figure 6-10, the validation of the proposed kMC model is conducted based on the experimental observations. The validation under different syngas compositions was performed by comparing the oxygen consumed predicted from the kMC model and the solid conversion ratio reported in previous experimental studies. The oxygen consumed per site,  $N_{O,con}$ , is proportional to the solid conversion ratio,  $X_{O,con}$ , shown as Equation 4-14.

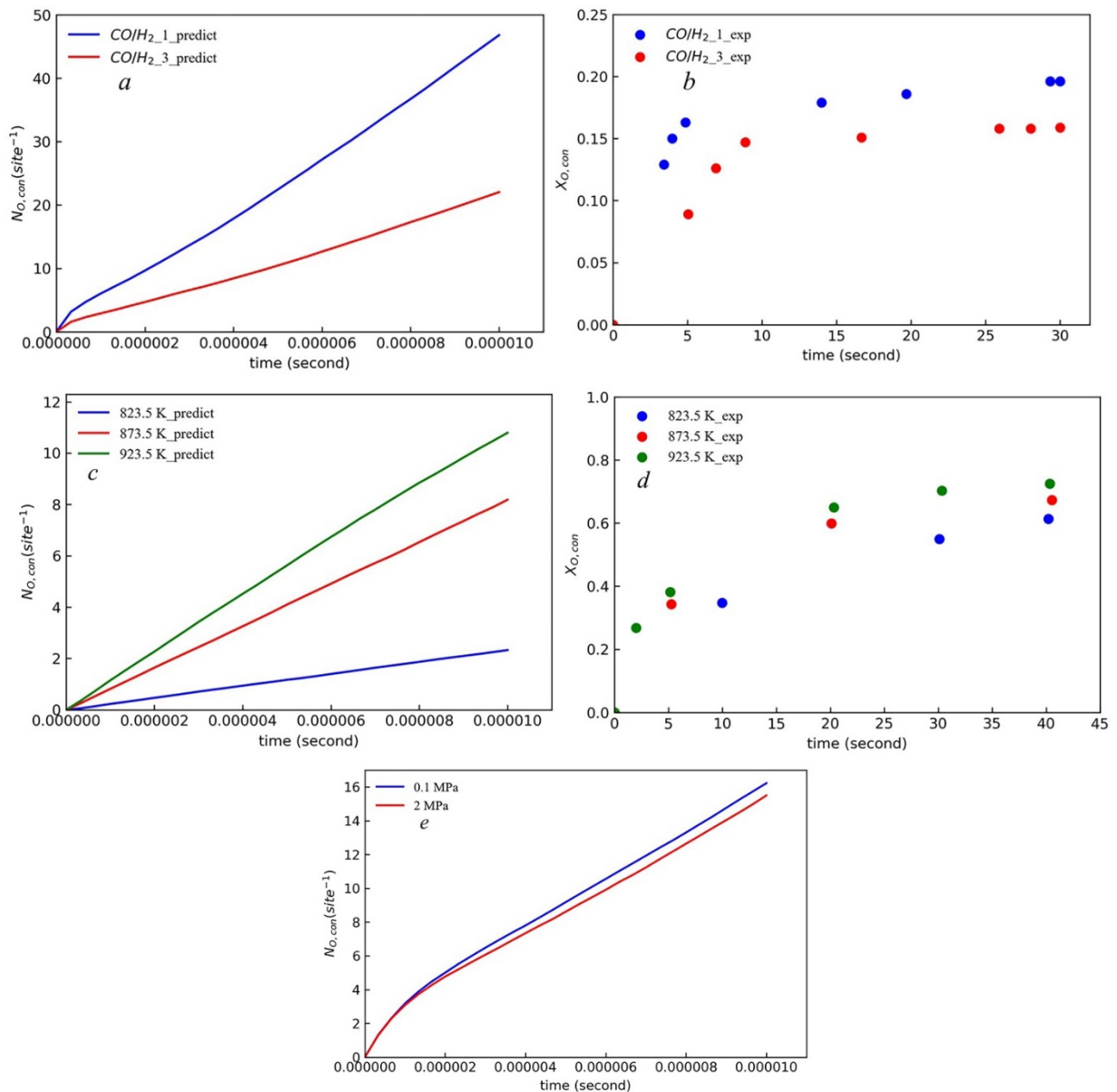


Figure 6-10 Comparison between (a) the oxygen consumed from the kMC model and (b) solid conversion from experimental observations<sup>190</sup> at compositions of  $\text{CO}/\text{H}_2 = 1$  (blue) and  $\text{CO}/\text{H}_2 = 3$  (red) in the gas phase; Comparison between (c) the solid conversion from the MF model and (d) the solid conversion from the experimental observations (scatter)<sup>191</sup> at temperatures of 823.15 K (blue), 873.15 K (red) and 923.15 K (green) (e) pressure analysis of the oxygen consumed from the MF model at 0.1 MPa (blue) and 2 MPa (red)

Since  $N_{O,con}$  is proportional to  $X_{O,con}$ , the comparison between the oxygen consumed from the kMC model and the solid conversion ratio from the experimental observations can provide a qualitative validation for the developed DFT-based kMC model. Moreover, due to the computational cost associated with this model, the kMC reaction time employed in the comparison is only  $10^{-5}$  s. Since the system reached steady-state within  $10^{-5}$  s as discussed in section 6.3.7.3 (constant surface coverages shown in Figure 6-9), the prediction in  $10^{-5}$  s is sufficient to capture the system behaviour under the studied conditions and provides a qualitative verification for the model. That is, no noticeable changes are expected in the long-term behaviour of the consumed oxygen as predicted by the kMC model; therefore, it is expected that these results may be extended to analyze the system behaviour over the longer time frames explored within the experimental work (30 s). Note that the estimated calculation time to simulate a single run of the kMC model over a 1s timeframe on a 30x30 lattice would be over one month (roughly requiring  $2 \times 10^9$  steps).

Figure 6-10 compares the predicted performance from the kMC model and the experimental observations under different operating conditions. The higher ratio of H<sub>2</sub> to CO in the syngas leads to higher consumed oxygen as presented in Figure 6-10(a), which follows the same tendency as the experimental report: the higher ratio of H<sub>2</sub> to CO benefits the oxygen transformation and results in a higher solid conversion ratio of solid conversion as shown in Figure 6-10(b).<sup>190</sup> Regarding the temperature effects, Figure 6-10 (c) shows that the increase in the temperature leads to more consumed oxygen. This temperature effect is observed in the previous experimental study presented in Figure 6-10(d): a higher solid conversion ratio is obtained under a higher system temperature.<sup>191</sup> Meanwhile, the oxygen transformation is suppressed by the high pressure, as shown in Figure 6-10(e), which agrees with the experimental outcomes reported in a previous study.<sup>192</sup>

Overall, the proposed kMC model captures the behaviour of the system at the early stages as their predictions follow experimental observations reported in the literature under different operating conditions, i.e. syngas composition, temperature and pressure.

#### **6.3.7.5. Sensitivity analysis for DFT-based kMC scenario**



Table 6-4 Sensitivity analysis

No neighbouring effects	CO coverage	H coverage	CO <sub>2</sub> production	H <sub>2</sub> O production	Consumed O/site
CO adsorption	+19.7%	-39.6%	-20.5%	-93.0%	-92.3%
H <sub>2</sub> chemisorption	-70.0%	+595.1%	+499.5%	+67.2%	+71.2%
CO oxidation	-1.7%	+7.7%	-58.3%	+0.6%	+0.3%
H <sub>2</sub> O formation	-28.2%	+294.7%	+239.2%	-83.1%	-80.2%

+ increase, - decrease

As mentioned above, the system reached a steady-state in a short time (within  $10^{-5}$  s). Hence, a sensitivity analysis of the neighbouring effects on different reactions at steady-state was performed. To perform this analysis, the neighbouring effects on each of the reactions are neglected respectively to be compared to the scenario in full consideration of the neighbouring effects. The changes in the system properties caused by the neighbouring effects are listed in Table 6-4 including the surface coverages of different species (CO or H), the product number per site (CO<sub>2</sub> and H<sub>2</sub>O) and the total consumed O number per site. The percent deviation,  $\Delta\sigma$ , caused by the neighboring effects is calculated as follows:

$$\Delta\sigma = (Num_{full} - Num_{nonei}) / Num_{full} \quad (6-6)$$

where  $Num_{full}$  is the predicted property from the scenario with full consideration of neighbouring effects, whereas  $Num_{nonei}$  is the predicted property from the scenario under no neighbouring considerations on one specific event (e.g. CO adsorption). Note that the predicted property ( $Num_{full} / Num_{nonei}$ ) can be coverage, produced product number per site or reacted oxygen per site.

Moreover, Figure 6-11 (a) to Figure 6-11 (d) compare the full neighbour consideration scenario and the scenario with no neighbour consideration on CO adsorption. Figure 6-11 (e) to Figure 6-11 (h) give the same comparison on H<sub>2</sub> chemisorption. Since the nearest neighbours significantly weaken CO adsorption rate as explained (see section 6.3.7.1), there is an increase

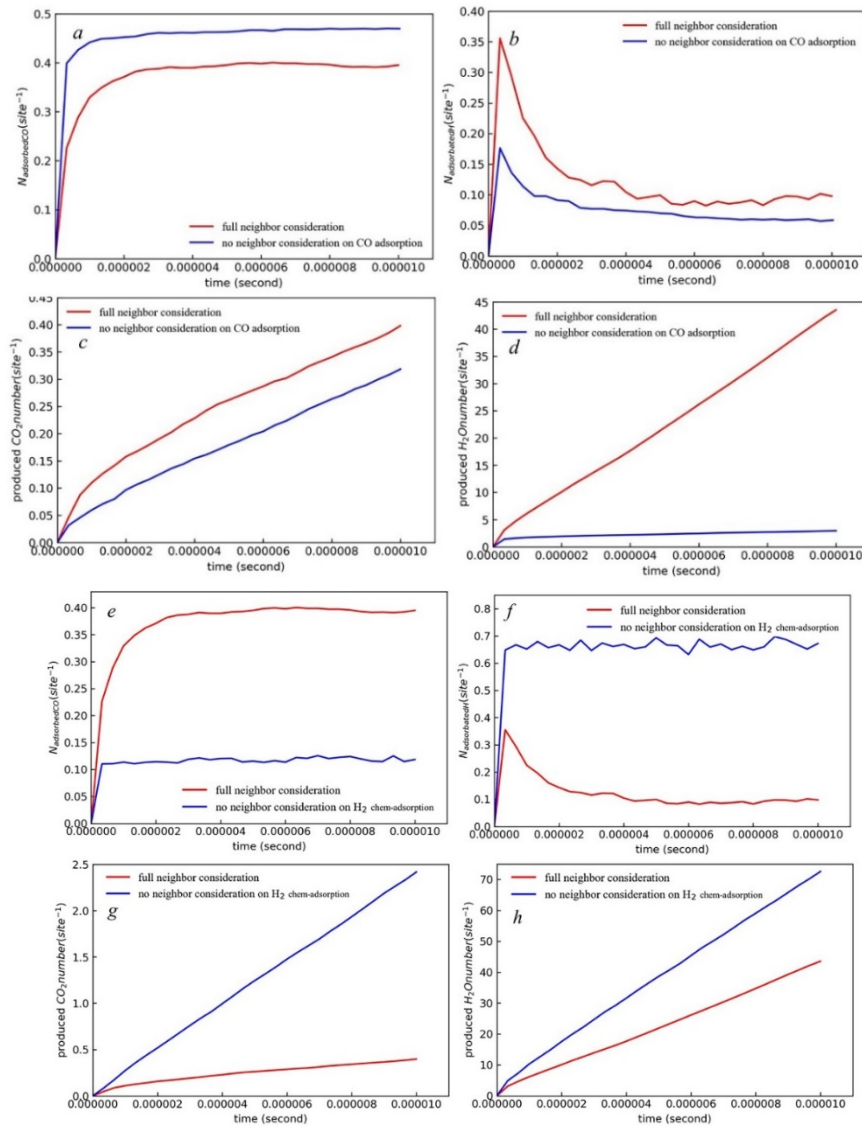


Figure 6-11 Comparison between the full neighbour consideration scenario (red) and no neighbour consideration on CO adsorption scenario (blue) of (a) CO coverage (b) H coverage (c) produced  $\text{CO}_2$  per site and (d) produced  $\text{H}_2\text{O}$  per site; or no neighbour consideration on  $\text{H}_2$  chemisorption scenario (blue) of (e) CO coverage (f) H coverage (g) produced  $\text{CO}_2$  per site and (h) produced  $\text{H}_2\text{O}$  per site

in the coverage of CO (Figure 6-11(a)) and a decrease in H coverage (Figure 6-11(b)) on the surface when the system eliminates the neighbouring effects on the CO adsorption. However, the CO<sub>2</sub> production is not increasing as the CO coverage increases because the CO neighbours slightly weaken the CO oxidation, as shown in the activation energy analysis provided in section 6.3.1. Therefore, neglecting the neighbouring effects on CO adsorption leads to a significant decrease in the consumed O per site (92.3%), as shown in Table 6-4; this effect is mostly due to the increase in the coverage ratio of CO to H on the NiO surface. Likewise, ignoring the neighbouring effects on H<sub>2</sub> chemisorption results in a considerable increase in H coverage (by six times larger as shown in Figure 6-11(f)) and a decrease in CO coverage (by 70.0% as shown in Figure 6-11(e)), respectively. The increase in H coverage comes from the elimination of the neighbouring effects on H<sub>2</sub> adsorption, which weakens the H<sub>2</sub> adsorption as explained in section 6.3.7.1. These changes lead to an increase in both CO<sub>2</sub> and H<sub>2</sub>O production, as shown in Figure 6-11(g) and Figure 6-11(h), respectively. This is because the H<sub>2</sub> neighbours are likely to enhance the CO oxidation and H<sub>2</sub>O formation reactions, as discussed in section 6.3.7.2. The consumed O number increased by 71.2% due to the increase in the H coverage in the scenario that neglects the neighbouring effects on H<sub>2</sub> chemisorption.

Figure 6-12(a) to Figure 6-12(d) provide a comparison between the scenario with full consideration of neighbouring effects and the scenario with no neighbour consideration on CO oxidation. Figure 6-12 (e) to Figure 6-12(h) provide the same comparison on H<sub>2</sub>O formation. As discussed in 6.3.7.3, the neighbouring effects generally enhance the CO oxidation reaction under the studied conditions. Therefore, neglecting the neighbouring effects on CO oxidation weakens the CO oxidation and leads to a significant decrease in CO<sub>2</sub> production (by 58.3% as shown in Figure 6-12(c)). This change only leads to a minor change in the coverages of CO and H. As shown in Figure 6-12(a), there is a slight increase in the CO coverage within a short timeframe at the initial stage due to the weakening of the CO oxidation. Then, increasing CO coverage weakens the CO adsorption, and therefore the CO coverage is slightly reduced at steady-state, as shown in Figure 6-12(a). Meanwhile, a slight increase (7.7%) in the coverage of H is observed at the steady-state in Figure 6-12(b).

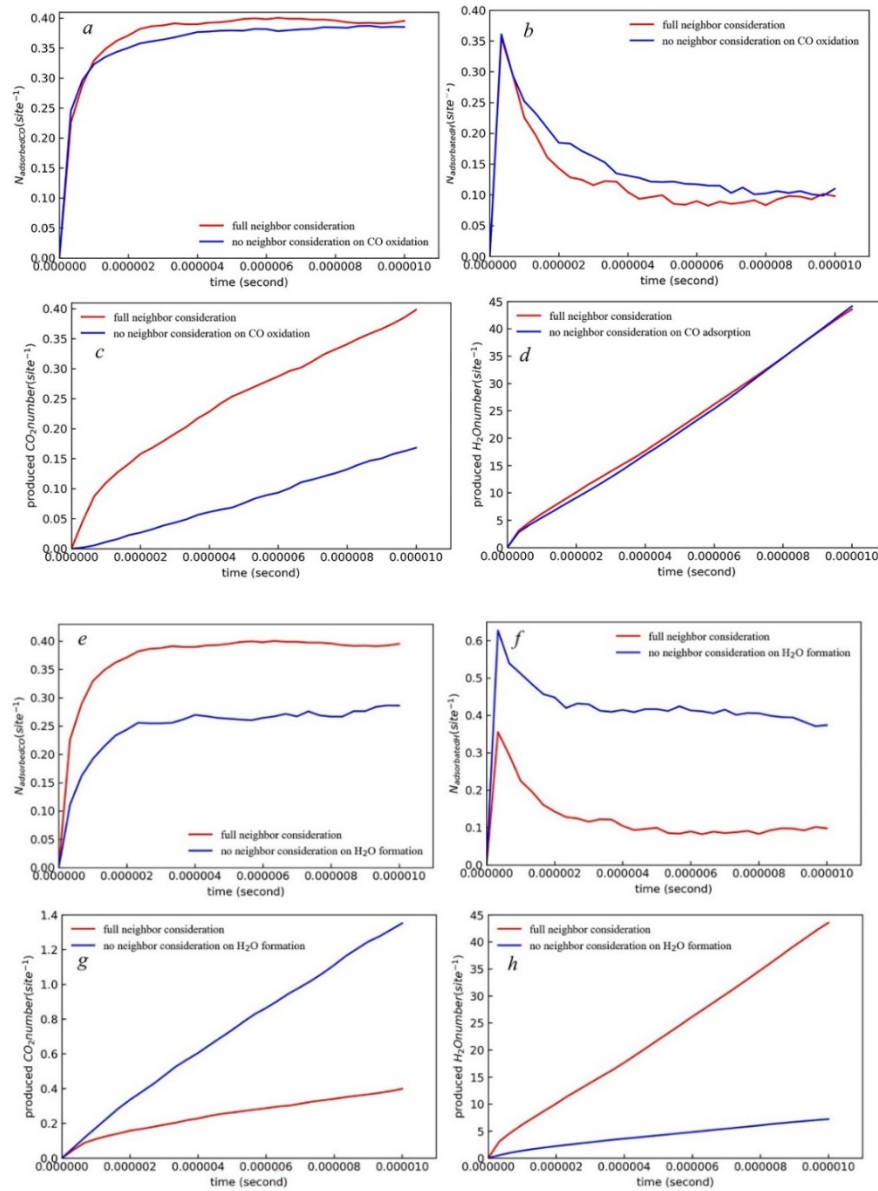


Figure 6-12 Comparison between the full neighbour consideration scenario (red) and no neighbour consideration on CO oxidation scenario (blue) of (a) CO coverage (b) H coverage (c) produced CO<sub>2</sub> per site and (d) produced H<sub>2</sub>O per site; or no neighbour consideration on H<sub>2</sub>O chemisorption scenario (blue) of (e) CO coverage (f) H coverage (g) produced CO<sub>2</sub> per site and (h) produced H<sub>2</sub>O per site

Though the H<sub>2</sub>O production only increased by 0.6% (Figure 6-12(d)) while the CO<sub>2</sub> production decreased by 58.3% (Figure 6-12(c)), the consumed O per site still increased slightly by 0.3%, as shown in Table 6-4. This is because the H<sub>2</sub>O formation reaction parameter is two order of magnitudes larger than the CO oxidation parameter, as shown in Table 4-1. Regarding H<sub>2</sub>O formation, the neighbouring effects generally enhance the H<sub>2</sub>O formation reaction as discussed in section 6.3.7.2. Therefore, H<sub>2</sub>O production is significantly reduced by 83.1% (Figure 6-12(h)), which is caused by ignoring the neighbouring effects, and consequently, the H coverage is significantly increased by 294.7% (Figure 6-12(f)). The H<sub>2</sub> neighbours will enhance the CO oxidation process such that the CO<sub>2</sub> production is considerably increased by 239.2% (Figure 6-12(g)), which also leads to a decrease in the CO coverage (28.2% in Figure 6-12(e)). The overall consumed oxygen per site is significantly decreased by 80.2% due to a significant drop in the H<sub>2</sub>O production, as listed in Table 6-4.

Overall, the changes caused by ignoring the neighbouring effects decreases in the following order: CO adsorption > H<sub>2</sub>O formation > H<sub>2</sub> chemisorption > CO oxidation. This suggests that the neighbouring effects on CO adsorption are the most significant to the system temporal evolution, while those on CO oxidation are the least notable. The neighbouring effects on CO adsorption and H<sub>2</sub>O formation benefit the oxygen transformation considerably under the studied operating conditions since neglecting the neighbouring effects leads to a decrease in the consumed oxygen number per site. Moreover, the neighbouring effects on H<sub>2</sub> chemisorption suppress the oxygen transformation. In addition, since the H<sub>2</sub>O formation is a much faster reaction compared to CO oxidation, the change in H<sub>2</sub>O production affects the system more significantly, which would be the key factor to be considered in order to improve the oxygen conversion ratio and product selectivity. Note that a high ratio of CO coverage to H<sub>2</sub> coverage tends to weaken the oxygen conversion. Furthermore, oxygen conversion changes significantly with and without consideration of the neighbouring effects, which implies that the reported neighbouring effects are key to capture the system behaviour.

## 6.4 Summary

In this chapter, the neighbouring effects were taken into account for syngas combustion on a NiO surface. The syngas oxidation kinetics were investigated in the presence of specific first nearest neighbour configurations. The dominant structural deviation caused by the neighbouring effects and the corresponding changes in the activation energies were explained. The forward and backward activation energies presented similar tendencies in almost all of the studied cases. CO oxidation was often slightly weakened by the CO neighbours and enhanced by the H<sub>2</sub> neighbours based on the analysis of the activation energies. The three step H<sub>2</sub> oxidation process was shown to benefit from the neighbouring effects except for the neighbour configuration involving full first H<sub>2</sub> nearest neighbours. The activation energy analysis showed that H<sub>2</sub>O formation is highly unlikely to happen with fully occupied H<sub>2</sub> neighbours. In addition, the backward activation energy tends to be more significantly affected by the nearest neighbours than the forward activation energy. The analysis of the reaction equilibrium revealed that the presence of CO neighbours resulted in more significant changes to the reaction equilibrium. A combined electronic analysis was performed to support the outcomes obtained from the DFT calculations.

A DFT-based kMC multi-scale model was constructed and used to estimate the neighbouring effects under practical operating conditions for this process. The results from this simulation showed that the neighbouring effects on CO adsorption and H<sub>2</sub>O formation benefit the oxygen transformation significantly whereas the neighbouring effects on H<sub>2</sub> chemisorption weaken the oxygen transformation. Among all the studied reactions, the system performance was most significantly affected by the neighbouring effects on CO adsorption, whereas the neighbouring effects on the CO oxidation led to an almost negligible change in the prediction of the system properties. The considerable changes caused by the neighbouring effects indicated that it is necessary to consider the neighbouring effects in order to capture the system performance under practical operating conditions.

Note that the developed DFT-based kMC only provides property predictions within 10<sup>-5</sup> seconds. However, the studied system has reached steady states based on the coverage analysis shown in section 6.3.7.3. Then the average event rates can be calculated in consideration of the

explicit neighboring effects, which are not expected to deviate over a longer time frame. These average event rates can be brought into the closed-form MF model or microkinetic model, so that the longer system time can be achieved in consideration of the explicit neighboring effects. This part of research is highly recommended in the future.

## Chapter 7 Conclusions and Future Work

### 7.1 Conclusions

This research study presented the theoretical study of syngas combustion on the NiO OC. The multi-scale models developed in this research provided a comprehensive understanding of the studied system, while taking into consideration the effects of oxygen vacancies and nearest neighbours. The major contributions from this work are outlined next.

The adsorption principle of syngas on the NiO surface was revealed while taking into account the surrounding surface environment. According to the structural property analysis, the adsorption sites tend to repel the attached CO or H<sub>2</sub> away with an increasing number of neighbours. This is an indication of the steric effects on the surface, which may become more significant for nonlinear molecules like methane. A CO neighbour leads to a larger distance between the adsorption site and the attached molecule as compared to the H<sub>2</sub> neighbour. For both CO and H<sub>2</sub> adsorption, the most significant decrease in the adsorption energy was caused by the first loaded neighbour. This suggests that once the first neighbouring molecule has been attached to the surface, an increasing number of the nearest neighbours does not significantly change the adsorption stability. The energetic analysis showed that the hybrid adsorbed neighbor configuration leads to a smaller reduction in the adsorption energy of CO and H<sub>2</sub> compared to the uniform neighbor configuration. Note that the steric effects should be considered when CO is the neighbouring molecule. Likewise, a higher degree of symmetry leaves the adsorption molecule no tilting space, which leads to weakening the adsorption stability. This part of the research showed that the adsorption stability can be predicted by the combination of the hybrid, steric and symmetry effects. An electronic property analysis on different configurations was performed to validate the insights gained through this study. The insights from this study were essential to develop microscopic models of the studied system while considering the neighbouring effects.

The elementary reaction mechanism for syngas combustion on NiO was obtained from a DFT analysis. The CO oxidation proceeded via a 1-step mechanism, while the H<sub>2</sub> oxidation proceeded via a 3-step mechanism. The H<sub>2</sub> decomposition proved to be extremely difficult to



advance due to its highest energy barrier among all the reactions. Therefore, the first step of H<sub>2</sub> oxidation, i.e. H<sub>2</sub> decomposition, is shown to be the controlling step dominating the overall reaction rate. An improvement in the H<sub>2</sub> decomposition is expected to benefit the syngas combustion significantly. To provide a deeper understanding of the established reaction mechanisms, a coupling electronic analysis was performed, with the results supporting the proposed elementary reactions. An DFT-based MF model was then established based on the DFT results to validate the proposed reaction mechanism and investigate the effects of syngas composition, temperature and pressure on the species evolution on the OC surface. The system with a higher ratio of H<sub>2</sub> in the syngas is likely to generate a higher OC conversion. Also, an increase in temperature resulted in a higher OC conversion ratio, while an increase in the total pressure resulted in a reduction of the consumed oxygen of OC. The predictions obtained from the MF model were in agreement with previous experimental observations, thus showing that the proposed mechanism is suitable for the prediction of the OC performance in the process of syngas combustion. The CO<sub>2</sub>/H<sub>2</sub>O product ratio was estimated under the coordinate effects of different operating conditions. The results show that high temperatures and low pressures will increase the CO<sub>2</sub>/H<sub>2</sub>O product ratios. The validated reaction kinetics laid a solid foundation for the later vacancy and neighbouring effect analyses performed in this study.

Based on the established reaction kinetics on a perfect NiO surface described above, the effects of the oxygen vacancies were systematically investigated on syngas adsorption, O migration and surface reactions. The vacancy effects were emphasized through a comparison of OC performance with and without defective sites (i.e. the absence of oxygen in the surface layer). The syngas oxidation continuously consumed the surface oxygen to form oxygen vacancies, which were substituted by the subsurface O through O migration. The outward diffusion of the lattice O has been shown to be the preferred direction of diffusion according to the DFT analysis. In the presence of vacancies, both the CO and H<sub>2</sub> adsorption configurations are expected to be more active in the subsequent oxidation reactions. Moreover, the CO adsorption at the vacancy-adjacent Ni top tends to be more active than the CO adsorption at the top of the vacancy. On the defective surface, two 1-step CO oxidation mechanisms were proposed based on the reactant configuration of CO adsorption on the vacancy and the reactant configuration of CO adsorption on the Ni top adjacent to the vacancy,

respectively. The corresponding energetic results show that vacancies benefit the CO oxidation process since they tend to reduce the reaction barriers of this reaction. In particular, the reaction with the reactant on the vacancy-adjacent Ni top has a lower energy barrier compared to that of the reaction with the reactant on the top of the vacancy. Regarding H<sub>2</sub> oxidation, a 2-step mechanism on the defective surface was established instead of the 3-step mechanism on a perfect surface explained above. Furthermore, the H<sub>2</sub> decomposition step, which serves as the rate-controlling step on the perfect surface, is significantly enhanced by the vacancy effects. Accordingly, the CO oxidation is shown to dominate the overall syngas combustion process. Based on these observations, vacancies have been shown to play a critical role in both syngas adsorption and oxidation. Electronic analyses were conducted to further support the insights gained on the reaction kinetics and the vacancy effects for this system. A validation of the proposed reaction kinetics was subsequently performed by analyzing the order of the reactivities and the predictions from a DFT-based MF model.

In addition to the vacancies, first nearest neighbours are also expected to affect the reaction mechanism of the studied system. Thus, neighbouring effects were investigated by developing a DFT-based kMC multi-scale model. A DFT analysis was first conducted to assess the neighbouring effects on syngas oxidation. According to the DFT analysis, the adsorbed species as the first nearest neighbours lead to significant changes in the atomic structures of syngas as well as the OC surface, the activation energies, and the surface electronic population. Compared to the oxidation reaction observed in the presence of the H<sub>2</sub> neighbours, the CO oxidation reaction experienced a more significant energetic change with a less visible structural deviation of TS<sub>CO</sub> due to the CO neighbours. The loading of the CO neighbours tends to weaken the CO oxidation while the H<sub>2</sub> neighbours enhance the CO oxidation based on the change in the activation energies. However, the changes in the activation energy of H<sub>2</sub> decomposition are not as significant as those observed in CO oxidation, i.e. the presence of CO neighbours and the first loaded H<sub>2</sub> neighbour leads to a lower forward activation energy of the H<sub>2</sub> decomposition. Regarding the H migration process, the neighbours tend to reduce the activation energy, except for the case of three H<sub>2</sub> neighbours. Moreover, H<sub>2</sub>O formation is generally enhanced by the neighbouring effects, excluding the fully occupied H<sub>2</sub> neighbour configuration. Note that the fully occupied H<sub>2</sub> neighbour configuration on the surface renders

the H<sub>2</sub>O formation process highly unlikely. The changes in the forward activation energy and backward activation energy usually present similar tendencies, except in the case of H<sub>2</sub>O formation in the presence of CO neighbours. In addition, the backward activation energy is normally more sensitive to the neighbouring effects as compared to the forward activation energy with the exception of the H migration process.

The reaction equilibrium was also affected by the neighbouring effects. The neighbours lead to the forward shift of CO oxidation, while the reaction equilibrium of H<sub>2</sub> decomposition shifts backward as a result of the neighbours, despite the three CO neighbour configuration. Moreover, the H migration reaction equilibrium was observed to slightly shift forward due to the neighbouring effects except in the case of the fully occupied CO neighbour configuration. In addition, the reaction equilibrium of the H<sub>2</sub>O formation is favoured by CO neighbours, but slightly suppressed by the presence of H<sub>2</sub> neighbours. The reaction equilibrium is usually more sensitive to the effects of the CO neighbours. The neighbouring effects were also described based on an electron population analysis thus further supporting the findings of the preceding structure-related energetic analysis.

The resulting neighboring effects are interpreted into reaction rate constants to develop a DFT-based kMC multiscale model. The validation of the DFT-based kMC multi-scale model showed that the proposed model can capture the properties of the studied system under practical operating conditions. A sensitivity analysis of the neighbouring effects on every event shows that the system performance is most significantly affected by the neighbouring effects on CO adsorption. Furthermore, this analysis also showed that neighbouring effects on CO oxidation only resulted in a moderate change in the predictions of the system properties. The neighbouring effects on CO adsorption and H<sub>2</sub>O formation were observed to enhance the OC conversion under practical operating conditions. Meanwhile, OC conversion is negatively affected by the neighbouring effects on H<sub>2</sub> chemisorption. H<sub>2</sub>O production is the controlling step that determines the overall OC conversion ratio for the system. In addition, a high coverage ratio of CO to H<sub>2</sub> tends to suppress the OC conversion ratio. The results from this study suggest that it is critical to consider the neighbouring effects to accurately capture the system performance, as implied by the considerable changes caused by the neighbouring effects predicted by the developed multi-scale model.

Note that the models presented in this study cannot be directly compared to the experimental observations due to the assumptions during model development. No effects of the oxygen migration and impurities on the system evolution are considered in this study. Also, the developed DFT-based MF model explained in Chapter 4 is established on the assumption of a perfect NiO surface, which does not take vacancy and neighboring effects into account. In addition, the proposed DFT-based MF model presented in Chapter 5 is developed based on the defective surface reaction kinetics. Therefore, the neighboring effects are not considered in this model. As for the DFT-based kMC model, the explicit neighboring effects are taken into consideration whereas the vacancy effects are not considered. Furthermore, the current studies available in this area do not allow a direct comparison to the present model. For instance, an experimental study using pure NiO, OC study of syngas combustion (measuring properties in short time interval) is not currently available.<sup>56</sup>

## 7.2 Future work

The findings and conclusions obtained from this study can be used as basis to develop future work in this emerging area. The suggested research avenues that can be pursued are described next.

- The developed DFT-based kMC only provides property predictions within  $10^{-5}$  seconds. However, the studied system has reached steady states based on the coverage analysis shown in section 6.3.7.3. Then the average event rates can be calculated in consideration of the explicit neighboring effects, which are not expected to deviate significantly over a longer time frame. These average event rates can be brought into the closed-form MF model or microkinetic model, such that larger simulation times can be achieved in consideration of the explicit neighboring effects.
- To date, no experimental pure NiO study can be adopted for the direct comparison of the multi-scale models developed in this research. Therefore, an experimental study that involves pure NiO as OC for the syngas combustion process within short contact time is recommended for a more direct comparison of the proposed models. Additionally, a

theoretical Al<sub>2</sub>O<sub>3</sub> supported NiO OC study is also recommended on the basis of the proposed OC models for a higher quality of validation.








- The proposed DFT-based MF model only considered vacancy effects in the system. In order to use variable-controlling method for the analysis of vacancy effects, the nearest neighbours are not considered for the establishment of the DFT-based MF model. To provide a more accurately prediction of the studied system, a DFT-based MF model that takes both vacancy and neighbouring effects into account is highly recommended for the future work.
- The proposed DFT-based kMC model considered the explicit neighbouring effects. Since this model used the variable-controlling method to study the dynamic neighbouring effects, the resulting vacancy effects and the bulk oxygen migration were not considered in the kMC model. A DFT-based kMC model that involves oxygen migration and vacancy formation processes is expected to improve the insights for this process and perhaps reveal new mechanisms that may impact OC performance.
- The current multi-scale model connects the information from the electronic population to the dynamic properties of the system from a microscopic kMC model. To reach larger scales, the proposed DFT-based kMC model can be coupled with an intra-particle diffusion model (mass balance equations) and a particle model (e.g. nucleation and nuclei growth model and shrinking core model) to predict OC performance at the larger spatial and temporal scales.
- This study investigated the reduction process of NiO by syngas. The oxidation process of the OC is likewise significant and necessary to be considered for OC development. A research of the reaction activity of Ni oxidized by air in consideration of the factors such as neighbouring effects is expected to provide new insights for the studied system.
- This study has showed that for syngas combustion, vacancies enhance CLC performance. CeO<sub>2</sub> has attracted attention due to its advantages of high oxygen storage and its ability to maintain a specific concentration of vacancies. The addition of a three-valent metal oxides such as Fe<sub>2</sub>O<sub>3</sub> to the CeO<sub>2</sub> could further increase the reaction activity and avoid the rapid sintering of CeO<sub>2</sub> at high temperatures. Therefore, a study that explores the use of this OC into this process can be key to further improve the overall process performance.


- CH<sub>4</sub> is a widely used fuel in chemical looping technology, especially in chemical looping reforming process for syngas production. Hence, it is recommended to explore the reaction mechanisms of CH<sub>4</sub> since this gas usually has many possible paths for its chemical transformation. A potential research of CH<sub>4</sub> reforming in a chemical looping process could lead to new discoveries that can accelerate commercialization of CLC.
- As mentioned in Chapter 2, metal promoters are trending due to their ability to improve the OC performance. Natural ores have attracted attention since they can be considered as OC with inherent metal promoters. Ilmenite ore mainly contains Fe<sub>2</sub>O<sub>3</sub> and TiO<sub>2</sub> in its structure, which are both proven to be active components of OCs. In addition, ilmenite ore is widely available and economically attractive. Theoretical studies involving this material are very limited. Thus, studies involving ilmenite ore as OC are highly recommended.
- Reaction kinetics are vital for OC development. The DFT analyses performed in this work provided comprehensive insights into the reaction mechanisms. However, to screen a large scope of materials for a specific utilization of OCs, DFT calculations can be somewhat expensive. Machine learning (ML) techniques are promising computational tools that can be used for computer aided materials design.<sup>86, 208-210</sup> In particular, ML can screen a large number of catalyst materials, as well as optimize and further design the catalysts in shorter time periods compared to the traditional experimental and/or computational methods. Therefore, developing a ML supported with DFT calculations can significantly aid in the optimization and selection of the OC for specific applications among a wide range of materials.

## Copyright Permissions

Reprinted (adapted) with permission from (Yuan, Yue, Xiuqin Dong, and Luis Ricardez-Sandoval. "Insights into Syngas Combustion on a Defective NiO Surface for Chemical Looping Combustion: Oxygen Migration and Vacancy Effects." The Journal of Physical Chemistry C (2020)). Copyright (2020) American Chemical Society.

1/3/2021 Rightslink® by Copyright Clearance Center

 **Copyright Clearance Center**  **RightsLink®**  Home  Help  Email Support  Sign in  Create Account

 **ACS Publications**  
Most Trusted. Most Cited. Most Read.

**Insights into Syngas Combustion on a Defective NiO Surface for Chemical Looping Combustion: Oxygen Migration and Vacancy Effects**

**Author:** Yue Yuan, Xiuqin Dong, Luis Ricardez-Sandoval  
**Publication:** The Journal of Physical Chemistry C  
**Publisher:** American Chemical Society  
**Date:** Dec 1, 2020  
*Copyright © 2020, American Chemical Society*

**PERMISSION/LICENSE IS GRANTED FOR YOUR ORDER AT NO CHARGE**

This type of permission/license, instead of the standard Terms & Conditions, is sent to you because no fee is being charged for your order. Please note the following:

- Permission is granted for your request in both print and electronic formats, and translations.
- If figures and/or tables were requested, they may be adapted or used in part.
- Please print this page for your records and send a copy of it to your publisher/graduate school.
- Appropriate credit for the requested material should be given as follows: "Reprinted (adapted) with permission from (COMPLETE REFERENCE CITATION). Copyright (YEAR) American Chemical Society." Insert appropriate information in place of the capitalized words.
- One-time permission is granted only for the use specified in your request. No additional uses are granted (such as derivative works or other editions). For any other uses, please submit a new request.

[BACK](#) [CLOSE WINDOW](#)

© 2021 Copyright - All Rights Reserved | [Copyright Clearance Center, Inc.](#) | [Privacy statement](#) | [Terms and Conditions](#)

<https://s100.copyright.com/AppDispatchServlet> 1/2

## Bibliography

1. Sun, W.; Zhai, X.; Zhao, L., Synthesis of ZIF-8 and ZIF-67 nanocrystals with well-controllable size distribution through reverse microemulsions. *Chem. Eng. J.* **2016**, *289*, 59-64.
2. Adanez, J.; Abad, A.; Garcia-Labiano, F.; Gayan, P.; de Diego, L. F., Progress in Chemical-Looping Combustion and Reforming technologies. *Prog. Energy Combust. Sci.* **2012**, *38* (2), 215-282.
3. Bayham, S. C.; Tong, A.; Kathe, M.; Fan, L. S., Chemical looping technology for energy and chemical production. *Wires. Energy. Environ.* **2016**, *5* (2), 216-241.
4. Total Energy Supply by Resource World 1990-2018. International Energy Agency: 2020.
5. Hossein Sahraei, M.; McCalden, D.; Hughes, R.; Ricardez-Sandoval, L. A., A survey on current advanced IGCC power plant technologies, sensors and control systems. *Fuel* **2014**, *137*, 245-259.
6. Almazán-Almazán, M. C.; López-Domingo, F. J.; Domingo-García, M.; Léonard, a.; Pérez-Mendoza, M.; Pirard, J. P.; López-Garzón, F. J.; Blacher, S., Influence of carbon xerogel textural properties on the dynamic adsorption of methyl iodide. *Chem. Eng. J.* **2011**, *173*, 19-28.
7. de Diego, L. F.; García-Labiano, F.; Gayán, P.; Celaya, J.; Palacios, J. M.; Adánez, J., Operation of A 10 kWth Chemical-looping Combustor during 200 h with A CuO-Al<sub>2</sub>O<sub>3</sub> Oxygen Carrier. *Fuel* **2007**, *86*, 1036-1045.
8. Nandy, A.; Loha, C.; Gu, S.; Sarkar, P.; Karmakar, M. K.; Chatterjee, P. K., Present status and overview of Chemical Looping Combustion technology. *Renew. Sust. Energ. Rev.* **2016**, *59*, 597-619.
9. Metz, B., *Carbon dioxide capture and storage: special report of the intergovernmental panel on climate change*. Cambridge University Press: 2005.
10. Nittaya, T.; Douglas, P. L.; Croiset, E.; Ricardez-Sandoval, L. A., Dynamic Modelling and Controllability Studies of a Commercial-scale MEA Absorption Processes for CO<sub>2</sub> Capture from Coal-fired Power Plants. *Energy Procedia* **2014**, *63*, 1595-1600.
11. Hossein Sahraei, M.; Ricardez-Sandoval, L. A., Controllability and optimal scheduling of a CO<sub>2</sub> capture plant using model predictive control. *Int. J. Greenh. Gas Con.* **2014**, *30*, 58-71.
12. Yang, H.; Xu, Z.; Fan, M.; Gupta, R.; Slimane, R. B.; Bland, A. E.; Wright, I., Progress in carbon dioxide separation and capture: A review. *J. Environ. Sci.* **2008**, *20* (1), 14-27.
13. De Vos, Y.; Jacobs, M.; Van Der Voort, P.; Van Driessche, I.; Snijkers, F.; Verberckmoes, A., Development of Stable Oxygen Carrier Materials for Chemical Looping Processes—A Review. *Catalysts* **2020**, *10* (8), 926.
14. Dong, C.; Sheng, S.; Qin, W.; Lu, Q.; Zhao, Y.; Wang, X.; Zhang, J., Density functional theory study on activity of alpha-Fe<sub>2</sub>O<sub>3</sub> in chemical-looping combustion system. *Appl. Surf. Sci.* **2011**, *257*, 8647-8652.
15. Tan, Q.; Qin, W.; Chen, Q.; Dong, C.; Li, W.; Yang, Y., Synergetic Effect of ZrO<sub>2</sub> on The Oxidation-reduction Reaction of Fe<sub>2</sub>O<sub>3</sub> during Chemical Looping Combustion. *Appl. Surf. Sci.* **2012**, *258*, 10022-10027.



16. Cheng, Z.; Qin, L.; Guo, M.; Xu, M.; Fan, J. A.; Fan, L.-S., Oxygen vacancy promoted methane partial oxidation over iron oxide oxygen carriers in the chemical looping process. *Phys. Chem. Chem. Phys.* **2016**, *18*, 32418-32428.
17. Zhang, Y.; Zhao, H.; Guo, L.; Zheng, C., Decomposition mechanisms of Cu-based oxygen carriers for chemical looping with oxygen uncoupling based on density functional theory calculations. *Combust. Flame* **2015**, *162*, 1265-1274.
18. Feng, Y.; Guo, X., Study of reaction mechanism of methane conversion over Ni-based oxygen carrier in chemical looping reforming. *Fuel* **2017**, *210*, 866-872.
19. Zhang, Q.; Zhang, M.; Wiltowski, T., Adsorption and dissociation of O<sub>2</sub> on MoO<sub>2</sub>(111) surfaces: a DFT study. *Phys. Chem. Chem. Phys.* **2017**, *19* (43), 29244-29254.
20. Liu, G.; Liao, Y.; Wu, Y.; Ma, X., Synthesis gas production from microalgae gasification in the presence of Fe<sub>2</sub>O<sub>3</sub> oxygen carrier and CaO additive. *Applied Energy* **2018**, *212*, 955-965.
21. Zhang, H.; Watanabe, T.; Okumura, M.; Haruta, M.; Toshima, N., Crown Jewel catalyst: How neighboring atoms affect the catalytic activity of top Au atoms? *J. Catal.* **2013**, *305*, 7-18.
22. Chen, W.; Gao, W.; Tu, P.; Robert, T.; Ma, Y.; Shan, H.; Gu, X.; Shang, W.; Tao, P.; Song, C., Neighboring Pt atom sites in an ultrathin FePt Nanosheet for the efficient and highly CO-tolerant oxygen reduction reaction. *Nano Lett.* **2018**, *18* (9), 5905-5912.
23. Hwang, J. H.; Lee, K.-T., Development of promoters for fast redox reaction of MgMnO<sub>3</sub> oxygen carrier material in chemical looping combustion. *Journal of Ceramic Processing Research* **2018**, *19* (5), 372-377.
24. Wong, B. M.; Collinge, G.; Hensley, A. J. R.; Wang, Y.; McEwen, J.-S., Benchmarking the accuracy of coverage-dependent models: adsorption and desorption of benzene on Pt (1 1 1) and Pt<sub>3</sub>Sn (1 1 1) from first principles. *Prog. Surf. Sci.* **2019**, *94* (2), 100538.
25. Chaffart, D.; Ricardez-Sandoval, L. A., Robust optimization of a multiscale heterogeneous catalytic reactor system with spatially-varying uncertainty descriptions using polynomial chaos expansions. *The Canadian Journal of Chemical Engineering* **2018**, *96* (1), 113-131.
26. Mei, D.; Sheth, P.; Neurock, M.; Smith, C., First-principles-based kinetic Monte Carlo simulation of the selective hydrogenation of acetylene over Pd(111). *J. Catal.* **2006**, *242* (1), 1-15.
27. Thuinet, L.; Nastar, M.; Martinez, E.; Bouobda Moladje, G. F.; Legris, A.; Soisson, F., Multiscale modeling of Radiation Induced Segregation in iron based alloys. *Comp Mater Sci* **2018**, *149*, 324-335.
28. Andersson, S.; Radl, S.; Svenum, I.-H.; Shevlin, S. A.; Guo, Z. X.; Amini, S., Towards rigorous multiscale flow models of nanoparticle reactivity in chemical looping applications. *Catalysis Today* **2019**, *338*, 152-163.
29. Yuan, Y.; You, H.; Ricardez-Sandoval, L., Recent advances on first-principles modeling for the design of materials in CO<sub>2</sub> capture technologies. *Chin. J. Chem. Eng.* **2018**, *27* (7), 1554-1565.
30. Benson, S. M.; Orr, F. M., Carbon Dioxide Capture and Storage. *MRS Bull.* **2011**, *33* (4), 303-305.
31. D'Alessandro, D. M.; Smit, B.; Long, J. R., Carbon dioxide capture: prospects for new materials. *Angew Chem Int Ed Engl* **2010**, *49* (35), 6058-82.
32. Figueroa, J. D.; Fout, T.; Plasynski, S.; McIlvried, H.; Srivastava, R. D., Advances in CO<sub>2</sub> capture technology-The U.S. Department of Energy's Carbon Sequestration Program. *Int. J. Greenh. Gas Con.* **2008**, *2*, 9-20.
33. Vasudevan, S.; Farooq, S.; Karimi, I. A.; Saeys, M.; Quah, M. C. G.; Agrawal, R., Energy penalty estimates for CO<sub>2</sub> capture: Comparison between fuel types and capture-combustion modes. *Energy* **2016**, *103*, 709-714.

34. Rajabi, M.; Mehrpooya, M.; Haibo, Z.; Huang, Z., Chemical looping technology in CHP (combined heat and power) and CCHP (combined cooling heating and power) systems: A critical review. *Applied Energy* **2019**, *253*, 113544.
35. Zhu, X.; Imtiaz, Q.; Donat, F.; Müller, C. R.; Li, F., Chemical looping beyond combustion – a perspective. *Energy Environ. Sci.* **2020**, *13* (3), 772-804.
36. Lyngfelt, A., Chemical Looping Combustion: Status and Development Challenges. *Energy Fuels* **2020**, *34* (8), 9077-9093.
37. Mehrpooya, M.; Moftakhari Sharifzadeh, M. M.; Rajabi, M.; Aghbashlo, M.; Tabatabai, M.; Hosseinpour, S.; Ramakrishna, S., Design of an integrated process for simultaneous chemical looping hydrogen production and electricity generation with CO<sub>2</sub> capture. *Int. J. Hydrogen Energy* **2017**, *42* (12), 8486-8496.
38. Lewis, W. K.; Gilliland, E. R., Production of Pure Carbon Dioxide. **1954**, 251.
39. Richter, H. J.; Knoche, K. F., Reversibility of Combustion Processes. *ACS Symposium Series; American Chemical Society: Washington, DC, 1983* **1983**, 71-85.
40. Ishida, M.; Zheng, D.; Akehata, T., Evaluation of A Chemical Looping Combustion Power Generation System by Graphic Exergy Analysis. *Energy* **1987**, *12*, 147-154.
41. Ishida, M.; Jin, H., A New Advanced Power-generation System Using Chemical Looping Combustion. *Energy* **1994**, *19*, 415-422.
42. Hossain, M. M.; Sedor, K. E.; de Lasa, H. I., Co-Ni/Al<sub>2</sub>O<sub>3</sub> Oxygen Carrier for Fluidized Bed Chemical-looping Combustion: Desorption Kinetics and Metal-support Interaction. *Chemical Engineering Science* **2007**, *62*, 5464-5472.
43. Feng, Y.; Wang, N.; Guo, X.; Zhang, S., Characteristics of dopant distribution and surface oxygen vacancy formation for modified Fe<sub>2</sub>O<sub>3</sub> in chemical looping combustion. *Fuel* **2020**, *276*, 117942.
44. Zhang, X.; Su, Y.; Pei, C.; Zhao, Z.-J.; Liu, R.; Gong, J., Chemical Looping Steam Reforming of Methane over Ce-doped Perovskites. *Chemical Engineering Science* **2020**, 115707.
45. Hamidouche, Z.; Ku, X.; Lin, J.; Wang, J., Numerical simulation of a chemical looping combustion of biomass: Hydrodynamic investigation. *Fuel Process. Technol.* **2020**, *207*, 106486.
46. Donat, F.; Müller, C. R., CO<sub>2</sub>-free conversion of CH<sub>4</sub> to syngas using chemical looping. *Applied Catalysis B: Environmental* **2020**, *278*, 119328.
47. Osman, M.; Zaabout, A.; Cloete, S.; Amini, S., Experimental demonstration of pressurized chemical looping combustion in an internally circulating reactor for power production with integrated CO<sub>2</sub> capture. *Chem. Eng. J.* **2020**, *401*, 125974.
48. Li, Y.; Zhao, C.; Chen, H.; Liu, Y., Enhancement of Ca-Based Sorbent Multicyclic Behavior in Ca Looping Process for CO<sub>2</sub> Separation. *Chemical Engineering & Technology* **2009**, *32* (4), 548-555.
49. Martínez, I.; Arias, B.; Grasa, G. S.; Abanades, J. C., CO<sub>2</sub> capture in existing power plants using second generation Ca-Looping systems firing biomass in the calciner. *Journal of Cleaner Production* **2018**, *187*, 638-649.
50. Liu, L.; Hong, D.; Guo, X., A study of metals promoted CaO-based CO<sub>2</sub> sorbents for high temperature application by combining experimental and DFT calculations. *Journal of CO<sub>2</sub> Utilization* **2017**, *22*, 155-163.
51. Fang, H.; Haibin, L.; Zengli, Z., Advancements in development of chemical-looping combustion: A review. *Int. J. Chem. Eng.* **2009**, *2009*, 1-16.
52. Bao, J.; Li, Z.; Cai, N., Interaction between iron-based oxygen carrier and four coal ashes during chemical looping combustion. *Applied Energy* **2014**, *115*, 549-558.

53. Schmitz, M.; Linderholm, C. J., Performance of calcium manganate as oxygen carrier in chemical looping combustion of biochar in a 10kW pilot. *Applied Energy* **2016**, *169*, 729-737.
54. Idziak, K.; Czakiert, T.; Krzywanski, J.; Zylka, A.; Kozłowska, M.; Nowak, W., Safety and environmental reasons for the use of Ni-, Co-, Cu-, Mn- and Fe-based oxygen carriers in CLC/CLOU applications: An overview. *Fuel* **2020**, *268*, 117245.
55. Akram, W.; Sanjay; Hassan, M. A., Chemical looping combustion with nanosize oxygen carrier: a review. *International Journal of Environmental Science and Technology* **2020**.
56. Ahmed, I., Syngas Chemical Looping Combustion Using A Fluidizable Oxygen Carrier: Reactivity, Kinetics, Reactor Simulation. **2018**.
57. Cao, Y.; He, B.; Yan, L., Cyclic reactivity of the sol-gel and graphite impregnation-derived Cu-based oxygen carriers for chemical looping with oxygen uncoupling. *J. Therm. Anal. Calorim.* **2020**.
58. Merrett, K. M.; Whitty, K. J., Evaluation of coal conversion pathways in fluidized bed chemical looping combustion with oxygen uncoupling (CLOU). *Fuel* **2019**, *258*, 116157.
59. Dai, J.; Whitty, K. J., Impact of fuel-derived chlorine on CuO-based oxygen carriers for chemical looping with oxygen uncoupling. *Fuel* **2020**, *263*, 116780.
60. Zhao, H.; Tian, X.; Ma, J.; Su, M.; Wang, B.; Mei, D., Development of tailor-made oxygen carriers and reactors for chemical looping processes at Huazhong University of Science & Technology. *Int. J. Greenh. Gas Con.* **2020**, *93*, 102898.
61. Mendiara, T.; Pérez, R.; Abad, A.; de Diego, L. F.; García-Labiano, F.; Gayán, P.; Adánez, J., Low-Cost Fe-Based Oxygen Carrier Materials for the iG-CLC Process with Coal. 1. *Industrial & Engineering Chemistry Research* **2012**, *51* (50), 16216-16229.
62. Gayán, P.; Luis, F.; García-Labiano, F.; Adánez, J.; Abad, A.; Dueso, C., Effect of support on reactivity and selectivity of Ni-based oxygen carriers for chemical-looping combustion. *Fuel* **2008**, *87* (12), 2641-2650.
63. Feng, Y.; Cai, X.; Guo, X.; Zheng, C., Influence mechanism of H<sub>2</sub>S on the reactivity of Ni-based oxygen carriers for chemical-looping combustion. *Chem. Eng. J.* **2016**, *295*, 461-467.
64. Ryu, H. J.; Shun, D.; Bae, D. H.; Park, M. H., Syngas combustion characteristics of four oxygen carrier particles for chemical-looping combustion in a batch fluidized bed reactor. *Korean J. Chem. Eng.* **2009**, *26*, 523-527.
65. Cai, X.; Wang, X.; Guo, X.; Zheng, C. g., Mechanism study of reaction between CO and NiO(001) surface during chemical-looping combustion: Role of oxygen. *Chem. Eng. J.* **2014**, *244*, 464-472.
66. Zeng, L.; Luo, S. W.; Sridhar, D.; Fan, L. S., Chemical looping processes - particle characterization, ionic diffusion-reaction mechanism and reactor engineering. *Rev. Chem. Eng.* **2012**, *28* (1), 1-42.
67. Li, D.; Xu, R.; Gu, Z.; Zhu, X.; Qing, S.; Li, K., Chemical - Looping Conversion of Methane: A Review. *Energy Technology* **2019**, *8* (8), 1900925.
68. Luo, S. W.; Zeng, L.; Fan, L. S., Chemical Looping Technology: Oxygen Carrier Characteristics. *Annu. Rev. Chem. Biomol.* **2015**, *6*, 53-75.
69. Wang, B.; Moldenhauer, P.; Leon, H., Using Mn-Si oxygen carriers supported with CaO or Al<sub>2</sub>O<sub>3</sub> for converting methane and syngas in chemical-looping with oxygen uncoupling (CLOU). *Fuel Process. Technol.* **2020**, *201*, 106315.
70. Kane, T.; Guerrero-Caballero, J.; Löfberg, A., Chemical looping selective oxidation of H<sub>2</sub>S using V<sub>2</sub>O<sub>5</sub> impregnated over different supports as oxygen carriers. *ChemCatChem* **2020**.
71. Feng, Y.; Wang, N.; Guo, X.; Zhang, S., Dopant screening of modified Fe<sub>2</sub>O<sub>3</sub> oxygen carriers in chemical looping hydrogen production. *Fuel* **2020**, *262*, 116489.

72. Liu, L.; Li, Z.; Wang, L.; Zhao, Z.; Li, Y.; Cai, N., MgO–Kaolin-Supported Manganese Ores as Oxygen Carriers for Chemical Looping Combustion. *Industrial & Engineering Chemistry Research* **2019**, *59* (15), 7238-7246.
73. Protasova, L.; Snijkers, F., Recent Developments in Oxygen Carrier Materials for Hydrogen Production via Chemical Looping Processes. *Fuel* **2016**, *181*, 75-93.
74. Ma, S. W.; Chen, S. Y.; Soomro, A.; Xiang, W. G., Effects of CeO<sub>2</sub>, ZrO<sub>2</sub>, and Al<sub>2</sub>O<sub>3</sub> Supports on Iron Oxygen Carrier for Chemical Looping Hydrogen Generation. *Energy Fuels* **2017**, *31* (8), 8001-8013.
75. Hossain, M. M.; de Lasa, H. I., Chemical-looping combustion (CLC) for inherent CO<sub>2</sub> separations—a review. *Chemical Engineering Science* **2008**, *63* (18), 4433-4451.
76. Liu, F.; Chen, L. Y.; Neathery, J. K.; Saito, K.; Liu, K. L., Cerium Oxide Promoted Iron-based Oxygen Carrier for Chemical Looping Combustion. *Industrial & Engineering Chemistry Research* **2014**, *53* (42), 16341-16348.
77. Hossain, M. M.; Lasa, H. I. d., Reactivity and Stability of Co-Ni/ Al<sub>2</sub>O<sub>3</sub> Oxygen Carrier in Multicycle CLC. *AIChE Journal* **2007**, *53*, 1817-1829.
78. Ma, S. W.; Chen, S. Y.; Soomro, A.; Zhu, M.; Xiang, W. G., Characterization of Fe<sub>2</sub>O<sub>3</sub>/CeO<sub>2</sub> oxygen carriers for chemical looping hydrogen generation. *Int. J. Hydrogen Energy* **2018**, *43* (6), 3154-3164.
79. Son, N.; Do, J. Y.; Park, N.-K.; Kim, U. S.; Baek, J.-I.; Lee, D.; Ryu, H.-J.; Kang, M., Oxygen transfer capacity of the copper component introduced into the defected-MgMnAlO<sub>4</sub> spinel structure in CH<sub>4</sub>-CO<sub>2</sub>/air redox cycles. *Korean J. Chem. Eng.* **2019**, *36* (12), 1971-1982.
80. Cheng, Z.; Baser, D. S.; Nadgouda, S. G.; Qin, L.; Fan, J. A.; Fan, L.-S., C<sub>2</sub> Selectivity Enhancement in Chemical Looping Oxidative Coupling of Methane over a Mg–Mn Composite Oxygen Carrier by Li-Doping-Induced Oxygen Vacancies. *ACS Energy Letters* **2018**, *3* (7), 1730-1736.
81. Rasoulian, S.; Ricardez-Sandoval, L. A., A robust nonlinear model predictive controller for a multiscale thin film deposition process. *Chemical Engineering Science* **2015**, *136*, 38-49.
82. Chen, Y.; Vlachos, D. D. G. In *Dehydrogenation, Hydrogenolysis and Oxidation of Ethane on Pt: Density Functional Theory Study and Microkinetic Analysis*, Proceedings of the 2009 AIChE Annual Meeting, Nashville, TN, USA, 2009; pp 8-13.
83. Goyal, H.; Vlachos, D. G., Multiscale modeling of microwave-heated multiphase systems. *Chem. Eng. J.* **2020**, 125262.
84. Xie, L.; Zhang, L.; Hu, T.; Huang, H.; Yi, Z., Neural networks model based on an automated multi-scale method for mammogram classification. *Knowledge-Based Systems* **2020**, *208*, 106465.
85. Kimaev, G.; Ricardez-Sandoval, L. A., A comparison of efficient uncertainty quantification techniques for stochastic multiscale systems. *AIChE Journal* **2017**, *63* (8), 3361-3373.
86. Chaffart, D.; Ricardez-Sandoval, L. A., Optimization and control of a thin film growth process: A hybrid first principles/artificial neural network based multiscale modelling approach. *Computers & Chemical Engineering* **2018**, *119*, 465-479.
87. Ren, B.; Li, J.; Wen, G.; Ricardez-Sandoval, L.; Croiset, E., First-Principles Based Microkinetic Modeling of CO<sub>2</sub> Reduction at the Ni/SDC Cathode of a Solid Oxide Electrolysis Cell. *The Journal of Physical Chemistry C* **2018**, *122* (37), 21151-21161.
88. Chaffart, D. Uncertainty Analysis and Robust Optimization of a Single Pore in a Heterogeneous Catalytic Flow Reactor System. University of Waterloo, 2017.
89. Ricardez-Sandoval, L. a., Current challenges in the design and control of multiscale systems. *The Canadian Journal of Chemical Engineering* **2011**, *89*, 1324-1341.

90. Choi, Y.; Liu, P., Understanding of ethanol decomposition on Rh(111) from density functional theory and kinetic Monte Carlo simulations. *Catalysis Today* **2011**, *165*, 64-70.
91. Li, J.; Croiset, E.; Ricardez-Sandoval, L., Carbon nanotube growth: First-principles-based kinetic Monte Carlo model. *J. Catal.* **2015**, *326*, 15-25.
92. You, H.; Yuan, Y.; Li, J.; Sandoval, L. R., A Multi-scale model for CO<sub>2</sub> capture: A Nickel-based oxygen carrier in Chemical-looping Combustion. *IFAC-PapersOnLine* **2018**, *51* (18), 97-102.
93. Orio, M.; Pantazis, D. A.; Neese, F., Density functional theory. *Photosynth. Res.* **2009**, *102*, 443-453.
94. Gu, G. H.; Choi, C.; Lee, Y.; Situmorang, A. B.; Noh, J.; Kim, Y. H.; Jung, Y., Progress in Computational and Machine-Learning Methods for Heterogeneous Small-Molecule Activation. *Adv. Mater.* **2020**, *32* (35), e1907865.
95. Lyon, K. From Fundamentals to Spectroscopic Applications of Density Functional Theory. UWSpace, 2020.
96. Perdew, J. P.; Zunger, A., Self-interaction correction to density-functional approximations for many-electron systems. *Phys. Rev. B* **1981**, *23* (10), 5048-5079.
97. Perdew, J. P.; Burke, K.; Ernzerhof, M., Generalized gradient approximation made simple. *Phys. Rev. Lett.* **1996**, *77* (18), 3865.
98. Zahariev, F.; Leang, S. S.; Gordon, M. S., Functional derivatives of meta-generalized gradient approximation (meta-GGA) type exchange-correlation density functionals. *J Chem Phys* **2013**, *138* (24), 244108.
99. Parr, R. G., *Density-functional theory of atoms and molecules*. Oxford University Press: New York, 1989.
100. Sholl, D.; Steckel, J. A., *Density functional theory: a practical introduction*. John Wiley & Sons: 2011.
101. Feng, Y.; Wang, N.; Guo, X., Influence mechanism of supports on the reactivity of Ni-based oxygen carriers for chemical looping reforming: A DFT study. *Fuel* **2018**, *229*, 88-94.
102. Bazhenova, E.; Honkala, K., Screening the bulk properties and reducibility of Fe-doped Mn<sub>2</sub>O<sub>3</sub> from first principles calculations. *Catalysis Today* **2017**, *285*, 104-113.
103. Li, W. Y.; Chen, Q. L., Density Functional Theory Study of Oxygen Carrier Mn<sub>3</sub>O<sub>4</sub>(001) surface Reaction with CO. *Advanced Materials Research* **2012**, *479*, 81-87.
104. Zhang, X.; Song, X.; Sun, Z.; Li, P.; Yu, J., Density functional theory study on the mechanism of calcium sulfate reductive decomposition by methane. *Fuel* **2013**, *110*, 204-211.
105. Qin, W.; Lin, C. F.; Long, D. T.; Xiao, X. B.; Dong, C. Q., Reaction Activity and Deep Reduction Reaction Mechanism of a High Index Iron Oxide Surface in Chemical Looping Combustion. *Acta Physico-Chimica Sinica* **2015**, *31*, 667-675.
106. Lin, C.; Qin, W.; Dong, C., Reduction effect of  $\alpha$ -Fe<sub>2</sub>O<sub>3</sub> on carbon deposition and CO oxidation during chemical-looping combustion. *Chem. Eng. J.* **2016**, *301*, 257-265.
107. Zhang, J.; Qin, W.; Dong, C.; Yang, Y., Density Functional Theory Study of Elemental Mercury Adsorption on Fe<sub>2</sub>O<sub>3</sub>[104] and Its Effect on Carbon Deposit during Chemical Looping Combustion. *Energ. Fuel.* **2016**, *30*, 3413-3418.
108. Wang, L.; Wu, L.; Dong, C.; Zhang, J.; Qin, W., Theoretical study on reactivity of Fe-based oxygen carrier with CH<sub>4</sub> during chemical looping combustion. *Applied Mechanics and Materials* **2013**, *345*, 298-301.
109. Huang, L.; Tang, M.; Fan, M.; Cheng, H., Density functional theory study on the reaction between hematite and methane during chemical looping process. *Applied Energy* **2015**, *159*, 132-144.

110. Tang, J. J.; Liu, B., Reactivity of the  $\text{Fe}_2\text{O}_3(0001)$  Surface for Methane Oxidation: A GGA + U Study. *Journal of Physical Chemistry C* **2016**, *120*, 6642-6650.
111. Kang, Y.; Tian, M.; Huang, C.; Lin, J.; Hou, B.; Pan, X.; Li, L.; Rykov, A. I.; Wang, J.; Wang, X., Improving Syngas Selectivity of  $\text{Fe}_2\text{O}_3/\text{Al}_2\text{O}_3$  with Yttrium Modification in Chemical Looping Methane Conversion. *ACS Catal.* **2019**, *9* (9), 8373-8382.
112. Bennett, J. W.; Huang, X.; Fang, Y.; Cwiertny, D. M.; Grassian, V. H.; Mason, S. E., Methane Dissociation on  $\alpha\text{-Fe}_2\text{O}_3(0001)$  and  $\text{Fe}_3\text{O}_4(111)$  Surfaces: First-Principles Insights into Chemical Looping Combustion. *The Journal of Physical Chemistry C* **2019**, *123* (11), 6450-6463.
113. Chang Qing, D.; Xiao Lei, Z.; Yong Ping, Y., Density Functional Study of the C Atom Adsorption on the  $\alpha\text{-Fe}_2\text{O}_3(001)$  Surface. *Chinese Journal of Structural Chemistry* **2011**, *30*, 17-24.
114. Qin, W.; Lin, C. F.; Long, D. T.; Wang, J. Y.; Dong, C. Q., Activity of  $\text{Fe}_2\text{O}_3$  with a high index facet for bituminous coal chemical looping combustion: a theoretical and experimental study. *RSC Adv.* **2016**, *6*, 85551-85558.
115. Miller, D. D.; Riley, J.; Siriwardane, R., Interaction of Methane with Calcium Ferrite in the Chemical Looping Partial Oxidation Application: Experimental and DFT Study. *Energy Fuels* **2019**, *34* (2), 2193-2204.
116. Dong, C.; Liu, X.; Qin, W.; Lu, Q.; Wang, X.; Shi, S.; Yang, Y., Deep reduction behavior of iron oxide and its effect on direct CO oxidation. *Appl. Surf. Sci.* **2012**, *258*, 2562-2569.
117. Qin, W.; Chen, Q.; Wang, Y.; Dong, C.; Zhang, J.; Li, W.; Yang, Y., Theoretical Study of Oxidation-reduction Reaction of  $\text{Fe}_2\text{O}_3$  Supported on MgO during Chemical Looping Combustion. *Appl. Surf. Sci.* **2013**, *266*, 350-354.
118. Zhao, H.; Zhang, Y.; Wei, Y.; Gui, J., Understanding CuO-support interaction in Cu-based oxygen carriers at a microcosmic level. *Proceedings of the Combustion Institute* **2017**, *36*, 4069-4077.
119. Xu, Z.; Zhao, H.; Wei, Y.; Zheng, C., Self-assembly template combustion synthesis of a core-shell  $\text{CuO}@(\text{TiO}_2\text{-Al}_2\text{O}_3)$  hierarchical structure as an oxygen carrier for the chemical-looping processes. *Combust. Flame* **2015**, *162*, 3030-3045.
120. Li, W.; Chen, Q.; Qin, W.; Wang, N.; Lai, J., Interaction of CO with CuO and CuO/graphene: Reactions mechanism and the Formation of  $\text{CO}_2$ . *Advanced Materials Research* **2012**, *354*, 279-285.
121. Wang, M.; Liu, J.; Shen, F.; Cheng, H.; Dai, J.; Long, Y., Theoretical Study of Stability and Reaction Mechanism of CuO Supported on  $\text{ZrO}_2$  during Chemical Looping Combustion. *Appl. Surf. Sci.* **2016**, *367*, 485-492.
122. Wang, M.; Liu, J.; Hu, J.; Liu, F.,  $\text{O}_2\text{-CO}_2$  Mixed Gas Production Using a Zr-Doped Cu-Based Oxygen Carrier. *Industrial and Engineering Chemistry Research* **2015**, *54*, 9805-9812.
123. Zheng, C.; Cao, J.; Zhang, Y.; Zhao, H., Insight into the Oxidation Mechanism of a Cu-Based Oxygen Carrier ( $\text{Cu} \rightarrow \text{Cu}_2\text{O} \rightarrow \text{CuO}$ ) in Chemical Looping Combustion. *Energy Fuels* **2020**, *34* (7), 8718-8725.
124. Li, L.; Wang, H.; Han, J.; Zhu, X.; Ge, Q., A density functional theory study on reduction-induced structural transformation of copper-oxide-based oxygen carrier. *J Chem Phys* **2020**, *152* (5), 054709.
125. Qin, L.; Cheng, Z.; Guo, M.; Fan, J. a.; Fan, L. S., Morphology evolution and nanostructure of chemical looping transition metal oxide materials upon redox processes. *Acta Mater.* **2017**, *124*, 568-578.
126. Haribal, V. P.; He, F.; Mishra, A.; Li, F., Iron-Doped  $\text{BaMnO}_3$  for Hybrid Water Splitting and Syngas Generation. *ChemSusChem* **2017**, *10*, 3402-3408.

127. Curnan, M. T.; Kitchin, J. R., Effects of Concentration, Crystal Structure, Magnetism, and Electronic Structure Method on First-Principles Oxygen Vacancy Formation Energy Trends in Perovskites. *The Journal of Physical Chemistry C* **2014**, *118*, 28776-28790.
128. Zhang, L.; Xu, W.; Wu, J.; Hu, Y.; Huang, C.; Zhu, Y.; Tian, M.; Kang, Y.; Pan, X.; Su, Y.; Wang, J.; Wang, X., Identifying the Role of A-Site Cations in Modulating Oxygen Capacity of Iron-Based Perovskite for Enhanced Chemical Looping Methane-to-Syngas Conversion. *ACS Catal.* **2020**, *10* (16), 9420-9430.
129. Sun, R.; Yan, J.; Shen, L.; Bai, H., Performance and mechanism study of LaFeO<sub>3</sub> for biomass chemical looping gasification. *Journal of Materials Science* **2020**, *55* (25), 11151-11166.
130. Liu, F.; Liu, J.; Yang, Y.; Wang, X., A mechanistic study of CO oxidation over spinel MnFe<sub>2</sub>O<sub>4</sub> surface during chemical-looping combustion. *Fuel* **2018**, *230*, 410-417.
131. Liu, F.; Liu, J.; Yang, Y.; Wang, Z.; Zheng, C., Reaction mechanism of spinel CuFe<sub>2</sub>O<sub>4</sub> with CO during chemical-looping combustion: An experimental and theoretical study. *Proceedings of the Combustion Institute* **2019**, *37* (4), 4399-4408.
132. Liu, F.; Dai, J.; Liu, J.; Yang, Y.; Fang, R., Density Functional Theory Study on the Reaction Mechanism of Spinel CoFe<sub>2</sub>O<sub>4</sub> with CO during Chemical-Looping Combustion. *The Journal of Physical Chemistry C* **2019**, *123* (28), 17335-17342.
133. Li, T.; Wu, Q.; Wang, W.; Xiao, Y.; Liu, C.; Yang, F., Solid-solid reaction of CuFe<sub>2</sub>O<sub>4</sub> with C in chemical looping system: A comprehensive study. *Fuel* **2020**, *267*, 117163.
134. Li, F.; Luo, S.; Sun, Z.; Bao, X.; Fan, L.-S., Role of metal oxide support in redox reactions of iron oxide for chemical looping applications: experiments and density functional theory calculations. *Energy Environ. Sci.* **2011**, *4*, 3661-3667.
135. Ridha, F. N.; Duchesne, M. A.; Lu, X.; Lu, D. Y.; Filippou, D.; Hughes, R. W., Characterization of an ilmenite ore for pressurized chemical looping combustion. *Applied Energy* **2016**, *163*, 323-333.
136. Jin, Y.; Sun, C.; Su, S., Experimental and theoretical study of the oxidation of ventilation air methane over Fe<sub>2</sub>O<sub>3</sub> and CuO. *Phys Chem Chem Phys* **2015**, *17* (25), 16277-84.
137. Zheng, C.; Zhao, H., Exploring the microscopic reaction mechanism of H<sub>2</sub>S and COS with CuO oxygen carrier in chemical looping combustion. *Fuel Process. Technol.* **2020**, *205*, 106431.
138. Ma, J.; Wang, C.; Zhao, H.; Tian, X., Sulfur fate during the lignite pyrolysis process in a chemical looping combustion environment. *Energy Fuels* **2017**, *32* (4), 4493-4501.
139. Wang, X.; Jayathilake, R.; Taylor, D. D.; Rodriguez, E. E.; Zachariah, M. R., Study of C/doped δ-Bi<sub>2</sub>O<sub>3</sub> redox reactions by in operando synchrotron X-ray diffraction: bond energy/oxygen vacancy and reaction kinetics relationships. *The Journal of Physical Chemistry C* **2018**, *122* (16), 8796-8803.
140. Zhu, Y.; Liu, R.; Sun, X.; Ma, X.; Wang, X.; Tian, H., Metal modified hexaaluminates for syngas generation and CO<sub>2</sub> utilization via chemical looping. *Int. J. Hydrogen Energy* **2019**, *44* (21), 10218-10231.
141. Zhao, K.; Zheng, A.; Li, H.; He, F.; Huang, Z.; Wei, G.; Shen, Y.; Zhao, Z., Exploration of the mechanism of chemical looping steam methane reforming using double perovskite-type oxides La<sub>1.6</sub>Sr<sub>0.4</sub>FeCoO<sub>6</sub>. *Applied Catalysis B: Environmental* **2017**, *219*, 672-682.
142. Jiang, Q.; Zhang, H.; Cao, Y.; Hong, H.; Jin, H., Solar hydrogen production via perovskite-based chemical-looping steam methane reforming. *Energy Convers. Manage.* **2019**, *187*, 523-536.
143. Wang, Y.; Niu, P.; Zhao, H., Chemical looping gasification of coal using calcium ferrites as oxygen carrier. *Fuel Process. Technol.* **2019**, *192*, 75-86.
144. Mishra, A.; Li, T.; Li, F.; Santiso, E. E., Oxygen Vacancy Creation Energy in Mn-Containing Perovskites: An Effective Indicator for Chemical Looping with Oxygen Uncoupling. *Chemistry of Materials* **2018**, *31* (3), 689-698.

145. Son, N.; Do, J. Y.; Park, N.-K.; Ryu, S. O.; Kim, U. S.; Baek, J.-I.; Lee, D.; Ryu, H.-J.; Kang, M., Improvement of oxygen transfer capacity by migration of oxygen defects formed in  $\text{Cu}_x\text{Mg}_{1-x}\text{Fe}_y\text{Ti}_{2-y}\text{O}_z$  particles. *Journal of Industrial and Engineering Chemistry* **2019**, *76*, 355-365.
146. Hanselman, C. L.; Tafen, D. N.; Alfonso, D. R.; Lekse, J. W.; Matranga, C.; Miller, D. C.; Gounaris, C. E., A framework for optimizing oxygen vacancy formation in doped perovskites. *Computers & Chemical Engineering* **2019**, *126*, 168-177.
147. Hwang, J. H., Effect of  $\text{Ce}_{0.9}\text{Gd}_{0.1}\text{O}_{1.95}$  as a promoter upon the oxygen transfer properties of  $\text{MgMnO}_{3-\delta}\text{Ce}_{0.9}\text{Gd}_{0.1}\text{O}_{1.95}$  composite oxygen carrier materials for chemical looping combustion. *Journal of Ceramic Processing Research* **2019**, *20* (1), 18-23.
148. Ma, Z.; Xiao, R.; Chen, L., Kinetics of sintering induced surface area decay of iron oxide in the reduction process of chemical looping combustion. *Fuel Process. Technol.* **2017**, *168*, 20-26.
149. Ren, X. Y.; Niu, C. Y.; Yi, S.; Li, S.; Cho, J. H., Hydrogen adsorption induced nanomagnetism at the  $\text{Si}(111)-(7 \times 7)$  surface. *Physical Review B* **2018**, *98* (19), 195424.
150. Zhang, S.; Li, Y.; Shi, C.; Guo, F.; He, C.; Cao, Z.; Hu, J.; Cui, C.; Liu, H., Induced-fit adsorption of diol-based porous organic polymers for tetracycline removal. *Chemosphere* **2018**, *212*, 937-945.
151. Wang, J.; Yang, M.; Deng, D.; Qiu, S., The adsorption of  $\text{NO}$ ,  $\text{NH}_3$ ,  $\text{N}_2$  on carbon surface: a density functional theory study. *Journal of Molecular Modeling* **2017**, *23* (9), 262.
152. Huang, X.; Chu, W.; Sun, W.; Jiang, C.; Feng, Y.; Xue, Y., Investigation of oxygen-containing group promotion effect on  $\text{CO}_2$ -coal interaction by density functional theory. *Appl. Surf. Sci.* **2014**, *299*, 162-169.
153. Gauthier, Y.; Schmid, M.; Padovani, S.; Lundgren, E.; Bus, V.; Kresse, G.; Redinger, J.; Varga, P., Adsorption sites and ligand effect for  $\text{CO}$  on an alloy surface: a direct view. *Phys. Rev. Lett.* **2001**, *87* (3), 036103.
154. Wang, H.; Schneider, W. F., Effects of coverage on the structures, energetics, and electronics of oxygen adsorption on  $\text{RuO}_2(110)$ . *J Chem Phys* **2007**, *127* (6), 064706.
155. Wang, Y.; Xia, X.; Urban, A.; Qiu, H.; Strunk, J.; Meyer, B.; Muhler, M.; Woll, C., Tuning the reactivity of oxide surfaces by charge-accepting adsorbates. *Angew Chem Int Ed Engl* **2007**, *46* (38), 7315-8.
156. Futamata, M.; Luo, L., Adsorbed water and  $\text{CO}$  on Pt electrode modified with Ru. *J. Power Sources* **2007**, *164* (2), 532-537.
157. Sharma, A.; Srivastava, A.; Husain, M.; Khan, M. S., Computational investigations of Cu-embedded  $\text{MoS}_2$  sheet for  $\text{CO}$  oxidation catalysis. *Journal of Materials Science* **2018**, *53* (13), 9578-9588.
158. Vazquez-Arenas, J.; Ramos-Sanchez, G.; Franco, A. A., A multi-scale model of the oxygen reduction reaction on highly active graphene nanosheets in alkaline conditions. *J. Power Sources* **2016**, *328*, 492-502.
159. Majumder, D.; Broadbelt, L. J., A multiscale scheme for modeling catalytic flow reactors. *AIChE Journal* **2006**, *52* (12), 4214-4228.
160. Voter, A., Introduction To the Kinetic Monte Carlo Method. *Radiation Effects in Solids* **2007**, *235*, 1-23.
161. Beeler, J. R., Displacement spikes in cubic metals. i.  $\alpha$ -iron, copper, and tungsten. *Physical Review* **1966**, *150*, 470-487.
162. Cheng, Z.; Qin, L.; Fan, J. A.; Fan, L.-S., New insight into the development of oxygen carrier materials for chemical looping systems. *Engineering* **2018**.



163. Qin, L.; Guo, M.; Liu, Y.; Cheng, Z.; Fan, J. A.; Fan, L.-S., Enhanced methane conversion in chemical looping partial oxidation systems using a copper doping modification. *Applied Catalysis B: Environmental* **2018**, *235*, 143-149.
164. Ruan, C.; Huang, Z.-Q.; Lin, J.; Li, L.; Liu, X.; Tian, M.; Huang, C.; Chang, C.-R.; Li, J.; Wang, X., Synergy of the catalytic activation on Ni and the CeO<sub>2</sub>-TiO<sub>2</sub>/Ce<sub>2</sub>Ti<sub>2</sub>O<sub>7</sub> stoichiometric redox cycle for dramatically enhanced solar fuel production. *Energy Environ. Sci.* **2019**, *12* (2), 767-779.
165. Daggash, H. A.; Heuberger, C.; Mac Dowell, N., The role and value of negative emissions technologies in decarbonising the UK energy system. *Int. J. Greenh. Gas Con.* **2019**, *81*, 181-198.
166. Yuan, Y.; Dong, X.; Ricardez-Sandoval, L., A density functional theory analysis on syngas adsorption on NiO (100) surface. *Appl. Surf. Sci.* **2019**, *498*, 143782.
167. Blöchl, P. E., Projector augmented-wave method. *Phys. Rev. B* **1994**, *50* (24), 17953.
168. Kresse, G.; Joubert, D., From ultrasoft pseudopotentials to the projector augmented-wave method. *Phys. Rev. B* **1999**, *59* (3), 1758.
169. Li, L.; Mi, J.; Yong, Y.; Mao, B.; Shi, W., First-principles study on the lattice plane and termination dependence of the electronic properties of the NiO/CH<sub>3</sub>NH<sub>3</sub>PbI<sub>3</sub> interfaces. *Journal of Materials Chemistry C* **2018**, *6* (30), 8226-8233.
170. Qin, L.; Cheng, Z.; Fan, J. A.; Kopechek, D.; Xu, D.; Deshpande, N.; Fan, L.-S., Nanostructure formation mechanism and ion diffusion in iron-titanium composite materials with chemical looping redox reactions. *J. Mater. Chem. A* **2015**, *3* (21), 11302-11312.
171. Li, L.; Kanai, Y., Antiferromagnetic structures and electronic energy levels at reconstructed NiO(111) surfaces: A DFT+U study. *Phys. Rev. B* **2015**, *91* (23), 23530.
172. Peng, G.; Merte, L. R.; Knudsen, J.; Vang, R. T.; Lægsgaard, E.; Besenbacher, F.; Mavrikakis, M., On the Mechanism of Low-Temperature CO Oxidation on Ni(111) and NiO(111) Surfaces. *The Journal of Physical Chemistry C* **2010**, *114* (49), 21579-21584.
173. Yang, M.-C.; Xu, B.; Meng, S.; Cheng, J.-H.; Pan, C.-J.; Hwang, B.-J., Electronic, Structural and Electrochemical Properties of LiNi<sub>x</sub> Cu<sub>y</sub>Mn<sub>2-x-y</sub>O<sub>4</sub> (0 < x < 0.5, 0 < y < 0.5) High-Voltage Cathode Materials in Li-Ion Batteries. In *The Electrochemical Society*, 2010; pp 1009-1009.
174. Rohrbach, A.; Hafner, J., Molecular adsorption of NO on NiO(100): DFT and DFT+U calculations. *Phys. Rev. B* **2005**, *71* (4), 045405.
175. Ferrari, A. M.; Pisani, C.; Cincini, F.; Giordano, L.; Pacchioni, G., Cationic and anionic vacancies on the NiO(100) surface: DFT+U and hybrid functional density functional theory calculations. *J Chem Phys* **2007**, *127* (17), 174711.
176. Klüner, T.; Freund, H. J.; Freitag, J.; Staemmler, V., Laser - induced desorption of NO from NiO(100): Ab initio calculations of potential surfaces for intermediate excited states. *J. Chem. Phys.* **1996**, *104* (24), 10030-10040.
177. Yan, M.; Chen, S.; Mitchell, T.; Gay, D.; Vyas, S.; Grimes, R., Atomistic studies of energies and structures of (hk0) surfaces in NiO. *Philos. Mag. A* **1995**, *72* (1), 121-138.
178. Tasker, P.; Duffy, D., The structure and properties of the stepped surfaces of MgO and NiO. *Surf. Sci.* **1984**, *137* (1), 91-102.
179. Mehdaoui, I.; Klüner, T., Bonding of CO and NO to NiO (100): a strategy for obtaining accurate adsorption energies. *J. Phys. Chem. A* **2007**, *111* (50), 13233-13237.
180. Jayapal, P.; Sundararajan, M.; Hillier, I. H.; Burton, N. A., How are the ready and unready states of nickel-iron hydrogenase activated by H<sub>2</sub>? A density functional theory study. *Phys. Chem. Chem. Phys.* **2006**, *8* (35), 4086-4094.

181. Hoefl, J. T.; Kittel, M.; Polcik, M.; Bao, S.; Toomes, R. L.; Kang, J. H.; Woodruff, D. P.; Pascal, M.; Lamont, C. L., Molecular adsorption bond lengths at metal oxide surfaces: failure of current theoretical methods. *Phys. Rev. Lett.* **2001**, *87* (8), 086101.
182. Badenhop, J.; Weinhold, F., Natural steric analysis: Ab initio van der Waals radii of atoms and ions. *J. Chem. Phys.* **1997**, *107* (14), 5422-5432.
183. Wichtendahl, R.; Rodriguez-Rodrigo, M.; Härtel, U.; Kuhlenbeck, H.; Freund, H.-J., TDS study of the bonding of CO and NO to vacuum-cleaved NiO (100). *Surf. Sci.* **1999**, *423* (1), 90-98.
184. Rodriguez, J. A.; Hanson, J. C.; Frenkel, A. I.; Kim, J. Y.; Pérez, M., Experimental and theoretical studies on the reaction of H<sub>2</sub> with NiO: role of O vacancies and mechanism for oxide reduction. *J. Am. Chem. Soc.* **2002**, *124* (2), 346-354.
185. Sung, S. S.; Hoffmann, R., How carbon monoxide bonds to metal surfaces. *J. Am. Chem. Soc.* **1985**, *107* (3), 578-584.
186. Shi, X.; Bernasek, S. L.; Selloni, A., Formation, Electronic Structure, and Defects of Ni Substituted Spinel Cobalt Oxide: a DFT+U Study. *The Journal of Physical Chemistry C* **2016**, *120* (27), 14892-14898.
187. Sun, D.; Gu, X.-K.; Ouyang, R.; Su, H.-Y.; Fu, Q.; Bao, X.; Li, W.-X., Theoretical Study of the Role of a Metal-Cation Ensemble at the Oxide-Metal Boundary on CO Oxidation. *The Journal of Physical Chemistry C* **2012**, *116* (13), 7491-7498.
188. Huang, D.-M.; Cao, D.-B.; Li, Y.-W.; Jiao, H., Density function theory study of CO adsorption on Fe<sub>3</sub>O<sub>4</sub> (111) surface. *J. Phys. Chem. B* **2006**, *110* (28), 13920-13925.
189. Yu, X.; Zhang, X.; Jin, L.; Feng, G., CO adsorption, oxidation and carbonate formation mechanisms on Fe<sub>3</sub>O<sub>4</sub> surfaces. *Phys. Chem. Chem. Phys.* **2017**, *19* (26), 17287-17299.
190. Dueso, C.; García-Labiano, F.; Adánez, J.; Luis, F.; Gayán, P.; Abad, A., Syngas combustion in a chemical-looping combustion system using an impregnated Ni-based oxygen carrier. *Fuel* **2009**, *88* (12), 2357-2364.
191. Ahmed, I.; de Lasa, H., 110th Anniversary: Kinetic Model for Syngas Chemical Looping Combustion Using a Nickel-Based Highly Performing Fluidizable Oxygen Carrier. *Industrial & Engineering Chemistry Research* **2019**, *58* (8), 2801-2811.
192. Leion, H.; Mattisson, T.; Lyngfelt, A., Reduction Kinetics of Cu-, Ni-, and Fe-Based Oxygen Carriers Using Syngas (CO + H<sub>2</sub>) for Chemical-Looping Combustion. *Fuel* **2007**, *86* (12-13), 1947-1958.
193. Yuan, Y.; Dong, X.; Ricardez-Sandoval, L., A Multi-scale Simulation of Syngas Combustion Reactions by Ni-based Oxygen Carriers for Chemical Looping Combustion. *Appl. Surf. Sci.* **2020**, 147277.
194. Maintz, S.; Deringer, V. L.; Tchougreeff, A. L.; Dronskowski, R., LOBSTER: A tool to extract chemical bonding from plane-wave based DFT. *J. Comput. Chem.* **2016**, *37* (11), 1030-1035.
195. Dronskowski, R.; Blöchl, P. E., Crystal orbital Hamilton populations (COHP): energy-resolved visualization of chemical bonding in solids based on density-functional calculations. *J. Phys. Chem.* **1993**, *97* (33), 8617-8624.
196. Deringer, V. L.; Tchougreeff, A. L.; Dronskowski, R., Crystal orbital Hamilton population (COHP) analysis as projected from plane-wave basis sets. *J. Phys. Chem. A* **2011**, *115* (21), 5461-5466.
197. Jansen, A. P. J., *An introduction to kinetic Monte Carlo simulations of surface reactions*. Springer: 2012; Vol. 856.
198. Klessinger, M., Bond angle deformation and hybridization in H<sub>2</sub>O. *Chemical Physics Letters* **1969**, *4* (3), 144-146.

199. Wilson, S.; Gerratt, J., A self-consistent pair function study of the equilibrium bond angle of the water molecule. *Mol. Phys.* **1975**, *30* (3), 789-795.
200. Chaabouni, H.; Bergeron, H.; Baouche, S.; Dulieu, F.; Matar, E.; Congiu, E.; Gavilan, L.; Lemaire, J. L., Sticking coefficient of hydrogen and deuterium on silicates under interstellar conditions. *Astronomy & Astrophysics* **2012**, *538*, A128.
201. Mishra, A.; Li, F., Chemical looping at the nanoscale- challenges and opportunities. *Curr. Opin. Chem. Eng.* **2018**, *20*, 143-150.
202. Zeng, L.; Cheng, Z.; Fan, J. A.; Fan, L.-S.; Gong, J., Metal oxide redox chemistry for chemical looping processes. *Nature Reviews Chemistry* **2018**, *2* (11), 349-364.
203. Yuan, Y.; Dong, X.; Ricardez-Sandoval, L., Insights into Syngas Combustion on Defective NiO surface for Chemical Looping Combustion: Oxygen migration and Vacancy effects. *The Journal of Physical Chemistry C* **2020**, *10.1021/acs.jpcc.0c07144*.
204. Zhao, S.; Liu, H.-X.; Qiu, Y.; Liu, S.-Q.; Diao, J.-X.; Chang, C.-R.; Si, R.; Guo, X.-H., An oxygen vacancy-rich two-dimensional Au/TiO<sub>2</sub> hybrid for synergistically enhanced electrochemical N<sub>2</sub> activation and reduction. *Journal of Materials Chemistry A* **2020**, *8* (14), 6586-6596.
205. Ahmed, I.; de Lasa, H., Syngas chemical looping combustion using a highly performing fluidizable oxygen carrier. *Catalysis Today* **2020**, *343*, 63-71.
206. Ulissi, Z.; Prasad, V.; Vlachos, D. G., Effect of multiscale model uncertainty on identification of optimal catalyst properties. *J. Catal.* **2011**, *281* (2), 339-344.
207. Prasad, V.; Karim, A.; Arya, A.; Vlachos, D., Assessment of overall rate expressions and multiscale, microkinetic model uniqueness via experimental data injection: Ammonia decomposition on Ru/ $\gamma$ -Al<sub>2</sub>O<sub>3</sub> for hydrogen production. *Industrial & engineering chemistry research* **2009**, *48* (11), 5255-5265.
208. Kimaev, G.; Ricardez-Sandoval, L. A., Artificial Neural Network Discrimination for Parameter Estimation and Optimal Product Design of Thin Films Manufactured by Chemical Vapor Deposition. *The Journal of Physical Chemistry C* **2020**, *124* (34), 18615-18627.
209. Kimaev, G.; Ricardez-Sandoval, L. A., Nonlinear model predictive control of a multiscale thin film deposition process using artificial neural networks. *Chemical Engineering Science* **2019**, *207*, 1230-1245.
210. Kimaev, G.; Ricardez-Sandoval, L. A., Artificial Neural Networks for dynamic optimization of stochastic multiscale systems subject to uncertainty. *Chem. Eng. Res. Des.* **2020**, *161*, 11-25.

## Appendix A

### A1 Structural change due to the neighbouring effects

#### A1.1 CO oxidation

Table A1 Angle of O-C-O /°

	clean	CO	4CO	clean	H <sub>2</sub>	4H <sub>2</sub>
TSCo	124.26	108.811	128.707	124.26	179.394	179.882
Product	179.911	179.518	179.686	179.911	179.928	179.956

Table A2 Distance between reacted surface molecule and the surface from reactant to TSCo

/Å

	clean	CO	4CO	clean	H <sub>2</sub>	4H <sub>2</sub>
CO and the surface	2.068	2.081	2.067	2.068	2.136	2.058
Reacted O and the surface	1.384	1.975	1.433	1.384	3.664	3.457

Table A3 Distance between reacted surface molecule and the surface from TSCo to product

/Å

	clean	CO	4CO	clean	H <sub>2</sub>	4H <sub>2</sub>
Reacted O and the surface	1.384	1.975	1.433	1.384	3.664	3.457
CO <sub>2</sub> and the surface	3.739	4.077	5.302	3.739	3.628	4.301

#### A1.2 H<sub>2</sub> decomposition

Table A4 Angle of H-Ni-Ni /°

	clean	CO	3CO	clean	H <sub>2</sub>	3H <sub>2</sub>
TS <sub>H1</sub>	70.174	70.469	72.41	70.174	70.178	69.736
Product	90.037	89.29	89.202	90.037	90.687	89.799

Table A5 Bond distance of H-H /Å

	clean	CO	3CO	clean	H <sub>2</sub>	3H <sub>2</sub>
TS <sub>H1</sub>	1.743	1.763	1.804	1.743	1.75	1.741
Product	2.943	2.933	2.910	2.943	2.969	2.944

Table A6 Bond distance of Ni-H /Å

	clean	CO	3CO	clean	H <sub>2</sub>	3H <sub>2</sub>
TS <sub>H1</sub>	1.572	1.582	1.600	1.572	1.576	1.573
Product	1.437	1.461	1.450	1.437	1.462	1.439

### A1.3 H migration

Table A7 Bond distance of H-O /Å

	clean	CO	3CO	clean	H <sub>2</sub>	3H <sub>2</sub>
Reactant	2.574	2.553	2.552	2.574	2.568	2.556
TS <sub>H2</sub>	1.543	1.53	1.543	1.543	1.538	1.537
TS <sub>H2</sub>	1.543	1.53	1.543	1.543	1.538	1.537
Product	1.031	1.047	1.028	1.031	1.037	1.064

Table A8 Bond distance of Ni-H /Å

	clean	CO	3CO	clean	H <sub>2</sub>	3H <sub>2</sub>
TS <sub>H2</sub>	1.464	1.467	1.461	1.464	1.464	1.464
Product	1.645	1.682	1.61	1.645	1.644	1.659

Table A9 Angle of H-Ni-O /°

	clean	CO	3CO	clean	H <sub>2</sub>	3H <sub>2</sub>
TS <sub>H<sub>2</sub></sub>	90.992	91.412	91.329	90.992	91.114	90.921
Product	73.196	70.667	73.828	73.196	72.561	70.158

## A1.4 H<sub>2</sub>O formation

Table A10 Distance between reacted surface molecule and the surface from TS<sub>H<sub>3</sub></sub> to product /Å

	clean	CO	3CO	clean	H <sub>2</sub>	3H <sub>2</sub>
Reacted O and the surface	1.008	1.354	1.125	1.008	0.833	1.201
H <sub>2</sub> O and the surface	2.192	2.159	2.207	2.192	2.812	2.159

Table A11 Bond distance of Ni-H /Å

	clean	CO	3CO	clean	H <sub>2</sub>	3H <sub>2</sub>
Reactant	1.645	1.682	1.61	1.645	1.644	1.659
TS <sub>H<sub>3</sub></sub>	1.443	1.626	1.501	1.443	1.539	1.698

## A2 Neighbouring effects on activation energy

Table A12 Activation energy /eV

		Forward activation energy	Backward activation energy	$E_{\text{diff}}$
CO oxidation	clean surface	1.862	0.239	1.623
	CO	2.563	1.649	0.915
	4 CO	1.801	1.262	0.539
	H <sub>2</sub>	1.596	0.000	1.602
	4 H <sub>2</sub>	1.586	0.000	1.584
H <sub>2</sub> decomposition	clean surface	2.918	0.311	2.607
	CO	2.849	0.211	2.637
	3 CO	2.743	0.231	2.512
	H <sub>2</sub>	2.885	0.213	2.672
	3 H <sub>2</sub>	2.963	0.311	2.652
H migration	clean surface	0.347	2.103	-1.756
	CO	0.282	2.072	-1.790
	3 CO	0.301	1.480	-1.179
	H <sub>2</sub>	0.268	2.034	-1.766
	3 H <sub>2</sub>	0.484	2.324	-1.841
H <sub>2</sub> O formation		1.640	0.674	0.967
	CO	1.523	1.150	0.373
	3 CO	1.119	1.400	-0.281
	H <sub>2</sub>	1.142	0.086	1.055
	3 H <sub>2</sub>	5.536	4.456	1.080

### A3 Reaction parameters

Table A13 CO oxidation parameters /s<sup>-1</sup>

$N_{\text{CO}}$	$N_{\text{H}_2}$	Reaction parameter
1	0	$9.36 \times 10^1$
2	0	$1.99 \times 10^4$
3	0	$3.97 \times 10^4$
4	0	$5.95 \times 10^4$
0	1	$1.21 \times 10^5$
0	2	$3.00 \times 10^6$
0	3	$5.88 \times 10^6$
0	4	$8.76 \times 10^6$

1	1	$2.44 \times 10^5$
1	2	$1.11 \times 10^6$
2	1	$2.10 \times 10^5$
1	3	$2.52 \times 10^6$
2	2	$7.22 \times 10^5$
3	1	$2.07 \times 10^5$

Table A14 H<sub>2</sub> dissociation parameters

$N_{\text{CO}}$	$N_{\text{H}_2}$	Reaction parameter
1	0	$6.25 \times 10^{11}$
2	0	$1.21 \times 10^{12}$
3	0	$1.79 \times 10^{12}$
4	0	$2.37 \times 10^{12}$
0	1	$5.86 \times 10^{11}$
0	2	$3.28 \times 10^{11}$
0	3	$6.97 \times 10^{10}$
0	4	0.00
1	1	$6.29 \times 10^{11}$
1	2	$2.06 \times 10^{11}$
2	1	$6.07 \times 10^{11}$
1	3	$1.24 \times 10^3$
2	2	$1.54 \times 10^6$
3	1	$1.91 \times 10^9$

Table A15 H<sub>2</sub>O formation parameters

$N_{\text{CO}}$	$N_{\text{H}_2}$	Reaction parameter
1	0	$1.03 \times 10^7$
2	0	$2.16 \times 10^8$
3	0	$4.21 \times 10^8$
4	0	$6.26 \times 10^8$
0	1	$1.56 \times 10^8$
0	2	$7.80 \times 10^7$
0	3	$1.09 \times 10^{-10}$
0	4	0.00
1	1	$1.30 \times 10^8$
1	2	$7.49 \times 10^2$
2	1	$5.62 \times 10^5$
1	3	$1.58 \times 10^2$



2	2	$2.50 \times 10^4$
3	1	$3.96 \times 10^6$

---

## Appendix B

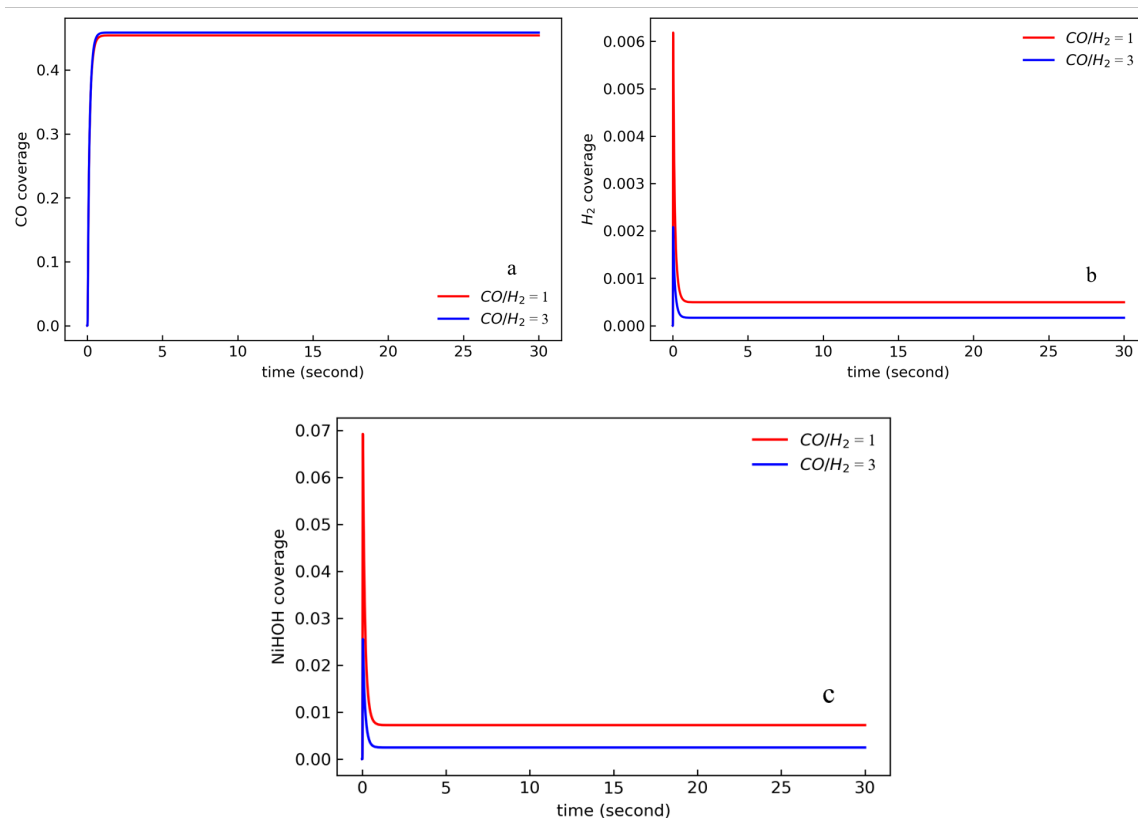


Figure B1 Coverage analysis of (a) the adsorbed CO, (b) the adsorbed  $H_2$  and (c) the surface NiHOH at compositions of  $CO/H_2 = 1$  (red) and  $CO/H_2 = 3$  (blue) in the gas phase

The coverage analysis of the studied system is presented in Figure B1 under the same operating condition presented in Figure 5-7. As shown in this figure, the coverages of the surface species share the same tendencies towards steady-state for the two syngas compositions considered in this analysis. The CO coverage reached steady-state fast because the reaction rate of CO oxidation is larger than that of the CO adsorption. Moreover, the coverage of the adsorbed  $H_2$  initially increased but then it experienced a decrease before reaching steady-state.

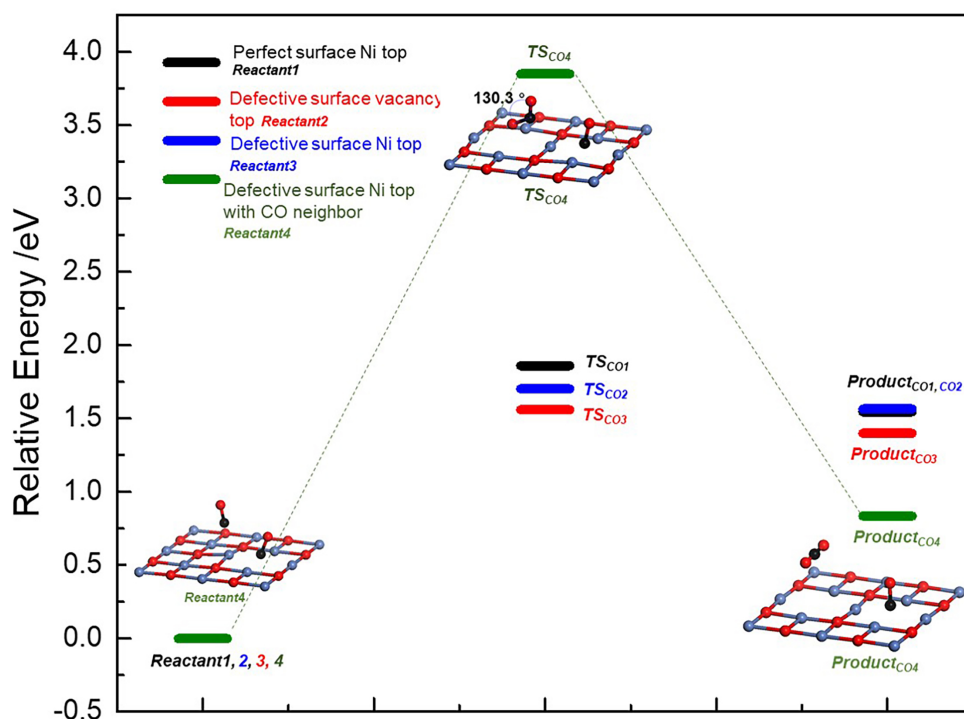


Figure B2 Comparison of the CO oxidation energy profile between the defective surface with a CO neighbor occupied at the adjacent vacancy top (green: from Reactant4 to Product<sub>CO4</sub> through TS<sub>CO4</sub>) and the perfect surface (black: from Reactant1 to Product<sub>CO1</sub> through TS<sub>CO1</sub>), the defective surface (blue: from Reactant2, CO adsorbed at vacancy top to Product<sub>CO2</sub> through TS<sub>CO2</sub>; red: from Reactant3, CO adsorbed at vacancy-adjacent Ni top to Product<sub>CO3</sub> through TS<sub>CO3</sub>)

This behaviour is due to the faster H<sub>2</sub> decomposition compared to H<sub>2</sub> adsorption. The drop in the H<sub>2</sub> coverage also resulted in a drop in the NiHOH coverage. Comparing the outcomes from the two different compositions reported in Figure S1, a higher syngas ratio of H<sub>2</sub> to CO resulted in larger coverages of H<sub>2</sub> and NiHOH and slightly lower coverage of CO.

Figure B2 presents the CO oxidation mechanism, from Reactant4 to Product<sub>CO4</sub> through TS<sub>CO4</sub>, on the defective surface with a CO neighbor occupying the adjacent vacancy top. The comparison between this studied configuration and the other studied systems shows that the CO neighbor at the adjacent vacancy top leads to larger forward and backward reaction barriers

than those observed in the other configurations. However, the difference between the forward and backward reaction barriers is much smaller on the defective surface with a nearest CO neighbor occupied at the vacancy site than those obtained on the perfect surface and the defective surfaces without any other absorbed molecules.

Table B1 Frequencies of clean surface mechanism	
	Imaginary frequency /cm <sup>-1</sup>
TS1 <sub>perfect</sub>	725.01
TS2 <sub>perfect</sub>	726.61
TS3 <sub>perfect</sub>	116.57

Table B1 presents the imaginary frequencies of the TSs of H<sub>2</sub> oxidation process on a perfect surface to verify the proposed mechanism.